Spatial Warping Techniques for Unstructured Transmission Line Modelling Method



Ekrem Altinozen

Faculty of Engineering

Department of Electrical and Electronic Engineering

The University of Nottingham

Thesis is submitted for the degree of

Doctor of Philosophy

Faculty of Engineering December 2022

I would like to dedicate this thesis to my loving parents and my grandparents who love and support me under all circumstances.

Declaration

I hereby declare that except where specific reference is made to the work of others, the contents of this dissertation are original and have not been submitted in whole or in part for consideration for any other degree or qualification in this, or any other University. This dissertation is the result of my own work and includes nothing which is the outcome of work done in collaboration, except where specifically indicated in the text. This dissertation contains less than 65,000 words including appendices, bibliography, footnotes, tables, and equations and has less than 150 figures.

Ekrem Altinozen

December 2022

Acknowledgements

During my PhD journey, I have received immense support from many individuals who have made this thesis possible. First and foremost, I would like to thank my supervisors Prof. Ana Vukovic, Prof. Phillip D. Sewell, and Prof. Ian Harrison, who have given me this great opportunity to carry out my PhD and to fulfil my passion to study electromagnetic applications. I have been extremely fortunate to have had such an approachable supervisor, Prof. Ana Vukovic, who despite my initial shortcomings, had the capability to educate me to such a high degree. She introduces me the subject of Unstructured Transmission Line Modelling method and spatial warping techniques. I am deeply grateful for Prof. Phillip D. Sewell for enlightening suggestions, constructive criticism and insightful comments which helped me to expand an idea a completed study. Additionally, I would like to thank them for giving me great opportunity to use their research software package, Virtual Evaluation Environment, with all the fabulous Jenna cluster available to visit workshops and conferences. Besides, I would like to thank them for being so approachable and understanding during the times of my confusing. Their supervision with constant support and immeasurable value of the feedback has helped me to develop professionally and to become a more complete researcher. I am very grateful for their patience reviewing my endless version of manuscripts and thesis. I very thankful to Prof. Ian Harrison, who supported me at the beginning of my PhD, which has ensured my quick progress in the topic. His feedback and comments have been invaluable and had a very important effect on my research. I am very grateful for his support after his retirement, which helped me during some dark times of my Ph.D. path and globe.

I would like to thank Dr. Tijana Dimitrijevic for fruitful collaboration and for discussing technical issues about cylindrical antenna simulations. I would like to thank all researchers in University of Nis, Serbia, Dr. Aleksandar Atanaskovic, Dr. Jugoslav Jokovic, and Prof. Nebojsa Doncov as well for online technical discussion about cylindrical antenna modelling. I would like to thank to Prof. Trevor M. Benson for his time and suggestions part of the online meeting.

I would like to thank annual reviewer, Dr. Sendy Phang, who has shared experiences with me, suggest for my research and my personal developments.

I consider myself a very lucky person since I have had an opportunity to be part of truly great scientific groups, George Green Institute for Electromagnetics Research, GGIEMR. I would like to thank all my officemates of the GGIEMR individually, Dr. Jomiloju Odeyemi, Luke Matthews, Kaiqi Yan, Venkatkumar Muneeswaran, Ifiok Asuquo, Latifah Abdul Aziz, and Hussein Talib for their tips, friendliness, and academic inspirations.

Also, I would like to thank my sponsor Republic of Turkey Ministry of National Education, which has been supported me throughout my preparatory English school, master and Ph.D. studies. Furthermore, I would like to thank to Royal Society Grant International exchanges which provided me opportunity with attending first in-person conference in Vienna, and a scientific visit to Nis University in Serbia.

Most importantly, none of this would have been possible without support of my family, my mother, Seher, my father, Orhan, and my sister, Esma Nur. I am forever indebted to them, who set me great example, whose inspire, encouragements, and supports under all circumstances.

Abstract

Flexible, foldable, and wearable antennas and interconnects play an indispensable role in the rise of wearable computing and wireless communications across many application areas. However, wearable components experience inevitable mechanical deformation, that can cause frequency shifting, performance detuning and component degradation making wireless data transmission and power transmission capabilities are limited. Thus, it is important to assess to what degree antenna and interconnect performance can be tolerant to in-situ deformations that can take the form of bending, crumpling and twisting and combinations of these effects. However, generating geometries of arbitrary antenna deformations such as bending, crumpling, and twisting, that can be processed by standard electromagnetic software is a major challenge that significantly complicates full assessment of in-situ antenna performance. Constructive Solid Geometry (CSG) methods of generating geometries is difficult to robustly apply to non-conformal antennas and more flexible techniques are required to progress the antenna and interconnect studies further. To address this challenge, this thesis investigates the utility of Spatial Warping Technique, specifically, Green Coordinates (GC), for generating arbitrary antenna and interconnect geometries. First a calibration of a straightforward application of the spatial warping techniques against a reference case of a patch antenna bent over a cylindrical surface, which can also be generated exactly, is undertaken. The thesis shows that systemic scaling distortions are introduced by the GC method and introduces a compensation method that can overcome these distortions. Subsequently, the compensated method is used to obtain new predictions of the electromagnetic performance of analyses how these complex deformations impact the performance of a flexible antenna operating in the 5-6 GHz band. with arbitrary deformations, namely, antennas bent over 2D surfaces, and with concave and convex spherical twisting or torsional deformations. Generating, full geometries is a key enabler in this thesis. The provided results for a flexible antenna operating in the 5-6 GHz band offer valuable insight to the stability of antenna performance under *in-situ* deformations.

Finally, the new methodology is applied to characterise flexible interconnect with realistic materials condition has been investigated with concave and convex bending and an arbitrary twisting deformation. This thesis also analyses the impact of these deformations on the transmission properties of a variety of commercially available polymer and elastomer-based interconnects and compares to the performance of flat interconnects fabricated on rigid substrates. The analysis of the impact of deformations also considers the degradation in the conductivity of the printed lines due to reported mechanical deformations.

The new technique introduced this thesis able to couple with an electromagnetic simulator is a promising design toolkit that can be confidently used to assess the impact of deformations on the antenna and interconnect performance and give an accurate prediction of a device under the arbitrary deformation.

Contents

Contents x
List of Figures xiii
List of Tables xix
Nomenclature xxi
Chapter 1 Introduction 1
1.1 Research Background for the Thesis 1
1.2 Overview of Thesis 9
References 12
Chapter 2 Antenna and Interconnect Basics and Modelling 21
2.1 Antenna and Interconnect - [S] parameters 21
2.1.1 Antenna Impedance 23
2.1.2 Radiation Pattern 25
2.1.3 Directivity 25
2.1.4 Gain and Realised Gain 26
2.1.1 Bandwidth 26
2.2 Numerical Modelling: Unstructured Transmission Line Modelling Method 27
2.3 Conclusions 32
References 33
Chapter 3 Flexible Antennas and Interconnects for Wearable Electronics Overview 37
3.1 Introduction 37
3.2 Substrates for Wearable Applications 39
3.3 Conductive Materials 42
3.4 Impact of Deformations on Wearable Antenna Performance 46
3.4.1 Wearable Antennas 46
3.4.2 Crumpling Deformation 56
3.4.3 Stretching Deformation 57
3.4.4 Torsional Deformation 59
3.4.5 Reported Flexible Antennas 60
3.4.6 Impact of Deformations on Wearable Interconnect Performance 63
3.4.7 Reported Flexible Interconnects 68
3.5 Conclusions 68
References 70

Chapter 4 Computational Cage Based Deformation Technique 83
4.1 Background Theory 83
4.1.1 Gaussian Curvature 83
4.1.2 Barycentric Coordinates 85
4.1.3 Affine Invariance 86
4.1.4 Cage Based Deformations 86
4.2 Computational Geometry Morphing Techniques 87
4.2.2 Comparison of Cage Techniques 93
4.3 Conclusions 98
References 99
Chapter 5 Systematic Generation of Arbitrary Antenna Geometries 103
5.1 GC Method for Generating Cylindrically Bent Antennas 103
5.2 Assessment of GC Induced Distortions for the Case of Cylindrically Bent Antenna 105
5.3 Methods for Compensating GC Induced Deformations 109
5.3.1 Centre of Gravity Compensation Method 110
5.3.2 Width and Length Compensating GC Induced Distortions 112
5.4 EM Performance of Cylindrically Bent Antennas 114
5.4.1 EM Performance of COG Compensation 115
5.4.2 EM Performance of WL Compensation 119
5.5 EM Performance of Arbitrary Deformed Antennas 122
5.6 Conclusions 126
References 127
Chapter 6 Assessment of Robustness of Flexible Antennas for Complex Deformations 129
6.1 Introduction 129
6.2 Complex Antenna Deformations 132
6.3 Deformed Model of Antenna Geometry and Numerical Simulation 136
6.3.1 Spherical Concave and Convex Deformations 137
6.3.2 Saddle Deformations 139
6.3.3 Twisting Deformations 141
6.3.4 Comparison with Cylindrical Deformations 143
6.4 Conclusions 147
References 149
Chapter 7 Characterisation of Flexible Interconnect 153
7.1 Introduction 154
7.2 Rigid Interconnect with the SMA connector model 156

7.3 Comparison of Flexible Interconnects 159
7.4 Performance of Flexible Interconnects Under Deformations 163
7.5 Conclusions 172
References 174
Chapter 8 Conclusions and Future Works 179
8.1 Conclusions 179
8.2 Future Works 183
References 185
Appendix A Algorithms for Green Coordinates A-1
A.1 Green Coordinates Algorithm 2D A-1
A.2 Green Coordinates Algorithm 3D A-2
References A-4

List of Figures

Figure 1.1 An arbitrary patch antenna deformation with crumpling along the width of antenna and twisting along the length of antenna. 4

Figure 1.2 Overall process of cage based deformation, specifically GC method (a) original flat antenna (b) enclosed antenna in the flat cage (c) the empty warped cage and flat cage that includes flat antenna to transfer the warped cage (d) the morphed antenna inside the warped cage (e) the final conformed antenna geometry [72]. 6

Figure 2.1 An arbitrary multiport antenna or interconnect system [9]. 23

Figure 2.2 Canonical tetrahedral cell scattering network (a) Tetrahedral element (b) Equivalent network representation and (c) Compact circuit representation [8]. 28

Figure 2.3 Clustering phenomena demonstrated by two neighbouring cells whose circumcentres are separated by a small distance Δ. (a) Without clustering, the time step is typically required to be $2c\delta t < \Delta$. (b) With clustering time step can be significantly raised [8]. 29

Figure 3.1 Comparison of elastic (Young's) modulus of various materials [13]. 38

Figure 3.2 (a) Simulation geometry of the microstrip antenna (b) textile fabric assembly (c) flat knitted antenna (d) conical deformation of knitted antenna [26]. 50

Figure 3.3 The picture of antenna (a) Front view (b) compression and tensile bending with the angle of 270°, 180°, and 90° [20]. 53

Figure 3.4 Multi-layer of microstrip patch antenna composed of liquid metal encased in polymer [77]. 54

Figure 3.5 Implemented flexible sinusoidal patterned antenna (a) fabricated metal sheet (b) ground plane of antenna with probe feeding of coaxial cable (c)-(e) bending patterned antenna with curvature radii of 1.25, 1, and 0.41 inches, respectively [109]. 54

Figure 3.6 The optical images of the antenna (a) front view (b) cylindrical deformation [112]. 56

Figure 3.7 (a) The picture of the top, bottom, side and perspective of double arch patterned antenna [59] (b) Optical images of the symmetric and asymmetric double-arched microstrip antenna [115]. 57

Figure 3.8 Stretching 15%, bending radius of 40 mm, and twisting 360° of parasitic dipole antenna [116]. 59

Figure 3.9 (a) Un-bended, (b) bended and (c-d) transmission lines [72]. 64

Figure 3.10 Measurement setup for torsion test at (a) 0°, (b) 20°, and (c) 40° [129]. . 66

Figure 4.1 The association between principal curvature $(\kappa 1, \kappa 2)$ and Gaussian curvature (K), such as (A) plane (B) cylinder, (C) sphere, (D) bowl surface with non-zero Gaussian curvature [1]. 84

Figure 4.2 Coordinates in a Triangle, T, [9]. 86

Figure 4.3 The MVC [14, 15] coordinates deformation applied on (a) horse model with enclosing cage (b-d) several deformations generated using MVC cage.....89

Figure 4.4 HC coordinates [17] applied on game character (a) game character with enclosing cage (b-c) the game character after applying the arm twist.....89

Figure 4.5 Chessboard is deformed with the original, GC's result [13, 16] and HC's result [17] reported by [13]. To retain conformal mapping, mapping extends outside the cage [13].....94

Figure 4.6 The MVC [14, 15] coordinates have more focus on details preservation on their main orientation, but GC's operator [13, 16] rotates and moves details relying on deforming cages [13]. 94

Figure 4.7 Cage based deformation of an Ogre which was reported by [13]. GC provides better for the preservation of the shape of the Ogre compared to MVC [13]. 95

Figure 4.8 Cage based deformation of an Armadillo which was reported by [13]. Second column reveals MVC results and third column GC results [13]. GC provides better preservation of the Armadillo's leg and arm [13].....95

Figure 4.9 Twisting a square cross section polygonal tube using Mean Value Coordinates (MVC) and Green Coordinates (GC). Two cross section location of captured polygonal tube demonstrated at the middle of the figure (red color indicates location of capturing plane) [13].....96

Figure 4.10 Comparisons of Green Coordinates (GC) [13, 16], Mean Value Coordinates (MVC) [14, 15], and Harmonic Coordinates (HC) [17]. (a) Two orthogonal planes each other with circle pattern captured by a polygonal tube (left) are bent twice: Each rows reveals GC, MVC, and HC deformation, demonstrated by red arrows. It should be noted that MVC and HC may well result in some shear, considerable bending and stretching. (b) The logarithmic scale of distortion values of GC, MVC, and HC deformation plotted for the first and second deformations [13]. .97

Figure 5.1 a) Microstrip antenna placed inside the flat cage separated by a padding Δ from the edges of the cage; b) deformed cage for the case of cylindrical bending; c) same as a) but showing vertices and faces; d) same as b) but showing vertices and faces; e) deformations of the warped cage are transferred onto the antenna and f) deformed cage is removed to reveal the final result of deformed antenna and, in the inset, its surface triangulation. 104

Figure 5.2 Midpoint morphing; tolerance for convergence (a) flat polyhedral cage (b) deformed polyhedral cage.....105

Figure 5.3 The antenna geometry generated with $N = 2,\ N = 10$ segments in the cage definition.....106

Figure 5.4 The schematic of the flat patch antenna a) top view and b) side view. The angles ϑ and φ define E and H plane of the antenna radiation pattern, respectively. 106

Figure 5.5 Relative surface distortions error of (a) metal patch and (b) substrate as a function of bending radius R and the padding Δ.....108

Figure 5.6 Relative surface distortion error of (a) metal patch and (b) substrate as a function of bending radius *R* and the number of cage segments *N*.....108

Figure 5.7 Relative error of GC generated area of antenna to that of the flat antenna for uncompensated GC method and GC compensated method using COG. 111

Figure 5.8 Relative error of GC generated a) the width and b) the length of antenna to that of the flat antenna for uncompensated, and COG compensated antennas. 112

Figure 5.9 Relative surface distortion error of GC generated antenna to that of the flat antenna for uncompensated GC method and compensated GC method.....112

Figure 5.10 Relative area error of WL approach for different degree of polynomials. The notation (***poly x, y***) indicates the order of the polynomial function used along the width and length of the patch, respectively. 113

Figure 5.11 Relative distortion error along the width and length of antenna to that of the flat antenna for uncompensated and compensated GC generated antennas.....114

Figure 5.12 Comparison of S_{11} parameter for the flat antenna and ideal cylindrical, antenna bent in the H-plane using uncompensated and COG compensated method for a) radius R=6.5 mm and b) R=10 mm. 116

Figure 5.13 E-plane bending: Comparison of S_{11} parameter of flat, ideal cylindrical, uncompensated and COG compensated method for a) radius R = 6.5 mm and b) R = 10 mm. S11 parameter of the fat antenna is also given for the reference. 117

Figure 5.14 Normalised far radiation patterns of antenna bend in the H-plane: (a) E and (b) H-plane far-field for bending radius of 6.5 mm, and (c) E- and (d) H-plane radiation pattern for bending radius of 10 mm. Results are presented for the flat, ideal cylindrical, uncompensated and COG compensated antenna. 118

Figure 5.15 Normalised far radiation patterns of antenna bend in the E-plane: (a) E and (b) H-plane far field for bending radius of 6.5 mm, and (c) E- and (d) H-plane radiation pattern for bending radius of 10 mm. Results are presented for the flat, ideal cylindrical, uncompensated and COG compensated antenna. 119

Figure 5.16 H-plane Bending: Comparison of S_{11} parameter for the flat antenna and antenna bent in the H-plane using the refence antenna and uncompensated and compensated GC methods for a bending radius of a) R = 6.5 mm and b) R = 10 mm. 120

Figure 5.17 E-plane bending: Comparison of S_{11} parameter for the flat antenna and antenna bent in the E-plane using the refence antenna and uncompensated and compensated GC methods for a bending radius of a) R=6.5 mm and b) R=10 mm. .120

Figure 5.18 Normalised far field radiation patterns of antenna bend in the H-plane: (a) E and (b) H-plane radiation pattern for bending radius of 6.5 mm, and (c) E- and (d) H-plane radiation pattern for bending radius of 10 mm. Results are presented for the flat, ideal cylindrical, uncompensated and compensated GC antennas. 121

Figure 5.19 Normalised far field radiation patterns of antenna bend in the E-plane: (a) E and (b) H-plane radiation patterns for bending radius of 6.5 mm, and (c) E- and (d) H-plane radiation pattern for bending radius of 10 mm. Results are presented for the flat, ideal cylindrical, uncompensated and compensated GC antennas. 121

Figure 5.20 Arbitrary antenna deformations showing a) convex, b) concave, c) saddle bending and d) antenna under twisting deformation.....123

Figure 5.21 Return loss S_{11} of the a) convex, b) concave, c) saddle and d) twisted antennas obtained using uncompensated and compensated GC method in comparison with the flat case. 123

Figure 5.22 Normalised far-field pattern in the E- and H-plane of antenna for: (a-b) convex bending, (c-d) concave bending, (e-f) saddle bending, and (g-h) twisting. .. 125

Figure 6.1 Two-dimensional deformations of antenna – example of a) spherical bending, b) saddle and c) twisting deformations. 131

Figure 6.2 GC methodology: a) flat antenna within a flat cage (only faces of the flat cage shown); b) warped cage that describes the nature and level of deformation required; c) deformed interconnect inside the warped cage (only edges of the warped cage shown) d) final geometry of a deformed antenna. 133

Figure 6.3 Geometry of the flat microstrip patch antenna with a) the top view where x-axis is the E-plane of antenna and z-axis is the H-plane of the antenna and b) the side view where y-axis is the propagation direction of excitation pulse. 133

Figure 6.4 Warped cages describe the nature and level of deformation geometry. (a) Concave (b) convex (c) saddle and (d) twisting deformation cages. 134

Figure 6.5 Iteration number versus relative error of the GC deformed antenna geometry for convex, saddle and twisting bending for its extreme deformation considered in the Chapter where solid line indicates error of width edge and dashed line indicates length error 135

Figure 6.6 Meshed the concave antenna with computational box with inset picture zoomed in concave antenna. 137

Figure 6.7. (a) Impact of the spherical concave and convex deformation on the resonant frequency change of the deformed antenna compared to that of the flat antenna (f_0) for different spherical radii. Values (dB) indicate the value of S_{11} parameter at the resonant frequency. (b) Impact of the spherical concave and convex deformations on the fractional bandwidth of the deformed antenna. 138

Figure 6.8 Comparison of the far field radiation pattern at 5.6 GHz in a) E-plane and b) H-plane of a flat patch antenna (solid line) with antenna deformed using spherical concave deformation with r = 30 mm, (dotted line) and antenna deformed using spherical convex deformation with r = 30 mm (dashed line). 138

Figure 6.9 (a) Impact of saddle deformations (convex bending along the width and length of antenna) on the resonant frequency change of deformed antenna compared to the resonant frequency of the flat antenna, f_0, Values (dB) indicate the value of S_{11} parameter at the resonant frequency. (b) Impact of the saddle deformations (convex bending along the width and length of antenna) on the fractional bandwidth of antenna. 140

Figure 6.10 Comparison of the far field radiation pattern at 5.6 GHz in a) E-plane and b) H-plane of a flat patch antenna (solid line) with antenna deformed using saddle deformation with convex bending along the length (dashed line) and along the width (dotted line) with A = 20 mm. 140

Figure 6.11(a) Impact of twisting deformation applied along the width and length of antenna on the change of the resonant frequency of deformed antenna. (b) Impact of the twisting deformation applied along the length and width of antenna on the fractional bandwidth of antenna 142

Figure 6.12 Comparison of the far field radiation pattern at 5.6 GHz in a) E-plane and b) H-plane of a flat patch antenna (solid line) with antenna deformed using twisting deformation with 0.0125 twist/m along the length (dashed line) and along the width (dotted line) of antenna. 142

Figure 6.13 (a) Resonant frequency of antenna for a concave spherical and E-plane and H-plane bending. Values (dB) indicate the value of S_{11} parameter at the resonant frequency. (b) The fractional bandwidth for a concave spherical and E-plane and H-plane bending. 144

Figure 6.14 Comparison of the far field radiation pattern at 5.6 GHz in a) E-plane and b) H-plane of a flat patch antenna (solid line) with antenna deformed using Concave deformation with radius 20mm, and respective E-plane and H-plane deformation of antenna. 144

Figure 6.15 (a) Resonant frequency of antenna for a convex spherical and E-plane and H-plane bending. Values (dB) indicate the value of S_{11} parameter at the resonant frequency. (b) The fractional bandwidth for a convex spherical and E-plane and H-plane bending. 146

Figure 6.16 Comparison of the far field radiation pattern at 5.6 GHz in a) E-plane and b) H-plane of a flat patch antenna with antenna deformed using a convex deformation with radius 30mm, and respective E-plane and H-plane deformation of antenna. 146

Figure 7.1 Twisting deformation of a flexible interconnect. 155

Figure 7.2 Schematic of a flexible interconnect with subminiature SMA. 156

Figure 7.3 Computational mesh of the a) flat and b) deformed interconnect. 157

Figure 7.4 The geometry of coax-to-microstrip transitions. The tapered size between end launch connector and the end of the 50 Ω impedance line is (a) 0.30 mm (b) 0.635 mm and (c)1.09 mm and (d) 1.27 mm respectively. 158

Figure 7.5 S_{21} and voltage standing wave ratio (VSWR) of feed port optimisation comparison with typical with metal as an imprinted PEC. The substrate thickness is 0.762 mm (30 mil) and the length of 25.4 mm (1 inch) board. 158

Figure 7.6 S_{21} and VSWR for 50 Ω line interconnects on flexible substrates (PET, PI, PDMS, and PU) compared to equivalent microstrip line on a rigid substrate RO4350. Line length is 25.4 mm and the substrate thickness is 0.508 mm. Metallic losses are neglected. 160

Figure 7.7 S_{21} and VSWR for 50 Ω line interconnects on flexible substrates (PET, PDMS, PI and PU) compared to equivalent microstrip line on a rigid substrate RO4350. Line length is 50.8 mm and the substrate thickness is 0.508 mm. Metallic losses are neglected. 161

Figure 7.8 S_{21} and VSWR for 50 Ω interconnects on flexible substrates (PET, PI, PDMS and PU). Line length is 50 mm and the substrate thickness is 1 mm. Metallic losses are neglected. 161

Figure 7.9 S_{21} and VSWR for 50 Ω line interconnects on flexible substrates (PET, PI, PDMS and PU) compared to equivalent microstrip line on a rigid substrate RO4350. Line length is 50.8 mm, and the substrate thickness is 0.508mm. 162

Figure 7.10 S_{21} and VSWR for 50 Ω line interconnects under bending 30° on flexible substrates PET, PI, PDMS and PU compared to equivalent microstrip line on a rigid substrate RO4350. 163

Figure 7.11 S_{21} and VSWR for 50 Ω line interconnects under bending 30° and 90° on flexible substrates a) PET, b) PI, c) PDMS, and d) PU compared to equivalent microstrip line on a rigid substrate RO4350. 164

Figure 7.12 S21 and VSWR for 50 Ω line interconnects under bending 30° and 90° on flexible substrates a) PET, b) PI, c) PDMS, and d) PU compared to equivalent microstrip line on a rigid substrate RO4350. 165

Figure 7.13 GC methodology: a) flat interconnect within a flat cage (only triangular faces of the flat cage shown); b) warped cage that describes the nature and level of deformation required; c) deformed interconnect inside the warped cage (only edges of the warped cage shown) d) final geometry of a deformed interconnect. 166

Figure 7.14 GC induced relative distortion error in the width and length of the microstrip transmission line as a function of the number of pre-scaling iteration for generation of twisting deformation with mean twisting ρ=0.0065 rad/m, ρ=0.0105 rad/m, and ρ=0.0290 rad/m. 167

Figure 7.15 GC deformed geometry of microstrip line on 1mm PDMS with coaxial cable port inner and outer radius 0.4233 mm and 1.37 mm with mean twisting rotation per meter (a) 0.0105, (b) 0.0205, (c) 0.0255, and (d) 0.0290 respectively. 168

Figure 7.16 S_{21} and VSWR for 1 mm PDMS substrates (GC deformed) with microstrip line with twisting angle ρ, 0.0015, 0.0025, 0.0050, 0.0065, 0.0105, 0.0125, 0.0205, 0.0255 and 0.0290 rad/m respectively. Inset figure shows the rotation direction of twisting deformation. Metallic losses are neglected. 169

Figure 7.17 S_{21} and VSWR for 1 mm PET, PI, PDMS, and PU substrates (GC deformed) with microstrip line with twisting angle ρ, 0.0065 rad/m respectively. 170

Figure 7.18 S_{21} and VSWR for of 1 mm PET, PI, PDMS, and PU substrates (GC deformed) with microstrip line with twisting angle ρ, 0.0065 rad/m respectively. Conductivity of line has changed according to [33, 34]. 170

Figure 7.19 S_{21} and VSWR for 1mm PET, PI, PDMS, and PU substrates (GC deformed) with microstrip line with twisting angle ρ, 0 0.0290 rad/m respectively. 171

Figure 7.20 S_{21} and VSWR for 1mm PET, PI, PDMS, and PU substrates (GC deformed) with microstrip line with twisting angle ρ, 0 0.0290 rad/m respectively. Conductivity of line has changed according to [33, 34]. 172

List of Tables

Table 1.1 The fundamental challenges and opportunities in the field of antenna and interconnect are determined by EPSRC [27] in 2014 and "*The 2021 flexible and printed electronics roadmap* *[28]" and CAD technologies and the related materials which may well address these challenges. 3

Table 3.1 Averaged Dielectric Constant for Different Materials 40

Table 3.2 Typical physical properties of polymeric and elastomer substrates 41

Table 3.3 Conductivity (DC) of conventional materials for fabrication of flexible, wearable interconnects : Data taken from [36, 47, 48] 43

Table 3.4 Electrical Properties of Conductive Sheets 45

Table 3.5 Reported flexible antenna with their materials of conductive and substrates and their rate of deformation 60

Table 3.6 Physical Properties of Transmission Line Made of Different Materials 67

Table 7.1 Parameters of different interconnects fabricated on different substrates. . 159

Nomenclature

ACAP	As-Consistent-As Possible
Ag	Silver
AJP	Aerosol Jet Printed
Al	Aluminium
ARAP	As-Rigid-As Possible
ASAP	As-Similar-As Possible
Au	Gold
BW	Bandwidth
CAD	Computer Assisted Design
CNT	Carbon Nanotubes
CPW	Coplanar Waveguide
CSG	Constructive Solid Geometry
Cu	Copper
E-GaIn	Gallium Indium Eutectic
EM	Electromagnetics
EMI	Electromagnetic Interference
FDTD	Finite Difference Time Domain
FEA	Finite Element Analysis
FEM	Finite Element Modelling

FSS	Frequency Selective Surface
GC	Green Coordinates
GK	Geometry Kernel
HC	Harmonic Coordinates
IoT	Internet-Of-Thing
LCP	Liquid Crystal Polymers
MoM	Methods Of Moment
MVC	Mean Value Coordinates
Ni	Nickel
NW	Nanowire
PANI	Polyaniline
PDMS	Polydimethylsiloxane
PEDOT::PSS	Poly(3,4-Ethylenedioxythiophene) – Poly(Styrenesulfonate)
PET	Polyethylene Terephthalate
PI	Polyimide
PPy	Polypyrrole
PTFE	Polytetrafluoroethylene
RFID	Radio Frequency Identification
SP	Screen Printed
SWNT	Single Walled Carbon Nanotube
TFT	Thin-Film Transistors
TL	Transmission Line
TLM	Transmission Line Modelling
TPU	Thermo Plastic Polyurethane

UTLM	Unstructured Transmission Line Modelling
UHF	Ultra-high Frequency
VEE	Virtual Evaluation Environment

Chapter 1 Introduction

This Chapter presents the research background and introduction to this thesis. It highlights an essential gap in the research that this thesis addresses. Besides, it demonstrates the need for research and the importance of real-life applications. Finally, this Chapter outlines the content of each Chapter of the thesis and how they structure to fit the fundamental view of the thesis.

1.1 Research Background for the Thesis

Wearable and foldable electronics can receive, store, or transmit digital information and are the focus of increased attention in many areas including healthcare, entertainment, and the sports industry. Flexible devices are required to operate with low power consumption to continuous synchronisation between other devices [1] and the main applications are focused on low power sensing applications and wireless communications [1]. The main applications of flexible electronics for high frequency are:

- Wireless communication applications [2-4] that need to be synchronised in an instant location are fundamental for a wide variety of internet service applications. Flexible and wearable electronics are the most promising non-invasive devices for tracking objects and users [5].
- Sensor applications for the measurement of body's vital variables, such as blood pressure, body temperatures, sweat rate monitoring, and monitoring of hand gestures, analysis of metabolites, and condition of scar healing monitoring [6-16].

- Energy harvesting applications [17-20] that transmit a reasonable amount of wireless energy or captures energy from changes in environmental conditions, such as radio signals and temperatures.
- The radio frequency identification (RFID) applications [21-25] that transmits a reasonable amount of wireless energy to use as an identification system [2, 26].

Furthermore, the ever-increasing demand for fully integrated and flexible, wearable, small size, and high-capacity systems exhibits more challenges for electromagnetic application engineers regarding conformal and multi-functional design. The Engineering and Physical Science Council (EPRSC) workshop (2014) [27] and '*The 2021 Flexible and Printing Electronic Roadmap**' [28] have identified challenges and required technologies to enable a step-change for antennas and soft and flexible electronics.

Table 1.1 summarises the research challenges for antennas and soft and flexible substrates and the required technologies and properties to lead a step-change. The main challenges for antennas are in the area of designing thin conformal antennas that can operate at multiple bands over narrow channels. For low and intermediate frequency antennas the aim is to overcome the Chu's limit (i.e., overcome the limit on the bandwidth that is proportional to the physical size of antenna [29]).

In terms of materials the research focus is on soft and flexible substrates and high conductivity materials suitable for flexible substrates. The substrates based on textiles with high permittivity are desired that are on-body reconfigurable. This in turn demands that effect of anisotropy of substrate materials is accounted for. The main components that are considered are flexible connector and interconnects and, antenna feed lines.

To address given challenges, it would require collaboration between software engineers, microwave engineers and material scientists. In essence, some of the research challenges are fundamentally associated with each other. For instance, a thin conformal antenna requires not only high conductivity and novel materials, such as nanoparticles [30-32], nanowires [33], polymers [34], 1D and 2D (i.e., carbon

Table 1.1 The fundamental challenges and opportunities in the field of antenna and interconnect are determined by EPSRC [27] in 2014 and "*The 2021 flexible and printed electronics roadmap* *[28]" and CAD technologies and the related materials which may well address these challenges.

Research Challenges	Required technologies and properties to lead a step change
Antennas	**CAD Modelling**
• **Thin Conformal Antennas** • Operation at multiple bands over narrow channels • Overcome the Chu's limit - particularly for intermediate and low frequency antennas • Doped graphene, transparent for antennas • Transparent antennas • Control dispersion in antenna materials • Integrated system of antenna plus frontend	• **Intelligent RF and microwave CAD** • RF with new materials-specification to end design CAD • **Models of new materials** • Multi-physics and multi-scale to system level • Thermodynamics coupled with E/M • RF modelling in house expertise combine with commercial software materials processing applications • *Modelling tools for efficient designs for weaving and knitting effect • *Comprehensive simulation framework
Soft and Flexible Substrates	**Materials**
• **Flexible connectors and interconnects, feeds** • **Wearable alternatives and substrate types** • High permittivity for fabrics for wearable antennas • **High conductivity** • **Flexible conductors** • **On body-modular-reconfigurable based on dynamics local EM environment and posture** • Effects of anisotropy • Biodegradable • Microwave capable textiles • Disposable disturbed sensing- single point change in function sense-transmit	• Physical material morphing • Anisotropic materials ($\varepsilon_x \neq \varepsilon_y \neq \varepsilon_z$) • Tunability of material (structure, ε, μ, σ) • Low-loss Materials • Metamaterials • Artificial dielectrics • Magnetic materials high frequencies • Composite multilayer and hybrid materials • Engineered composite materials • Nanomaterials • Controlled grading materials • Ability to print metal and non-metal 3D shapes • 3D Printing of full systems

nanotubes [35], graphene [36-40], MXenes [41, 42]) but also alternatives substrate types from soft and flexible substrates. For example, graphene and its related materials can be used to enhance the mechanical endurance of antennas to environmental stretch and strain [43, 44]. In addition, the advances in material processing [45-47] and additive manufacturing technologies [48-52] have shown to have significant advantages for direct printing electronics on the conformal and flexible surface for wearable antenna

design [49, 53-56]. For instance, the improvement in material science and their usage of advanced manufacturing technologies has provided the alternative capability of designing microwave systems directly on spherical surfaces with enhanced functionalities, such as wider coverage [53] or adding multi-functionality of desired constraints, such as sensing temperatures [14].

The roadmap, identified by EPSRC, identifies specific areas for flexible antennas and in specific, it outlines a necessity for CAD models that can deal with multi-physics and multi-scale problems. The CAD modelling should aim to build in a library of new materials and also be able to deal with issues that weaving and knitting effect has on components. Individual components, such as RFIDs, medical sensors and antennas can be integrated into a variety of substrates including knits, embroidery or non-woven materials [57-59]. More generally, non-flat antennas are routinely found mounted on curved surfaces such as airplane wings and fuselages [60] and as 5G antenna arrays on cylindrical surfaces [61]. The design and integration of individual components are often crucial aspects of the overall system design.

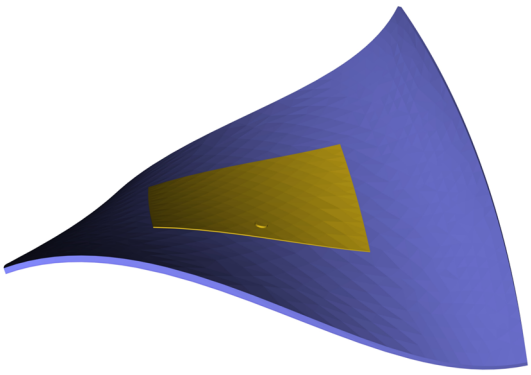


Figure 1.1 An arbitrary patch antenna deformation with crumpling along the width of antenna and twisting along the length of antenna.

One of the most challenging cases for predicting in-situ performance is that of wearable textile antennas fabricated on woven and non-woven materials that will experience bending, twisting, and crumpling when pulled in different directions by human activity, as illustrated in Figure 1.1. Whilst woven and non-woven materials are more stable than knits, [57], it is still expected that all textile antennas will to some extent, experience

elongation and compression when in use. To date there has been an increasing effort to predict performance changes caused by antenna deformations, but these have primarily focused on patch antennas and antenna arrays bent over *cylindrical surfaces* [18, 62-71]. The results reported were obtained from practical measurements [62, 63] and only a few predictive results have been reported using the modelling techniques embodied in CST's and Ansys software [64, 65, 70, 71]. Both the experimental and simulated results demonstrate that bending has a significant influence on antenna performance; specifically, increased curvature decreases the overall gain of antenna and shifts the resonant frequency, although the bandwidth remains approximately the same across all measured cases [18, 62, 64, 65, 67, 70, 71].

The virtually exclusive focus on purely cylindrical deformations can be attributed to the difficulty in robustly generating *arbitrary deformed antenna geometries* suitable for predictive simulations. Clearly, to advance understanding and to develop practical design guidelines, the problems associated with generating arbitrary geometries need to be fully understood and resolved and this motivates the contribution presented in this thesis.

The specific and critical CAD issue for the generation of deformed antenna geometries is to obtain well behaved and consistent interfaces between the different elements that make up the antenna. This is clearly illustrated by a finite thickness metal patch on a substrate: Either the patch and the substrate are generated separately as deformed parts and *stitched* together or, a flat patch-substrate combination is generated with a well behaved interface, which is easy to do, and this combination is deformed to the final desired geometry.

It is important to explain the phrase *a well behaved interface.* Stitching together non-coordinate aligned and separately created parts inevitably leads to *dirty interfaces* that do not perfectly align and typically have microscopic non-physical *gaps* and *overlaps* which are disastrous for subsequent mesh generation and electromagnetic (EM) simulations. At best, *dirty interfaces* result in unrealistically small mesh cells that severely compromise the computational efficiency and at worst, mesh generation proves impossible. It is commented here that the subsequent choice of modelling

method, Finite Elements, Finite Differences, Method of Moments, or their implementation within particular software packages is not the issue, rather it is the geometrical data upon which they operate that has the failing.

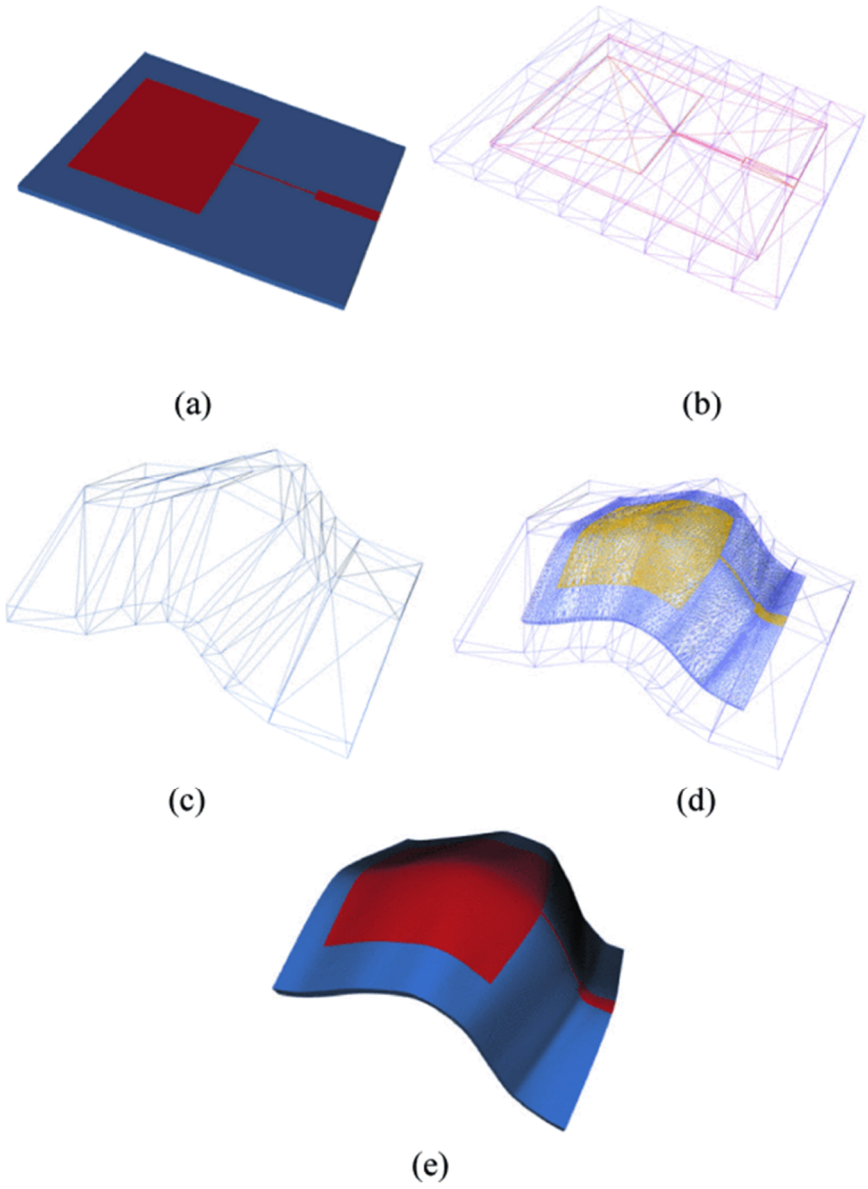


Figure 1.2 Overall process of cage based deformation, specifically GC method (a) original flat antenna (b) enclosed antenna in the flat cage (c) the empty warped cage and flat cage that includes flat antenna to transfer the warped cage (d) the morphed antenna inside the warped cage (e) the final conformed antenna geometry [72].

Experience shows that even the CAD models generated using mechanical software need *CAD repair* techniques to clean these interfaces lacks robustness and require significant

manual intervention.

Overall, the number of trial cases a designer can easily consider is severely curtailed which explains the existing focus on purely cylindrical geometries that are amenable to exact generation [64-67, 71, 73]. To avoid the issue of dirty interfaces, the strategy pursued in this thesis is to generate flat antenna geometries and deform them holistically using a technique borrowed from computer graphics.

Computer graphics offers a number of techniques for spatial manipulation of 3D objects, for example Mean Value Coordinates (MVC), Harmonic Coordinates (HC) and Green Coordinates (GC) [74-77]. The common feature of these techniques is to enclose the object of interest by a so called bounding *cage* that has a similar, but less complicated shape than the object of interest, as shown in Figure 1.2. All spatial points within the interior of the cage can be expressed in terms of the cage's geometry (e.g. vertex locations in the case of MVC) and by subsequently manipulating the vertices of the simple cage, for example interactively *dragging* one of its vertices, smooth deformations are induced into the complex geometry of the enclosed object (See Figure 1.2). This approach is extensively used in computer animation and the fast and simple modification of objects is the feature that is also sought in this thesis for systemic performance studies on deformed antennas.

Each of the particular methods listed above differ in (i) the extent to which they preserve the *physically realistic* nature of practical deformations of the object's shape (shape-preserving property) and (ii) the efficiency of their numerical implementation, i.e., either exploiting closed form formulae or requiring substantive numerical processes [76]. Shape preservation in the context of this work is a measure of whether the object deformation follows the expected behaviour of stress-strain physics which is clearly desirable. Two points to note here are that (i) it would be difficult to theoretically express the complexity of such deformations in the general case with a view to explicitly *code* geometry generation, vertex by vertex, as one can obviously do for the purely cylindrical case, and (ii) the scope of this work does not extend to the further complexities of the materials, for example the opening and closing of woven fabrics.

The Green Coordinates approach stands out from the alternatives listed above as that which best preserves the shape of 3D objects and is implemented using only closed form analytical formulae [76, 77]. The good shape preservation properties trace to the fact that the two-dimensional (2D) and three-dimensional (3D) GC method induce purely conformal and quasi-conformal maps respectively with minimal anisotropic scaling [76, 77].

However, the GC approach does introduce systematic global distortion of the resulting antenna geometry and it is important to assess how these affect antenna performance and if needed to minimise them. For clarity, we use the term *deformation* for the desired change of shape of an antenna from the flat to the in-situ case and *distortion* to denote these undesirable systemic errors that GC method introduces.

A suitable benchmark geometry for assessing and then removing the GC distortions is the purely cylindrical case as it is a developable surface that ought to be generatable without any distortion. The quantification of antenna deformations is done in the context of the subsequent impact on its performance, that is characterised by antenna reflection coefficient S_{11} and radiation pattern. After calibration against a known canonical case whose geometry can be exactly generated, final GC-generated antenna performance in terms of return loss and radiation patterns can be examined. Furthermore, the approach can then be extended to address the bigger challenge of undertaking a systematic design sweep over the problem space of possible doubly curved deformations, such as concave and convex spherical, saddle, and twisting deformations as well as to extend the method to other components such as interconnects.

To obtain these a suitable EM software needs to be used. As the antennas under investigation are clearly not coordinate aligned, discretisation with an unstructured mesh is advantageous for minimising discretisation errors and managing computational effort. The thesis used an in-house 3D Delaunay Mesher and EM software based on Transmission Line Modelling (TLM) method [78-80].

The Delaunay mesher [80] is a robust 3D implementation of the techniques described

in [81] augmented by many features that ensure that the meshes produced are sympathetic to the needs of subsequent large-scale EM simulation and has been widely used for the purpose [82-88].

The unstructured TLM method is a well-established extension to the Cartesian mesh TLM method, the latter having over 50 years of practical use for EM simulations [89, 90]. The TLM approach has the distinct advantages that all field component samples are co-located in time and space, and crucially, that stability is provable on a cell-by-cell basis without resorting to estimators such as the Courant condition. For large-scale simulations this is a critical advantage and late time instability has never been observed with TLM. The unstructured mesh variant of the TLM algorithm has been demonstrated to be second order accurate with respect to wavelength, provide both smooth boundary and graded mesh capabilities, and has been industrially characterised and deployed for a range of applications including EMC and aerospace [83, 85, 91] and readers are specifically referred to [78, 79] for further details.

1.2 Overview of Thesis

The thesis is structured as follows:

To determine the performance of an antenna and interconnect, the definitions of different parameters is necessary. The definition of essential parameters for this thesis are introduced according to the *IEEE Standards* [92-94] in Chapter 2. Then, Chapter 2 gives the basic theory of Unstructured Transmission-Line Modelling (UTLM) method and some of the solver consideration will be given in this Chapter.

Chapter 3 overviews available, flexible antennas and interconnects for wearable applications. The Chapter overviews various flexible materials available for antenna and interconnects design. The Chapter overviews the recent advances in flexible substrate materials and novel conductive materials that can be printed onto the flexible substrates. The Chapter then overviews reported results on the flexible antennas and

interconnects and the impact a particular deformation (cylindrical, twisting and stretching) makes on their performance. This is also done for flexible interconnects.

Chapter 4 describes the concept of geometry deformation based upon computer graphics techniques. This Chapter also defines non-developable surfaces and the barycentric coordinates formalism which is an essential concept for modelling geometry with triangular meshes. Then, the Green Coordinates method is defined by closed-form formulae in 2D and 3D. This Chapter also compares the Green Coordinates method with Mean Value Coordinates and Harmonic Coordinates with regard to their shape preserving property. This Chapter aligns against the EPSRC challenge of intelligent RF and microwave CAD in Table 1.1.

Chapter 5 applies the GC methodology to deform antennas and explores to what extend the GC method introduces unwanted geometrical distortions. The effectiveness of methods is assessed by comparing the EM performance of the GC compensated antennas with the canonical case of cylindrical bending whose geometries are in closed form. Chapter 4 uses the GC techniques to analyse the performance of antennas bent over doubly curved surfaces and compares it to the flat case. Deformation, such as average concave, convex, saddle and torsional deformation have been considered.

In Chapter 6, the compensation method developed in Chapter 5 was applied to study the systematic parameter sweeps of wearable antennas fabricated on a polymer substrate. The specific deformations, such as spherical, crumpling, and twisting, are investigated with varied deformation rates. The impact of deformations on antenna's resonant frequency, bandwidth and radiation patterns are analysed and compared against the flat case. The Chapter then further considers whether changes introduced by the double curved deformations can be characterised by a cylindrical deformation if the antenna is bent along the two principal axes. This Chapter aligns against a specific challenge identified in Table 1.1, namely thin conformal antennas, wearable alternatives, and substrate types, on body-modular-reconfigurable based on dynamics local EM environment and posture.

Chapter 7 compares the electromagnetic performance (EM) of the interconnects fabricated on several flexible substrates, namely, polyethylene terephthalate, (PET), polyimide, (PI), elastomer-based substrates such as polydimethylsiloxane (PDMS) and polyurethane (PU). First, the computational model of flat interconnect designed on a rigid substrate is calibrated against published experimental results. The model is then extended to other flexible interconnects based on PET, PI, PDMS, and PU substrates. Finally, this Chapter uses GC technique and described in Chapter 5 to investigate the impact of arbitrary deformations on the performance of interconnects. This Chapter aligns against several identified challenges in Chapter 1, such as models of new materials, flexible connectors and interconnects, feeds, wearable alternatives, and substrate types, and on body-modular-reconfigurable based on dynamics and posture.

Finally, Chapter 8 summarises the main conclusion of the thesis and discusses possibilities for further development of the GC method for modelling flexible electronics.

References

[1] M. U. Ali Khan, R. Raad, F. Tubbal, P. I. Theoharis, S. Liu, and J. Foroughi, "Bending Analysis of Polymer-Based Flexible Antennas for Wearable, General IoT Applications: A Review," *Polymers (Basel),* vol. 13, no. 3, Jan 22 2021, doi: 10.3390/polym13030357.

[2] L. Corchia *et al.*, "Fully-Textile, Wearable Chipless Tags for Identification and Tracking Applications," *Sensors (Basel),* vol. 20, no. 2, Jan 12 2020, doi: 10.3390/s20020429.

[3] E. Welbourne *et al.*, "Building the Internet of Things Using RFID: The RFID Ecosystem Experience," *IEEE Internet Computing,* vol. 13, no. 3, pp. 48-55, 2009, doi: 10.1109/MIC.2009.52.

[4] K. Pan *et al.*, "Sustainable Production of Highly Conductive Multilayer Graphene Ink for Wireless Connectivity and IoT Applications," *Nat Commun,* vol. 9, no. 1, p. 5197, Dec 5 2018, doi: 10.1038/s41467-018-07632-w.

[5] W. Zhou and S. Piramuthu, "Security/Privacy of Wearable Fitness Tracking IoT Devices," in *2014 9th Iberian Conference on Information Systems and Technologies (CISTI)*, 18-21 June 2014 2014, pp. 1-5, doi: 10.1109/CISTI.2014.6877073.

[6] Q. Xue, X. Tang, Y. Li, H. Liu, and X. Duan, "Contactless and Simultaneous Measurement of Water and Acid Contaminations in Oil Using a Flexible Microstrip Sensor," *ACS Sens,* vol. 5, no. 1, pp. 171-179, Jan 24 2020, doi: 10.1021/acssensors.9b01965.

[7] C. Zhang, H. Dong, C. Zhang, Y. Fan, J. Yao, and Y. S. Zhao, "Photonic Skins Based on Flexible Organic Microlaser Arrays," *Science Advances,* vol. 7, no. 31, p. eabh3530, 2021, doi: doi:10.1126/sciadv.abh3530.

[8] B. Sindhu, A. Kothuru, P. Sahatiya, S. Goel, and S. Nandi, "Laser-Induced Graphene Printed Wearable Flexible Antenna-Based Strain Sensor for Wireless Human Motion Monitoring," *IEEE Transactions on Electron Devices,* vol. 68, no. 7, pp. 3189-3194, 2021, doi: 10.1109/ted.2021.3067304.

[9] Q. Lyu, S. Gong, J. Yin, J. M. Dyson, and W. Cheng, "Soft Wearable Healthcare Materials and Devices," *Adv Healthc Mater,* p. e2100577, May 21 2021, doi: 10.1002/adhm.202100577.

[10] L. W. Lo, J. Zhao, H. Wan, Y. Wang, S. Chakrabartty, and C. Wang, "An Inkjet-Printed PEDOT:PSS-Based Stretchable Conductor for Wearable Health Monitoring Device Applications," *ACS Appl Mater Interfaces,* vol. 13, no. 18, pp. 21693-21702, May 12 2021, doi: 10.1021/acsami.1c00537.

[11] C. Lim *et al.*, "Tissue-like Skin-device Interface for Wearable Bioelectronics by Using Ultrasoft, Mass-permeable, and Low-impedance Hydrogels,"

Science Advances, vol. 7, no. 19, p. eabd3716, 2021, doi: 10.1126/sciadv.abd3716.

[12] Y. Li *et al.*, "Hybrid Strategy of Graphene/Carbon Nanotube Hierarchical Networks for Highly Sensitive, Flexible Wearable Strain Sensors," *Sci Rep,* vol. 11, no. 1, p. 21006, Oct 25 2021, doi: 10.1038/s41598-021-00307-5.

[13] C. H. Kim, D. H. Lee, J. Youn, H. Lee, and J. Jeong, "Simple and Cost-effective Microfabrication of Flexible and Stretchable Electronics for Wearable Multi-functional Electrophysiological Monitoring," *Sci Rep,* vol. 11, no. 1, p. 14823, Jul 20 2021, doi: 10.1038/s41598-021-94397-w.

[14] M. Bhattacharjee, F. Nikbakhtnasrabadi, and R. Dahiya, "Printed Chipless Antenna as Flexible Temperature Sensor," *IEEE Internet of Things Journal,* vol. 8, no. 6, pp. 5101-5110, 2021, doi: 10.1109/jiot.2021.3051467.

[15] W. Gao *et al.*, "Fully Integrated Wearable Sensor Arrays for Multiplexed in situ Perspiration Analysis," *Nature,* vol. 529, no. 7587, pp. 509-514, Jan 28 2016, doi: 10.1038/nature16521.

[16] M. Baghelani, Z. Abbasi, M. Daneshmand, and P. E. Light, "Non-invasive Continuous-time Glucose Monitoring System Using a Chipless Printable Sensor Based on Split Ring Microwave Resonators," *Sci Rep,* vol. 10, no. 1, p. 12980, Jul 31 2020, doi: 10.1038/s41598-020-69547-1.

[17] D. Vital, S. Bhardwaj, and J. L. Volakis, "Textile-Based Large Area RF-Power Harvesting System for Wearable Applications," *IEEE Transactions on Antennas and Propagation,* vol. 68, no. 3, pp. 2323-2331, 2020, doi: 10.1109/tap.2019.2948521.

[18] S.-E. Adami *et al.*, "A Flexible 2.45-GHz Power Harvesting Wristband With Net System Output From −24.3 dBm of RF Power," *IEEE Transactions on Microwave Theory and Techniques,* vol. 66, no. 1, pp. 380-395, 2018, doi: 10.1109/tmtt.2017.2700299.

[19] J. Zhu *et al.*, "Stretchable Wideband Dipole Antennas and Rectennas for RF Energy Harvesting," *Mater Today Phys,* vol. 18, May 2021, doi: 10.1016/j.mtphys.2021.100377.

[20] M. R. M. Hashemi *et al.*, "A Flexible Phased Array System With Low Areal Mass Density," *Nature Electronics,* vol. 2, no. 5, pp. 195-205, 2019, doi: 10.1038/s41928-019-0247-9.

[21] M. A. S. Tajin, C. E. Amanatides, G. Dion, and K. R. Dandekar, "Passive UHF RFID-based Knitted Wearable Compression Sensor," *IEEE Internet of Things Journal,* pp. 1-1, 2021, doi: 10.1109/jiot.2021.3068198.

[22] J. Pei, J. Fan, and R. Zheng, "Protecting Wearable UHF RFID Tags With Electro-Textile Antennas: The challenge of machine washability," *IEEE Antennas and Propagation Magazine,* vol. 63, no. 4, pp. 43-50, 2021, doi: 10.1109/map.2020.2988465.

[23] C. L. Baumbauer *et al.*, "Printed, Flexible, Compact UHF-RFID Sensor Tags Enabled by Hybrid Electronics," *Sci Rep,* vol. 10, no. 1, p. 16543, Oct 6 2020, doi: 10.1038/s41598-020-73471-9.

[24] L. Teng, K. Pan, M. P. Nemitz, R. Song, Z. Hu, and A. A. Stokes, "Soft Radio-Frequency Identification Sensors: Wireless Long-Range Strain Sensors Using Radio-Frequency Identification," *Soft Robot,* vol. 6, no. 1, pp. 82-94, Feb 2019, doi: 10.1089/soro.2018.0026.

[25] R. Singh, E. Singh, and H. S. Nalwa, "Inkjet Printed Nanomaterial Based Flexible Radio Frequency Identification (RFID) Tag Sensors for the Internet of Nano Things," *RSC Adv.*, vol. 7, no. 77, pp. 48597-48630, 2017, doi: 10.1039/c7ra07191d.

[26] D. Betancourt, K. Haase, A. Hubler, and F. Ellinger, "Bending and Folding Effect Study of Flexible Fully Printed and Late-Stage Codified Octagonal Chipless RFID Tags," *IEEE Transactions on Antennas and Propagation,* vol. 64, no. 7, pp. 2815-2823, 2016, doi: 10.1109/tap.2016.2559522.

[27] E. P. S. R. Council, "New Materials for RF and Microwave Technologies," presented at the IEEE Antennas and Wireless Propagation Workshop, The Hilton Birmingham Metropole, Birmingham NEC, 2014.

[28] Y. Bonnassieux *et al.*, "The 2021 Flexible and Printed Electronics Roadmap," *Flexible and Printed Electronics,* vol. 6, no. 2, 2021, doi: 10.1088/2058-8585/abf986.

[29] L. J. Chu, "Physical Limitations of Omni-Directional Antennas," *Journal of Applied Physics,* vol. 19, no. 12, pp. 1163-1175, 1948/12/01 1948, doi: 10.1063/1.1715038.

[30] L. B. Kong *et al.*, "Recent Progress in Some Composite Materials and Structures for Specific Electromagnetic Applications," *International Materials Reviews,* vol. 58, no. 4, pp. 203-259, 2013, doi: 10.1179/1743280412y.0000000011.

[31] A. Kamyshny and S. Magdassi, "Conductive Nanomaterials for 2D and 3D Printed Flexible Electronics," *Chem Soc Rev,* vol. 48, no. 6, pp. 1712-1740, Mar 18 2019, doi: 10.1039/c8cs00738a.

[32] M. Park *et al.*, "Highly Stretchable Electric Circuits from a Composite Material of Silver Nanoparticles and Elastomeric Fibres," *Nat Nanotechnol,* vol. 7, no. 12, pp. 803-9, Dec 2012, doi: 10.1038/nnano.2012.206.

[33] J. Lee, P. Lee, H. Lee, D. Lee, S. S. Lee, and S. H. Ko, "Very Long Ag Nanowire Synthesis and Its Application in a Highly Transparent, Conductive and Flexible Metal Electrode Touch Panel," *Nanoscale,* vol. 4, no. 20, pp. 6408-14, Oct 21 2012, doi: 10.1039/c2nr31254a.

[34] Y. Wang *et al.*, "A Highly Stretchable, Transparent, and Conductive Polymer," *Science Advances,* vol. 3, no. 3, p. e1602076, 2017, doi: 10.1126/sciadv.1602076.

[35] E. Amram Bengio *et al.*, "Carbon Nanotube Thin Film Patch Antennas for Wireless Communications," *Applied Physics Letters*, vol. 114, no. 20, 2019, doi: 10.1063/1.5093327.

[36] V. P. Gusynin, S. G. Sharapov, and J. P. Carbotte, "Unusual Microwave Response of Dirac Quasiparticles in Graphene," *Physical Review Letters*, vol. 96, no. 25, p. 256802, 06/30/ 2006, doi: 10.1103/PhysRevLett.96.256802.

[37] A. K. Geim and K. S. Novoselov, "The Rise of Graphene," *Nature Materials*, vol. 6, no. 3, pp. 183-191, 2007/03/01 2007, doi: 10.1038/nmat1849.

[38] K. S. Novoselov, V. I. Fal′ko, L. Colombo, P. R. Gellert, M. G. Schwab, and K. Kim, "A Roadmap for Graphene," *Nature*, vol. 490, no. 7419, pp. 192-200, 2012/10/01 2012, doi: 10.1038/nature11458.

[39] J. Zhang, Z. Li, L. Shao, F. Xiao, and W. Zhu, "Active Modulation of Electromagnetically Induced Transparency Analog in Graphene-based Microwave Metamaterial," *Carbon*, vol. 183, pp. 850-857, 2021, doi: 10.1016/j.carbon.2021.07.069.

[40] J. Zhang and W. Zhu, "Graphene-Based Microwave Metasurfaces and Radio-Frequency Devices," *Advanced Photonics Research*, vol. 2, no. 11, 2021, doi: 10.1002/adpr.202100142.

[41] A. Sarycheva, A. Polemi, Y. Liu, K. Dandekar, B. Anasori, and Y. Gogotsi, "2D Titanium Carbide (MXene) for Wireless Communication," *Science Advances*, vol. 4, no. 9, p. eaau0920, 2018, doi: 10.1126/sciadv.aau0920.

[42] A. VahidMohammadi, J. Rosen, and Y. Gogotsi, "The World of Two-Dimensional Carbides and Nitrides (MXenes)," *Science*, vol. 372, no. 6547, p. eabf1581, 2021, doi: 10.1126/science.abf1581.

[43] A. Scidà *et al.*, "Application of Graphene-based Flexible Antennas in Consumer Electronic Devices," *Materials Today*, vol. 21, no. 3, pp. 223-230, 2018, doi: 10.1016/j.mattod.2018.01.007.

[44] I. Ibanez-Labiano, M. S. Ergoktas, C. Kocabas, A. Toomey, A. Alomainy, and E. Ozden-Yenigun, "Graphene-based Soft Wearable Antennas," *Applied Materials Today*, vol. 20, 2020, doi: 10.1016/j.apmt.2020.100727.

[45] B. Zhu, S. Gong, and W. Cheng, "Softening Gold for Elastronics," *Chem Soc Rev*, vol. 48, no. 6, pp. 1668-1711, Mar 18 2019, doi: 10.1039/c8cs00609a.

[46] K. S. Novoselov, A. Mishchenko, A. Carvalho, and A. H. Castro Neto, "2D Materials and Van der Waals Heterostructures," *Science*, vol. 353, no. 6298, p. aac9439, 2016, doi: 10.1126/science.aac9439.

[47] D. Wang, Y. Zhang, X. Lu, Z. Ma, C. Xie, and Z. Zheng, "Chemical Formation of Soft Metal Electrodes for Flexible and Wearable Electronics," *Chem Soc Rev*, vol. 47, no. 12, pp. 4611-4641, Jun 18 2018, doi: 10.1039/c7cs00192d.

[48] J. Shi *et al.*, "Smart Textile-Integrated Microelectronic Systems for Wearable Applications," *Advanced Materials*, vol. 32, no. 5, p. 1901958, 2020, doi: https://doi.org/10.1002/adma.201901958.

[49] K. Yan, J. Li, L. Pan, and Y. Shi, "Inkjet Printing for Flexible and Wearable Electronics," *APL Materials,* vol. 8, no. 12, p. 120705, 2020, doi: 10.1063/5.0031669.

[50] J. Suikkola *et al.*, "Screen-Printing Fabrication and Characterization of Stretchable Electronics," *Sci Rep,* vol. 6, p. 25784, May 13 2016, doi: 10.1038/srep25784.

[51] M. T. Craton, X. Konstantinou, J. D. Albrecht, P. Chahal, and J. Papapolymerou, "Additive Manufacturing of a W-Band System-on-Package," *IEEE Transactions on Microwave Theory and Techniques,* pp. 1-1, 2021, doi: 10.1109/tmtt.2021.3076066.

[52] S. I. Rich, Z. Jiang, K. Fukuda, and T. Someya, "Well-rounded Devices: the Fabrication of Electronics on Curved Surfaces – A Review," *Materials Horizons,* vol. 8, no. 7, pp. 1926-1958, 2021, doi: 10.1039/d1mh00143d.

[53] J. J. Adams *et al.*, "Conformal Printing of Electrically Small Antennas on Three-Dimensional Surfaces," *Adv Mater,* vol. 23, no. 11, pp. 1335-40, Mar 18 2011, doi: 10.1002/adma.201003734.

[54] J. J. Adams, S. C. Slimmer, T. F. Malkowski, E. B. Duoss, J. A. Lewis, and J. T. Bernhard, "Comparison of Spherical Antennas Fabricated via Conformal Printing: Helix, Meanderline, and Hybrid Designs," *IEEE Antennas and Wireless Propagation Letters,* vol. 10, pp. 1425-1428, 2011, doi: 10.1109/lawp.2011.2178999.

[55] I. Cherukhin, S. P. Gao, and Y. X. Guo, "Fully Flexible Polymer-based Microwave Devices: Materials, Fabrication Technique, and Application to Transmission Lines," *IEEE Transactions on Antennas and Propagation,* pp. 1-1, 2021, doi: 10.1109/TAP.2021.3083855.

[56] A. A. Gupta, M. H. Rahmani, M. C. M. Soer, S. G. Cloutier, and R. Izquierdo, "Aerosol Jet Printed, Microwave Microstrip Ring Resonators for System-In-Package Applications," *IEEE Transactions on Components, Packaging and Manufacturing Technology,* vol. 10, no. 11, pp. 1913-1920, 2020, doi: 10.1109/tcpmt.2020.3025186.

[57] R. Salvado, C. Loss, R. Gonçalves, and P. Pinho, "Textile Materials for the Design of Wearable Antennas: A Survey," (in English), *Sensors,* vol. 12, no. 11, pp. 15841-15857, 2012.

[58] L. M. Castano and A. B. Flatau, "Smart Fabric Sensors and E-textile Technologies: A review," *Smart Materials and Structures,* vol. 23, no. 5, p. 053001, 2014/04/01 2014, doi: 10.1088/0964-1726/23/5/053001.

[59] S. Rao *et al.*, "Miniature Implantable and Wearable On-body Antennas: Towards the New Era of Wireless Body-centric Systems [Antenna Applications Corner]," *IEEE Antennas and Propagation Magazine,* vol. 56, no. 1, pp. 271-291, 2014, doi: 10.1109/MAP.2014.6821799.

[60] J. Monica and P. Jothilakshmi, "Gain Enhanced Conformal Patch Antenna with Defected Ground for Aircraft Applications," *IET Communications*, vol. 14, no. 2, pp. 290-299, 2020, doi: 10.1049/iet-com.2018.6042.

[61] S. F. Jilani, M. O. Munoz, Q. H. Abbasi, and A. Alomainy, "Millimeter-Wave Liquid Crystal Polymer Based Conformal Antenna Array for 5G Applications," (in en), *IEEE Antennas and Wireless Propagation Letters*, vol. 18, no. 1, pp. 84-88, 2019/01// 2019, doi: 10.1109/LAWP.2018.2881303.

[62] I. Locher, M. Klemm, T. Kirstein, and G. Troster, "Design and Characterization of Purely Textile Patch Antennas," *IEEE Transactions on Advanced Packaging*, vol. 29, no. 4, pp. 777-788, 2006, doi: 10.1109/tadvp.2006.884780.

[63] C. Hertleer, A. Tronquo, H. Rogier, L. Vallozzi, and L. Van Langenhove, "Aperture-Coupled Patch Antenna for Integration Into Wearable Textile Systems," *IEEE Antennas and Wireless Propagation Letters*, vol. 6, pp. 392-395, 2007, doi: 10.1109/lawp.2007.903498.

[64] S. Zhu and R. Langley, "Dual-Band Wearable Textile Antenna on an EBG Substrate," *IEEE Transactions on Antennas and Propagation*, vol. 57, no. 4, pp. 926-935, 2009, doi: 10.1109/TAP.2009.2014527.

[65] Y. Bayram *et al.*, "E-Textile Conductors and Polymer Composites for Conformal Lightweight Antennas," *IEEE Transactions on Antennas and Propagation*, vol. 58, no. 8, pp. 2732-2736, 2010, doi: 10.1109/TAP.2010.2050439.

[66] Y. Zhou, Y. Bayram, F. Du, L. Dai, and J. L. Volakis, "Polymer-Carbon Nanotube Sheets for Conformal Load Bearing Antennas," *IEEE Transactions on Antennas and Propagation*, vol. 58, no. 7, pp. 2169-2175, 2010, doi: 10.1109/TAP.2010.2048852.

[67] Z. Wang, L. Zhang, Y. Bayram, and J. L. Volakis, "Embroidered Conductive Fibers on Polymer Composite for Conformal Antennas," *IEEE Transactions on Antennas and Propagation*, vol. 60, no. 9, pp. 4141-4147, 2012, doi: 10.1109/TAP.2012.2207055.

[68] Z. Wang, L. Z. Lee, D. Psychoudakis, and J. L. Volakis, "Embroidered Multiband Body-Worn Antenna for GSM/PCS/WLAN Communications," *IEEE Transactions on Antennas and Propagation*, vol. 62, no. 6, pp. 3321-3329, 2014, doi: 10.1109/TAP.2014.2314311.

[69] F. Boeykens, H. Rogier, and L. Vallozzi, "An Efficient Technique Based on Polynomial Chaos to Model the Uncertainty in the Resonance Frequency of Textile Antennas Due to Bending," *IEEE Transactions on Antennas and Propagation*, vol. 62, no. 3, pp. 1253-1260, 2014, doi: 10.1109/tap.2013.2294021.

[70] D. Ferreira, P. Pires, R. Rodrigues, and R. F. S. Caldeirinha, "Wearable Textile Antennas: Examining the Effect of Bending on Their Performance," *IEEE Antennas and Propagation Magazine*, vol. 59, no. 3, pp. 54-59, 2017, doi: 10.1109/map.2017.2686093.

[71] L. Song and Y. Rahmat-Samii, "A Systematic Investigation of Rectangular Patch Antenna Bending Effects for Wearable Applications," *IEEE Transactions on Antennas and Propagation*, vol. 66, no. 5, pp. 2219-2228, 2018, doi: 10.1109/tap.2018.2809469.

[72] A. Vukovic, E. Altinozen, T. Dimitrijevic, and P. Sewell, "Simulation Platform for Flexible Electronics," in *2021 15th International Conference on Advanced Technologies, Systems and Services in Telecommunications (TELSIKS)*, 20-22 Oct. 2021 2021, pp. 135-138, doi: 10.1109/TELSIKS52058.2021.9606324.

[73] J. Zhong, A. Kiourti, T. Sebastian, Y. Bayram, and J. L. Volakis, "Conformal Load-Bearing Spiral Antenna on Conductive Textile Threads," *IEEE Antennas and Wireless Propagation Letters*, vol. 16, pp. 230-233, 2017, doi: 10.1109/LAWP.2016.2570807.

[74] M. S. Floater, G. Kós, and M. Reimers, "Mean Value Coordinates in 3D," *Computer Aided Geometric Design*, vol. 22, no. 7, pp. 623-631, 2005, doi: 10.1016/j.cagd.2005.06.004.

[75] P. Joshi, M. Meyer, T. DeRose, B. Green, and T. Sanocki, "Harmonic Coordinates for Character Articulation," *ACM Transactions on Graphics*, vol. 26, no. 99, 2007, doi: 10.1145/1276377.1276466.

[76] Y. Lipman, D. Levin, and D. Cohen-Or, "Green Coordinates," *ACM Trans. Graph.*, vol. 27, no. 3, pp. 1-10, 2008, doi: 10.1145/1360612.1360677.

[77] Y. Lipman and D. Levin, "Derivation and Analysis of Green Coordinates," *Computational Methods and Function Theory*, journal article vol. 10, no. 1, pp. 167-188, June 01 2010, doi: 10.1007/bf03321761.

[78] P. Sewell, T. M. Benson, C. Christopoulos, D. W. P. Thomas, A. Vukovic, and J. G. Wykes, "Transmission-line Modeling (TLM) Based upon Unstructured Tetrahedral Meshes," *IEEE Transactions on Microwave Theory and Techniques*, vol. 53, no. 6, pp. 1919-1928, 2005, doi: 10.1109/TMTT.2005.848078.

[79] P. D. Sewell, T. M. Benson, C. Christopoulos, D. W. P. Thomas, A. Vukovic, and J. G. Wykes, "Implicit Element Clustering for Tetrahedral Transmission-Line Modeling (TLM)," *IEEE Transactions on Microwave Theory and Techniques*, vol. 57, no. 8, pp. 2005-2014, 2009, doi: 10.1109/TMTT.2009.2025451.

[80] GGIEMR. "George Green Institute for Electromagnetics Research." https://www.nottingham.ac.uk/research/groups/ggiemr/our-research/large-scale-electromagnetic-modelling/utlm-unstructured-transmission-line-modelling.aspx (accessed 2021).

[81] S. W. Cheng, T. K. Dey, and J. Shewchuk, *Delaunay Mesh Generation*. CRC Press, 2013.

[82] C. Jones, P. Sewell, T. M. Benson, A. Vukovic, X. Meng, and H. Bucklow, "Advanced Computational Electromagnetics at BAE Systems," 2016.

[83] X. Meng, A. Vukovic, T. M. Benson, and P. Sewell, "Extended Capability Models for Carbon Fiber Composite (CFC) Panels in the Unstructured Transmission Line Modeling (UTLM) Method," *IEEE Transactions on Electromagnetic Compatibility*, vol. 58, no. 3, pp. 811-819, 2016, doi: 10.1109/temc.2016.2531791.

[84] X. Meng, P. Sewell, N. H. Rahman, A. Vukovic, and T. M. Benson, "Experimental Benchmarking of Unstructured Transmission-line Modelling (UTLM) Method in Modelling Twisted Wires," *ACES Express Journal*, vol. 1, no. 3, 2016.

[85] P. Sewell, A. Vukovic, T. M. Benson, and X. Meng, "Extracting Modal Field Profiles from 3D Unstructured Transmission Line Modelling Meshes for Use as Sources and Observers," *IET Science, Measurement & Technology*, vol. 11, no. 6, pp. 780-785, 2017, doi: 10.1049/iet-smt.2016.0357.

[86] A. Vukovic, P. Sewell, T. M. Benson, C. Earl, and C. Jones, "Modelling of Structural Joints for Lightning Direct Effect Studies," in *Tenth International Conference on Computational Electromagnetics (CEM 2019)*, 19-20 June 2019 2019, pp. 1-5, doi: 10.1049/cp.2019.0125.

[87] A. Vukovic, P. Sewell, and T. M. Benson, "Holistic Appraisal of Modeling Installed Antennas for Aerospace Applications," *IEEE Transactions on Antennas and Propagation*, vol. 67, no. 3, pp. 1396-1409, 2019, doi: 10.1109/tap.2018.2884769.

[88] A. Vukovic, P. Sewell, and T. M. Benson, "Impact of In Situ Radome Lightning Diverter Strips on Antenna Performance," *IEEE Transactions on Antennas and Propagation*, vol. 68, no. 11, pp. 7287-7296, 2020, doi: 10.1109/TAP.2020.2998169.

[89] C. Christopoulos, *The Transmission-line Modeling Method: TLM*. IEEE press, 1995.

[90] P. Russer, in *'The Transmission Line Matrix Method, in Applied Computational Electromagnetics'*: Springer-Verlag, 2000.

[91] X. Meng, P. Sewell, A. Vukovic, Z. Zhang, and T. Benson, "Experimental Benchmarking of Unstructured Transmission-line Modelling (UTLM) Method for Simulations of Explicitly Meshed Wiring," in *2015 Computational Electromagnetics International Workshop (CEM)*, 1-4 July 2015 2015, pp. 1-2, doi: 10.1109/CEM.2015.7237433.

[92] "IEEE Standard for Definitions of Terms for Antennas," *IEEE Std 145-2013 (Revision of IEEE Std 145-1993)*, pp. 1-50, 2014, doi: 10.1109/IEEESTD.2014.6758443.

[93] "IEEE Recommended Practice for Antenna Measurements," *IEEE Std 149-2021 (Revision of IEEE Std 149-1977)*, pp. 1-207, 2022, doi: 10.1109/IEEESTD.2022.9714428.

[94] "IEEE Standard Test Procedures for Antennas," *ANSI/IEEE Std 149-1979*, pp. 1-144, 1979, doi: 10.1109/IEEESTD.1979.120310.

Chapter 2 Antenna and Interconnect Basics and Modelling

This Chapter provides an overview of the basic antenna and interconnect parameters and briefly overviews the main principle of the time-domain Transmission Line Modelling method used in this thesis. The numerical tool is based on unstructured tetrahedral mesh to which we refer as Unstructured Transmission Line Modelling (UTLM) method. Chapter is not intended to give comprehensive background on antenna theory and time-domain numerical modelling technique, UTLM. The reader is referred to extensive literature available on the subject, listed in this Chapter.

This Chapter is organised as follows; In the first part, the main antenna and interconnect parameters will be given in accordance with the IEEE Standard Definition of Terms of Antennas [1] and with the IEEE Standard Test Procedure for Antennas [2, 3] which will be adopted throughout this thesis. The main parameters that will be defined are reflection and transmission coefficient, antenna impedance, radiation pattern, directivity, and gain and bandwidth. Secondly, the governing method equations and the philosophy behind the UTLM method will be given with accordance to [4-8], which will be adopted throughout this Chapter.

2.1 Antenna and Interconnect - [S] parameters

A wide range of parameters exist for characterising the performance of antenna and interconnects and in the following subsections the most important ones for this thesis are reviewed. For that purpose a general multi-port system that can be a multi-port

antenna, typically for an antenna array, or a multi-port interconnects, is defined schematically in Figure 2.1 shows two arbitrary ports i and j for which the reflected and incident voltages are defined at the port reference planes. The most common network used in characterisation of passive components is such as an antenna and interconnect is the scattering $[\boldsymbol{S}]$ matrix networks that relates the reflected voltages at each port, V^-, to the incident voltage at each port , V^+, as [9, 10]:

Here,

$$[\boldsymbol{V}^-] = [\boldsymbol{S}][\boldsymbol{V}^+] \tag{2.1}$$

$[\boldsymbol{S}]$ matrix (as a $N \times N$ matrix for a N-port network) is very useful at defining the reflection at each port and the transmission properties through the network. Reflection coefficient quantifies the electromagnetic wave that is reflected by impedance mismatch in the transmission medium.

The reflection coefficient at the i port is given by

$$S_{ii} = \frac{V_i^-}{V_j^+} = S_{ii} + \frac{\sum_{j \neq i} S_{ij}\, V_j^+}{V_i^-} \tag{2.2}$$

under the condition that all other ports are matched (therefore $V_j^+ = 0$ for $j \neq i$). Under these conditions all reflections at a particular port will come only from the antenna networks itself.

In this thesis only single antenna is considered for which, as a one port device, the reflection coefficient Γ becomes the scattering coefficient S_{11}. If the antenna is passive element, reflection coefficient is $\Gamma \leq 1$ [9, 10]. In this thesis the microstrip antennas have a defined threshold limit is $S_{11} < -10$ dB [11].

The voltage standing wave ratio (VSWR) is determined directly from the reflection coefficient as [9, 10]; and is given by

$$\text{VSWR} = (1 + |\Gamma|)/(1 - |\Gamma|). \tag{2.3}$$

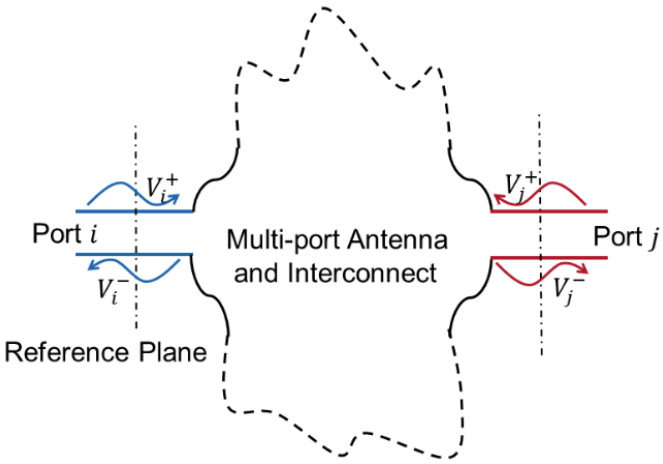


Figure 2.1 An arbitrary multiport antenna or interconnect system [9].

For the characterisation of interconnects both the reflection coefficient and transmission coefficient are used. For the simplest case the interconnect is a two-port device and the reflection coefficient, S_{11}, and transmission coefficient, S_{21}, are defined as

$$S_{11} = \frac{V_1^-}{V_1^+} \text{ when } V_2^+ = 0 \tag{2.4}$$

$$S_{21} = \frac{V_2^-}{V_1^+} \text{ when } V_2^+ = 0 \tag{2.5}$$

by applying an incident wave at port 1, V_1^+, and observing reflecting and outcoming waves at port 1, V_1^-, and at port 2, V_2^-, respectively.

2.1.1 Antenna Impedance

The input impedance of an antenna Z_A is "*the impedance presented by antenna at its terminals or the ratio of the voltage V and current I at the port of the antenna, or the ratio of the appropriate components of the electric field to magnetic field at a point when the antenna is isolated in free space; that is, without presence of other scattering structures and antennas*." [1, 9, 12]. Therefore, this is sometimes defined as the *isolated input impedance*. The input impedance of antenna is defined by the characteristic impedance Z_C of transmission line connected to the desired port of the antenna and antenna reflection coefficient Γ as [9, 10],

$$Z_A = \frac{V}{I} = Z_C \frac{1+\Gamma}{1-\Gamma} \tag{2.6}$$

Considering a linear multi-port antenna the voltage and the ith port can be associated with the currents at all port via a network impedance $[\boldsymbol{Z}]$ matrix as [9],

$$V_i = Z_{ii} I_i + \sum_{j \neq i} Z_{ij} I_j \tag{2.7}$$

where Z_{ii} is the self-impedance of the ith port Z_{ij} is mutual impedance between the ith and jth ports. The input impedance of the ith port is then derived as [9, 10, 13],

$$Z_{A,i} = V_i / I_i + \sum_{j \neq i} Z_{ij}\, I_j / I_i \tag{2.8}$$

under the condition that all other ports are open circuit i.e., that $I_{j \neq i} = 0$ which is related to the excitations (currents) of the other ports and therefore differs from the isolated input impedance. The active input impedance is defined as the input impedance of a port in a multi-port system [9, 10, 13]. For an active impedance of array element may be different from identical isolated input impedance due to the mutual coupling. Individual port active impedance can vary significantly when the excitation of the ports is varied with the aim of beamforming can become a significantly mismatched to the transmission line impedance [9, 10, 13].

One can derive impedance matrix from the scattering matrix and vice versa. With assumptions of all the ports of identical characteristic impedance Z_C [9, 10, 13];

$$\bar{\bar{Z}} = Z_C\left(\bar{\bar{U}} + \bar{\bar{S}}\right) \cdot \left(\bar{\bar{U}} - \bar{\bar{S}}\right)^{-1} \tag{2.9}$$

where $\bar{\bar{U}}$ is unit matrix. Therefore, the scattering matrix in terms of the impedance matrix given by [9, 10, 13];

$$\bar{\bar{S}} = \left(\bar{\bar{Z}} + Z_C \bar{\bar{U}}\right)^{-1} \cdot \left(\bar{\bar{Z}} - Z_C \bar{\bar{U}}\right) \tag{2.10}$$

2.1.2 Radiation Pattern

The radiation pattern is a "*mathematical function or graphical representation of the radiation properties of the antenna as a function of space coordinates*" [1, 9]. The most general way of determining radiation pattern is in far-field region [9, 12]. That region is "*where the angular field distribution is essentially independent of the distance from a specified point in the antenna region*" [1, 9]. The far-field region is defined by those distances higher than $2D^2/\lambda$, D being the maximum overall dimension of the antenna and λ is the free-space wavelength [2, 3, 9, 12]. For time-harmonic fields, the simple form of the radiated electric field $\boldsymbol{E}$ in the far-field region can be expressed as [2, 3, 9, 12],

$$\lim_{\boldsymbol{r}\to\infty} \boldsymbol{E}(\boldsymbol{r}) = \boldsymbol{P}(\boldsymbol{a_r})\, e^{-jkr}/r \tag{2.11}$$

where the position vector $\boldsymbol{r}$ is the reference to the origin of the antenna coordinate system and $\boldsymbol{P}$ is a pattern function that is related only to the direction $\boldsymbol{a_r}$ of the position vector and the term $\exp(-jkr)/r$ that depends on the length of the position vector [2, 3, 9, 12]. A pattern function $\boldsymbol{P}$ and the direction $\boldsymbol{a_r}$ of the position vector are orthogonal to each other so that; that is $\boldsymbol{P} \cdot \boldsymbol{a_r} = 0$ [2, 3, 9, 12]. In essence, the pattern function $\boldsymbol{P}$ defines all the radiation properties for the antenna [2, 3, 9, 12].

2.1.3 Directivity

The directivity, D, of an antenna defined as "*the ratio of the radiation pattern intensity in a given direction from the antenna to the radiation intensity averaged over all directions. The average radiation intensity is equal to the total power radiated by the antenna divided by* 4π. *If the direction is specified, the direction of maximum radiation intensity is implied*" [2, 3, 14]. The radiation intensity in given direction, U, is the radiated power per solid angle $\boldsymbol{\Omega}$ and hence, $U = |\boldsymbol{P}|^2/2\eta_0$ where η_0 being the free-space intrinsic impedance and $|\boldsymbol{P}|^2$ the power radiated in given direction [2, 3, 9, 12]. Therefore, the directivity D is given direction can be mathematically written as [2, 3, 9, 12],

$$D \equiv \frac{4\pi U}{\boldsymbol{P}_{rad}} = \frac{2\pi|\boldsymbol{P}|^2}{\eta_0 \boldsymbol{P}_{rad}} = \frac{4\pi|\boldsymbol{P}|^2}{\int_{4\pi}|\boldsymbol{P}|^2 d\boldsymbol{\Omega}} \tag{2.12}$$

where the *total* radiated power $\boldsymbol{P}_{rad}$ can be calculated by integrating the power radiated in given direction over entire radiation sphere [2, 3, 9, 12].

2.1.4 Gain and Realised Gain

The gain, G, of an antenna is defined as "*the ratio of the intensity, in a given direction, to the radiation intensity that would be obtained if the power accepted by an antenna were radiated isotopically* [2, 3, 13]. *The radiation intensity corresponding to the isotopically radiated power is equal to the accepted (input) by antenna divided by* 4π" [2, 3, 9, 12]. Mathematically, this can be expressed as,

$$D \equiv \frac{U}{\boldsymbol{P}_{acc}/4\pi} = \frac{2\pi|\boldsymbol{P}|^2}{\eta_0 \boldsymbol{P}_{acc}} \tag{2.13}$$

where $\boldsymbol{P}_{acc}$ is the power accepted by the antenna [2, 3, 9, 12, 14].

The antenna radiation efficiency, e_{cd} which can be associated with rate of gain G and the directivity,D, that is expressed as $e_{cd} = G/D$ [2, 3, 9, 12]. The realised gain $G_{realised}$ of antenna that considers the reflection or mismatch losses defined by

$$G_{realised} \equiv \frac{U}{\boldsymbol{P}_{in}/4\pi} = G(1 - |\Gamma|^2) = e_0 D \tag{2.14}$$

where $e_0 = e_{cd}(1 - |\Gamma|^2)$ is the overall antenna efficiency [2, 3, 9, 12].

2.1.1 Bandwidth

In IEEE standards, the *bandwidth* (BW) of antenna is defined as "*the range of frequencies within which in the performance of the antenna, with respect to some characteristic, conforms to a specified standard*" [2, 3, 9, 12, 14]. Bandwidth refers to the frequency range over which the reflection coefficient Γ is less than a specified maximum allowable value $\Gamma_{\max}$ [2, 3, 9, 12]. In this thesis, $\Gamma_{\max} = -10$ dB.

The *fractional bandwidth* (FBW) is

$$\text{FBW} = \frac{f_u - f_l}{f_c} \text{ with } f_c = \frac{f_u + f_l}{2} \tag{2.15}$$

with f_u and f_l denoting the upper and lower limits of the frequency range, and the centre frequency f_c coincides with frequency of operation [2, 3, 9, 12].

2.2 Numerical Modelling: Unstructured Transmission Line Modelling Method

The purpose of this section is it give a brief description of the in-house electromagnetic (EM) simulator, based on Transmission-line Modelling (TLM) [15] and tetrahedral Delaunay mesh, namely Unstructured Transmission Line Modelling (UTLM) method [4-8]. The full in-house software is referred to as Virtual Evaluation Environment (VEE) and consists of a Geometry Kernel (GK), robust tetrahedral Delaunay mesher, and the time-domain EM solver based on UTLM, which is the main software and simulator tool for this thesis [16].

The Transmission-line Modelling (TLM) method [15] is a well-established time-domain numerical tool for solving electromagnetic problems. The beginning point for any numerical software is the discretisation of a problem space. For two-dimensional (2D) problems, these discrete cells are cartesian grid, triangular or hybrid mesh (combination of cartesian and triangular cells). In three-dimensional problems (3D) discretisation is done using a cartesian cuboidal cells, tetrahedral or hybrid cells. [4-7, 17-19]. For Unstructured-TLM, EM problem space is decomposed into tetrahedral cells based on Delaunay mesh [8] [20] as shown Figure 2.2a). On the four triangular faces, tangential electric and magnetic field is sampled by deriving local analytical solutions to Maxwell's equations [4-8, 17-19]. Therefore, it is possible to write mathematically an admittance operator that associates sampled electric and magnetic field values [4-8, 17-19]. This operator provides one on opportunity to implement an electrical network of transmission lines of different characteristic impedances but with the same transient time δ_t [4-8, 17-19]. The network of transmission lines follows the Voronoi mesh that

connects tetrahedron circumcentres and is orthogonal to the Delaunay mesh. The voltage pulses propagate on the Voronoi mesh between tetrahedron circumcentres and get scattered at the junctions between neighbouring tetrahedra. This is described by a time-stepping algorithm, which alternates between the scatter phase, at which the voltage pulses scatter at the junctions between transmission lines, and a connect phase in which the exchange of pulses between the neighbouring cells takes place [4-8, 17-19].

One of the important parameters to consider is the minimum length of the transmission line in the meshed problem, Δ. The causality requires that the timestep δ_t satisfies the condition $2c\delta_t < \Delta$. In any practical mesh the parameter Δ can be very small and can negatively impact the runtime. To alleviate that a clustering approach is introduced that clusters all cells that share a transmission line below defined threshold. That approach can improve the timestep by a factor of 10 [8]. The essence of clustering approach, schematically presented in Figure 2.3, is to replace the short transmission line by the inductive stub and determine overall scattering response implicitly [8].

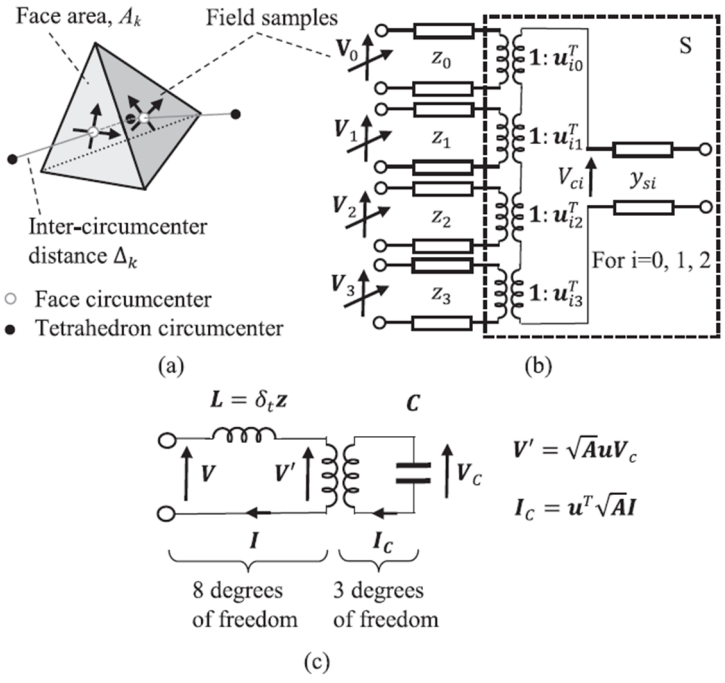


Figure 2.2 Canonical tetrahedral cell scattering network (a) Tetrahedral element (b) Equivalent network representation and (c) Compact circuit representation [8].

The canonical network equivalent network associated with two neighbouring of unclustered tetrahedral cells [8]. The main electromagnetic response of each cells comprises a superposition of the behaviour of lower-order electric and magnetic-type dipoles and multipoles. The link line joining the pairs yields to provide an inductance (magnetic dipole behaviour) proportional to the distance between cell circumcentre [8]. In order to deals with the parasitic capacitance behaviour related to the line, the time steps need to be remained below $2c\delta_t < \Delta$ [8]. The essence of clustering approach: replace the link line by inductive stub and determine overall scattering response of the pair [8].

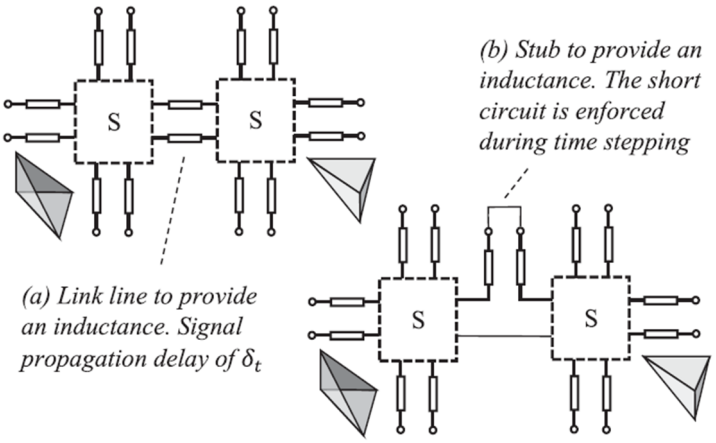


Figure 2.3 Clustering phenomena demonstrated by two neighbouring cells whose circumcentres are separated by a small distance Δ. (a) Without clustering, the time step is typically required to be $2c\delta_t < \Delta$. (b) With clustering time step can be significantly raised [8].

In order to solve network problem of Figure 2.3b), first, one need to consider the compact representation of the Figure 2.2c) [8],

$$\begin{pmatrix} \boldsymbol{V} \\ 0 \end{pmatrix} = \begin{pmatrix} j\omega\delta_t \boldsymbol{z} & \sqrt{\boldsymbol{A}}\boldsymbol{u} \\ \boldsymbol{u}^T\sqrt{\boldsymbol{A}} & -j\omega\boldsymbol{C} \end{pmatrix} \begin{pmatrix} \boldsymbol{I} \\ \boldsymbol{V}_C \end{pmatrix} \tag{2.16}$$

where $\boldsymbol{C} = 0.5\varepsilon\boldsymbol{u}^T\boldsymbol{A}\boldsymbol{\Delta}(1 - \hat{\boldsymbol{n}}\hat{\boldsymbol{n}})\boldsymbol{u}$ (See Eq.(8) in [7]) [8]. The diagonal matrix $\boldsymbol{z}$ and $\boldsymbol{A}$ contains values for the transmission line characteristic impedance and the area of associated cell faces, respectively [8]. Each characteristic impedance is of value $Z_o\Delta/c\,\delta_t$ where $Z_o = \sqrt{\mu/\varepsilon}$ is the characteristic impedance of the material μ and ε being the permeability and permittivity [8]. Δ is the distance between neighbouring

tetrahedral circumcentres. The term $\boldsymbol{u}$ denotes the face sampled constant field vectors related to the three electric dipoles modelling the quasi-electrostatic behaviour of each tetrahedron and their orientations are computed by a small eigenvalue equation in [4]. $\boldsymbol{V_C}$ is a vector amplitude for electric dipoles [8].

The UTLM technique is to seek eigen responses of (2.16), which are defined as pairs of $\boldsymbol{V}_k$ and $\boldsymbol{I}_k$, which are associated by a simple scaling factor, i.e., $\boldsymbol{z}\boldsymbol{I}_k = j\omega\tau_k\boldsymbol{V}_k$ [8]. After introducing the incident and reflecting voltages on the transmission lines of Figure 2.2b), i.e., $\boldsymbol{V} = \boldsymbol{V^i} + \boldsymbol{V^r}$ and $\boldsymbol{zI} = \boldsymbol{V^i} - \boldsymbol{V^r}$ [8]. Each eigensolution provides a set of amplitudes such that if this set values were incident from the transmission lines onto the cell, it would reflect without distortion via a simple reflection coefficient [8]

$$\boldsymbol{V}_\tau^r = \frac{1 - j\omega\tau}{1 + j\omega\tau} \sim e^{-j\omega 2\tau}\boldsymbol{V}_\tau^i \tag{2.17}$$

Furthermore, such solution, Eq. (2.16) is rank deficient and possesses solutions with $\boldsymbol{V}_C = 0, \boldsymbol{I} \neq 0$ and with $\tau = \infty$. This is physically related to the quasi magneto-static fields and in a similar manner to (2.17) gives [8]

$$\boldsymbol{V}_{\tau=\infty}^r = -e^{-j\omega\delta_t}\boldsymbol{V}_{\tau=\infty}^i \tag{2.18}$$

This can be mathematically rewritten as [8],

$$\sqrt{\boldsymbol{y}}\boldsymbol{V^r} = -e^{-j\omega\delta_t}(-1 + 2\boldsymbol{Q}e^{-j\omega(2\tau-\delta_t)}\boldsymbol{Q^T})\sqrt{\boldsymbol{y}}\boldsymbol{V^i} \tag{2.19}$$

where $\boldsymbol{y}$= $\boldsymbol{z^{-1}}$ and $\boldsymbol{Q}$ is a unitary matrix, whose columns are solutions of (2.16) [8]

$$Q = (\sqrt{\boldsymbol{z}}\boldsymbol{I}_{\tau_1}\sqrt{\boldsymbol{z}}\boldsymbol{I}_{\tau_2} \ldots) \tag{2.20}$$

The time delays $2\tau - \delta_t$ are implemented by utilising the open-circuit stubs y_{si} as demonstrated in Figure 2.2b)[8],

Essentially, algorithm depends upon the $\boldsymbol{Q}$ is frequency dependent. One considers frequency independent eigenproblem [8]

$$\begin{pmatrix} \boldsymbol{z} & 0 \\ 0 & 0 \end{pmatrix} \begin{pmatrix} \boldsymbol{V} \\ 0 \end{pmatrix} = \tau' \begin{pmatrix} 0 & \sqrt{\boldsymbol{A}}\boldsymbol{u} \\ \boldsymbol{u}^T\sqrt{\boldsymbol{A}} & -\boldsymbol{C} \end{pmatrix} \begin{pmatrix} \boldsymbol{I} \\ \boldsymbol{V_C} \end{pmatrix}. \tag{2.21}$$

It is simple to show by inspection that the eigenvector of (2.12) and that the eigenvalues are related as [8]

$$\tau = \frac{\tau'}{1 - \omega^2 \tau' \delta_t} \tag{2.22}$$

which has same second order accuracy [8]. Article [8] also addressed robust solution of (2.21) for moderated size of cell cluster, and complexity reduction process reducing the number of solutions in the column of (2.19) and the number of inductive stubs needed to be present when time stepping. The full theory of derivation is not in the scope of this section and for further information, the reader is referred to [4-8].

Overall, the EM simulation includes the following steps:

1. Geometry generation.
2. Generation of suitable Delaunay meshes [8, 17, 19, 21] (See Figure 6.6 and Figure 7.3).
3. Assigning suitable materials models and boundary conditions to discretised geometry [21-27].
4. Defining excitations and observation parameters.
5. Adopting a suitable clustering threshold that would keep the maximum cluster size to below 200 cells. Clusters bigger than that negatively impact the runtime [7, 8].
6. Perform EM simulation [4-8].
7. Post processing of the results to obtain desired observables and figures-of-merit [21-27].

UTLM's stability is provable priori on a cell-by-cell basis without need to stick to guidelines, such as Courant [28] criterion to guarantee the convergence of the solution of electromagnetic problem [4-8]. Besides, the late time instability has never been observed [4-8]. Selection of mesh size in UTLM is critical to reducing the numerical dispersion. Dispersion is well known as the propagation velocity of the wave depends

on frequency [9, 15, 21]. Dispersion may exist even in non-dispersive medium, which is widely known as numerical dispersion due to obtaining a solution of Maxwell's equations only locally [9, 15, 21]. Numerical dispersion can deteriorate the pulse waveform and can cause non-physical refraction, cumulative phase error and numerical anisotropy [9, 15, 21]. Therefore, to decrease undesirable numerical dispersion error, the advisable cell size is $\Delta < \lambda/10$, where Δ is the maximum cell size of the mesh and λ is the minimum wavelength of problem [21]. In many practical applications a more accurate guidance is $\Delta \leq \lambda/20$ [21].

2.3 Conclusions

This Chapter reviews various figure-of-merit applied broadly on antenna and interconnect simulations and measurements. These were introduced based on their basic definitions according to IEEE standards. The main parameters that are defined are reflection and transmission coefficient, radiation profile, directivity, gain and the bandwidth. The time-domain numerical modelling technique based on unstructured mesh; Unstructured Transmission Line Modelling (UTLM) method is briefly overviewed to give a reader a brief idea about main electromagnetic simulator used in this thesis. The next Chapter introduces the main materials used in flexible electronics and summarises the current understanding of how a particular deformation impacts the performance of flexible antennas and interconnects.

References

[1] "IEEE Standard for Definitions of Terms for Antennas," *IEEE Std 145-2013 (Revision of IEEE Std 145-1993)*, pp. 1-50, 2014, doi: 10.1109/IEEESTD.2014.6758443.

[2] "IEEE Recommended Practice for Antenna Measurements," *IEEE Std 149-2021 (Revision of IEEE Std 149-1977)*, pp. 1-207, 2022, doi: 10.1109/IEEESTD.2022.9714428.

[3] "IEEE Standard Test Procedures for Antennas," *ANSI/IEEE Std 149-1979*, pp. 1-144, 1979, doi: 10.1109/IEEESTD.1979.120310.

[4] P. Sewell, T. M. Benson, C. Christopoulos, D. W. P. Thomas, A. Vukovic, and J. G. Wykes, "Transmission-line Modeling (TLM) Based upon Unstructured Tetrahedral Meshes," *IEEE Transactions on Microwave Theory and Techniques*, vol. 53, no. 6, pp. 1919-1928, 2005, doi: 10.1109/tmtt.2005.848078.

[5] P. Sewell, C. Christopoulos, A. Vukovic, J. G. Wykes, D. W. P. Thomas, and T. M. Benson, "Transmission Line Modelling Using Unstructured Meshes," *IEE Proceedings - Science, Measurement and Technology*, vol. 151, no. 6, pp. 445-448, 2004, doi: 10.1049/ip-smt:20041024.

[6] P. Sewell, J. G. Wykes, T. M. Benson, C. Christopoulos, D. W. P. Thomas, and A. Vukovic, "Transmission-line Modeling Using Unstructured Triangular Meshes," *IEEE Transactions on Microwave Theory and Techniques*, vol. 52, no. 5, pp. 1490-1497, 2004, doi: 10.1109/TMTT.2004.827027.

[7] P. D. Sewell, T. M. Benson, C. Christopoulos, D. W. P. Thomas, A. Vukovic, and J. G. Wykes, "Implicit Element Clustering for Tetrahedral Transmission-Line Modeling (TLM)," *IEEE Transactions on Microwave Theory and Techniques*, vol. 57, no. 8, pp. 2005-2014, 2009, doi: 10.1109/tmtt.2009.2025451.

[8] P. D. Sewell, T. M. Benson, A. Vukovic, and X. Meng, "Complexity Reduction of Multiscale UTLM Cell Clusters," *IEEE Journal on Multiscale and Multiphysics Computational Techniques*, vol. 2, pp. 18-28, 2017, doi: 10.1109/jmmct.2017.2670613.

[9] W. A. Imbriale, S. Gao, and L. Boccia, *Space Antenna Handbook*. New York,: John Wiley & Sons, Incorporated, 2012.

[10] D. M. Pozar, *Microwave Engineering*, 4th ed. Hoboken, N.J. : Wiley, 2012.

[11] M. Gustafsson and S. Nordebo, "Bandwidth, Q Factor, and Resonance Models of Antennas," *Progress In Electromagnetics Research*, vol. 62, pp. 1-20, 2006.

[12] C. A. Balanis, *Antenna Theory : Analysis and Design*, 4th ed. Hoboken, N.J.: Hoboken, N.J. : Wiley, 2016.

[13] J. R. James, P. S. Hall, and C. Wood, *Microstrip Antenna: Theory and Design*. Iet, 1986.

[14] V. Monebhurrun, "Revision of IEEE Standard 145-2013: IEEE Standard for Definitions of Terms for Antennas [Stand on Standards]," *IEEE Antennas and Propagation Magazine*, vol. 62, no. 3, pp. 117-117, 2020.

[15] C. Christopoulos, *The Transmission-Line Modeling Method: TLM*. John Wiley & Sons, 1995.

[16] GGIEMR. "George Green Institute for Electromagnetics Research, Unstructured Transmission Line Modelling Method (UTLM)." https://www.nottingham.ac.uk/research/groups/ggiemr/our-research/large-scale-electromagnetic-modelling/utlm-unstructured-transmission-line-modelling.aspx (accessed 14/12/2022, 2022).

[17] P. Sewell, J. Wykes, A. Vukovic, D. W. P. Thomas, T. M. Benson, and C. Christopoulos, "Multi-grid Interface in Computational Electromagnetics," *Electronics Letters*, vol. 40, no. 3, pp. 162-163, 2004, doi: 10.1049/el:20040107.

[18] P. Sewell, T. M. Benson, A. Vukovic, and S. Cole, "Mesh Optimisation Methods for Unstructured Transmission-line Modelling," *IET Science, Measurement & Technology*, vol. 7, no. 1, pp. 32-40, 2013, doi: 10.1049/iet-smt.2012.0069.

[19] K. Yan, A. Vukovic, and P. Sewell, "Two-dimensional TE Series Node Transmission-Line Modelling Based on Unstructured Triangular Meshes," in *2022 52nd European Microwave Conference (EuMC)*, 27-29 Sept. 2022 2022, pp. 448-451, doi: 10.23919/EuMC54642.2022.9924316.

[20] S. W. Cheng, T. K. Dey, and J. Shewchuk, *Delaunay Mesh Generation*. CRC Press, 2013.

[21] A. Vukovic, P. Sewell, and T. M. Benson, "Holistic Appraisal of Modeling Installed Antennas for Aerospace Applications," *IEEE Transactions on Antennas and Propagation*, vol. 67, no. 3, pp. 1396-1409, 2019, doi: 10.1109/tap.2018.2884769.

[22] P. Sewell, A. Vukovic, X. Meng, and T. M. Benson, "A Note on Material Losses in Unstructured Transmission line Modeling," *Microwave and Optical Technology Letters*, vol. 57, no. 9, pp. 2218-2222, 2015, doi: 10.1002/mop.29300.

[23] X. Meng, P. Sewell, S. Phang, A. Vukovic, and T. M. Benson, "Modeling Curved Carbon Fiber Composite (CFC) Structures in the Transmission-Line Modeling (TLM) Method," *IEEE Transactions on Electromagnetic Compatibility*, vol. 57, no. 3, pp. 384-390, 2015, doi: 10.1109/temc.2015.2400055.

[24] A. Vukovic, S. Zongyuan, P. Sewell, L. A. Aziz, and T. M. Benson, "Geometric Challenges of Modelling Textile Antennas," in *2017 European*

Modelling Symposium (EMS), 20-21 Nov. 2017 2017, pp. 34-37, doi: 10.1109/EMS.2017.17.

[25] A. Vukovic, P. Sewell, T. M. Benson, C. Earl, and C. Jones, "Modelling of Structural Joints for Lightning Direct Effect Studies," in *Tenth International Conference on Computational Electromagnetics (CEM 2019)*, 19-20 June 2019 2019, pp. 1-5, doi: 10.1049/cp.2019.0125.

[26] A. Vukovic, P. Sewell, and T. M. Benson, "Generating Radome Geometries for Full Lightning Protection Studies," in *2019 ESA Workshop on Aerospace EMC (Aerospace EMC)*, 20-22 May 2019 2019, pp. 1-5, doi: 10.23919/AeroEMC.2019.8788907.

[27] A. Vukovic, P. Sewell, and T. M. Benson, "Impact of In Situ Radome Lightning Diverter Strips on Antenna Performance," *IEEE Transactions on Antennas and Propagation*, vol. 68, no. 11, pp. 7287-7296, 2020, doi: 10.1109/TAP.2020.2998169.

[28] R. Courant, K. Friedrichs, and H. Lewy, "On the Partial Difference Equations of Mathematical Physics," *IBM Journal of Research and Development*, vol. 11, no. 2, pp. 215-234, 1967, doi: 10.1147/rd.112.0215.

Chapter 3 Flexible Antennas and Interconnects for Wearable Electronics Overview

This Chapter overviews different substrate and conductive materials that are used for design of flexible antennas and interconnects. The Chapter also overviews the impact on particular deformation, namely, cylindrical bending, twisting and stretching, on the performance of antennas and interconnects. Finally, the main findings from the overview are summarised.

3.1 Introduction

This section focuses on the main materials used in flexible electronics.

Flexible electronics devices are constructed utilising a wide range of different novel conductive and dielectric substrate materials. Flexible materials used in wearable and flexible electronics applications need high mechanical durability and a good level of integrity to other electronic devices [1-11]. Furthermore, the stretchability and elasticity of materials are essential physical characteristic properties to generate reversible deformations [11].

Flexible materials need to have mechanical properties to provide a desired performance under deformation. For instance, any wearable antenna and interconnects must be bent to conform to the human body and deform to accommodate strain during dynamics of motions [7, 12]. The mechanical requirement for antenna substrate material medium is high elasticity and strain with low Young's modulus. Young's modulus of the material is determined as the ratio of the strain to stress in the linear elasticity system of uniaxial

deformation [13]. Thus, a low value of Young's modules ensures a wide stress range without degradation of desired electrical and mechanical properties. The thickness of the film, h_s, is inversely proportional to the modulus and directly related to the applied in-plane stress [13]. The average elastic modulus can written as $E = 54.872h_s^{0.226}$, where GPa is h_s in size nm [13, 14]. Figure 3.1 demonstrates an overview of materials, such as, elastomers, polymer plastic, and natural fibres categorised by their Young's modulus. It can be seen that the elastomers provide the highest elasticity for conforming the human body compared to polymer plastics and natural fibres. In terms of elastomers, Polydimethylsiloxane, PDMS, has three order higher elasticity than the other elastomers. Similarly, Polyethylene Terephthalate, PET, has the highest elasticity (three order) compared with Polyimide, PI, and Polyethylene naphthalate, PEN. Besides, natural fibres, such as cotton, cellulose, silk, wool, and jute, maintain similar elasticity as PI, and PEN materials [13].

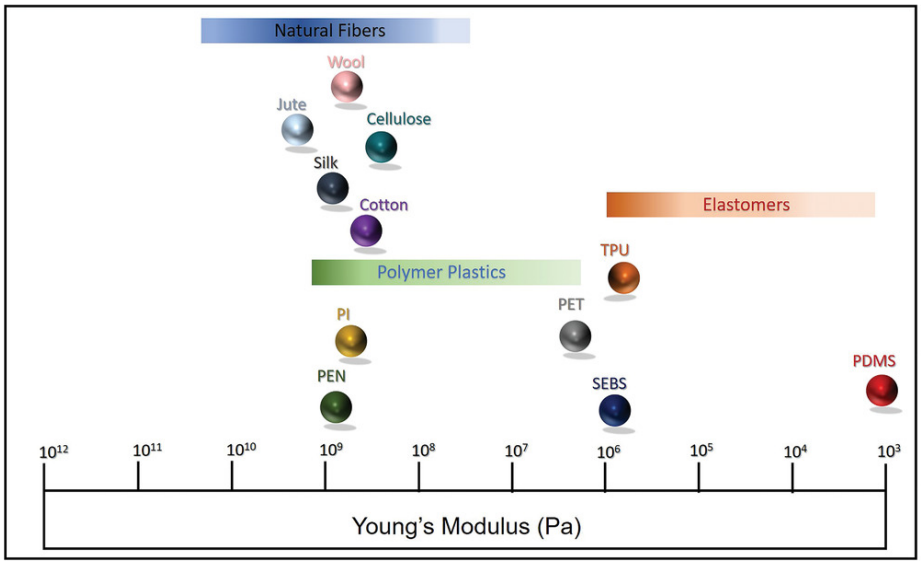


Figure 3.1 Comparison of elastic (Young's) modulus of various materials [13].

Textile materials are structured fibrous materials with electrical properties defined by the properties of constructive fibrous components, yarns, and weaving of the fabric [1]. Textiles are flexible materials whose density and thickness may change with applied compression [1]. Their porosity depends on the weaving density of the yarn or fabric, which in turn impacts on desired permeability of substrate or electrical properties of

conductive parts [1]. Furthermore, different weaving of the threads and the fibres results in anisotropy of general material [1, 15].

Flexible antennas have advantages over planar rigid antennas in terms of small thickness, lightweight, and small profile [16-19]. In addition, flexible antennas operate robustly and can exhibit extreme mechanical deformation with their lightweight structure [16, 20]. One specific target needs flexible and foldable antennas for their planar and *in-situ* performance. Several properties of flexible construction materials affect the figure of merit of the electromagnetic performance. For example, the antenna efficiency is fundamentally limited by the refractive index and thickness of media [1]. Therefore, the utilisation of bendable and flexible material in wearable RF electronics needs the characterisation of its properties. On the other hand, little information on electromagnetics properties and *in-situ* performance of conventional substrates with conductive parts can be found [1].

3.2 Substrates for Wearable Applications

When it comes to electrical properties of wearable antennas and interconnects, substrate medium generally is isotropic and the dielectric permittivity of, ε determined by a complex value $\varepsilon = \varepsilon_r \varepsilon_0$ where a relative permittivity $\varepsilon_r = \varepsilon_r' - j\varepsilon_r''$, and ε_0 is the permittivity of the vacuum medium [1, 21, 22]. In practice, the dielectric properties of the medium depend on the frequency, homogeneity, purity, temperature, and the surface roughness of the medium [1, 22]. The dielectric substrate materials are specified by the real part of permittivity of the medium, ε_r', and by loss tangent, $tan\delta = \varepsilon_r''/\varepsilon_r'$ [1, 21]. The weaving structure and the complex cross-sections of material can generate a significant amount of uniaxial and biaxial anisotropy; that can be extracted from electric field orientation and determines a relative electric permittivity tensor where ($\varepsilon_{xx} \neq \varepsilon_{yy} \neq \varepsilon_{zz}; tan\delta_{xx} \neq tan\delta_{yy} \neq tan\delta_{zz}$). The dielectric material is defined by the weaving density of yarns [23, 24] and electrical properties of constructive yarn elements [1].

Table 3.1 Averaged Dielectric Constant for Different Materials

	Materials	**Permittivity ε_r**	**Loss Tangent $tan\delta$**	**Thickness t (mm)**	**Frequency (GHz)**	**Refs.**
Natural Fibres or Textiles	Silk	1.75	0.0120	0.580	2.60-3.95	[25]
	Tween	1.69	0.0084	0.685	2.60-3.95	[25]
	Panama	2.12	0.0180	0.347	2.60-3.95	[25]
	Felt	1.38	0.0230	1.100	2.60-3.95	[25]
	Fleece	2.55	0.0035	2.550	2.60-3.95	[25]
	3D Orthogonal Weave	3.20	0.0080	2.700	1.575	[26]
Polymers	Polytetrafluoroethylene (PTFE)	2.05	0.0035	11.660	2.60-3.95	[25]
	Polyimide (PI)	3.50	0.0026	0.1270	5.0-7.0	[11, 27]
	Polyethylene Terephthalate (PET)	3.00	0.0080	0.1000	2.0-4.0	[11, 28]
	Liquid Crystal Polymers (LCP)	2.90	0.0020	0.0500	3.0-12.0	[11, 29]
Elastomers	Polyurethane (PU)	2.60	0.0700	1.200	1.0-5.0	[30, 31]
	Polydimethylsiloxane (PDMS)	3.20	0.0100	0.500	1.0-3.0	[32]
	Thermo Plastic Polyurethane (TPU)	3.20	0.1000	0.50	0.8-1.0	[33]

Table 3.1 summarises electrical properties, such as dielectric and loss tangent, their thickness, of widely used materials (natural fibres or textiles, polymers, and elastomers) for flexible antennas and interconnects as well as their recommended operation frequency range. This table also shows that polymers and elastomers provide higher dielectric constants than textile materials except for the orthogonal weave structure [26]. Furthermore, elastomers have higher dielectric losses than polymers. The conventional thickness of the flexible substrate is around 200 μm for industrial applications and consumer electronics; however, an ultra-thin substrate with an extremely small thickness of 100 μm has also been reported for biocompatible

applications [34, 35]. The shaded rows in Table 3.1 indicates the most popular materials for substrates in flexible electronics. According to Table 3.1, a variety of polymers and elastomers have been developed as substrates for flexible devices. Polymers and elastomers are inexpensive and have a simple manufacturing process. Up to now, bendable, flexible electronic widely used polymers, e.g., polyethylene terephthalate (PET), polyimide (PI), and elastomers such as polydimethylsiloxane (PDMS) and polyurethane (PU) [35-37].

Table 3.2 Typical physical properties of polymeric and elastomer substrates

	Polymers		**Elastomers**	
Properties	**PI**	**PET**	**PDMS**	**PU**
Density (g cm^{-3})	1.42	1.39	0.95-0.98	1.0-1.30
Young Modulus (GPa)	2.5	5	<0.01	<0.01
Ultimate Elongation (%)	80	90	50-500	300-800
Dielectric Constants (ε_r) 1 GHz–10 GHz	3.5–3.4	3.0	2.9-2.75	2.14-3.5
$tan\delta$ at 1 GHz–10 GHz	0.0026–0.0020	0.008-0.002	0.008–0.07	0.02-0.1
Deformability	Low	Low	High	High
Thermal Stability	High	High	Low	Low
Electrical Stability	High	High	Low	Low
Fabrication	Simple	Moderate	Moderate	Moderate

Note: Data taken from refs. [11, 36, 38].

A Polyimide (PI) is a flexible, thin, lightweight polymer that is widely utilised for a flexible material to support printed circuit boards. PI has a low-dielectric constant, dissipation factor, and high flexibility, making it highly compatible with signal traces due to its thermal endurance and thin structure [11]. PI has high thermal stability and has good electronic properties, and it is manufactured with predefined thickness. PI has been used as a substrate to implement antennas for different range of frequencies [39-41].

Polyethylene Terephthalate (PET) film has rigid dimensionally stable and flexible thermoplastic polymer, known as Polyester [11]. PET has either transparent or semi-crystalline form depending on the thermal history and processing. It is a well-known substrate for RFID tags, optoelectronics, where both transparency and flexibility are needed for their application [11].

Polydimethylsiloxane (PDMS) is a soft and flexible, highly deformable, and transparent elastomer. Besides, its low electric conductivity, and isotropic and homogenous properties have made PDMS a suitable substrate selection for flexible and stretchable passive microwave devices [11]. PDMS properties may well be adjustable by dopant materials [11]. For example, electrical properties and mechanical flexibility can be varied by inserting materials with different permittivity compared to PDMS [11]. Polyurethane (PU) has similar properties as PDMS exception of higher dielectric loss.

Table 2.2 summarises the main material properties for PI, PET, PDMS and PU substrates. According to the table, PDMS and PU provide higher deformability, whereas PI and PET offer higher electrical and thermal stability in the environmental conditions. PI and PET provide higher dielectric constant leads to smaller size for antenna dimensions compared to PDMS and PU. However, they have smaller elongation constants resulting in smaller flexibility compared to PDMS and PU.

Another option in antennas and interconnects relies on textile substrates for integrating electronics into clothing that provide more comfortable and breathable wearing experience than the semi-rigid polymers [10, 42]. Moreover, the expansion of electronic textile applications that can be powered by solid-state fibre batteries can be integrated seamlessly into multifunctional on-body devices to provide stable and continuous power for wireless communication devices and sensors [43, 44].

3.3 Conductive Materials

This section overviews the most commonly used new conductive materials for flexible electronics. Electrical properties of the conductor is determined by its surface resistivity

[1]. The surface resistivity is the ratio of the DC voltage drop per unit length to the surface current per unit width, and it is expressed in Ohm/square ($\Omega/sq;\ \Omega/\square$) [1, 45].

For wearable antenna, the essential design choice is the conductivity of radiating part, σ, (Siemens per metre $(\mathrm{S/m})$, which can be expressed in terms of surface resistivity, ρ_s, as:

$$\sigma = 1/(\rho_s \cdot h) \tag{1}$$

where ρ_s is the surface resistivity and h is the thickness of the electrically conductive part [46].

Table 3.3 Conductivity (DC) of conventional materials for fabrication of flexible, wearable interconnects : Data taken from [36, 47, 48]

Materials (bulk)	**Conductivity, σ_{dc} ($\mathbf{S\ m^{-1}}$) at $\mathbf{20^oC}$**
Ag	6.30×10^7
Cu	5.96×10^7
Au	4.10×10^7
Al	3.72×10^7
Ni	1.43×10^7

Conventional conductive materials typically used in rigid electronics include Silver (Ag), Copper (Cu), Gold (Au), Nickel (Ni), and their conductivity values are given in Table 3.3. Table 3.3 shows that bulk silver has the highest conductivity, followed by bulk copper and gold [36, 47]. These materials have been traditionally utilised for electrodes and interconnect, and owing to their high electrical conductivity and they have very low loss [49]. A conductive part of an RF components should remain electrically robust and active under large mechanical deformations [50, 51]. However, the conventional conductive materials perform poorly in terms of flexibility, stretchability and have limited elasticity [49, 52].

Stretchable and flexible systems can be acquired in two different ways: (1) by strategically engineered desired shapes and (2) by using intrinsically stretchable materials [49, 53, 54]. Engineering shapes strategy for generating stretchable interconnect involves the shaping of signal traces as serpentine, meander, or wavy structures [55-62] that are shown to be able to accommodate stress and stretch.

To date, several different intrinsically flexible materials have been proposed and can be grouped in six different groups that are including (a) silver inks, (b) conductive polymers, (c) graphene or carbon-based materials, (d) 2D materials, (e) liquid metals and (f) textiles. A brief comparative analysis of the main conductive materials within each group is listed in Table 3.4. The Table 3.4 also list on which substrate a particular conductive material is fabricated. According to Table 3.4 the silver ink reported in [39] has the highest conductivity, followed by liquid metals [63], 2D material [64], and graphene [20].

Silver inks provide one opportunity with printing transmission lines or antennas on a flexible and deformable surface, but the conductivity of silver inks is still at least an order below the bulk silver [65].

Another option in wearable electronics relies on conductive polymers, but it has low flexibility, around 5% fracture of strain [50, 51, 54, 66] such as polyaniline (PANI), polypyrrole (PPy), and poly(3,4-ethylene dioxythiophene) – poly(styrene sulfonate) (PEDOT: PSS). Inserting conductivity-enhanced materials is applied to improve the conductivity and enhance the stretchability of the material [54, 67]. In 2012, a transparent poly(3,4-ethylene dioxythiophene)–poly(styrene sulfonate) (PEDOT: PSS) /PDMS film was reported with the stretchability of 188 % [67]. The demonstrated polymer film has comparable to the best values of PEDOT::PSS, with 3100 S/cm and 4100 S/cm for the strain value of 0% and 100%, respectively.

Table 3.4 Electrical Properties of Conductive Sheets

Material Types	Conductive Materials	Substrate	Conductivity, σ	Refs.
(a) Silver Ink	Ag-PDMS	PDMS	10^5 S/m	[68]
	Ag Inkjet	PI	6×10^6 S/m	[39]
	Ag-pastes	Ninja Flex	1.7×10^4 S/m	[69]
(b) Conductive Polymers	PANI / SWNT	PI	4500 S/m	[40]
	AgNW / PDMS	PDMS	8130 S/m	[70]
	Dupont CI-1036	PDMS	1.6×10^6 S/m	[71]
	Dupont DA6534	PDMS	0.45×10^6 S/m	[71]
(c) Graphene Based Materials	GAF	PET	1.0×10^6 S/m	[20]
	rGO	Paper	4.3×10^4 S/m	[72]
	Ag/SWNT	Polymer Composite	22 Ω/sq	[73]
	Graphene Sheet	Textile	≤ 0.06 Ω/sq	[74]
(d) 2D Materials	$Ti_3C_2T_x$ MXene	PET	1.5×10^6 S/m	[64]
	$Ti_3C_2T_x$ MXene	PET	0.02 Ω/sq	[75]
	$Ti_3C_2T_x$ MXene and single-walled carbon nanotubes (SWNTs)	Latex Tape	2.9×10^5 S/m	[76]
(e) Liquid Metal	E-GaIn	PDMS	3.4×10^6 S/m	[77]
	E-GaIn/SWNT	PDMS	3.4×10^6 S/m / 8.5×10^6 S/m	[63]
(f) Textiles	E-textile	PDMS	1.14×10^3 S/m	[78]
	Zelt Fabric	Felt	≤ 0.01 Ω/sq	[79]

Although Graphene and carbon-based materials have two orders lower conductivity than metal counterparts, they have received tremendous attention due to their flexibility and durability [16]. Moreover, with the improvement of the chemical material processing technology, the carbon-based materials increased conductivity from around

10^4 S m^{-1}, to 1.8×10^6 S m^{-1} over the years for the reported refs [16, 80, 81] which is comparable to the conductivity of ideal graphite (~10^6 S m^{-1}).

The 2D nanomaterials are promising materials for conducting layers and traces [82-86]. MXenes is the most popular variant with high conductivity of up to 1.5×10^6 S m^{-1} [64, 87].

Finally, electro-textiles and metallic coated textile fabrics have been widely used for wearable and textile antennas [88, 89]. The intensity of fibre knitting is the main parameter that characterise its conductivity [88, 89]. However, textiles require precise control for reproducibility and limited accuracy of flexible components [88, 89].

3.4 Impact of Deformations on Wearable Antenna Performance

This section overviews the main issues that designer needs to consider when designing a wearable antenna and summarises reports on how particular deformations of antenna affect their performance. The section aims to summarise both experimental and computational attempts taken to quantify impact of deformations.

3.4.1 Wearable Antennas

Flexible substrates for wearable antenna applications have a lower dielectric constant that results in good radiation efficiency and increases the antenna's bandwidth [90]. The radiating conductive component of the flexible antenna is implemented on a dielectric substrate layer that defines the rate of the flexibility of the antenna [46]. To achieve high radiation performance of an antenna with a higher capacity of flexibility, electrical and mechanical properties are fundamental for designing [46]. In general, flexible wearable antennas are characterised by mechanical robustness, lower weight, and a front-to-back ratio [46]. However, bendability and deformability of the antenna not only determine its resonant frequency of antenna, bandwidth, and matching level, but also radiation pattern, energy, efficiency, and directivity [11, 39].

Since some flexible materials are porous mediums filled with air, the dielectric constant is closer to the vacuum. This reduction of the dielectric constant of the antenna substrate provides higher spatial wave and impedance bandwidth, which are essential factors of higher gain and efficiency resulting from the reduction of the surface wave losses [1]. Substrate thickness is another fundamental variable in determining flexibility as well as the efficiency and bandwidth of the patch antenna [91]. Since some flexible antennas are compressible mediums, the antenna's thickness may well change uni- or bi-axial anisotropy. Thus, the decision of selection of the dielectric constant is a fundamental bit for in-situ antenna efficiency and bandwidth [91, 92]. There is a compromise between the radiation efficiency and the thickness of the substrate [46]:raising the thickness of the dielectric medium allows for higher antenna bandwidth, whereas the radiation efficiency and practical flexibility of antenna decreases [21, 91]. The section is structured by the type of deformations, namely, cylindrical, crumpling, stretching and torsional deformations.

3.4.1.1 Cylindrical Deformation

A large volume of published studies describes the role of the cylindrical deformation or one-dimensional bending on the antenna performance. Antenna can be bent along its length (also referred as E-plane bending), or along its width (H-plane bending). The impact of cylindrical deformation on antennas is classified into group according to their substrate materials, namely, textiles, elastomers, and polymers. Textile group is further divided in terms of conductive materials, namely (a) E-textiles, (b) metal sheet, and (c) knitting. Similarly, antennas with elastomer and polymer substrates are separated in terms of their conductive parts, namely (a) silver inks, (b) graphene, (c) liquid metals, (d) strategically engineered structure and (e) e-textiles.

3.4.1.1.1 Textiles

The most extensively used flexible substrate is textile as a substrate for wearable antennas. Textile antennas and interconnects require precise control to overcome the limited quality and scalability of textile weaving and knitting pattern [89]. For a textile

material, increasing the thickness of the dielectric medium yields a lower dielectric constant and larger radiating patch , whereas the permittivity of a thin substrate closes its yarns, resulting in a smaller radiating element size [93]. Experimental measurements of bending of textile antenna in E- and H-plane reported that bending along the E-plane shifted the main resonance to lower frequency region, whereas for bending along the H-plane, the resonant frequency stayed stable [94]. In the same manner experimental study of [95] implemented four e-textile patch antennas fed by microstrip lines concluded that by increasing the bending in both the H- and E-plane shifted resonant frequency to lower frequencies and that E-plane bending had more significant impact of the resonant frequency.

(A) E-Textile

The soft e-textile conductive material is one of the most popular choices of wearable antenna deformation studies. In 2009, the paper [25] reported a coplanar patch antenna, which operates dual-band, backed by electromagnetic bandgap materials, to operate with a bandwidth of 4% at 2.45 GHz and 16% at 5.8 GHz wireless bands. Bending of antenna on E-plane resulted in reducing the antenna resonant frequency by 2% whilst bending the antenna along the H-plane increased antenna resonant frequency by 2%. However, the bandwidth of the antenna remained stable.

A method based on polynomial chaos theory with a well-known cavity model was suggested to statistically quantify the stochastic behaviour of the resonance frequency of bending microstrip textile antenna [96]. The method estimated the probability density function, the cumulative distribution function, the moment of the statistical distribution of the resonance frequency, and the confidence interval when the radii of the patch randomly change. A good agreement was achieved for numerical data and experimental data set radius from around 7 mm to 3 mm. when the radius of curvature of the textile patch is a random variable, the method generated statistical prediction about shifting behaviour with a range of some interval. In 2015, the textile antenna for a space suit application was reported [97]. The cylindrical bending of radius degraded the antenna's performance and shifted the resonant frequency to lower frequencies by

0.02 GHz for experiments, whilst simulated results resulted in antenna resonant frequency being shifted to higher frequencies.

An investigation of the bending behaviour of inset-fed textile microstrip antennas was reported [98]. Nine prototypes of wearable antennas bent along the H-plane and E-plane respectively. The H-plane bending is found to not affect the resonant frequency significantly from simulation and experiments. Full-wave simulation without the strain of the patch was increased resonant frequency by around 2%. The experimental measurement showed resonant frequency shifted to lower by around 4.5%. Adding strain elongation to the dimension of the antenna provided good agreement with experimental measurements for radii up to 40 mm.

In 2018, a flexible wireless power harvesting wristband operating at 2.45 GHz was presented [99]. Antenna implemented on flexible woven and polyester substrate, where a rectifier was fabricated on a rigid substrate. The simulated result had a 10 MHz discrepancy on the resonant frequency during the flat condition of the antenna element. Bending antenna on principle H-plane bending shifting frequency lower approximately 0.8%, whereas E-plane of antenna varied main resonance to higher frequencies around 2% compared for a cylindrical radius around 20 mm and 40 mm. Furthermore, the directivity of the flat antenna was decreasing trend (around 17%) to bend onto the wrist.

(B) Metal Sheet

Another option in wearable textile antennas relies on metal sheet incorporated with fabric substrates. The bending effect of the performance of wearable denim antenna was examined [100]. The antenna simulated with curvature angle from 0° to 200° with bending antenna along the width and length axis of rectangular microstrip antenna fed by a probe (See Figure 5.1f)). For the lowest curvature wrist case, the gain of the antenna element decreased around 2 - 4 dB. Furthermore, while bending along the H-plane, the main resonance of the patch moved the region downwards, whereas upward shifting had been observed by bending along E-plane of the patch.

The effect of cylindrical bending of the rectangular microstrip patch antenna fed by a coax probe was systematically investigated [101]. Different thicknesses of the antenna

were simulated as 1 mm, 2 mm, and 3 mm; Thinner antenna substrate impacted more substantially than in thicker cases during E-plane bending. The principal H-plane bending of the antenna element impact slightly on the resonance response of the antenna, whilst the E-plane bending significantly shift resonant, by ~15%. It was also observed that frequency shift during E-plane bending could divide into the downshift for bending angles below 45°, while the upshift for above 45°, where radius of the antenna times deformation angle equals to patch length antenna.

(C) Knitting

A third approach focuses on wearable textile antennas implemented with incorporating conductive threads onto fabric substrates. A knitted conical microstrip antenna and antenna array were reported in [26] (See Figure 3.2). Bending along E-plane of the antenna and array slightly shifted to higher frequencies; however, bending along H-plane of the antenna and antenna array stayed significantly stable in terms of the resonant frequency. Simulation geometries did not include complex knitting structure. For single antenna, simulation results of main resonant frequency had a good agreement with experiments: however, there is a slight discrepancy between simulation and experimental results for resonant frequencies of antenna array.

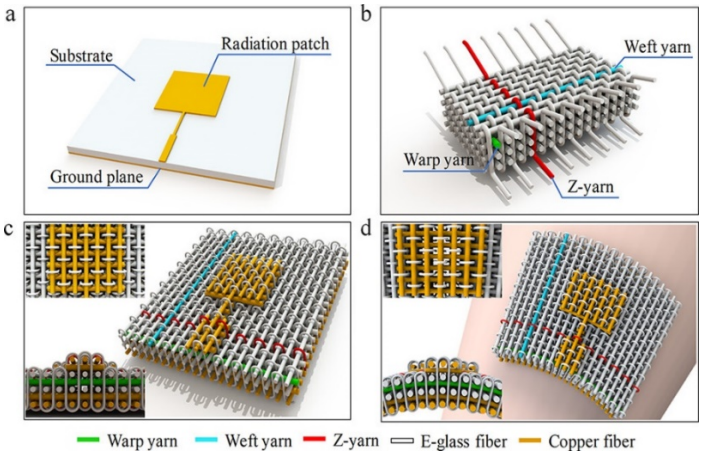


Figure 3.2 (a) Simulation geometry of the microstrip antenna (b) textile fabric assembly (c) flat knitted antenna (d) conical deformation of knitted antenna [26].

3.4.1.1.2 Elastomers and Polymers

With high deformability, the most extensively utilised elastomer is PDMS as a substrate of wearable antenna. In article [102], a conformal SU-8 / Polydimethylsiloxane (PDMS)-based inset fed antenna was proposed; the flexible substrate consists of a SU-8 layer and a PDMS layer, respectively. As a result, the semi-parabolic curve at the middle of the antenna varied along bending of antenna in E-plane from 0 mm to 66.9 mm resulted in slightly shift resonant frequencies to lower frequencies.

The medical wearable antenna was structured by a two-by-two array of I-shaped meta-surface and monopole antenna elements [103]. The main contribution of meta-surface improves radiation performances while decreasing the specific absorption rate of the antenna. When the radius of bending curvature reduces from 40 mm to 15 mm, the impedance bandwidth of the antenna became broader.

The work of [104] simulated compressive and bending loads for microstrip patch antenna using a multi-physics numerical simulations. Loads or pressure were applied at the middle of the patch, on one side of the patch, and at the top and bottom side of the patch antenna, respectively, to characterise performance under the deformation. Increasing load at the middle of the patch resulted in increasing the resonant frequency, whereas increasing load on one side of the patch resulted in reducing the resonant frequency. Increasing loads on the top and bottom side of the patch antenna had a more significant impact and reduced the main resonant frequency by around 0.5 GHz.

(A) Silver Inks

With widely availability and easy fabrication properties of silver inks makes them good candidates for wearable antennas. A flexible and stretchable antenna consisting of silver conductive paste and TPU were investigated [69]. The antenna was tested with three different cylindrical bending radii, 1.5 cm, 3.5 cm, and 5.0 cm, respectively. When bending curvature along the H-plane, resonant frequency has shifted through the lower frequency region in both in simulation and experiments. Besides, the radiation efficiency was decreased by 17.5%.

In article [39] proposed inkjet-printed multiband antenna reported with concave and convex bending cylindrically with the maximum deformation radius of 59 mm (see Figure 6.13). During concave bending, multiband frequency resonant shifts around 3% lower frequency region, whereas there was no considerable frequency shift in convex bending. The gain and directivity of a high-frequency region of the spectrum were increased during convex bending (See Figure 6.14). In study [41], silver nanoparticles were printed on PI substrate. During E-plane bending, the highest frequency shift was observed.

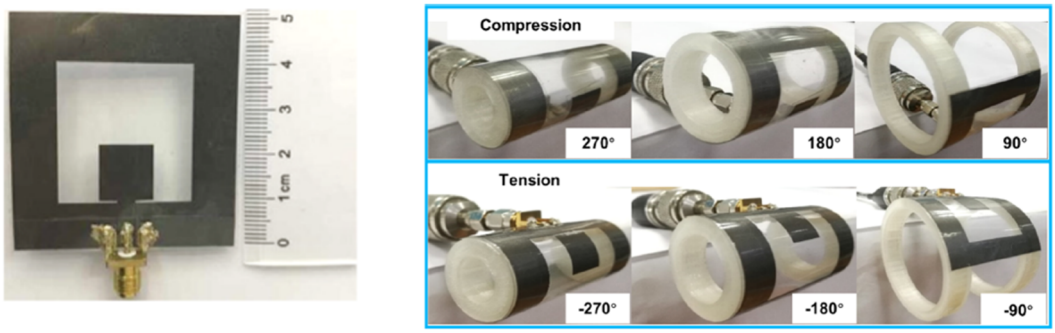
Flexible loop temperature sensor antenna with polyvinyl chloride (PVC) substrate was introduced in [105]. The changing resistance with temperature of PEDOT:PSS behaves as a sensor from 25° C to 90° C. Reducing cylindrical bending radius of antenna shifted resonant frequency upwards for E-plane bending, whereas H-plane bending of loop antenna stayed stable.

(B) Graphene

Widely active research efforts have been focused on implementing graphene based antenna owing to its significant durability. In article [72], the graphene based coplanar waveguide antenna implemented for wireless communication bands was analysed. The antenna was designed to operate in the frequency band 1.73 - 3.77 GHz with a reflection coefficient below -8 dB. The graphene-based antenna was bent experimentally on a cylinder from a radius of 5 cm to 2.5 cm. Bending of antenna decreased antenna gain at 3 GHz but it has improved reflection coefficient for operating frequency range.

With the outstanding mechanical durability of graphene film, article [106] revealed printed antennas for wearable sensor applications. The quarter wavelength match patch antenna was operating at 1.63 GHz. It is approximately two times more sensitive to tensile and compressive bending conditions than conventional copper antenna sensors. The compressive and tensile bending along the antenna length had a decrease in the resonant frequency of around 5%.

A circularly polarised with low SAR based on graphene film was presented [107]. Bending along the H-plane of the antenna shifted resonant frequency downwards trend, whereas bending along the E-plane of the antenna leaded to a shift frequency upward.



(a) (b)

Figure 3.3 The picture of antenna (a) Front view (b) compression and tensile bending with the angle of 270°, 180°, and 90° [20].

Another example is in the article [20], a graphene film-based coplanar waveguide antenna for strain sensor at 3.5 GHz (sub 6 GHz for 5G range) (See Figure 3.3). During the E-plane bending, the antenna resonant shifted to higher frequencies with a maximum of approximately 12% higher frequency symmetrically for each concave and convex bending radius (see Figure 6.13-6.14).

In the same vein, coplanar waveguide antenna based upon a conductive composite of poly(3,4-ethylene dioxythiophene) (PEDOT) and N-doped reduced graphene oxide was reported [108]. The antenna performance was considerably reduced its bandwidth by the length deformation with decreasing in the radius of cylindrical bending along the length axis, resulting in reducing main bandwidth. However, bending along the width axis had not significantly affected the main bandwidth of the antenna.

(C) Liquid Metal

The capability of undergoing large deformation with stable and good electrical properties of liquid metals attract significant attention for wearable antennas. A bendable liquid metal alloy patch antenna operating at 3.45 GHz [77] was suggested

(See Figure 3.4). The antenna bent along the H-plane with 25.4 mm and 12.7 mm radius curvature, respectively. Decreasing curvature of antenna improved matching around primary resonance by approximately 10 dB, shifting resonant frequency slightly upward.

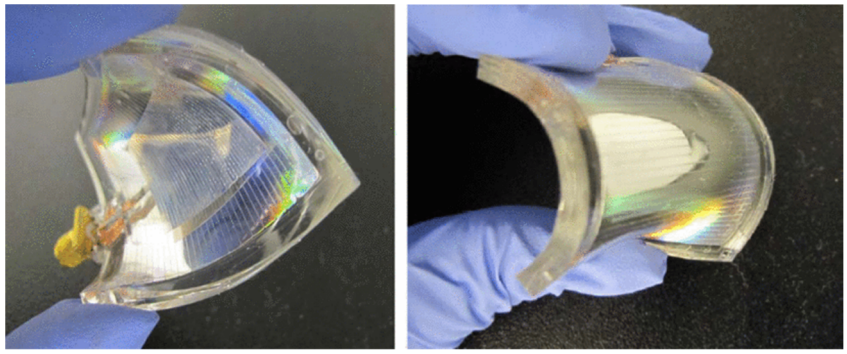


Figure 3.4 Multi-layer of microstrip patch antenna composed of liquid metal encased in polymer [77].

A liquid metal alloy with walled carbon-nanotube antenna was reported for S-band operation [63]. By reducing of bending radius of the antenna, the return loss of performance of the antenna is reduced by ~3 times for experiment and simulations. Besides, the resonant return loss at resonant frequency of simulation was approximately 10 dB higher than the experimental results.

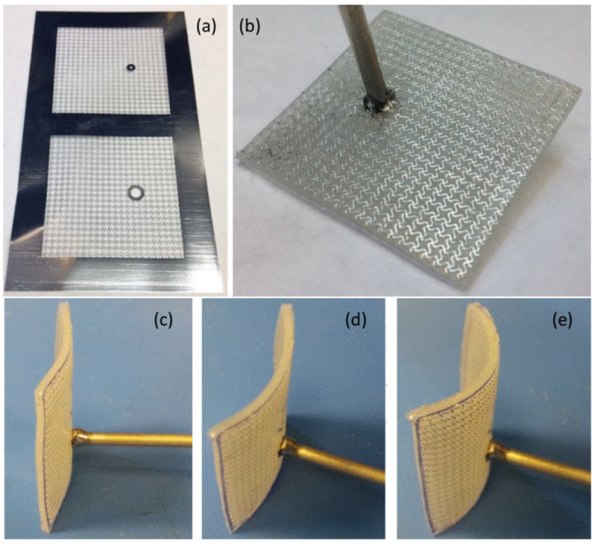


Figure 3.5 Implemented flexible sinusoidal patterned antenna (a) fabricated metal sheet (b) ground plane of antenna with probe feeding of coaxial cable (c)-(e) bending patterned antenna with curvature radii of 1.25, 1, and 0.41 inches, respectively [109].

(D) Strategically Engineered

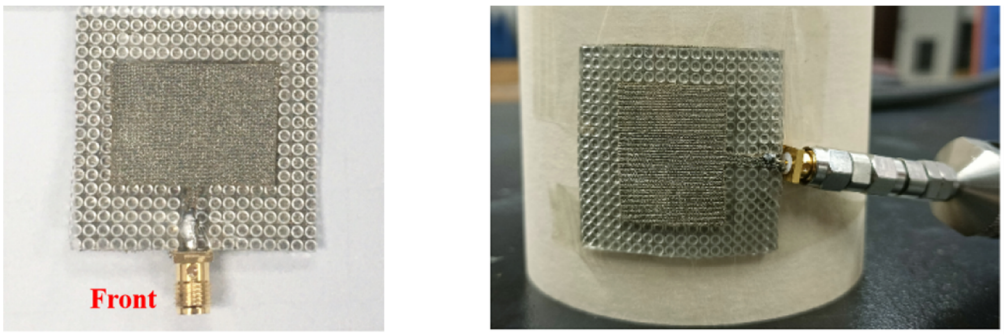
The controlled design of complex microstructures exhibits advance flexibility. Generating shapes strategy for stretchable antenna involved as serpentine, meander, or wavy structures [55-62]. Article [109] fabricated an antenna that had patterned metal sheets on the silicon substrates (See Figure 3.5). The H-plane bending of antenna leaded to the main resonant stable, while bending along the E-plane of the square shape antenna moved resonant frequency to the lower frequency.

(E) E-Textile

Textile conductive parts are important alternative for designing antenna for wearable antennas with its high elasticity. A wearable circular patch dual-band antenna that operates the main modes of at 2.4 GHz and 5.8 GHz of the circular patch antenna was suggested [110]. E-plane bending had more impact in reducing the resonant frequency than H-plane bending.

An antenna has embedded conductive fabric inside an elastomer and has three diodes that add a patch edge cut line to control the shifting of different resonances [111]. The deformation study of the antenna was conducted experimentally; E-plane bending of the antenna had a substantial effect on the antenna performance and increased the main resonant frequency, whereas H-plane bending had minimal impact on the antenna performance.

A flexible force-sensitive frequency reconfigurable antenna was proposed [112] (See Figure 3.6). The antenna substrate had a hemispheric array with different radii and periods on a thick cuboid. Increasing bending along E-plane of the antenna lead to reduction of the main resonant frequency. Besides, when force applied on antenna, the antenna resonant frequency reduced depending on the rate of the force.



(a) (b)

Figure 3.6 The optical images of the antenna (a) front view (b) cylindrical deformation [112].

3.4.2 Crumpling Deformation

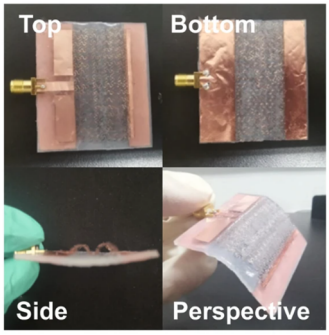
Another topic of interest in the area of deformation of flexible antenna is crumpling bending. Further, the impact of crumpling on the electromagnetic performance of a 2×2 microstrip patch antenna array was investigated [79]. The crumpling condition was studied with 5 mm, 12 mm, and 20 mm crumpling depth with 10mm, 10mm, and 24 mm periodicity along the width and length side of the antenna array respectively. When crumpling along the E-plane, the measurement results shifted from 2.4 GHz to 2.45 GHz with a close agreement with simulation, however, the highest crumpling depth reduced to resonant frequency to 2.30 GHz and raised impedance bandwidth by around 40%. In contrast, the width axis crumpling of antenna array relatively stable compares the first conditions and it has around 24 MHz impedance bandwidth change at severe condition. It was observed that mutual coupling between antenna array elements significantly increased with the crumpling along the length axis while crumpling along the array's width axis decreased the antenna array's mutual coupling. The radiation pattern of the antenna array broadens in lots of cases, and the antenna directivity and gain decreased by around 6 dB under some crumpling conditions.

Elliptical planar antenna with dual-band operating region was reported in [40]. The antenna was crumpled along the E-plane. During crumpling, the primary mode of the antenna shifted through the lower frequency region, whilst the second mode was turned

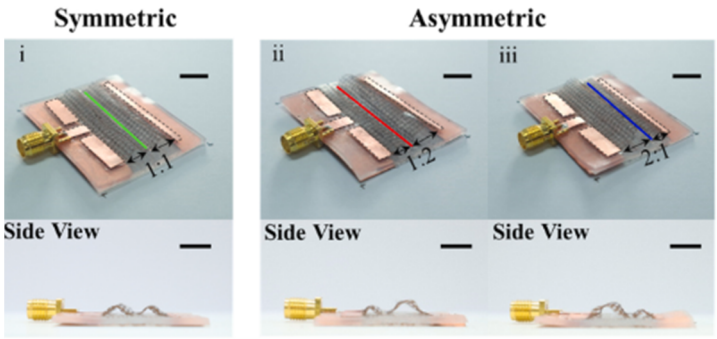
higher frequency region-discrepancy between simulation and measurement at higher below reflection coefficient (-15 dB).

3.4.3 Stretching Deformation

An exemplary results within stretching flexible antenna, the works of [113, 114] demonstrated that a stretchable unbalanced loop antenna is implemented by liquid metal-filled electrometric microstructure. The prototyped antenna is operating at 2.4 GHz, and it is stretched along the width and length axis of the antenna experimentally; the radiation efficiency of the antenna is reduced by 17%, and the main resonant frequency reduced by around 25%. Similarly, an ultra-wideband planar inverted cone antenna with return loss was below the 10 dB at 3-10 GHz [114].



(a)



(b)

Figure 3.7 (a) The picture of the top, bottom, side and perspective of double arch patterned antenna [59] (b) Optical images of the symmetric and asymmetric double-arched microstrip antenna [115].

A study was conducted about stretchable antennas, including silver nanowires [70]. Silver nanowires used for conductive sheet combining antenna on a PDMS substrate that was providing reversely deformable structure. The antenna stretched experimentally with varying strain levels from 0% to 15%. With raising strain, the primary resonance frequency increased reasonably linearly with a stable impedance bandwidth region.

A stretchable conductor produced by composing $Ti_3C_2T_x$ and single-walled carbon nanotubes (SWNTs) for omnidirectional dipole antenna was reported [76]. The antenna was resistant to 500 bending cycles of uniaxial strain stably. However, uniaxial stretching from flat case to 1.5 times longer dipoles shifted primary resonance from 1.575 GHz to 1.375 GHz, and the relative change of the reflection coefficient was just over 20% in terms of before and after stretching values.

A sinusoidal patterned patch antenna based upon e-textile conductive part was reported [78] (see Figure 2.5). Two antennas were designed to verify the performance of the serpentine structure; one has a conductive part made of textile, and the other is constructed from gold. The resonant frequency of the textile-based antenna shifted from 3.45 GHz to 2.75 GHz after applying 100% unidirectional strain. On the other hand, a gold serpentine antenna with a solid ground plane maintained resonant frequency at 2.58 GHz up to 15% strain, which is critical for wireless communication applications. However, the serpentine antenna structure led to additional lobe broadside of radiation patterns and significantly degradation of beamwidth of the antenna.

Recently, a strategically engineering microstrip antenna was reported [59] to overcome shifting resonant behaviour of antenna for a wearable antenna with the aid of buckling and serpentine structure (See Figure 3.7a)). To do this, the patch layer of horseshoe patterned mesh antenna buckled out of plane. To validate the method, researchers implemented patch antennas operating GPS frequency range and 2.45 GHz ISM band, and three different pre-stretch cases, 5%, 10%, and 15%, respectively. For 15% pre-stretch provided minimum resonant fluctuation ~0.1 GHz from strain 0% to 25% for its operating range and allowed lower buckling arc height compared to 5% case. Similarly, an asymmetric double-arched microstrip antenna was reported [115] (See Figure 3.7b)).

According to their results, the asymmetric 1:2 provided similar performance with the double-arched symmetric version in [59]; the asymmetric 2:1 resonant significantly fluctuated around the main resonance compared to case of [59]. Similarly, there was a compromise between the stability of resonant behaviour and radiation pattern performance. The using meshing structure caused significant degradation the main beamwidth of radiation pattern on E-plane and H-plane of the antenna.

3.4.4 Torsional Deformation

Another critical and complex deformation example is torsional bending. The work of [68] reported ultra-high frequency (UHF) dipole antenna, the antenna has the main resonance at 920 MHz, and raising enforced strain to 15%, the resonance and the radiation efficiency gradually decreased. Due to the increased effective length of polymer composite conductive, the resonance frequency shifted through the lower frequency range. Moreover, the dipole antenna was stretched, twisted, and bent experimentally. The experimentally conducted stretching along arm from 0% to 15% led to reduction of the resonant frequency, whereas curving the antenna along arm length from cylindrical diameter of from 15 mm to 8 mm resulted in increase of the resonant frequency. On the contrary, twisting along arm of dipole from 0° to 60° did not change resonant frequency significantly compared the flat case.

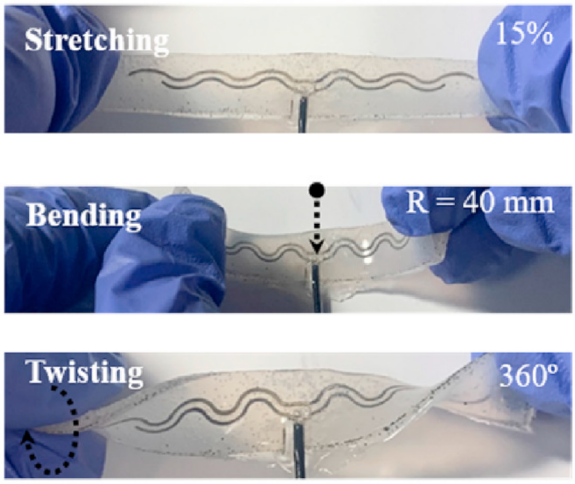


Figure 3.8 Stretching 15%, bending radius of 40 mm, and twisting 360° of parasitic dipole antenna [116].

A stretchable wideband dipole antenna with dual resonance was reported [116]. With additional parasitic arms, antenna bandwidth increased from approximately 0.23 GHz to around 0.5 GHz with the help of second resonance. The paper shows that when antenna was twisted by the angle of 360° or bent by a radius of 40 mm, the antenna retained its bandwidth stably.

3.4.5 Reported Flexible Antennas

Table 3.5 summarises the main characteristics of reported flexible antennas realised using different conductive materials and substrates. The table compares the thickness of trace, H_t, and substrate, H_s, conductivity, and operation frequency of different antennas.

Table 3.5 Reported flexible antenna with their materials of conductive and substrates and their rate of deformation

Conductive Material	**Type**	H_t **(mm)**	F_{res} **(GHz)**	**Substrate**	ε_r	H_s **(mm)**	**Conductivity**	**Bending**
Woven Fabric [94]	Probe Fed MS	0.125	2.5	Felt	1.43	1	0.05 Ω/sq	$\theta = 90^o$ $\theta = 180^o$
Knitting [95]	Inset Fed MS	-	2.4	Felt	1.45	3.5	1 Ω/sq	R=37.5 mm
Woven [95]	Inset Fed MS	-	2.4	Spacer	1.14	6.0	0.02 Ω/sq	R=37.5 mm
Zelt Fabric [25]	CPW and EBG Ground	0.060	2.45, 5.2-5.8	Felt EBG	1.38	1.1 2.2	≤ 0.01 Ω/sq	R=80 mm R=140 mm
E-Textile and SWNT [73]	Probe Fed MS	-	2.40	PDMS and ceramics	4.0	7.62 mm	2 Ω/sq	R=80 mm
Textile Antenna [117]	Probe Fed MS	-	2.45	Polyester	1.44	2.85	-	R=50 mm -90 mm
Cu and Ti [102]	Inset Fed MS	5 μm / 200 nm	6.00	SU8 / PDMS	2.9 / 2.65	50 μm / 500 μm	-	R=19.41 mm R=53 mm R=66.91 mm
Liquid Alloy E-GaIn [77]	Inset Fed MS	100	3.45	PDMS	2.9	4	3.46	R=12.7 mm R=25.4 mm
nickel–copper polyester ripstop [97]	Probe / Inset Fed MS	0.08	2.45	Pellon Peltex 72F	1.19	1.51	0.03 Ω/sq	R=43.2 mm R=101.6 mm
Conductive	Probe Fed	0.5	2.4	Denim	1.6	2	0.07 Ω/sq	$0^o - 203^o$

Textile [100]	MS							$0^o - 193^o$
Inkjet-Printed [39]	MultiBand CPW	30 μm	0.88–1.5, 1.93–2.2, 2.31–2.96 3.11–3.58	PI	3.5	0.11 mm	6×10^6 S/m	R=59 mm R=78 mm Concave, Convex
AgNP [41]	CPW (UWB)	8 μm	3.1–10.6	PI	3.4	50 μm	-	R=9 mm R=7 mm
Patterned Metal Sheets [109]	Probe Fed	-	1.575-1.595	Silicon	3.25	1.6 mm	-	Cylindrically, R=0.41,1, 1.25 inches
EGaIn / SWNT [63]	Inset Fed MS	100	4.0	PDMS	2.5	1	3.46 / 85	R=5 mm-30 mm
Woven Copper Plated Polyester Fiber [99]	Multilayer Aperture Coupled MS	0.08	2.45	Felt/ Woven Polyester / Felt	1.2 / 1.5 / 1.2	1.65 / 0.33 / 1.65	0.18 Ω/sq	R=21 and 40 mm
Copper Sheet [101]	Probe Fed MS	-	2.49	Cotton	2.1	1,2,3	-	R=35-250 mm
GO Film [106]	Patch MS	-	1.6	Paper	3.06	0.04	$\sim 10^6$ S/m	$\theta = 0^o, 60^o$ 9 0^o, and 120^o
Graphene Film [107]	Circularly Polarised / AMC	24	5.75–5.83	PDMS / PDMS	2.7	1/ 0.5	1.13×10^6 S/m	R=100 mm, 30 mm
Graphene Film [20]	CPW	28	3.13−4.42	PET	3.5	0.06	$\sim 10^6$ S/m	$\theta = 0^o - 360^o$ Inner and Outer
Warp and Weft copper strands [26]	Quarter Matched Fed MS	0.3 mm / 0.5 mm	1.575	Knitted	3.2	2.7	0.36 Ω/m 0.20 Ω/cm	Conical
N-doped reduced graphene oxide-PEDOT [108]	Elliptical CPW	55	3 to 8	Adhesive Tape.	-	-	0.56 Ω/sq	R=10,30, 50 mm
Zelt [79]	2 × 2 Inset MS Array	-	2.4	Felt	1.38	1.1	≤ 0.01 Ω/sq	5mm depth of Crumpling 1D

Ni/Cu plated Textile [118]	Probe Fed MS	0.08 mm	2.45	Polyester 10 layers	1.55	0.32 mm	0.01 Ω/sq	R=70mm, 85mm, 105mm
PANI + MWCNT [40]	CPW (UWB)	75 μm	1.65–2.62, 4.2–7.58	PI	3.48	0.130 mm	4500 S/m	Crumpled r=5.5 mm
Liquid Alloy [113]	Unbalanced Loop	100	2.4	PDMS	3.0	1	3.46×10^6 S /m	20-40 % stretch W and L
Silver Nanowire [70]	Inset Fed MS	0.5 mm	2.92	PDMS	2.67	1 mm	8.13×10^5 S /m	0 %-15 % Strain
2D Titanium Carbide and GO [76]	Dipole antenna	2.0	1.575 to 1.375	S-MXene Latex	2.1	-	2900 S/cm	Stretch from 0 % -150 %
Serpentine E-textile [78]	Inset Fed MS	0.55 mm	3.4	Ecoflex	2.8	2 mm	-	Stretch from 0% - 40%
Serpentine Gold [78]	Inset Fed MS	0.25 μm	2.75	PI	-	1 mm	-	Stretch from 0 % - 15 %
Hierarchically Structured Copper [59]	Inset Fed MS	20 μm	2.45	Ecoflex	3.125	1 mm	-	Stretch from 5 %, 10 %, 15 %
Hierarchically Structured Copper [115]	Inset Fed MS	20 μm	2.45	Ecoflex	3.125	1 mm	-	Stretch from 0 % to 20 %
Ag/LIG [116]	Parasitic Dipole	-	2.0-2.5	Ecoflex PI	-	-	-	0 % - 15 %, 40 mm bending, 360° twisting
Copper and Zoflex [32]	Aperture-Coupling Fed	0.035 mm / 100 μm	2.70	PDMS	2.8	2 mm	$5 \times 10^4\ S/m$	9 % - 12 % strain
Textile [119]	Electronically Tunable MS	0.13 mm	2.3-2.65	PDMS	2.82	5.46 mm	$0.01\ \Omega\ /\ sq$	R=28,42,110 and 135 mm
Silver [69, 120]	Inset Fed MS	26.52 μm	2.5	PU	2.5	1.2 mm	$1 \times 10^4\ S/m$	R=1.5, 3.5, and 5.0 cm
Low Profile Antenna [121]	Inset Fed MS	-	5.8	PI	3.6	0.254 mm	-	$0^o - 35^o$
Ag Loop Antenna [105]	Loop Antenna	-	1.2 and 5.8.	PVC	-	-	0.001 Ω / cm	R=5.7 cm, 11 cm
Inject Printing E-GaIn [122]	2x4 Array	-	2.45	PI	3.5	0.8 mm	3.46×10^6 S/m	R=5 ,25, 50 mm

GO/LIG [27]	Inset Fed MS	-	5.8	PI	3.5	0.127	7.18×10^2 S/m	R=10, 7.5 and 5.0 mm
Liquid Alloy [114]	Inverted Cone UWB	100	3-10	PDMS	3.0	1	3.46	20 % - 40 % stretch W and L

3.4.6 Impact of Deformations on Wearable Interconnect Performance

This section overviews critical deformation, namely, bending, stretching, and torsional deformation for flexible interconnects, namely microstrip and coplanar waveguide transmission line with novel flexible substrate and conductive materials. The section of deformation of flexible interconnect constructed bending and cylindrical deformation, torsional and stretching deformation. For interconnects design, a lower dielectric constant leads to wider track width and high reflection losses for interconnects due to fringing fields. Increasing the height of substrates results in higher reflection losses and losing its flexibility significantly. In this section, all the microstrip lines and coplanar waveguides have designed impedance of 50 Ω.

3.4.6.1 Cylindrical Deformation

Bending deformation similar to wearable antennas is one of the main concern in ensuring performance of the interconnects. In 2013, a multilayer stretchable microstrip line, Zoflex, with 100 µm thickness, on PDMS substrate was published [32]. In their experiments, several microstrip lines were analysed, i.e., microstrip line with one layer of conductive rubber (Zoflex, that has conductivity just under 10^4 S/m, double layer line consisting of copper and Zoflex (conductivity well over 10^4 S/m); and trip-layer line which Zoflex sandwiched between two copper layers (which conductivity has well over 10^5 S/m). Besides, the flat triple-layer microstrip line has measured insertion loss of 1.54 dB, approximately half of the single layer microstrip line. Bending of curvature just over 43 mm and 15 mm have increased insertion loss by 0.17 dB and 0.7 dB, respectively.

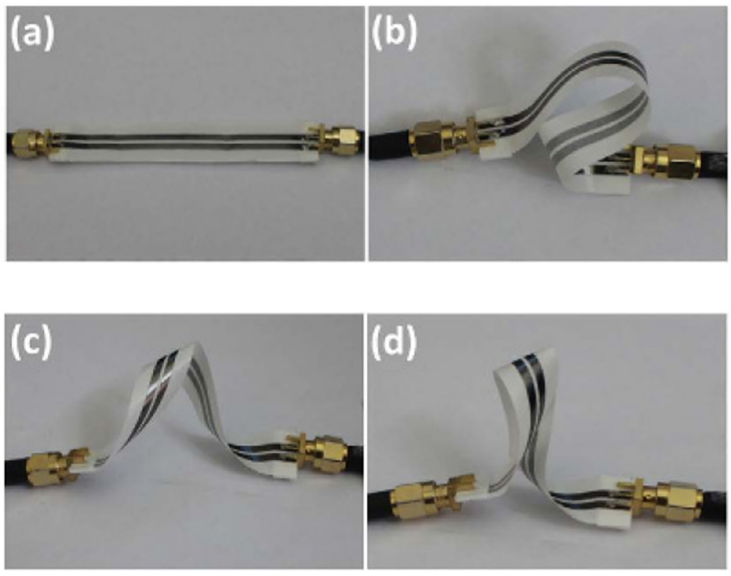


Figure 3.9 (a) Un-bended, (b) bended and (c-d) transmission lines [72].

Huang *et al*. [72] fabricated a coplanar transmission line with graphene (See Figure 3.9). When the coplanar transmission line was bent and twisted, there was a slight difference between the flat case at lower frequency region (1 GHz - 2 GHz) in terms of the transmission losses. Similarly, article [123] reported on a coplanar transmission line realised on paper, the transmission loss of TL with length from 20 mm to 50 mm measured under applied bending along the length deformation and the experimentally measured results of bending had a reasonable correlation for operating region at higher frequency.

A microstrip transmission line was implemented by screen printing silver paste on a flexible polyethylene terephthalate (PET) substrate with different thicknesses (0.5 mm, 0.7 mm and 1.4 mm) [124]. The insertion and reflection loss of the flat transmission line was experimentally measured and compared to the one that is bent at an angle of approximately 30^{o}. It was shown that bending decreased the operating region by 12.5% with the induced transmission losses in the operating range.

Moreover, the paper [125] presented the fabricated coplanar waveguide with graphene flake on a polyimide substrate. It was also important to note that compressed graphene flakes provide good durability, for example, fabricated graphene strip's resistance

changed only 1% after 32500 cyclic bending with a radius of approximately 43 mm, whereas the resistance of the silver paste case varied just over 20%.

Researchers fabricated a coplanar waveguide (CPW) [75]. According to the active region of CPW, the MXene offered the lowest attenuations compared to lines fabricated with Ag, Au, Al, Cu, graphene, and carbon nanotube. It was also reported that CPW could withstand the bending deformation; however, repeated bending cycles increased losses around 15% [87, 126].

The complex shaping (which is a technique for improving stretchability) of the transmission lines improves the flexibility and optical transparency of bulk metal materials [127]. The work of [127] reported an investigation of the stretchable and transparent microstrip lines, that solid metallic lines replaced by mesh metals, such as a horseshoe, sinusoidal, and oval type. The fabricated microstrip line was measured with different meshes under flat, cylindrical inner bending, and 1.3 times stretch. The flat oval pattern amongst the others provided the closest S_{21} value to the flat microstrip line for simulation and experiments. Sinusoidal had more lossy than the other others during the inside bending test in experiment, however, for the stretching test, horseshoe pattern had comparably higher loss than other patterned structure experimentally.

Modelling of aerosol jet printed (AJP) and screen printed (SP) transmission lines and power inductors was reported by using the finite element modelling method [128]. They had used two different software; one used for simulating finite element analysis (FEA) and the other for full-wave simulation, FEM. Tensile and compressive bending of radius from 30 mm and 100 mm provided significant agreement and no changes in terms of S_{21} and S_{11} values for experimental results. However, simulation results have slight discrepancy for different bending radius.

3.4.6.2 Torsional Deformation

There is a limited available data about performance of an interconnect under torsional deformation. A microstrip line with inkjet-printed silver on a polyimide (PI) substrate was fabricated and compared it to one printed on a conventional FR-4 substrate [129].

According to their experimental results, although correlated insertion loss in their simulations, PI substrate had three times higher losses than standard FR-4. During the cylindrical bending of the transmission line, transmission loss of the microstrip line was stable, even if the applied bending radius was varied from 50 mm to 92 mm. Torsion was applied along the length of the transmission line with a twisting angle from 0° to 40° (See Figure 3.10) and the measured results had shown robust performance.

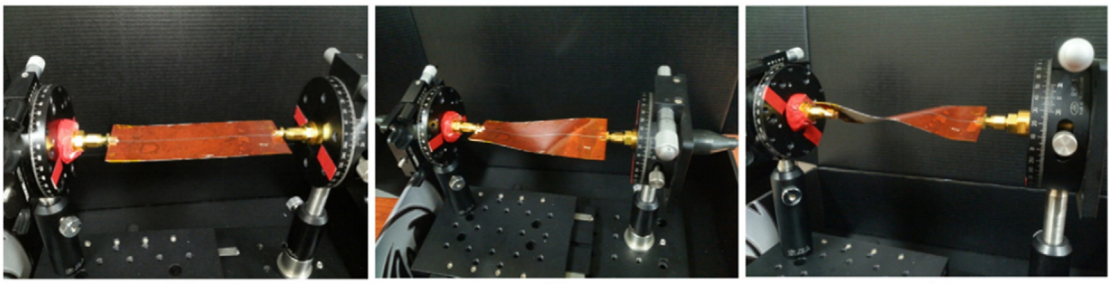


Figure 3.10 Measurement setup for torsion test at (a) 0°, (b) 20°, and (c) 40° [129].

3.4.6.3 Stretching Deformation

Another significant deformation for interconnect is stretching. An interconnect, which was screen printed with a stretchable silver-polymer composite on an ultrathin (50 μm) thermoplastic PU, was characterised [33]. For thickness (6.4 μm) of averaged trace offered conductivity of 4.3×10^5 S/m, which is just over one order less than the conductivity of bulk silver. Cyclic resistance test applied to the interconnects. Besides, the resistance was increased 30%, 40%, and 70% for the strain rate of 10%, 15%, and 20%, respectively.

The paper [68] implemented a coplanar transmission line on the 400 μm thick PDMS sheet , and two parallel signal trace were placed with a gap between 1mm. The signal traces were implemented with different volume fractions, which indicated rates of Ag particle to PDMS liquid form in terms of their rate in total volume for composite, ranging from 18 v% to 24 v%. The measured conductivity of silver-PDMS was around 1000 S/cm. The volume fraction bigger than 20 v% significantly correlates to the transmission loss up to 3 GHz, and electromagnetic simulation with adjusted

conductivity was a good agreement with the experimental setup. The fabricated transmission line performance remained largely unaffected by the strain for up to 20%.

The impact of microcracks on the transmission properties of a silver microstrip line on a polydimethylsiloxane (PDMS) substrate was investigated [130]. The microcracks were caused by increasing the strain rate from 0% to 12% and had resulted in blocking the current flow and over four times higher transmission losses.

Table 3.6 Physical Properties of Transmission Line Made of Different Materials

Group	Materials	TL	Thickness Trace (μm)	Thickness Substrate (mm)	Conductivity ($S\ m^{-1}$)	Frequency (GHz)	Refs.
Metal Nanoparticles	**Ag paste / PET**	ML (exp.)	20	$0.5 - 1.4$	3×10^5	0.05-8.0	[124]
	Ag ink / PI	ML (exp.)	3	0.2	1×10^5	0.5-3.0	[129]
	Ag-MP/ PDMS	ML (exp. and sim.)	140	1	3.33×10^5	1.0-18.0	[130]
	Nano silver Ink	ML (exp. and sim.)	0.650	0.127	1×10^7	0.0-8.0	[128]
	Dupont 5025	ML (exp. and sim.)	10	0.127	3.57×10^6	0.0-8.0	[128]
Conductive Polymers	**Ag and PDMS**	CPW (exp. and sim.)	120	0.4	1×10^5	0.5-3.0	[68]
	Zoflex	ML (exp.)	100	1	0.83×10^4	1.0-5.0	[32]
Graphene Based Materials and 2D materials	**Graphene / Paper**	CPW (exp.)	7.7	0.1	4.3×10^4	2.0-8.0	[72, 123]
	Graphene Flake / PI	CPW (exp. and sim.)	10	0.076	$\sim 2.4 \times 10^4$	0.0-20	[125]
	MXene TL / PET	CPW (exp. and sim.)	0.062-8	0.001	8×10^5	1.0-8.0	[75]
Intrinsically stretchable metals	**Patterned Titanium and Gold**	MTL (exp. and sim.)	0.05 0.300	1.0	-	0.0-20.0	[127]

Note: polyethylene terephthalate (PET), polyimide (PI), polydimethylsiloxane, silver (Ag) microparticles (MP), polydimethylsiloxane (PDMS), metallic mesh (MM), nanowires (NW), microstrip line (ML), and coplanar waveguide (CPW), exp: denotes experiments, and sim: denotes simulations.

3.4.7 Reported Flexible Interconnects

Table 3.6 summarises the main characteristics of reported flexible interconnects realised using different conductive materials and substrates. The table compares the thickness of trace and substrate, conductivity, and operation frequency of different interconnects.

3.5 Conclusions

In summary, wearable antennas and interconnects are the essential parts for the implementation of fully wearable devices and applications. With their flexibility, they are ubiquitous for wireless and sensing applications. This Chapter reported on the variety of novel flexible substrates and conductor materials used for flexible electronics. The main consideration for flexible antenna design are also summarised. Highly flexible materials for substrates, elastomers such as PDMS and PU and textiles provide higher deformability with higher materials losses. On the other hand, Polymers, such as PI and PET, have low deformability with lower dielectric losses.

The Chapter highlights the need to experimentally or computationally assess the performance of antenna under deformation in order to predict the stability of antenna. The most widely used deformation is the cylindrical deformation for which a wealth or result sand reports exits. However, the reported results are often conflicting.

For example, in the case of E-plane bending, the works of [99, 100, 105, 107, 111] report an increase in the resonant frequency along increasing bending rate along with the antenna, whereas other papers [25, 41, 94, 95, 102, 109, 110, 112, 117, 118, 121] reveals frequency shift through downward with that bending rate. Besides, the reported work [106] demonstrates that the concave and convex bending along the E-plane decreases the resonant frequency; however, paper [20] reports that bending leads to an increase in the resonant frequency. However, a similar kind of antenna in the article [123] stays significantly stable under a similar type of convex deformation along the E-plane. On the other hand, the study [27] reports that concave bending of antenna increases the resonant frequency, while convex bending reduces the resonant frequency

of antenna. The paper [101] reveals that frequency shift during E-plane bending is divided into the downshift for bending below 45° and upshift for bending above 45°.

Similarly, the works of [25, 68, 77] report bending along H-plane of the antenna increases the resonant frequency , whilst [69, 95, 97, 100, 110, 118] reported the reduction in the resonant frequency or stable performance in [72, 94, 98, 99, 103, 105, 108, 109, 111, 123]. For the case of concave bending in the H-plane [39], , resonant frequency decreases, whereas there is no considerable frequency shift for the convex H-plane bending.

For stretching cases, according to [70] the resonant frequency increases with stretching along the width of antenna, but in [78] increasing stretch along the width leads to a reduction of the resonant frequency. In the case of stretching of a dipole antenna, [68, 76], extended arms of dipole lead to a reduction of the resonant frequency.

In the case of torsional deformation, the work of [68] demonstrated that the main operating band of the antenna is not significantly affected. However, [116] states that torsional deformation of the antenna leads to a shift of the main operating band to higher frequencies.

When it comes to interconnects, reports have shown that bending can significantly degrade the performance of interconnects depending on microcracks and the severity of bending conditions. New materials such as graphene related materials and silver inks provide good flexibility on polymer substrates for wearable devices. There is a limited data about their complex deformation performance in terms of EM performance [124, 129].

All these conflicting results conclude that a systematic analysis is complicated. The main results are obtained using experimental measurements and the computational analysis is only possible for the case of simple cylindrical bending. Thus, there is a requirement for a computer-aided and graphical tool to systematically predict the impact of deformation on devices performance. The next Chapter will introduce one of the computer graphics techniques that can be used for introducing arbitrary deformations on the devices under the test.

References

[1] R. Salvado, C. Loss, R. Gonçalves, and P. Pinho, "Textile Materials for the Design of Wearable Antennas: A Survey," (in English), *Sensors,* vol. 12, no. 11, pp. 15841-15857, 2012.

[2] P. J. Soh, G. A. E. Vandenbosch, M. Mercuri, and D. M. M. Schreurs, "Wearable Wireless Health Monitoring: Current Developments, Challenges, and Future Trends," *IEEE Microwave Magazine,* vol. 16, no. 4, pp. 55-70, 2015, doi: 10.1109/MMM.2015.2394021.

[3] P. Nepa and H. Rogier, "Wearable Antennas for Off-Body Radio Links at VHF and UHF Bands: Challenges, the State of the Art, and Future Trends Below 1 GHz," *IEEE Antennas and Propagation Magazine,* vol. 57, no. 5, pp. 30-52, 2015, doi: 10.1109/MAP.2015.2472374.

[4] M. Sanchez-Fernandez, A. Tulino, E. Rajo-Iglesias, J. Llorca, and A. G. Armada, "Blended Antenna Wearables for an Unconstrained Mobile Experience," *IEEE Communications Magazine,* vol. 55, no. 4, pp. 160-168, 2017, doi: 10.1109/MCOM.2017.1500722.

[5] N. F. M. Aun, P. J. Soh, A. A. Al-Hadi, M. F. Jamlos, G. A. E. Vandenbosch, and D. Schreurs, "Revolutionizing Wearables for 5G: 5G Technologies: Recent Developments and Future Perspectives for Wearable Devices and Antennas," *IEEE Microwave Magazine,* vol. 18, no. 3, pp. 108-124, 2017, doi: 10.1109/MMM.2017.2664019.

[6] S. Lemey, S. Agneessens, and H. Rogier, "Wearable Smart Objects: Microwaves Propelling Smart Textiles: A Review of Holistic Designs for Wireless Textile Nodes," *IEEE Microwave Magazine,* vol. 19, no. 6, pp. 83-100, 2018, doi: 10.1109/MMM.2018.2844030.

[7] K. N. Paracha, S. K. Abdul Rahim, P. J. Soh, and M. Khalily, "Wearable Antennas: A Review of Materials, Structures, and Innovative Features for Autonomous Communication and Sensing," *IEEE Access,* vol. 7, pp. 56694-56712, 2019, doi: 10.1109/access.2019.2909146.

[8] J. Biggs *et al.,* "A Natively Flexible 32-bit Arm Microprocessor," *Nature,* vol. 595, no. 7868, pp. 532-536, 2021/07/01 2021, doi: 10.1038/s41586-021-03625-w.

[9] Y. Bonnassieux *et al.,* "The 2021 Flexible and Printed Electronics Roadmap," *Flexible and Printed Electronics,* vol. 6, no. 2, 2021, doi: 10.1088/2058-8585/abf986.

[10] K. Yan, J. Li, L. Pan, and Y. Shi, "Inkjet Printing for Flexible and Wearable Electronics," *APL Materials,* vol. 8, no. 12, p. 120705, 2020, doi: 10.1063/5.0031669.

[11] M. U. Ali Khan, R. Raad, F. Tubbal, P. I. Theoharis, S. Liu, and J. Foroughi, "Bending Analysis of Polymer-Based Flexible Antennas for Wearable, General IoT Applications: A Review," *Polymers (Basel),* vol. 13, no. 3, Jan 22 2021, doi: 10.3390/polym13030357.

[12] Y. Liu, M. Pharr, and G. A. Salvatore, "Lab-on-Skin: A Review of Flexible and Stretchable Electronics for Wearable Health Monitoring," *ACS Nano,* vol. 11, no. 10, pp. 9614-9635, Oct 24 2017, doi: 10.1021/acsnano.7b04898.

[13] M. Hassan *et al.*, "Significance of Flexible Substrates for Wearable and Implantable Devices: Recent Advances and Perspectives," *Advanced Materials Technologies,* 2021, doi: 10.1002/admt.202100773.

[14] A. I. Fedorchenko, A.-B. Wang, and H. H. Cheng, "Thickness Dependence of Nanofilm Elastic Modulus," *Applied Physics Letters,* vol. 94, no. 15, 2009, doi: 10.1063/1.3120763.

[15] P. I. Dankov, P. K. Sharma, and N. Gupta, "Numerical and Experimental Investigation of the Opposite Influence of Dielectric Anisotropy and Substrate Bending on Planar Radiators and Sensors," *Sensors (Basel),* vol. 21, no. 1, Dec 22 2020, doi: 10.3390/s21010016.

[16] A. Scidà *et al.*, "Application of Graphene-based Flexible Antennas in Consumer Electronic Devices," *Materials Today,* vol. 21, no. 3, pp. 223-230, 2018, doi: 10.1016/j.mattod.2018.01.007.

[17] A. Sharif *et al.*, "Making Assembly Line in Supply Chain Robust and Secure Using UHF RFID," *Sci Rep,* vol. 11, no. 1, p. 18041, Sep 10 2021, doi: 10.1038/s41598-021-97598-5.

[18] W. Zhou *et al.*, "Flexible Radiofrequency Filters Based on Highly Conductive Graphene Assembly Films," *Applied Physics Letters,* vol. 114, no. 11, 2019, doi: 10.1063/1.5074172.

[19] M. R. M. Hashemi *et al.*, "A Flexible Phased Array System With Low Areal Mass Density," *Nature Electronics,* vol. 2, no. 5, pp. 195-205, 2019, doi: 10.1038/s41928-019-0247-9.

[20] J. Zhang *et al.*, "Flexible Graphene-Assembled Film-Based Antenna for Wireless Wearable Sensor with Miniaturized Size and High Sensitivity," *ACS Omega,* vol. 5, no. 22, pp. 12937-12943, Jun 9 2020, doi: 10.1021/acsomega.0c00263.

[21] C. A. Balanis, *Antenna Theory : Analysis and Design,* 4th ed. Hoboken, N.J.: Hoboken, N.J. : Wiley, 2016.

[22] C. A. Balanis, *Advanced Engineering Electromagnetics,* 2nd ed. Hoboken, N.J.: Hoboken, N.J. : John Wiley & Sons, 2012.

[23] J. Baker-Jarvis, M. D. Janezic, and D. C. Degroot, "High-frequency Dielectric Measurements," *IEEE Instrumentation & Measurement Magazine,* vol. 13, no. 2, pp. 24-31, 2010, doi: 10.1109/MIM.2010.5438334.

[24] J. W. Hearle and W. E. Morton, *Physical Properties of Textile Fibres*. Elsevier, 2008.

[25] S. Zhu and R. Langley, "Dual-Band Wearable Textile Antenna on an EBG Substrate," *IEEE Transactions on Antennas and Propagation,* vol. 57, no. 4, pp. 926-935, 2009, doi: 10.1109/TAP.2009.2014527.

[26] K. Zhang, L. Zheng, F. I. Farha, L. Wang, and F. Xu, "Three-Dimensional Textile Structural Conical Conformal Microstrip Antennas for Multifunctional Flexible Electronics," *ACS Applied Electronic Materials,* vol. 2, no. 5, pp. 1440-1448, 2020, doi: 10.1021/acsaelm.0c00200.

[27] B. Sindhu, A. Kothuru, P. Sahatiya, S. Goel, and S. Nandi, "Laser-Induced Graphene Printed Wearable Flexible Antenna-Based Strain Sensor for Wireless Human Motion Monitoring," *IEEE Transactions on Electron Devices,* vol. 68, no. 7, pp. 3189-3194, 2021, doi: 10.1109/ted.2021.3067304.

[28] S. M. Saeed, C. A. Balanis, and C. R. Birtcher, "Radiation Characteristics of Flexible Reconfigurable Antenna with Curved Cylindrical Configurations," in *2016 IEEE International Symposium on Antennas and Propagation (APSURSI)*, 26 June-1 July 2016 2016, pp. 1433-1434, doi: 10.1109/APS.2016.7696423.

[29] M. Ur-Rehman, Q. H. Abbasi, M. Akram, and C. Parini, "Design of Band-Notched Ultra Wideband Antenna for Indoor and Wearable Wireless Communications," *IET Microwaves, Antennas & Propagation,* vol. 9, no. 3, pp. 243-251, 2015, doi: 10.1049/iet-map.2014.0378.

[30] D. Mitra *et al.*, "Conductive Electrifi and Nonconductive NinjaFlex Filaments based Flexible Microstrip Antenna for Changing Conformal Surface Applications," *Electronics,* vol. 10, no. 7, p. 821, 2021. [Online]. Available: https://www.mdpi.com/2079-9292/10/7/821.

[31] S. Roy, M. B. Qureshi, S. Asif, S. Sajal, and B. D. Braaten, "A Study of Microstrip Transmission Lines on Substrates Created Using Additive Manufacturing and Flexible or Semi-rigid Filaments," in *2017 IEEE International Conference on Electro Information Technology (EIT)*, 14-17 May 2017 2017, pp. 200-205, doi: 10.1109/EIT.2017.8053355.

[32] R. A. Liyakath, A. Takshi, and G. Mumcu, "Multilayer Stretchable Conductors on Polymer Substrates for Conformal and Reconfigurable Antennas," *IEEE Antennas and Wireless Propagation Letters,* vol. 12, pp. 603-606, 2013, doi: 10.1109/lawp.2013.2260123.

[33] J. Suikkola *et al.*, "Screen-Printing Fabrication and Characterization of Stretchable Electronics," *Sci Rep,* vol. 6, p. 25784, May 13 2016, doi: 10.1038/srep25784.

[34] M. S. White *et al.*, "Ultrathin, Highly Flexible and Stretchable PLEDs," *Nature Photonics,* vol. 7, no. 10, pp. 811-816, 2013, doi: 10.1038/nphoton.2013.188.

[35] M. Kaltenbrunner *et al.*, "An Ultra-lightweight Design for Imperceptible Plastic Electronics," *Nature,* vol. 499, no. 7459, pp. 458-63, Jul 25 2013, doi: 10.1038/nature12314.

[36] D. Wang, Y. Zhang, X. Lu, Z. Ma, C. Xie, and Z. Zheng, "Chemical Formation of Soft Metal Electrodes for Flexible and Wearable Electronics," *Chem Soc Rev*, vol. 47, no. 12, pp. 4611-4641, Jun 18 2018, doi: 10.1039/c7cs00192d.

[37] B. Mohamadzade, R. M. Hashmi, R. Simorangkir, R. Gharaei, S. Ur Rehman, and Q. H. Abbasi, "Recent Advances in Fabrication Methods for Flexible Antennas in Wearable Devices: State of the Art," *Sensors (Basel)*, vol. 19, no. 10, May 19 2019, doi: 10.3390/s19102312.

[38] S. Baron, B. Guiffard, and A. Sharaiha, "Polyurethane Membranes for Flexible Centimeter-wave Patch Antennas," *Journal of Micromechanics and Microengineering*, vol. 24, no. 7, 2014, doi: 10.1088/0960-1317/24/7/075020.

[39] S. Ahmed, F. A. Tahir, A. Shamim, and H. M. Cheema, "A Compact Kapton-Based Inkjet-Printed Multiband Antenna for Flexible Wireless Devices," *IEEE Antennas and Wireless Propagation Letters*, vol. 14, pp. 1802-1805, 2015, doi: 10.1109/LAWP.2015.2424681.

[40] Z. Hamouda *et al.*, "Dual-Band Elliptical Planar Conductive Polymer Antenna Printed on a Flexible Substrate," *IEEE Transactions on Antennas and Propagation*, vol. 63, no. 12, pp. 5864-5867, 2015, doi: 10.1109/tap.2015.2479643.

[41] H. R. Khaleel, "Design and Fabrication of Compact Inkjet Printed Antennas for Integration Within Flexible and Wearable Electronics," *IEEE Transactions on Components, Packaging and Manufacturing Technology*, vol. 4, no. 10, pp. 1722-1728, 2014, doi: 10.1109/tcpmt.2014.2352254.

[42] J. Shi *et al.*, "Smart Textile-Integrated Microelectronic Systems for Wearable Applications," *Advanced Materials*, vol. 32, no. 5, p. 1901958, 2020, doi: https://doi.org/10.1002/adma.201901958.

[43] H. Li *et al.*, "Waterproof and Tailorable Elastic Rechargeable Yarn Zinc Ion Batteries by a Cross-Linked Polyacrylamide Electrolyte," *ACS Nano*, vol. 12, no. 4, pp. 3140-3148, Apr 24 2018, doi: 10.1021/acsnano.7b09003.

[44] X. Xiao *et al.*, "An ultrathin rechargeable solid-state zinc ion fiber battery for electronic textiles," *Science Advances*, vol. 7, no. 49, p. eabl3742, 2021, doi: doi:10.1126/sciadv.abl3742.

[45] D. M. Pozar, *Microwave Engineering*, 4th ed. Hoboken, N.J. : Wiley, 2012.

[46] R. Salvado, C. Loss, R. Goncalves, and P. Pinho, "Textile Materials for the Design of Wearable Antennas: A Survey," *Sensors (Basel)*, vol. 12, no. 11, pp. 15841-57, Nov 15 2012, doi: 10.3390/s121115841.

[47] B. Zhu, S. Gong, and W. Cheng, "Softening Gold for Elastronics," *Chem Soc Rev*, vol. 48, no. 6, pp. 1668-1711, Mar 18 2019, doi: 10.1039/c8cs00609a.

[48] S. Ramo, J. R. Whinnery, and T. Van Duzer, *Fields and Waves in Communication Electronics*, 3rd Ed. ed. John Wiley & Sons, 1994.

[49] W. Dang, V. Vinciguerra, L. Lorenzelli, and R. Dahiya, "Printable Stretchable Interconnects," *Flexible and Printed Electronics*, vol. 2, no. 1, 2017, doi: 10.1088/2058-8585/aa5ab2.

[50] M. Park *et al.*, "Highly Stretchable Electric Circuits from a Composite Material of Silver Nanoparticles and Elastomeric Fibres," *Nat Nanotechnol*, vol. 7, no. 12, pp. 803-9, Dec 2012, doi: 10.1038/nnano.2012.206.

[51] T. Sekitani, Y. Noguchi, K. Hata, T. Fukushima, T. Aida, and T. Someya, "A Rubberlike Stretchable Active Matrix Using Elastic Conductors," *Science*, vol. 321, no. 5895, pp. 1468-1472, 2008, doi: 10.1126/science.1160309.

[52] S. P. Lacour, J. Jones, S. Wagner, L. Teng, and S. Zhigang, "Stretchable Interconnects for Elastic Electronic Surfaces," *Proceedings of the IEEE*, vol. 93, no. 8, pp. 1459-1467, 2005, doi: 10.1109/JPROC.2005.851502.

[53] S. I. Rich, Z. Jiang, K. Fukuda, and T. Someya, "Well-rounded Devices: the Fabrication of Electronics on Curved Surfaces – A Review," *Materials Horizons*, vol. 8, no. 7, pp. 1926-1958, 2021, doi: 10.1039/d1mh00143d.

[54] Q. Lyu, S. Gong, J. Yin, J. M. Dyson, and W. Cheng, "Soft Wearable Healthcare Materials and Devices," *Adv Healthc Mater*, p. e2100577, May 21 2021, doi: 10.1002/adhm.202100577.

[55] B. Huyghe, H. Rogier, J. Vanfleteren, and F. Axisa, "Design and Manufacturing of Stretchable High-Frequency Interconnects," *IEEE Transactions on Advanced Packaging*, vol. 31, no. 4, pp. 802-808, 2008, doi: 10.1109/tadvp.2008.927811.

[56] D. Brosteaux, A. Fabrice, M. Gonzalez, and J. Vanfleteren, "Design and Fabrication of Elastic Interconnections for Stretchable Electronic Circuits," *IEEE Electron Device Letters*, vol. 28, no. 7, pp. 552-554, 2007, doi: 10.1109/led.2007.897887.

[57] R. Verplancke, F. Bossuyt, D. Cuypers, and J. Vanfleteren, "Thin-film Stretchable Electronics Technology Based on Meandering Interconnections: Fabrication and Mechanical Performance," *Journal of Micromechanics and Microengineering*, vol. 22, no. 1, 2012, doi: 10.1088/0960-1317/22/1/015002.

[58] D. H. Kim *et al.*, "Optimized Structural Designs for Stretchable Silicon Integrated Circuits," *Small*, vol. 5, no. 24, pp. 2841-7, Dec 2009, doi: 10.1002/smll.200900853.

[59] J. Zhu *et al.*, "Strain-Insensitive Hierarchically Structured Stretchable Microstrip Antennas for Robust Wireless Communication," *Nanomicro Lett*, vol. 13, no. 1, p. 108, Apr 9 2021, doi: 10.1007/s40820-021-00631-5.

[60] S. Wagner and S. Bauer, "Materials for Stretchable Electronics," *MRS Bulletin*, vol. 37, no. 3, pp. 207-213, 2012, doi: 10.1557/mrs.2012.37.

[61] W. Wu, "Stretchable Electronics: Functional Materials, Fabrication Strategies and Applications," *Science and Technology of Advanced Materials*, vol. 20, no. 1, pp. 187-224, 2019, doi: 10.1080/14686996.2018.1549460.

[62] B. Plovie *et al.*, "Arbitrarily Shaped 2.5D Circuits using Stretchable Interconnects Embedded in Thermoplastic Polymers " *Advanced Engineering Materials,* vol. 19, no. 8, 2017, doi: 10.1002/adem.201700032.

[63] B. Aïssa *et al.*, "Fluidic Patch Antenna Based on Liquid Metal Alloy/Single-wall Carbon-nanotubes Operating at the S-Band Frequency," *Applied Physics Letters,* vol. 103, no. 6, 2013, doi: 10.1063/1.4817861.

[64] M. Han *et al.*, "Solution-Processed Ti3 C2 Tx MXene Antennas for Radio-Frequency Communication," *Adv Mater,* vol. 33, no. 1, p. e2003225, Jan 2021, doi: 10.1002/adma.202003225.

[65] I. J. Fernandes *et al.*, "Silver Nanoparticle Conductive Inks: Synthesis, Characterization, and Fabrication of Inkjet-printed Flexible Electrodes," *Scientific Reports,* vol. 10, no. 1, p. 8878, 2020/06/01 2020, doi: 10.1038/s41598-020-65698-3.

[66] K. Sim, Z. Rao, F. Ershad, and C. Yu, "Rubbery Electronics Fully Made of Stretchable Elastomeric Electronic Materials," *Adv Mater,* vol. 32, no. 15, p. e1902417, Apr 2020, doi: 10.1002/adma.201902417.

[67] Y. Wang *et al.*, "A Highly Stretchable, Transparent, and Conductive Polymer," *Science Advances,* vol. 3, no. 3, p. e1602076, 2017, doi: 10.1126/sciadv.1602076.

[68] Z. Chen, J. Xi, W. Huang, and M. M. F. Yuen, "Stretchable Conductive Elastomer for Wireless Wearable Communication Applications," *Sci Rep,* vol. 7, no. 1, p. 10958, Sep 8 2017, doi: 10.1038/s41598-017-11392-w.

[69] M. Rizwan, M. W. A. Khan, L. Sydanheimo, J. Virkki, and L. Ukkonen, "Flexible and Stretchable Brush-Painted Wearable Antenna on a Three-Dimensional (3-D) Printed Substrate," *IEEE Antennas and Wireless Propagation Letters,* vol. 16, pp. 3108-3112, 2017, doi: 10.1109/lawp.2017.2763743.

[70] L. Song, A. C. Myers, J. J. Adams, and Y. Zhu, "Stretchable and Reversibly Deformable Radio Frequency Antennas Based on Silver Nanowires," *ACS Appl Mater Interfaces,* vol. 6, no. 6, pp. 4248-53, Mar 26 2014, doi: 10.1021/am405972e.

[71] I. Cherukhin, S. P. Gao, and Y. X. Guo, "Fully Flexible Polymer-based Microwave Devices: Materials, Fabrication Technique, and Application to Transmission Lines," *IEEE Transactions on Antennas and Propagation,* pp. 1-1, 2021, doi: 10.1109/TAP.2021.3083855.

[72] X. Huang *et al.*, "Highly Flexible and Conductive Printed Graphene for Wireless Wearable Communications Applications," *Sci Rep,* vol. 5, p. 18298, Dec 17 2015, doi: 10.1038/srep18298.

[73] Y. Bayram *et al.*, "E-Textile Conductors and Polymer Composites for Conformal Lightweight Antennas," *IEEE Transactions on Antennas and Propagation,* vol. 58, no. 8, pp. 2732-2736, 2010, doi: 10.1109/TAP.2010.2050439.

[74] T. N. Kapetanakis, C. D. Nikolopoulos, K. Petridis, and I. O. Vardiambasis, "Wearable Textile Antenna with a Graphene Sheet or Conductive Fabric Patch for the 2.45 GHz Band," *Electronics*, vol. 10, no. 21, 2021, doi: 10.3390/electronics10212571.

[75] A. Sarycheva, A. Polemi, Y. Liu, K. Dandekar, B. Anasori, and Y. Gogotsi, "2D Titanium Carbide (MXene) for Wireless Communication," *Science Advances*, vol. 4, no. 9, p. eaau0920, 2018, doi: 10.1126/sciadv.aau0920.

[76] Y. Li *et al.*, "Reversible Crumpling of 2D Titanium Carbide (MXene) Nanocoatings for Stretchable Electromagnetic Shielding and Wearable Wireless Communication," *Advanced Functional Materials*, vol. 30, no. 5, 2019, doi: 10.1002/adfm.201907451.

[77] G. J. Hayes, J. So, A. Qusba, M. D. Dickey, and G. Lazzi, "Flexible Liquid Metal Alloy (EGaIn) Microstrip Patch Antenna," *IEEE Transactions on Antennas and Propagation*, vol. 60, no. 5, pp. 2151-2156, 2012, doi: 10.1109/TAP.2012.2189698.

[78] F. Nikbakhtnasrabadi, H. El Matbouly, M. Ntagios, and R. Dahiya, "Textile-Based Stretchable Microstrip Antenna with Intrinsic Strain Sensing," *ACS Appl Electron Mater*, vol. 3, no. 5, pp. 2233-2246, May 25 2021, doi: 10.1021/acsaelm.1c00179.

[79] Q. Bai, J. Rigelsford, and R. Langley, "Crumpling of Microstrip Antenna Array," *IEEE Transactions on Antennas and Propagation*, vol. 61, no. 9, pp. 4567-4576, 2013, doi: 10.1109/tap.2013.2269133.

[80] K. Pan *et al.*, "Sustainable Production of Highly Conductive Multilayer Graphene Ink for Wireless Connectivity and IoT Applications," *Nat Commun*, vol. 9, no. 1, p. 5197, Dec 5 2018, doi: 10.1038/s41467-018-07632-w.

[81] B. Zhang *et al.*, "Flexible Anti-Metal RFID Tag Antenna Based on High-Conductivity Graphene Assembly Film," *Sensors (Basel)*, vol. 21, no. 4, Feb 22 2021, doi: 10.3390/s21041513.

[82] B. Anasori and Y. Gogotsi, *2D Metal Carbides and Nitrides (MXenes): Structure, Properties and Applications*. Springer International Publishing, 2019.

[83] A. VahidMohammadi, J. Rosen, and Y. Gogotsi, "The World of Two-Dimensional Carbides and Nitrides (MXenes)," *Science*, vol. 372, no. 6547, p. eabf1581, 2021, doi: 10.1126/science.abf1581.

[84] M. A. S. Tajin and K. R. Dandekar, "Anomalous Radio Frequency Conductivity and Sheet Resistance of 2D Ti3C2Tx MXene," *IEEE Access*, vol. 10, pp. 25850-25856, 2022, doi: 10.1109/access.2022.3154038.

[85] B. Sindhu, V. Adepu, P. Sahatiya, and S. Nandi, "An MXene Based Flexible Patch Antenna for Pressure and Level Sensing Applications," *FlatChem*, vol. 33, 2022, doi: 10.1016/j.flatc.2022.100367.

[86] Y. Shao *et al.*, "Room-temperature High-precision Printing of Flexible Wireless Electronics Based on MXene Inks," *Nat Commun,* vol. 13, no. 1, p. 3223, Jun 9 2022, doi: 10.1038/s41467-022-30648-2.

[87] J. Zhang *et al.*, "Scalable Manufacturing of Free-Standing, Strong Ti3 C2 Tx MXene Films with Outstanding Conductivity," *Adv Mater,* vol. 32, no. 23, p. e2001093, Jun 2020, doi: 10.1002/adma.202001093.

[88] Z. Xie, R. Avila, Y. Huang, and J. A. Rogers, "Flexible and Stretchable Antennas for Biointegrated Electronics," *Adv Mater,* vol. 32, no. 15, p. e1902767, Apr 2020, doi: 10.1002/adma.201902767.

[89] L. Song, B. Zhang, D. Zhang, and Y. Rahmat-Samii, "Embroidery Electro-Textile Patch Antenna Modeling and Optimization Strategies with Improved Accuracy and Efficiency," *IEEE Transactions on Antennas and Propagation,* pp. 1-1, 2022, doi: 10.1109/tap.2022.3145443.

[90] B. Almohammed, A. Ismail, and A. Sali, "Electro-textile Wearable Antennas in Wireless Body Area Networks: Materials, Antenna Design, Manufacturing Techniques, and Human Body Consideration—A Review," *Textile Research Journal,* vol. 91, no. 5-6, pp. 646-663, 2021, doi: 10.1177/0040517520932230.

[91] R. Garg, P. Bhartia, I. J. Bahl, and A. Ittipiboon, *Microstrip Antenna Design Handbook*. Artech house, 2001.

[92] K.-L. Wong, *Design of Nonplanar Microstrip Antennas and Transmission Lines*. John wiley & sons, 2004.

[93] C. Hertleer, H. Rogier, L. Vallozzi, and L. Van Langenhove, "A Textile Antenna for Off-Body Communication Integrated Into Protective Clothing for Firefighters," *IEEE Transactions on Antennas and Propagation,* vol. 57, no. 4, pp. 919-925, 2009, doi: 10.1109/tap.2009.2014574.

[94] M. Tanaka and J. Jae-Hyeuk, "Wearable Microstrip Antenna," in *IEEE Antennas and Propagation Society International Symposium. Digest. Held in conjunction with: USNC/CNC/URSI North American Radio Sci. Meeting (Cat. No.03CH37450)*, 22-27 June 2003 2003, vol. 2, pp. 704-707 vol.2, doi: 10.1109/APS.2003.1219333.

[95] I. Locher, M. Klemm, T. Kirstein, and G. Troster, "Design and Characterization of Purely Textile Patch Antennas," *IEEE Transactions on Advanced Packaging,* vol. 29, no. 4, pp. 777-788, 2006, doi: 10.1109/tadvp.2006.884780.

[96] F. Boeykens, H. Rogier, and L. Vallozzi, "An Efficient Technique Based on Polynomial Chaos to Model the Uncertainty in the Resonance Frequency of Textile Antennas Due to Bending," *IEEE Transactions on Antennas and Propagation,* vol. 62, no. 3, pp. 1253-1260, 2014, doi: 10.1109/tap.2013.2294021.

[97] T. Haagenson, S. Noghanian, P. de Leon, and Y.-h. Chang, "Textile Antennas for Spacesuit Applications: Design, simulation, manufacturing, and testing of

textile patch antennas for spacesuit applications," *IEEE Antennas and Propagation Magazine,* vol. 57, no. 4, pp. 64-73, 2015, doi: 10.1109/map.2015.2453890.

[98] H. R. Sanjari, A. A. Merati, S. M. Hosseini Varkiyani, and A. Tavakoli, "Evaluation of the Effect of Bending on the Resonance Frequency of Inset-fed Rectangular Textile Patch Antenna," *Journal of Industrial Textiles,* vol. 46, no. 1, pp. 19-44, 2015, doi: 10.1177/1528083715569377.

[99] S.-E. Adami *et al.,* "A Flexible 2.45-GHz Power Harvesting Wristband With Net System Output From −24.3 dBm of RF Power," *IEEE Transactions on Microwave Theory and Techniques,* vol. 66, no. 1, pp. 380-395, 2018, doi: 10.1109/tmtt.2017.2700299.

[100] D. Ferreira, P. Pires, R. Rodrigues, and R. F. S. Caldeirinha, "Wearable Textile Antennas: Examining the Effect of Bending on Their Performance," *IEEE Antennas and Propagation Magazine,* vol. 59, no. 3, pp. 54-59, 2017, doi: 10.1109/map.2017.2686093.

[101] L. Song and Y. Rahmat-Samii, "A Systematic Investigation of Rectangular Patch Antenna Bending Effects for Wearable Applications," *IEEE Transactions on Antennas and Propagation,* vol. 66, no. 5, pp. 2219-2228, 2018, doi: 10.1109/tap.2018.2809469.

[102] C. Lin, C. Chang, Y. T. Cheng, and C. F. Jou, "Development of a Flexible SU-8/PDMS-Based Antenna," *IEEE Antennas and Wireless Propagation Letters,* vol. 10, pp. 1108-1111, 2011, doi: 10.1109/LAWP.2011.2170398.

[103] Z. H. Jiang, D. E. Brocker, P. E. Sieber, and D. H. Werner, "A Compact, Low-Profile Metasurface-Enabled Antenna for Wearable Medical Body-Area Network Devices," *IEEE Transactions on Antennas and Propagation,* vol. 62, no. 8, pp. 4021-4030, 2014, doi: 10.1109/tap.2014.2327650.

[104] A. H. Hamad and A. Mian, "Radio Frequency Response of Flexible Microstrip Patch Antennas under Compressive and Bending Loads Using Multiphysics Modeling Approach," *International Journal of RF and Microwave Computer-Aided Engineering,* vol. 29, no. 3, 2018, doi: 10.1002/mmce.21649.

[105] M. Bhattacharjee, F. Nikbakhtnasrabadi, and R. Dahiya, "Printed Chipless Antenna as Flexible Temperature Sensor," *IEEE Internet of Things Journal,* vol. 8, no. 6, pp. 5101-5110, 2021, doi: 10.1109/jiot.2021.3051467.

[106] D. Tang *et al.,* "Highly Sensitive Wearable Sensor Based on A Flexible Multi-layer Graphene Film Antenna," *Science Bulletin,* vol. 63, no. 9, pp. 574-579, 2018/05/15/ 2018, doi: https://doi.org/10.1016/j.scib.2018.03.014.

[107] H.-R. Zu, B. Wu, Y.-H. Zhang, Y.-T. Zhao, R.-G. Song, and D.-P. He, "Circularly Polarized Wearable Antenna With Low Profile and Low Specific Absorption Rate Using Highly Conductive Graphene Film," *IEEE Antennas and Wireless Propagation Letters,* vol. 19, no. 12, pp. 2354-2358, 2020, doi: 10.1109/lawp.2020.3033013.

[108] T. Thanh Tung, S. Chen, C. Fumeaux, T. Kim, and D. Losic, "N-doped Reduced Graphene Oxide-PEDOT Nanocomposites for Implementation of A Flexible Wideband Antenna for Wearable Wireless Communication Applications," *Nanotechnology,* Mar 9 2021, doi: 10.1088/1361-6528/abed04.

[109] R. Quarfoth, Y. Zhou, and D. Sievenpiper, "Flexible Patch Antennas Using Patterned Metal Sheets on Silicone," *IEEE Antennas and Wireless Propagation Letters,* vol. 14, pp. 1354-1357, 2015, doi: 10.1109/lawp.2015.2406887.

[110] R. B. V. B. Simorangkir, Y. Yang, L. Matekovits, and K. P. Esselle, "Dual-Band Dual-Mode Textile Antenna on PDMS Substrate for Body-Centric Communications," *IEEE Antennas and Wireless Propagation Letters,* vol. 16, pp. 677-680, 2017, doi: 10.1109/lawp.2016.2598729.

[111] R. B. V. B. Simorangkir, Y. Yang, R. M. Hashmi, T. Bjorninen, K. P. Esselle, and L. Ukkonen, "Polydimethylsiloxane-Embedded Conductive Fabric: Characterization and Application for Realization of Robust Passive and Active Flexible Wearable Antennas," *IEEE Access,* vol. 6, pp. 48102-48112, 2018, doi: 10.1109/access.2018.2867696.

[112] L. Shao *et al.*, "Flexible Force Sensitive Frequency Reconfigurable Antenna Base on Stretchable Conductive Fabric," *Journal of Physics D: Applied Physics,* vol. 55, no. 19, 2022, doi: 10.1088/1361-6463/ac4f91.

[113] S. Cheng, A. Rydberg, K. Hjort, and Z. Wu, "Liquid Metal Stretchable Unbalanced Loop Antenna," *Applied Physics Letters,* vol. 94, no. 14, p. 144103, 2009, doi: 10.1063/1.3114381.

[114] S. Cheng, Z. Wu, P. Hallbjorner, K. Hjort, and A. Rydberg, "Foldable and Stretchable Liquid Metal Planar Inverted Cone Antenna," *IEEE Transactions on Antennas and Propagation,* vol. 57, no. 12, pp. 3765-3771, 2009, doi: 10.1109/TAP.2009.2024560.

[115] S. Zhang *et al.*, "Standalone Stretchable RF Systems Based on Asymmetric 3D Microstrip Antennas with On-body Wireless Communication and Energy Harvesting," *Nano Energy,* vol. 96, 2022, doi: 10.1016/j.nanoen.2022.107069.

[116] J. Zhu *et al.*, "Stretchable Wideband Dipole Antennas and Rectennas for RF Energy Harvesting," *Mater Today Phys,* vol. 18, May 2021, doi: 10.1016/j.mtphys.2021.100377.

[117] S. Sankaralingam and B. Gupta, "Development of Textile Antennas for Body Wearable Applications and Investigations on Their Performance under Bent Conditions," *Progress In Electromagnetics Research B,* vol. 22, pp. 53-71, 2010, doi: 10.2528/pierb10032705.

[118] Y. Mukai, V. T. Bharambe, J. J. Adams, and M. Suh, "Effect of Bending and Padding on the Electromagnetic Performance of a Laser-cut Fabric Patch Antenna," *Textile Research Journal,* vol. 89, no. 14, pp. 2789-2801, 2018, doi: 10.1177/0040517518801202.

[119] R. B. V. B. Simorangkir, Y. Yang, K. P. Esselle, and B. A. Zeb, "A Method to Realize Robust Flexible Electronically Tunable Antennas Using Polymer-Embedded Conductive Fabric," *IEEE Transactions on Antennas and Propagation,* vol. 66, no. 1, pp. 50-58, 2018, doi: 10.1109/tap.2017.2772036.

[120] S. Moscato *et al.*, "Infill-Dependent 3-D-Printed Material Based on NinjaFlex Filament for Antenna Applications," *IEEE Antennas and Wireless Propagation Letters,* vol. 15, pp. 1506-1509, 2016, doi: 10.1109/lawp.2016.2516101.

[121] J. Zhang, J. Huang, P. Sun, F. Meng, J. Zhang, and P. Zhao, "Analysis Method of Bending Effect on Transmission Characteristics of Ultra-Low-Profile Rectangular Microstrip Antenna," *Sensors (Basel),* vol. 22, no. 2, Jan 13 2022, doi: 10.3390/s22020602.

[122] W. Chen, D. Xiao, H. Xiao, X. Wang, W. Peng, and H. Zhang, "Inkjet-printed Radiation Pattern Reconfigurable Receiving Antenna for 2.45 GHz Wireless Power Transfer Application," *AIP Advances,* vol. 12, no. 2, 2022, doi: 10.1063/5.0077533.

[123] X. Huang, T. Leng, K. H. Chang, J. C. Chen, K. S. Novoselov, and Z. Hu, "Graphene Radio Frequency and Microwave Passive Components for Low Cost Wearable Electronics," *2D Materials,* vol. 3, no. 2, 2016, doi: 10.1088/2053-1583/3/2/025021.

[124] Y. Shi, Z. Jiang, S. Lam, M. Leach, J. Wang, and E. G. Lim, "Multi-GHz Microstrip Transmission Lines Realised by Screen Printing on Flexible Substrates," presented at the 2017 IEEE Electrical Design of Advanced Packaging and Systems Symposium (EDAPS), 2017.

[125] A. Lamminen *et al.*, "Graphene-Flakes Printed Wideband Elliptical Dipole Antenna for Low-Cost Wireless Communications Applications," *IEEE Antennas and Wireless Propagation Letters,* vol. 16, pp. 1883-1886, 2017, doi: 10.1109/lawp.2017.2684907.

[126] K. Hantanasirisakul *et al.*, "Fabrication of Ti3C2Tx MXene Transparent Thin Films with Tunable Optoelectronic Properties," *Advanced Electronic Materials,* vol. 2, no. 6, 2016, doi: 10.1002/aelm.201600050.

[127] H. Chen, S. Tang, W. Tian, Q. Xue, H. Wang, and W. Che, "Direct Sputtering on PDMS for Investigation of Stretchable and Transparent Microstrip Line," *IEEE Transactions on Components, Packaging and Manufacturing Technology,* vol. 9, no. 9, pp. 1741-1747, 2019, doi: 10.1109/tcpmt.2019.2927504.

[128] S. Sivapurapu *et al.*, "Multi-Physics Modeling and Characterization of Components on Flexible Substrates," *IEEE Transactions on Components, Packaging and Manufacturing Technology,* vol. 9, no. 9, pp. 1730-1740, 2019, doi: 10.1109/tcpmt.2019.2931452.

[129] S.-m. Sim, Y. Lee, H.-L. Kang, K.-Y. Shin, S.-H. Lee, and J.-M. Kim, "RF Performance of Ink-jet Printed Microstrip Lines on Rigid and Flexible

Substrates," *Microelectronic Engineering,* vol. 168, pp. 82-88, 2017, doi: 10.1016/j.mee.2016.11.011.

[130] D. Ding, R. Li, J. Yan, J. Liu, Y. Fang, and Y. Yu, "Influence of Microcracks on Silver/Polydimethylsiloxane-Based Flexible Microstrip Transmission Lines," *Applied Sciences,* vol. 11, no. 1, 2020, doi: 10.3390/app11010005.

Chapter 4 Computational Cage Based Deformation Technique

This Chapter introduces the definitions for the developable and non-developable surfaces and reviews the most popular cage-based deformation techniques for object deformations, such as Mean Value Coordinates (MVC), Harmonic Coordinates (HC), and Green Coordinates (GC). The background theory for the Green Coordinates method is introduced and overviewed. Finally, this Chapter discusses and compares the shape preserving property of MVC, HC and GC methods.

4.1 Background Theory

This section provides a brief background theory for required computational deformation techniques.

4.1.1 Gaussian Curvature

Conventional fabrication methods are designed for planar sheet surfaces, however, flat objects cannot be wrapped onto doubly curved surface such as sphere, saddle, concave and convex shapes without stretch and shrink [1]. The criterion to deform a sheet surface conformally is by mapping its surface point by point onto the curvature was proved by Carl Friedrich Gauss in 1828 [1] [2]. A fundamental figure of merit is the Gaussian curvature, K, that is equivalent to the multiplication of the principal curvatures, [3],

$$K = \kappa_1 \cdot \kappa_2$$

where κ_1 and κ_2 are the maximum and minimum values of the curvature determined by eigenvalues of shape operator (the derivative of the unit normal vector field of a surface [4]) at that point.

If Gaussian curvature of surface is zero, the surface is defined as a developable surface [1, 2]. However, if it is not zero, surface is a non-developable surface [1, 2]. For example, for a flat sheet, the curvature in principal directions is zero $(\kappa_1 = 0, \kappa_1 = 0)$(See Figure 4.1a)). For cylinder surface, the directional curvature is $\kappa_2 = 0$, whereas other directional is non-zero (See Figure 4.1b)). For non-developable surfaces, however, directional curvature for both κ_1 and κ_2 are not equal to zero, i.e.,

$$K = \kappa_1 \cdot \kappa_2 \neq 0.$$

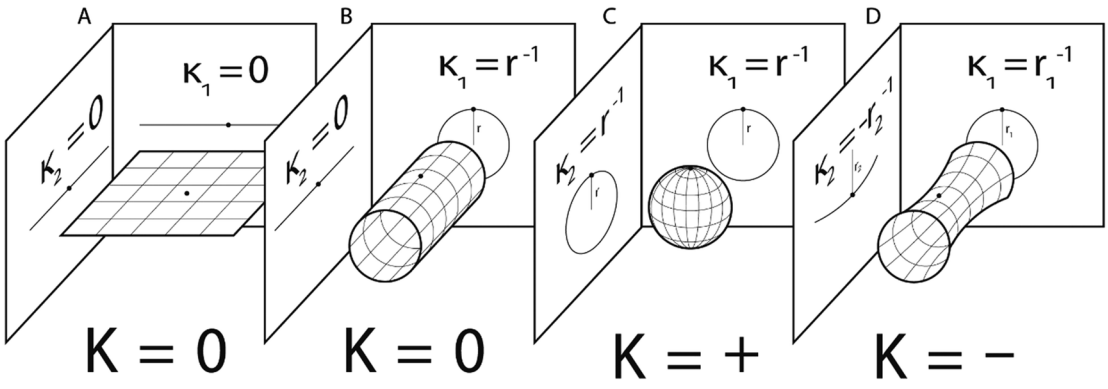


Figure 4.1 The association between principal curvature (κ_1, κ_2) and Gaussian curvature (K), such as (A) plane (B) cylinder, (C) sphere, (D) bowl surface with non-zero Gaussian curvature [1].

Depending on the doubly curved geometry, K may be a positive sign if κ_1 and κ_2 are positive value, such as sphere (See Figure 4.1c)), or negative value, if κ_1 and κ_2 have different signs (See Figure 4.1d)) [1, 2]. If Gaussian curvature of a surface is not equal to zero, flat shape cannot be mapped to curved surface accurately point by point and certain amount of stress and shrink will be introduced [1, 2].

Hence, non-developable surface electronics must either be implemented (1) on a flat sheet and then compressed or stretched to fit onto desired non-developable surface (2) developed onto non-developable surface directly [1].

In this thesis, terminology “non-developable surface” is used throughout and also represents equivalent phrases such as, “double-curved surfaces”, “surface with two-dimensional curvature”, and “surface with non-zero Gaussian curvature” [1].

4.1.2 Barycentric Coordinates

In the case of 2D geometries, barycentric coordinates define the location of a point inside a triangle [5-10]. For the triangle T with vertices $\boldsymbol{v}_1$, $\boldsymbol{v}_2$ and $\boldsymbol{v}_3$, any point $\boldsymbol{r_p}$ in the interior of T can defined as [11];

$$\boldsymbol{r_p} = \phi_1 \boldsymbol{v}_1 + \phi_2 \boldsymbol{v}_2 + \phi_3 \boldsymbol{v}_3 \tag{4.1}$$

where $\phi_i = \frac{A_i}{A}$, $i = 1, 2, 3$ are known as Barycentric coordinates, where A is the area of the whole triangle T and A_i are areas of sub-elements to area A as shown in Figure 3.2. In two dimensions, the functions ϕ_1, ϕ_2, ϕ_3 are computed from (4.1) and usual triangular barycentric coordinates with regards to the triangle P,

$$\phi_i(\boldsymbol{r_p}) = \frac{A(\boldsymbol{r_p}, \boldsymbol{v}_{i+1,} \boldsymbol{v}_{i+2})}{A(\boldsymbol{v}_1, \boldsymbol{v}_2, \boldsymbol{v}_3)}, \tag{4.2}$$

and $A(\boldsymbol{v}_1, \boldsymbol{v_2}, \boldsymbol{v}_3)$ is the signed surface area of the triangle according to their vertices $\boldsymbol{v}_k = (x_k, y_k)$, $k = 1, 2, 3$ [9, 11],

$$A(\boldsymbol{v}_1, \boldsymbol{v_2}, \boldsymbol{v}_3) \coloneqq \frac{1}{2} \begin{vmatrix} 1 & 1 & 1 \\ x_1 & x_2 & x_3 \\ y_1 & y_2 & y_3 \end{vmatrix} \tag{4.3}$$

In the three dimensions, $\phi_i(\boldsymbol{r_p})$ defines four volumetric ratios that are rate of volume tetrahedron to entire volume of cell T.

In the same way, a point $\boldsymbol{r_p}$ in a tetrahedron T in 3D geometries subdivide T into four sub-cells, and the proportion of each volumes to the total volume T defines the barycentric coefficients of $\boldsymbol{r_p}$ [9].

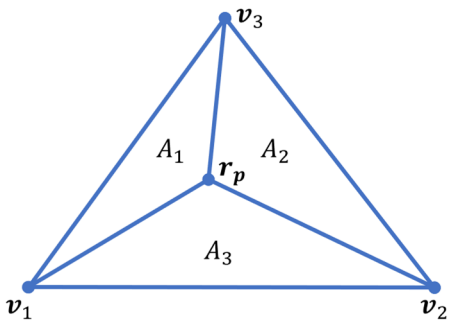


Figure 4.2 Coordinates in a Triangle, *T*, [9].

In the case of a polygon *P* in two dimension, with vertices $\boldsymbol{v}_1, \boldsymbol{v}_2, \boldsymbol{v}_3$ in anticlockwise ordering, hence any real functions $\phi_i: P \to \mathbb{R}$, $i = 1,2,3$ is widely known as generalised form of the barycentric coordinates [9, 11], when for all $\boldsymbol{r}_p$ in the interior of *P*, $\phi_i(\boldsymbol{r}_p) \geq 0, i = 1,2,3$, and the following is ensured:,

$$\sum_{i=1}^{3} \phi_i(\boldsymbol{r}_p) = 1, \tag{4.4}$$

$$\sum_{i=1}^{3} \phi_i(\boldsymbol{r}_p)\boldsymbol{v}_i = \boldsymbol{r}_p.$$

4.1.3 Affine Invariance

Affine-invariant which is known as surfaces are considered the same under affine transformations (or affine map between two vector spaces consists of a linear transformation followed by a translation. In geometry, these are accurately the functions that map straight lines to straight lines), i.e., linear transformations, $\boldsymbol{v} \mapsto \mathbf{A}\boldsymbol{v} + \mathbf{b}$, where **A** and **b** some constant, including shearing and squeezing [12, 13].

4.1.4 Cage Based Deformations

Up to this point, we have considered fundamental properties barycentric coordinates for 2D, but the essential application domain of barycentric coordinates is cage-based

surface deformations in 3D [9, 11]. The simple cage-based techniques define a point $\boldsymbol{r_p}$ enclosed by a cage T as a finite extent superposition of the vertices $\mathbb{V} = \{\boldsymbol{v}_i\}_{i \in I_{\mathbb{V}}}$ in 3D:

$$\boldsymbol{r_p} = F(r_p; T) = \sum_{i \in I_{\mathbb{V}}} \phi_i(\boldsymbol{r_p}) \boldsymbol{v}_i \tag{4.5}$$

where $\phi_i(.)$ are *coordinates* and $I_{\mathbb{V}}$ is the list of vertices. Then, the surface manipulation determined by a manipulated cage T' is determined by

$$\boldsymbol{r_p} \mapsto F(r_p; T') = \sum_{i \in I_{\mathbb{V}}} \phi_i(\boldsymbol{r_p}) \boldsymbol{v_i'} \tag{4.6}$$

where $\mathbb{V}' = \{\boldsymbol{v}_i'\}_{i \in I_{\mathbb{V}}}$ are the manipulated vertices of cage [13]. The fundamental form of this equations has *affine-invariant* operator. However, the general form of this operator cannot generate shape-preserving property, thus this affine transformations may well consist of *anisotropic* scaling and *shear* resulting in violation of shape-preserving property [13]. This results from the *Jacobian operators* (the derivative operator that the rate of change of each component of vector-valued functions with respect to each components of the coordinates variables) that include isotropic scaling and rotation, which reflects dependency between different axis [13].

4.2 Computational Geometry Morphing Techniques

Computer graphics has significantly focused on cages-based space deformation to manipulate 3D models [13-17]. The essence of these approaches is to define a relatively similar polyhedron shape to the enclosed object, which are widely known as a *cage.* Whole object spatial points *inside cage* defined by the linear accumulation of the enclosure vertices multiplied by weighted linear functions, which is widely known as *coordinates*. When cage polyhedron is subject to space manipulation, these deformations are translated the object of interest with deformed cage polyhedron's vertices. Since transforming a point only requires weight functions combinations, the

computational cost is small. Besides, each points transforming independently, the methods free from discretisation errors. Firstly, Sederberg and Parry [18] reported this type of space deformation techniques for Constructive Solid Geometry, CSG, in 1986, and the techniques were further extended and studied in articles [19-21]. In the essence deformation techniques generate a polygonal tube that encloses the object. The polygonal tube has a minimal number of manipulation points, whose positions are locally adjustable. By changing the positions of the tube vertices smooth deformation of whole of the space enclosed by the polygonal tube in [13, 16].

Several different cage-based methods have been reported namely, Mean Value Coordinates, MVC, Harmonic Coordinates, HC, and Green Coordinates, GC. MVC reported by Floater [14] for polygons in 2D with smooth interpolation in a closed-form derivation, and further improvement for generalisation of MVC, higher dimension derivation in [15, 22, 23]. Space warping technique based upon closed-form derivation of MVC presented by Ju *et al.* [15] and MVC was investigated analytically in the whole plane for practical image applications [24] (See Figure 3.3) . Another cage-based coordinates which was widely known as Harmonic Coordinates (HC) for game character shape manipulation (See Figure 3.4), reported by Joshi *et al.* [17]. HC coordinates are non-negative even in significantly concave bending cases and have no local extremum. Thus, it performs considerably better than MVC in terms of concave bending case, however, HC is not implemented as a closed-form derivation. These deformation methods do not support shape-preserving, because of affine-invariant interpolation weight functions derivations [13]. Lipman *et al*. [13, 16] introduced Green Coordinates (GC) for closed form polyhedral cages that uses not only vertex position but also the orientation of the cage's faces to define the enclosed object. The GC method is implemented in the closed-form expressions.

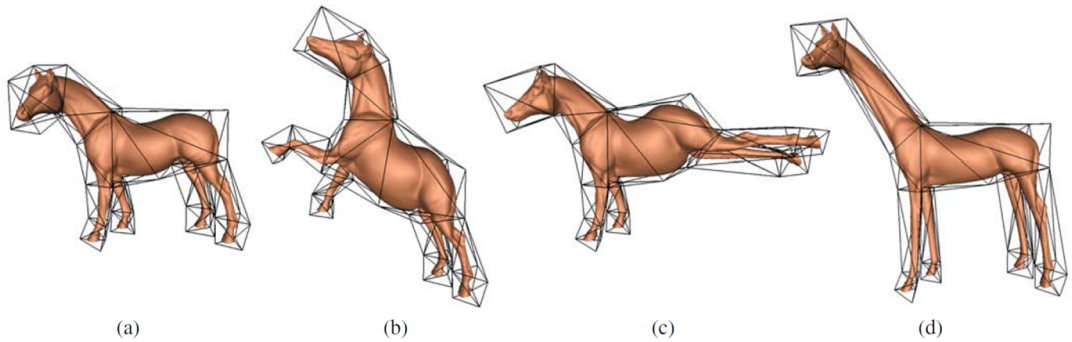


Figure 4.3 The MVC [14, 15] coordinates deformation applied on (a) horse model with enclosing cage (b-d) several deformations generated using MVC cage.

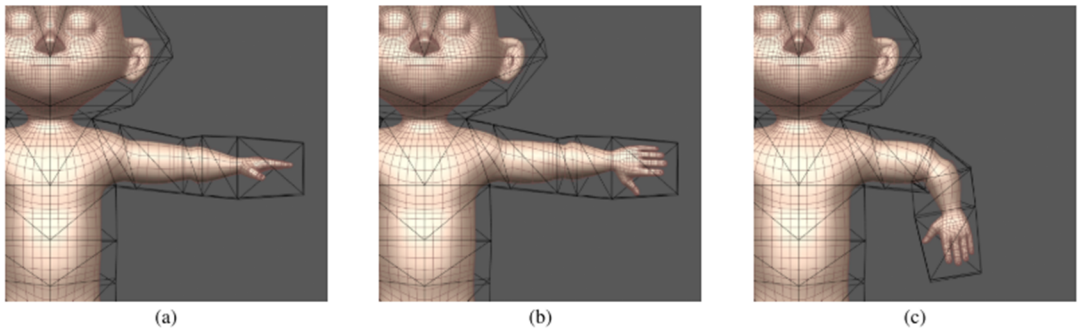


Figure 4.4 HC coordinates [17] applied on game character (a) game character with enclosing cage (b-c) the game character after applying the arm twist

Other sets of deformation techniques directly manipulate to surfaces based upon Laplacian surfaces [25-30], As-Rigid-As possible (ARAP) [31], As-Similar-As possible (ASAP) [32], As-Consistent-As possible (ACAP) [33]. These methods are based upon minimising bending energy and relaying on the least square error computation directly over the surface or demonstrating of the surface on skeleton of the object, and then manipulating them with single, several or cascaded constraints to generate target deformation. Although a good quality of shape-preserving deformations has been maintained, these deformations require solving large and often non-linear matrices, large iteration times and quality of deformation may be suffered from discretisation errors [13].

4.2.1.1 Derivation of Green Coordinates

In this section, Green Coordinates functions derivation is demonstrated. The theoretical basis of the GC method is that any spatial coordinate variable $\boldsymbol{r}$ within the cage satisfies Laplace's equation and thus introduction of a Green's function [21, 34], and use of Green's third identity expresses the value of any particular point $\boldsymbol{r_p}$within the cage as an integral of the values of $\boldsymbol{r}$ and its normal derivative over the cage surface.

Let $u(r_p)$, $\boldsymbol{r_p} = (r_{p1}, \dots, r_{pd})$ be a harmonic function in a domain $S \subset \mathbb{R}^d$ inside the piecewise-smooth boundary ∂S [13, 16]. When Laplacian u is equal to zero, the function u is called harmonic, and it can be written mathematically, i.e.,

$$\Delta u = \frac{\partial^2 u}{\partial r_{p1}^2} + \frac{\partial^2 u}{\partial r_{p2}^2} + \dots + \frac{\partial^2 u}{\partial r_{pd}^2} = 0. \tag{4.7}$$

Moreover, the *fundamental solutions* of the Laplace equation in $\mathbb{R}^d$, $G(.,.)$, can be written as mathematically,

$$\Delta_{r_p} G(\boldsymbol{r_p}, \boldsymbol{r'_p}) = \delta(\mathbf{r_p} - \mathbf{r'_p}) \tag{4.8}$$

where $\delta(.)$ is Dirac delta function.

Then, for any $\boldsymbol{r'_p}$ inside cage interior Green's third identity defines $u(\boldsymbol{r'_p})$ by its boundary values and boundary normal derivatives based upon [13, 16] the Green's third identity

$$u(\boldsymbol{r'_p}) = \int_{\partial S} \left(u(\boldsymbol{r_p}) \frac{\partial G(\boldsymbol{r_p}, \boldsymbol{r'_p})}{\partial \boldsymbol{n}(\boldsymbol{r_p})} - G(\boldsymbol{r_p}, \boldsymbol{r'_p}) \frac{\partial u(\boldsymbol{r_p})}{\partial \boldsymbol{n}(\boldsymbol{r_p})} \right) d\sigma_{r_p} \tag{4.9}$$

where $\boldsymbol{n}$ is the outward boundary normal to ∂S and $d\sigma_{\boldsymbol{r_p}}$ is the area element on ∂S [13, 16]. The solution of (4.8) in $\mathbb{R}^d$ without applying additional boundary conditions yields the *fundamental solutions* of the Laplace equation in $\mathbb{R}^d$, which can be mathematically defined as,

$$G(\boldsymbol{r_p}, \boldsymbol{r'_p}) = \begin{cases} \frac{1}{(2-d)\omega_d} \left\| \boldsymbol{r_p} - \boldsymbol{r'_p} \right\|^{2-d} & d \geq 3 \\ \frac{1}{2\pi} \log \left\| \boldsymbol{r_p} - \boldsymbol{r'_p} \right\| & d = 2 \end{cases} \tag{4.10}$$

where surface area of the unit sphere is ω_d [13, 16]. When the cage T encloses the domain S, the coordinate functions $\boldsymbol{r'_p} = (\boldsymbol{r'_{p1}}, \dots, \boldsymbol{r'_{pd}})$, which are linear functions, can be used as harmonic function u in (4.8), that is $u(\boldsymbol{r'_p}) = \boldsymbol{r'_p}$,

$$\boldsymbol{r'_p} = \int_{\partial S} \left(u(\boldsymbol{r_p}) \frac{\partial G(\boldsymbol{r_p}, \boldsymbol{r'_p})}{\partial \boldsymbol{n}(\boldsymbol{r_p})} - G(\boldsymbol{r_p}, \boldsymbol{r'_p}) \frac{\partial u(\boldsymbol{r_p})}{\partial \boldsymbol{n}(\boldsymbol{r_p})} \right) d\sigma_{\boldsymbol{r_p}} \tag{4.11}$$

If the outward normal $\boldsymbol{n}(\boldsymbol{r_p})$ is constant for each face f_j, we have $\partial \boldsymbol{r_p} / \partial \boldsymbol{n}(\boldsymbol{r_p}) = \partial \boldsymbol{r_p} / \partial \boldsymbol{n}(f_j)$, where $\boldsymbol{n}(f_j)$ indicates the outward normal of the face, f_j [13, 16]. When integrating over (4.11) finite extent superposition of the faces of surface element f_j,

$$\boldsymbol{r'_p} = \sum_{\boldsymbol{j} \in \boldsymbol{I_{\mathbb{F}}}} \left(\int_{f_j} \boldsymbol{r_p} \frac{\partial G(\boldsymbol{r_p}, \boldsymbol{r'_p})}{\partial \boldsymbol{n}(\boldsymbol{r_p})} d\sigma_{\zeta} - \int_{f_j} G(\boldsymbol{r_p}, \boldsymbol{r'_p}) \boldsymbol{n}(f_j) \, d\sigma_{\boldsymbol{r_p}} \right) \tag{4.12}$$

where $\boldsymbol{r'_p}$ is defined for the interior of domain S ($S^{in} \coloneqq interior(S)$) and $I_{\mathbb{F}}$ s the list of faces of triangular surface elements. Let the function Γ_i indicate the piecewise-linear hat function on $\mathrm{U}\{\boldsymbol{r_{v_i}}\}$, where $\mathrm{U}\{\boldsymbol{r_{v_i}}\}$ is the union of all surface elements of faces in the 1-ring adjacent of vertex $\boldsymbol{r_v}$ denoted by $\mathrm{U}\{\boldsymbol{r_{v_i}}\}$, which is equal to 1 at $\boldsymbol{r_{v_i}}$, and 0 at all the other vertices, and it is linear on each surface element [13, 16].

When $\boldsymbol{r_p}$ is barycentric coefficient superposition on the surface face element f_j, $\boldsymbol{r_p} = \sum_{k=1}^{d} \Gamma_k(\boldsymbol{r_p}) \boldsymbol{r_{v_i}}$, where $\boldsymbol{r_{v_i}}$ are the vertices of surface element f_j. The expression can be rewritten mathematically to obtain,

$$\boldsymbol{r'_p} = \sum_{i \in I_{\mathbb{V}}} g^V_{v_i}(\boldsymbol{r'_p}) \boldsymbol{r_{v_i}} + \sum_{j \in I_{\mathbb{F}}} g^F_{f_j}(\boldsymbol{r'_p}) \boldsymbol{n}(f_j) \tag{4.13}$$

where $\boldsymbol{r'_p}$ inside $S^{in} := interior(S)$, and g_v^V and g_f^F are the coordinate functions and can defined analytic mathematical expression are given as,

$$g_v^V(\boldsymbol{r'_p}) = \int_{\boldsymbol{r_p} \in U\{\boldsymbol{r}_{v_i}\}} \Gamma_k(\boldsymbol{r_p}) \frac{\partial G(\boldsymbol{r_p}, \boldsymbol{r'_p})}{\partial \boldsymbol{n}(\boldsymbol{r_p})} d\sigma_{\boldsymbol{r_p}} \quad i \in I_{\mathbb{V}} \tag{4.14}$$

$$g_f^F(\boldsymbol{r'_p}) = -\int_{\boldsymbol{r_p} \in \boldsymbol{f_j}} G(\boldsymbol{r_p}, \boldsymbol{r'_p}) d\sigma_{\boldsymbol{r_p}} \quad j \in I_{\mathbb{F}}.$$

where $I_{\mathbb{V}}$ and $I_{\mathbb{F}}$ are the list of vertices and faces for all triangular surface elements.

4.2.1.2 Calculation of Green Coordinates

For a triangulated cage surface, these integrals can be evaluated in closed form such that $\boldsymbol{r_p}$ is expressed as a discrete and finite extent superposition of the cage's vertices, $\boldsymbol{r_v}$, and face normals, $\boldsymbol{n_f}$, total number of vertices, N_v, and faces, N_f, with suitable coefficients g_v^V and g_f^F [13, 16], which is mathematically written as,

$$\boldsymbol{r_p} = \sum_{v=0}^{v=N_v} \boldsymbol{r_v}\ g_v^V(\boldsymbol{r_p}) + \sum_{f=0}^{f=N_f} \boldsymbol{n_f}\ g_f^F(\boldsymbol{r_p}). \tag{4.15}$$

The key point to note is that the *continuous* space within the cage (or in practice here, the relatively large number of topologically related vertices defining the object being deformed) is expressed in terms of a relatively few discrete quantities. The GC method deforms the enclosed space by making a one-to-one mapping of the set $\boldsymbol{r_v} \rightarrow \boldsymbol{r'_v}$ (and consequently $\boldsymbol{n_f} \rightarrow \boldsymbol{n'_f}$) and using the above superposition with the same weight coefficients as before, i.e.,

$$\boldsymbol{r'_p} = \sum_{v=0}^{v=N_v} \boldsymbol{r'_v}\ g_v^V(\boldsymbol{r_p}) + \sum_{f=0}^{f=N_f} \boldsymbol{n'_f}\ s_f g_f^F(\boldsymbol{r_p}). \tag{4.16}$$

The scale invariance property of shape deformations are computed by scale or stretch factor, s_f for each faces. In 2D, this scale or stretch factor is $s_f = \|t'_f\| / \|t_f\|$, where

the scaling of the edge is t_f. With using linear transformation in 3D [7], when a triangular face with edges is determined by the vectors u, v and a deformed geometry triangular face is associated with u', v', then,

$$s_f = \frac{\sqrt{\|\boldsymbol{u}'\|^2\|\boldsymbol{v}\|^2 + \mathbf{2}(\boldsymbol{u}' \cdot \boldsymbol{v}')(\boldsymbol{u} \cdot \boldsymbol{v}) + \|\boldsymbol{v}'\|^2\|\boldsymbol{u}\|^2}}{\sqrt{8}area(t_f)}. \tag{4.17}$$

where t_f is the triangular face element. It is important to note that this scale factor definitions provides least distorting deformation. Non-uniformly stretching of object can be provided by simply changing scaling factor, s_f [13, 16]. The full detail of the GC method is not given here and the reader is referred to the available literature on the method and the particular closed form expressions used [13, 16] and algorithm reported in [13, 16] is added in the appendix A.1 and A.2 for 2D and 3D computations, respectively.

4.2.2 Comparison of Cage Techniques

This section gives a comparison between GC method, and MVC and HC.

GC method provides suitable rotation with space warping with the preservation of shape [13, 16]. The operator has been proved to induces a conformal mapping in 2D. Conformal mappings are essential for requiring the preservation of the shape, they constructed form the rotations and isotropic scaling only (See Figure 4.5). In 3D, the GC's operator yield quasi-conformal mappings, which means that it has minimal amount of anisotropic scaling [13]. For 2D and 3D, GC's operator has closed form analytical formula, meaning that coordinates can computed analytically from cage positions without discretisation and approximations [13].

For MVC and their vertex-using-only variants, according to Eq. (4.5) and Eq. (4.6), the preservation of shape cannot be fully preserved. The main source of this problem is that the *Jacobian matrix* with *rotation and isotropic* scaling, fundamentally needs that the operators reproduces a dependency between the *different axis* directions. However, MVC is based only upon eq. (4.5), each directional axis deformation behaves

independently from each other. For instance, mapping the *x-axis* direction has no impact on the respective *y* and *z-axis* coordinates. Figure 4.6 compares the GC and MVC method when applied to a surface with bumps. The MVC [14, 15] coordinates have more focus on details preservation on their main orientation, but GC's operator [13, 16] rotates and moves details relying on deforming cages. However, the cage based deformation technique, MVC [14, 15] is limited in terms of shape and details preservation. The *preservation of shape* requires smooth mappings that transform are closes to their Jacobian matrices are similar to rotations with isotropic scaling.

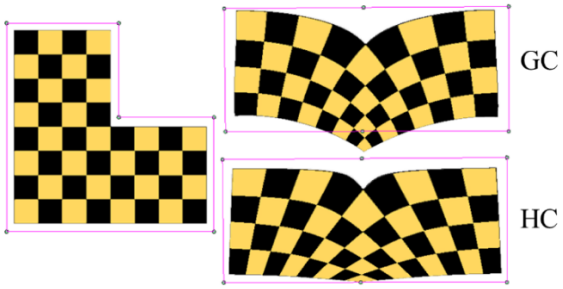


Figure 4.5 Chessboard is deformed with the original, GC's result [13, 16] and HC's result [17] reported by [13]. To retain conformal mapping, mapping extends outside the cage [13].

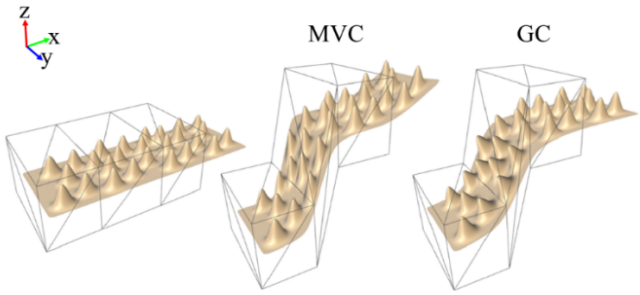


Figure 4.6 The MVC [14, 15] coordinates have more focus on details preservation on their main orientation, but GC's operator [13, 16] rotates and moves details relying on deforming cages [13].

According to the reported example visuals of cage based deformation of an Ogre by GC and MVC methods [13] (See Figure 4.7), although GC [13, 16] generates some

distortion around the chins, the GC [13, 16] provides better shape preservation than MVC [14, 15].

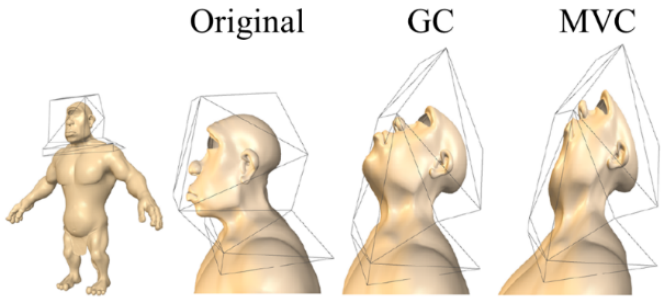


Figure 4.7 Cage based deformation of an Ogre which was reported by [13]. GC provides better for the preservation of the shape of the Ogre compared to MVC [13].

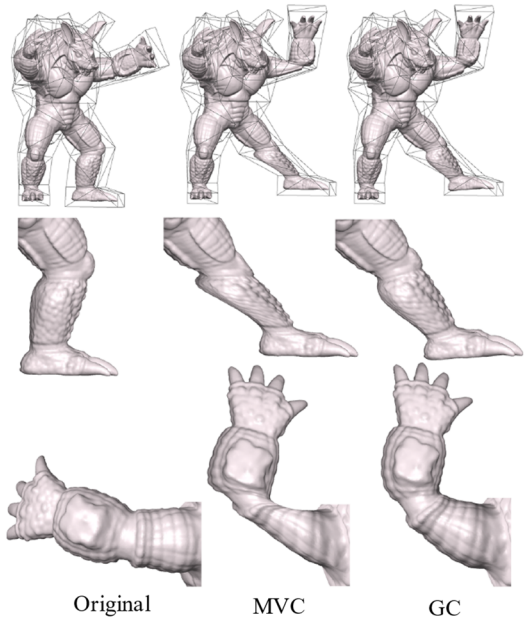


Figure 4.8 Cage based deformation of an Armadillo which was reported by [13]. Second column reveals MVC results and third column GC results [13]. GC provides better preservation of the Armadillo's leg and arm [13].

Another reported example is illustrated in Figure 4.8, where the game character arm and length are deformed with GC and MVC. According to visual view of geometry, the objects parts are better preserved with GC method [13, 16] compared to MVC method [14, 15].

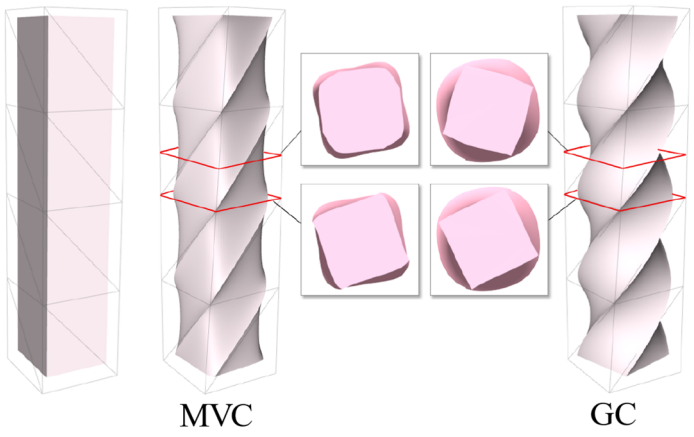
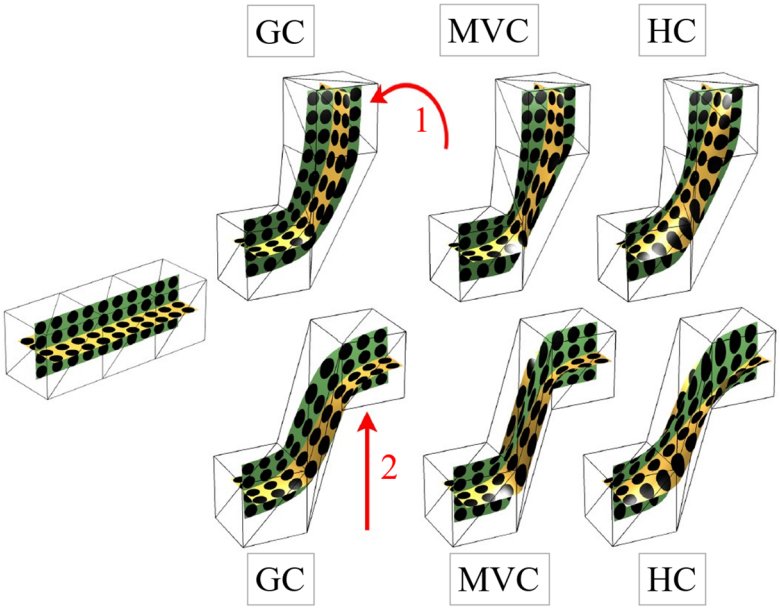


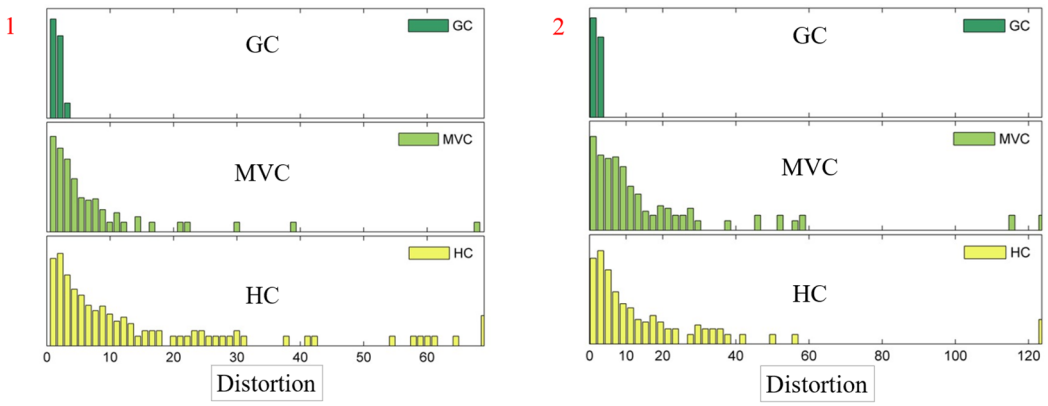
Figure 4.9 Twisting a square cross section polygonal tube using Mean Value Coordinates (MVC) and Green Coordinates (GC). Two cross section location of captured polygonal tube demonstrated at the middle of the figure (red color indicates location of capturing plane) [13].

Figure 4.9 illustrates the full circle twisting of a bar model where each section of the cages is rotated by $\pi/2$. Although MVC and GC distorts the square shape of tube, the cuts reveal that the MVC more distorts the square shape of a cross section of the bar than the GC method [13].

Strictly conformal mapping is unachievable, a map function has been a constrained maximal distortion, which is widely known as quasi-conformal [13]. Figure 4.10a) shows a comparison of the deformation of a polygonal tube generated with Green Coordinates (GC) [13, 16], Mean Value Coordinates (MVC) [14, 15], and Harmonic coordinates (HC) [17]. The polygonal tube has two planes, which has an intersection, with a circle pattern on the top of them, and also illustrates that the distortions of GC, MVC, and HC are in the interior of the cage. *Distortion* of a map at each point $\boldsymbol{r_p}$ with the rate of $\sigma_{max}(\boldsymbol{r'_p})$ and $\sigma_{min}(\boldsymbol{r'_p})$ are maximal and minimal singular values of each mapping deformation a differential (Jacobian matrix) at the point $\boldsymbol{r_p}'$. Quasi-conformality described as mapping with bounded maximal distortion. Figure 4.10b) compares this distortion histogram of each mapping, GC, MVC and HC with two orthogonal planes with circular pattern on it. It should be noted that although each



(a)



(b)

Figure 4.10 Comparisons of Green Coordinates (GC) [13, 16], Mean Value Coordinates (MVC) [14, 15], and Harmonic Coordinates (HC) [17]. (a) Two orthogonal planes each other with circle pattern captured by a polygonal tube (left) are bent twice: Each rows reveals GC, MVC, and HC deformation, demonstrated by red arrows. It should be noted that MVC and HC may well result in some shear, considerable bending and stretching. (b) The logarithmic scale of distortion values of GC, MVC, and HC deformation plotted for the first and second deformations [13].

deformations distorts circular pattern, the GC induces one-order lower distortions (~3.2) compared to the other methods [13]. Enforcing the second deformation the same cage reveals that while MVC and HC have unbounded total distortion (linearly depends

on a number of the distortions to the cage, GC provides maximum bounded distortion smaller than a constant (~6).

4.3 Conclusions

This Chapter introduced non-developable surface, and emphasise their creations leads shrinks or expansion of initial geometry. The basis for computational geometry deformation techniques is introduced and focused on cage-based deformation that are expressed in closed form expressions. The Green Coordinates for cage-based deformation is introduced. Closed-form deformation of GC provides conformal deformation in 2D and quasi-conformal deformation in 3D. The GC method uses both the faces of the cage and the vertices of the cage; hence the computations have three times higher number of vertices compared to MVC and HC.

The GC's operator yield quasi-conformal mappings, which means that it has minimal amount of anisotropic scaling [13]. Compared to MVC and HC techniques the GC method introduces minimal amount of distortion. This quality of GC makes it a suitable candidate to be used for arbitrary deformations of EM components. The next Chapter assessed GC method in the context of wearable antenna modelling and simulation.

References

[1] S. I. Rich, Z. Jiang, K. Fukuda, and T. Someya, "Well-rounded Devices: the Fabrication of Electronics on Curved Surfaces – A Review," *Materials Horizons*, vol. 8, no. 7, pp. 1926-1958, 2021, doi: 10.1039/d1mh00143d.

[2] K. Gauss, "Disquisitiones Generales Circa Superficies Curvas [General Investigations of Curved Surfaces]," *Göttingen: Dieterich,* 1828.

[3] A. Gray, E. Abbena, and S. Salamon, "Modern Differential Geometry of Curves and Surfaces with Mathematica," 2006.

[4] A. Gray, *Modern Differential Geometry of Curves and Surfaces with Mathematica* (Computers & Mathematics with Applications, no. 8). Boca Raton, FL: CRC Press, 1998, p. 121.

[5] H. S. M. Coxeter, *Introduction to Geometry*, 2nd ed. Wiley Classics Library, 1989.

[6] G. J. Fix, "A Rational Finite Element Basis (Eugene L. Wachpress)," ed: Society for Industrial and Applied Mathematics, 1978.

[7] U. Pinkall and K. Polthier, "Computing Discrete Minimal Surfaces and Their Conjugates," *Experimental mathematics,* vol. 2, no. 1, pp. 15-36, 1993.

[8] M. Meyer, A. Barr, H. Lee, and M. Desbrun, "Generalized Barycentric Coordinates on Irregular Polygons," *Journal of Graphics Tools*, vol. 7, no. 1, pp. 13-22, 2002/01/01 2002, doi: 10.1080/10867651.2002.10487551.

[9] M. S. Floater, "Generalized Barycentric Coordinates and Applications," *Acta Numerica,* vol. 24, pp. 161-214, 2015, doi: 10.1017/S0962492914000129.

[10] J. Warren, "Barycentric Coordinates for Convex Polytopes," *Advances in Computational Mathematics,* vol. 6, no. 1, pp. 97-108, 1996.

[11] M. S. Floater, K. Hormann, and G. Kós, "A General Construction of Barycentric Coordinates Over Convex Polygons," *Advances in Computational Mathematics,* vol. 24, no. 1, pp. 311-331, 2006/01/01 2006, doi: 10.1007/s10444-004-7611-6.

[12] Y. Wang and J. Solomon, "Chapter 2 - Intrinsic and extrinsic operators for shape analysis," in *Handbook of Numerical Analysis*, vol. 20, R. Kimmel and X.-C. Tai Eds.: Elsevier, 2019, pp. 41-115.

[13] Y. Lipman, D. Levin, and D. Cohen-Or, "Green Coordinates," *ACM Trans. Graph.*, vol. 27, no. 3, pp. 1-10, 2008, doi: 10.1145/1360612.1360677.

[14] M. S. Floater, "Mean Value Coordinates," *Computer Aided Geometric Design*, vol. 20, no. 1, pp. 19-27, 2003/03/01/ 2003, doi: https://doi.org/10.1016/S0167-8396(03)00002-5.

[15] T. Ju, S. Schaefer, and J. Warren, "Mean Value Coordinates for Closed Triangular Meshes," *ACM Trans. Graph.*, vol. 24, no. 3, pp. 561–566, 2005, doi: 10.1145/1073204.1073229.

[16] Y. Lipman and D. Levin, "Derivation and Analysis of Green Coordinates," *Computational Methods and Function Theory*, journal article vol. 10, no. 1, pp. 167-188, June 01 2010, doi: 10.1007/bf03321761.

[17] P. Joshi, M. Meyer, T. DeRose, B. Green, and T. Sanocki, "Harmonic Coordinates for Character Articulation," *ACM Trans. Graph.*, vol. 26, no. 3, pp. 71–es, 2007, doi: 10.1145/1276377.1276466.

[18] T. W. Sederberg and S. R. Parry, "Free-form Deformation of Solid geometric Models," in *Proceedings of the 13th annual conference on Computer graphics and interactive techniques*, 1986, pp. 151-160.

[19] S. Coquillart, "Extended Free-form Deformation: A Sculpturing Tool for 3D Geometric Modeling," *SIGGRAPH Comput. Graph.*, vol. 24, no. 4, pp. 187–196, 1990, doi: 10.1145/97880.97900.

[20] R. MacCracken and K. I. Joy, "Free-form Deformations with Lattices of Arbitrary Topology," presented at the Proceedings of the 23rd annual conference on Computer graphics and interactive techniques, 1996. [Online]. Available: https://doi.org/10.1145/237170.237247.

[21] K. G. Kobayashi and K. Ootsubo, "t-FFD: free-form deformation by using triangular mesh," presented at the Proceedings of the eighth ACM symposium on Solid modeling and applications, Seattle, Washington, USA, 2003. [Online]. Available: https://doi.org/10.1145/781606.781641.

[22] M. S. Floater, G. Kós, and M. Reimers, "Mean Value Coordinates in 3D," *Computer Aided Geometric Design*, vol. 22, no. 7, pp. 623-631, 2005/10/01/ 2005, doi: https://doi.org/10.1016/j.cagd.2005.06.004.

[23] T. Langer, A. Belyaev, and H.-P. Seidel, "Spherical Barycentric Coordinates," presented at the Proceedings of the fourth Eurographics symposium on Geometry processing, Cagliari, Sardinia, Italy, 2006.

[24] K. Hormann and M. S. Floater, "Mean Value Coordinates for Arbitrary Planar Polygons," *ACM Trans. Graph.*, vol. 25, no. 4, pp. 1424–1441, 2006, doi: 10.1145/1183287.1183295.

[25] O. Sorkine, D. Cohen-Or, Y. Lipman, M. Alexa, C. Rössl, and H.-P. Seidel, "Laplacian Surface Editing," presented at the Proceedings of the 2004 Eurographics/ACM SIGGRAPH symposium on Geometry processing, Nice, France, 2004. [Online]. Available: https://doi.org/10.1145/1057432.1057456.

[26] Y. Yu *et al.*, "Mesh Editing with Poisson-based Gradient Field Manipulation," *ACM Trans. Graph.*, vol. 23, no. 3, pp. 644–651, 2004, doi: 10.1145/1015706.1015774.

[27] K. Zhou *et al.*, "Large Mesh Deformation Using the Volumetric Graph Laplacian," *ACM Trans. Graph.*, vol. 24, no. 3, pp. 496–503, 2005, doi: 10.1145/1073204.1073219.

[28] J. Huang *et al.*, "Subspace Gradient Domain Mesh Deformation," in *ACM SIGGRAPH 2006 Papers*, 2006, pp. 1126-1134.

[29] M. Botsch, M. Pauly, M. Gross, and L. Kobbelt, "PriMo: Coupled Prisms for Intuitive Surface Modeling," presented at the Proceedings of the fourth Eurographics symposium on Geometry processing, Cagliari, Sardinia, Italy, 2006.

[30] X. Shi, K. Zhou, Y. Tong, M. Desbrun, H. Bao, and B. Guo, "Mesh Puppetry: Cascading Optimization of Mesh Deformation with Inverse Kinematics," *ACM Trans. Graph.*, vol. 26, no. 3, pp. 81–es, 2007, doi: 10.1145/1276377.1276479.

[31] O. Sorkine and M. Alexa, "As-Rigid-As-Possible Surface Modeling," presented at the Proceedings of the fifth Eurographics symposium on Geometry processing, Barcelona, Spain, 2007.

[32] T. Jiang, K. Qian, S. Liu, J. Wang, X. Yang, and J. Zhang, "Consistent As-Similar-As-Possible Non-isometric Surface Registration," *The Visual Computer*, vol. 33, no. 6, pp. 891-901, 2017/06/01 2017, doi: 10.1007/s00371-017-1390-9.

[33] L. Gao, Y. K. Lai, J. Yang, L. X. Zhang, S. Xia, and L. Kobbelt, "Sparse Data Driven Mesh Deformation," *IEEE Trans Vis Comput Graph*, vol. 27, no. 3, pp. 2085-2100, Mar 2021, doi: 10.1109/TVCG.2019.2941200.

[34] Z. Nehari, *Conformal Mapping*. New York London: McGraw Hill, 1952.

Chapter 5 Systematic Generation of Arbitrary Antenna Geometries

This Chapter applies the GC method to antenna deformation to investigate the impact of the GC parameters on antenna distortions, and introduces a simple GC compensation methods. The effectiveness of these are assessed by comparing the EM performance of compensated-GC antennas with the special case of cylindrical bending whose geometries are in closed form. Finally, the Chapter demonstrates the performance of antennas bent over double curved surfaces compared to the flat case, which are new results beyond the possibility of using Constructive Solid Geometry (CSG), to straightforwardly generate the geometries.

5.1 GC Method for Generating Cylindrically Bent Antennas

In this section, the Green Coordinates method is applied to generate antenna deformation where a simple cage of a polyhedral shape encloses the object of interest [1, 2]. In the case of a flat microstrip antenna, the undeformed cage is a segmented cuboid and the antenna is positioned in the middle of it surrounded by a padding of length Δ, as shown in Figure 5.1a). Here, the same padding is used in all directions. By definition the flat cage (See Figure 5.1c)) with respect to only edges of geometry) is chosen to be a simple shape capturing only the global spatial characteristics of the enclosed object so that it is easy for a user to manipulate its overall shape by relocating (dragging and dropping) a few of its defining vertices to yield a *deformed cage*, (Figure 5.1b)). Figure 5.1d) shows the deformed antenna inside the warped cage. This is to be compared with attempting to

manually deform the antenna, vertex by vertex, in a topologically consistent and physically realistic manner, which is clearly untenable in case of general deformation. Finally, the warped cage is removed to reveal the deformed antenna (See Figure 5.1e-f)).

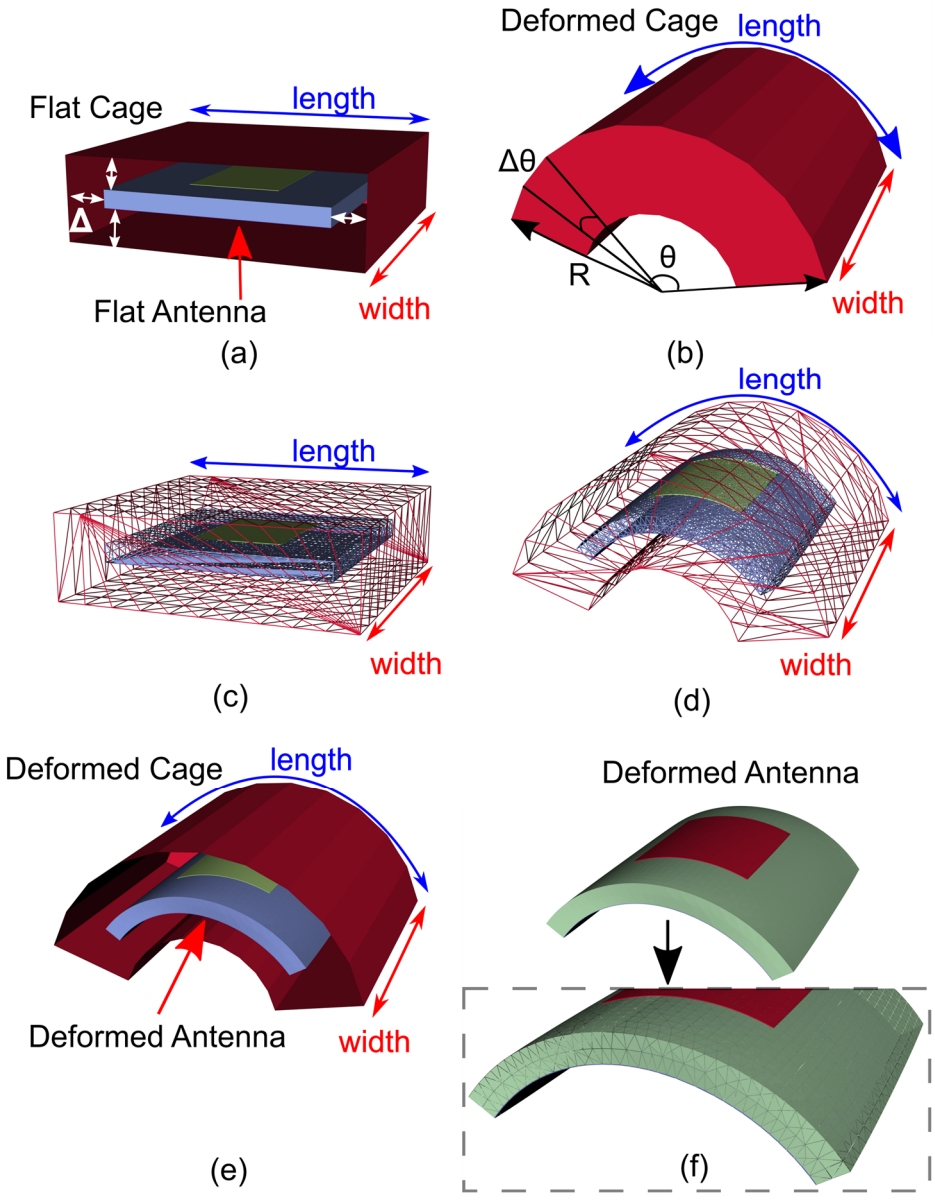


Figure 5.1 a) Microstrip antenna placed inside the flat cage separated by a padding Δ from the edges of the cage; b) deformed cage for the case of cylindrical bending; c) same as a) but showing vertices and faces; d) same as b) but showing vertices and faces; e) deformations of the warped cage are transferred onto the antenna and f) deformed cage is removed to reveal the final result of deformed antenna and, in the inset, its surface triangulation.

The GC methodology is implemented in our in-house Geometry Kernel (GK) [3] which also contains an extension to the published GC approach in order to avoid self-intersection of the deformed object. As the GC method does not embody an affine transformation, deforming long straight edges defined by a pair of end points, for example the sides of the patch, cannot be achieved by simply deforming the end vertices. An iterative splitting of such edges is required which terminates when the deformed midpoint of the edge coincides, within a given tolerance, with the linear interpolation of the deformed end points (See Figure 5.2a,b)). For reference, we will refer to this tolerance as the *edge split tolerance* and all the results presented below used a value of 0.01 mm.



(a) (b)

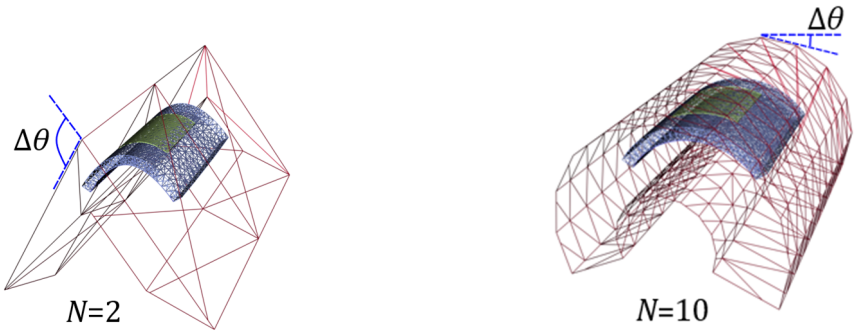
Figure 5.2 Midpoint morphing; tolerance for convergence (a) flat polyhedral cage (b) deformed polyhedral cage.

5.2 Assessment of GC Induced Distortions for the Case of Cylindrically Bent Antenna

In this section the distortions introduced by the GC method are quantified. The degrees of freedom examined are first the complexity of the cage used. The degree of freedom is quantified by the number of piece-wise segments used to describe the undeformed cuboidal cage, each of which deforms to one of the piecewise sectors of angle Δ_θ seen in the deformed cage of Figure 5.1b) and more dramatically in Figure 5.3a,b). The second degree of freedom is the extent of the padding, Δ, shown in Figure 5.1a).

The figure of merit used to assess the undesirable distortion of the geometry is chosen to be consistent with one of the simple parameters used to design standard patch antennas, i.e., the radiating surface area. In fact, both the total (top + bottom + sides) surface area of the radiating patch and the total surface area of the substrate are observed.

Noting that the intention is to deform a flat antenna of prescribed patch area into curved antenna with the same patch area (which is only exactly possible for developable surfaces). The relative distortion surface error, ρ, is thus defined as $\rho = (A_{GC} - A_{Flat})/A_{Flat}$, where A indicates the surface area of either the metallic patch or the substrate.



(a) (b)

Figure 5.3 The antenna geometry generated with $N = 2$, $N = 10$ segments in the cage definition.

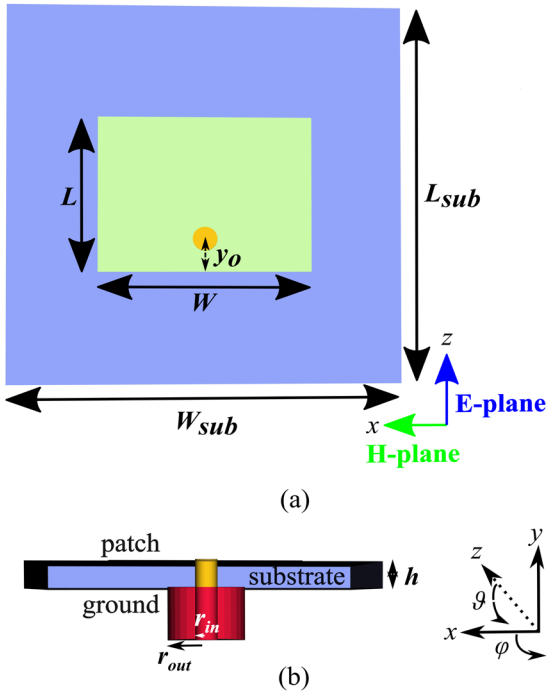


Figure 5.4 The schematic of the flat patch antenna a) top view and b) side view. The angles ϑ and φ define E and H plane of the antenna radiation pattern, respectively.

The microstrip patch antenna used for this study is designed to resonate at 10.4 GHz and has patch width, W, of 10.830 mm and length, L, of 8.177 mm as shown in Figure 5.4a,b). The substrate is Rogers Corporation Duroid 5880 of relative permittivity 2.2, width, W_{sub} and length, L_{sub}, of 20 mm and thickness, h, 1.575 mm. The antenna is fed from below by a coaxial cable positioned at (W/2, y_o) where y_o = 1.75 mm. The coaxial cable has inner radius, r_{in}, of 0.625 mm, outer radius, r_{out}, of 2.16 mm, and the relative permittivity of the sheath is 2.2. The metallic patch and the ground plane of the antenna both have a thickness of 0.035 mm and are treated as perfect conductors. The radius of curvature in the results below is defined to the top plane of the patch.

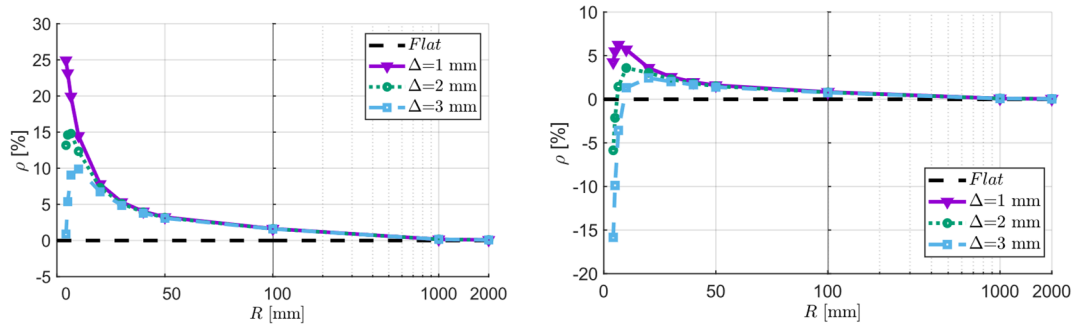
There are two potential causes of undesirable distortion: poor choice of method parameters and any systematic spatial stretching introduced by the GC method. This section seeks to identify the latter by converging to eliminate the former.

The relevant GC method parameters are the padding, Δ, and the number of piece-wise segments, N, that are used to describe the cross section of the cage as illustrated for N=2 and N=10 in Figure 5.3. An understanding of the likely impact of these parameters may be gauged from the description of the space within the cage by the GC method in terms of solutions to Laplace's equation and that these solutions exhibit the usual smoothing behaviour with distance from sharp features such as corners. Therefore, although the cage is actually polygonal, at sufficient distance from its boundaries, the Laplacian solutions will be more dominated by the large-scale arc geometry that the cage approximates, rather than the exact detail of its piecewise linear nature. This behaviour is clear in Figure 5.3 for the case of N=2. It is also noted that both using more segments in the cage, N, to approximate a fixed length antenna of given bending radius or increasing the bending radius for fixed N reduces the angular steps in the cage's boundary, $\Delta\theta$ in Figure 5.3, that further smoothens the deformed space around the antenna.

It is tempting to conclude that one should use a large value of padding as this has no impact on the computational effort of the approach and ought to reduce the error. However, in the more general case, this would also mean loss of control of the detail of the antenna's deformation, so in fact there is a conflicting driver to minimise the

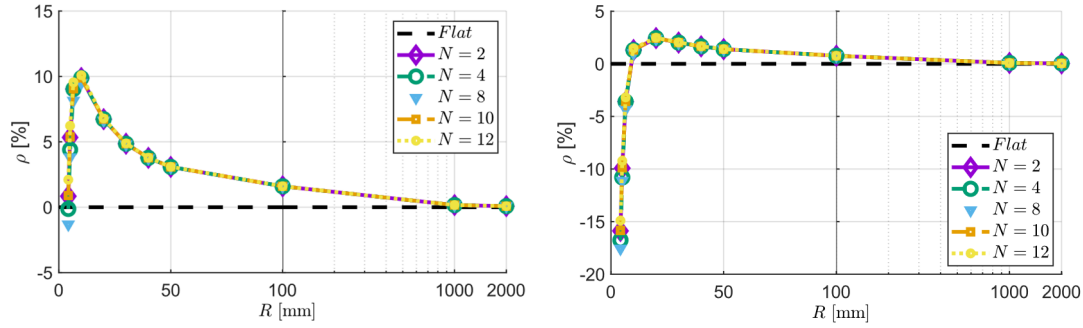
padding. Similarly, although using a larger value for N would appear advisable, this does linearly impact on the computational cost.

Figure 5.5a,b) show the impact of the padding, Δ, on the relative surface distortion error, ρ, for both the metal patch and the substrate of the antenna, as the radius of curvature is varied with N=10 piece-wise segments used to describe the cross section of the cage. Similarly, Figure 5.6a,b) show relative deformation error for fix the padding to Δ=3 mm and varied number of presence of segments, N, between 2 and 12.



(a) (b)

Figure 5.5 Relative surface distortions error of (a) metal patch and (b) substrate as a function of bending radius R and the padding Δ.



(a) (b)

Figure 5.6 Relative surface distortion error of (a) metal patch and (b) substrate as a function of bending radius R and the number of cage segments N.

Together, these figures reveal that for bending radii above 50 mm the choice of Δ and N have negligible impact, but there remains a systematic error introduced by the GC method. For smaller radii, the errors do increase reaching a peak in some cases before

rapidly increasing again with the opposite sign, i.e. the areas shrink rather than expand. In this regime, the choice of a larger Δ is appropriate, however there remains a remarkable insensitivity to the choice of N.

Overall it is noted that, given an antenna length of 20 mm, bending radii below 50 mm, are certainly severe deformations in shape, the *systematic* errors of Figure 5.5 and Figure 5.6 for all radii are deemed to be unacceptably large.

In fact, this is partially a positive result as the intention is to keep the cage as simple as possible. The explanation of the systematic error is actually found in a subtlety of the GC algorithm which is used to ensure that in the 3D case least deforming and quasi-conformal spatial deformations are produced [1, 2] compared to other space manipulation techniques. A local stretch factor appears in the 3D algorithm which although generally successful in preserving shape, does not decouple to the known 2D stretch factor and an axial stretch factor if the geometry happens to be separable as is the case for a cylinder.

Therefore, it has been shown that GC method can simply produce bent antennas, but that a spatially varying stretch factor in its algorithm introduces an error that must be managed. In the context of textile antennas, the next section describes how this systemic error can be successfully compensated for *on average*.

5.3 Methods for Compensating GC Induced Deformations

The results presented in the previous section confirm that the GC method introduces unwanted deformations in the surface area of the patch antenna and the issue is now how to minimise them. From an engineering viewpoint, the resonant frequency and radiation pattern are key performance metrics of an antenna, and these are, for the above case of patch antenna, predominantly determined by the size of the radiating patch. Since the GC method preserves the overall shape, pre-scaling of the patch should be sufficient to compensate for introduced deformations. In this section two methods of pre-scaling are proposed: a) method based on minimizing the standard deviation of centres of gravity of triangular faces that define the surface of the radiation patch, to

which we refer as *Centre of Gravity (CG) compensation method*, and b) method that preserve both the width and length of the radiating patch, to which we refer as *Width and Length (WL) compensation method*. This section describes these compensation approaches and evaluate their effectiveness in terms of relative surface deformation area of the radiating patch.

5.3.1 Centre of Gravity Compensation Method

The patch surface (*F*) is described by a tessellation of *K* triangles. For each triangle, the centre of gravity (COG), or triangle centroid, can be defined ($\boldsymbol{v_k^{COG}}$). The COG of a triangle is defined as an intersection of triangle medians and will always be inside the triangle. We define the mean COG for the surface as $\boldsymbol{\mu^{COG}}$and the COG standard deviation, $\boldsymbol{\sigma'}$, for all triangles forming the surface of the radiating patch as

$$\boldsymbol{\sigma'} = \sqrt{\frac{\sum_{k=1}^{K} \left\| \boldsymbol{v_k^{COG}} - \boldsymbol{\mu^{COG}} \right\|^2}{K-1}} \longrightarrow [\sigma_W, \sigma_L].$$

The standard deviation is calculated for each coordinate direction so that it is possible to extract the deviation along the width and length of antenna i.e., σ_W and σ_L. Standard deviation along the width and length is calculated for both the flat and warped radiating patch and to avoid confusion, the standard deviations of the warped surface are given the symbols $[\sigma'_W, \sigma'_L]$.

The stretch factor can now be defined as a ration of standard deviation along the width and the length of the patch of the warped and flat patch surfaces as:

$$[S_W, S_L] = \left[\frac{\sigma'_W}{\sigma_W}, \frac{\sigma'_L}{\sigma_L}\right].$$

The compensation method is iterative whereby in the first iteration the overall stretch factors produced by GC method for the width and the length of the radiating patch are obtained. The flat antenna is pre-scaled, i.e., rescale in size accordingly so that in the next iteration the stretch factor is reduced. Iterations continue until the difference between the surface area of the warped and flat radiating patch are below given

tolerance. Typically, 3-5 iterations are required.

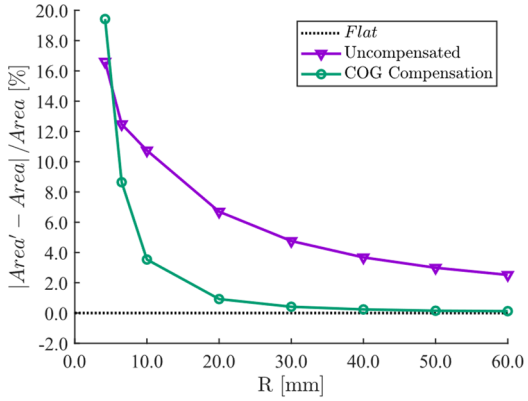
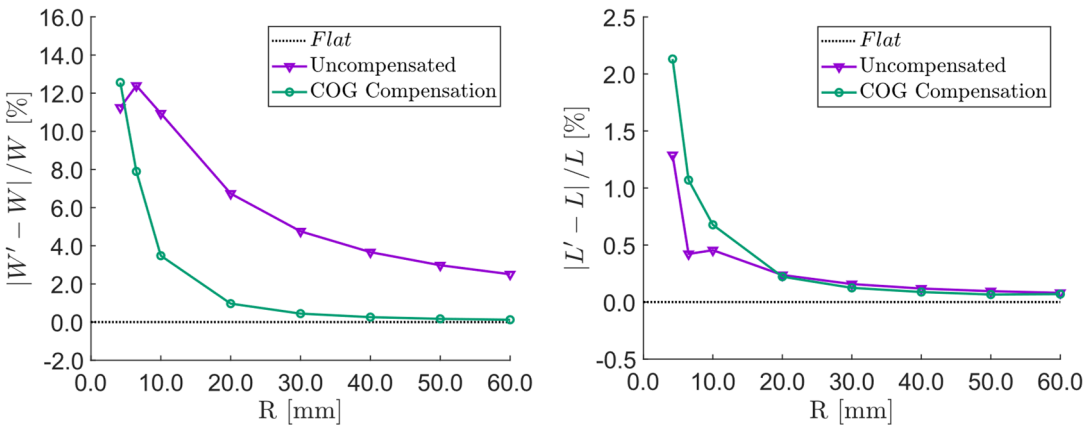


Figure 5.7 Relative error of GC generated area of antenna to that of the flat antenna for uncompensated GC method and GC compensated method using COG.

Figure 5.7 compares the relative surface deformation error of the radiating patch for three cases, namely without any pre-scaling compensations and with COG for a range of bending radii from 4.2 mm to 60 mm. Relative error of 0% is presented as a reference case and denoted with a dotted line. Figure 5.7 shows that uncompensated CG method results in large surface errors. For large bending radii, COG effectively compensate for GC surface deformations. As the radius of curvature is increased, the performance of the COG method progressively gets worse, especially when the radius of curvature is comparable to the size of the patch i.e., 10 mm.

Figure 5.8a,b) show the same information but with respect to the width and length of the radiating patch. Since the bending is occurring along the width of the patch it is expected that the deformations between the morphed antenna and the flat antenna will mainly be along the width of the patch. This is confirmed by Figure 5.8a,b) where relative errors in the patch width and length are compared for uncompensated GC and COG compensated methods. Figure 5.8a,b) show that the relative error in the patch width is much higher than the relative error in the patch length.



(a) (b)

Figure 5.8 Relative error of GC generated a) the width and b) the length of antenna to that of the flat antenna for uncompensated, and COG compensated antennas.

5.3.2 Width and Length Compensating GC Induced Distortions

From an engineering viewpoint, the resonant frequency and radiation pattern are key performance metrics of an antenna and these are, for the above case of patch antenna, predominantly determined by the size of the radiating patch. Since the GC method does preserve the overall shape, pre-scaling of the size of the patch ought to minimise the distortions just observed. This section describes a straightforward pre-scaling method referred to as the *Width and Length (WL) compensation method*.

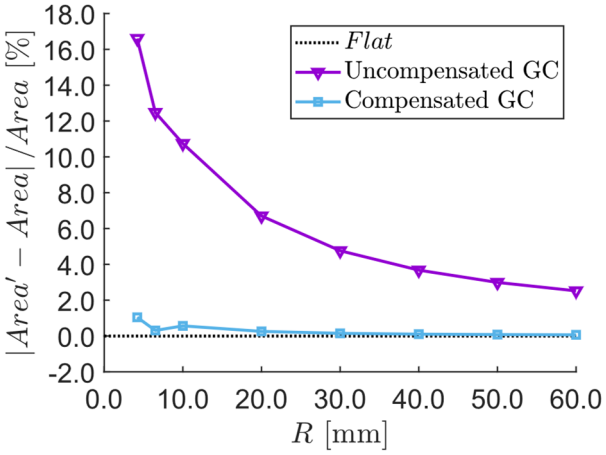


Figure 5.9 Relative surface distortion error of GC generated antenna to that of the flat antenna for uncompensated GC method and compensated GC method.

The compensation method is based on comparing the widths and lengths of the radiating patch before and after deformation. The width and length of the deformed patch are extracted by fitting a (*x*,*y*) order polynomial function of the top of surface, where *x* and *y* indicate the order of the polynomial function used along the width and length of the patch respectively. The actual width and length of the deformed patch are then analytically evaluated by integrating over the polynomial approximation.

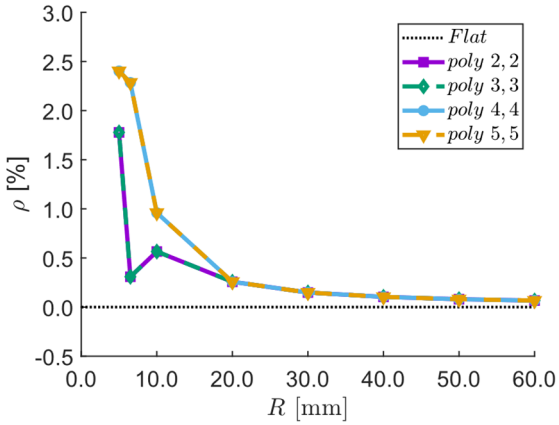


Figure 5.10 Relative area error of WL approach for different degree of polynomials. The notation (***poly x, y***) indicates the order of the polynomial function used along the width and length of the patch, respectively.

Each of the ratios of the width and length of the radiating patch before and after deformation gives a scaling factor e.g. $s_W = {W'}/{W}$ and $s_L = {L'}/{L}$, with which the flat antenna can be scaled before the GC method is applied, i.e. $W \to W'/s_W$ and $L \to L'/s_L$. This process is iterated until a prescribed relative difference in the width and/or length of the patch is satisfied and typically this converges within 3-5 iterations.

Figure 5.9 compares the relative surface distortion error of the radiating patch with and without the pre-scaling compensation for a range of bending radii from 4.2 mm to 60 mm, the padding, Δ = 1 mm and N=10 (i.e. as in Figure 5.3a). It is clear that this relatively simple pre-scaling approach is highly effective at removing the undesirable patch distortion over a wide range of radii.

It is important to adopt a good surface fitting approach for the GC compensation without incurring a notable computational cost. Figure 5.10, confirms that the adequacy of a

(3,3) order polynomial surface approximation. Slight improvement is obtained for higher order models for small radii (noting that symmetry pairs the curves), with virtually no impact on the approximately 3 mins calculation time of the overall deformation calculation.

Figure 5.11 further explores how the area distortions decompose into width and length distortions and confirms that, as the bending is applied along the width of antenna, the largest distortion is occurring along the width of the patch.

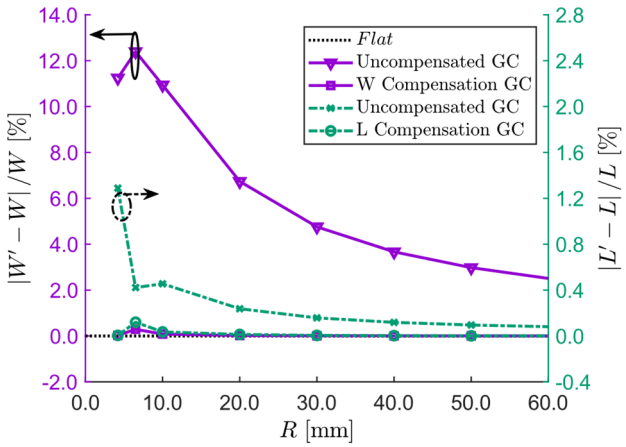


Figure 5.11 Relative distortion error along the width and length of antenna to that of the flat antenna for uncompensated and compensated GC generated antennas.

5.4 EM Performance of Cylindrically Bent Antennas

The previous results demonstrate the success of a simple distortion compensation scheme quantified in terms of a geometrical measure of error. This section now extends this by exploring its effect on the more practically important figures of merit of the antenna's performance. The return loss, S_{11}, and the far field radiation pattern are presented for bending along both the width (H-plane bending), and the length (E-plane bending) of the antenna. Throughout, results are compared to both the *flat* antenna and an *ideal cylindrical* version of the antenna. The geometry of the latter is generated directly in cylindrical coordinates and as such may be regarded as a perfect model without any CAD artefacts for a given sampling resolution and is hence used as the benchmark when comparing against GC generated versions. We show both the results

for the GC geometry antenna with and without the compensation applied. Generally, the success of the compensation scheme can be gauged by how close the *compensated GC* results agree with the *ideal cylindrical* results.

This section investigates how the EM performance of antenna bent over a cylindrical plane and generated using uncompensated and compensated GC methods compares against the reference antenna generated using CSG geometry to which we will refer as an ideal cylindrical deformation. Antenna reflection coefficient, S_{11}, and the far field radiation pattern are considered for antenna bending along the width of antenna (H-plane bending), and along the length of antenna (E-plane bending).

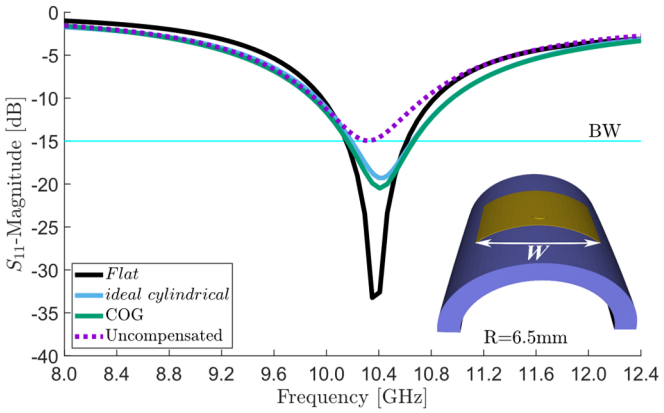
5.4.1 EM Performance of COG Compensation

Firstly, the COG compensation method has been studied with the clearance parameter Δ in the GC method is fixed to 6 mm. The relative error in the surface deformation for COG method is fixed to 0.01%. All antenna geometries are meshed using our in-house Delaunay mesher and antennas are simulated using the TLM method based on the tetrahedral Delaunay mesh [4, 5].

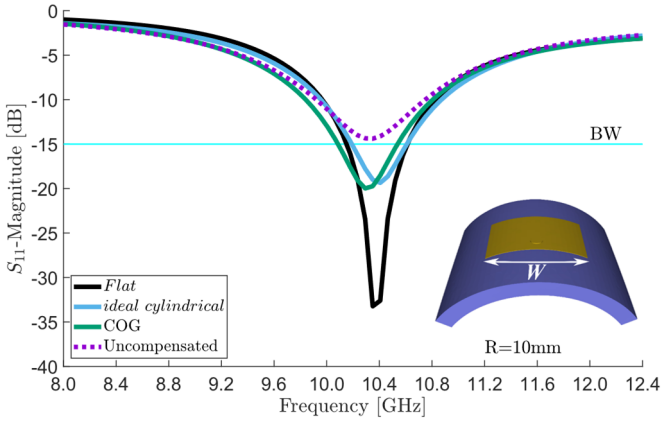
Figure 5.12 compares the S_{11} parameters for antenna bent in the H-plane obtained using a reference CSG antenna and antennas obtained using uncompensated and compensated GC methods. Two cases are considered namely antenna with a bending radius of R=6.5 mm, Figure 5.12a) and R=10mm, Figure 5.12b). The result for the flat antenna geometry is also included to show relative shift of the antenna resonant frequency due to bending. Figure 5.12a,b) show that overall the impact of H-plane bending on the antenna resonant frequency is not significant which is in agreement with other published results [6, 7]. Besides, the compensated GC antenna has similar performance as ideal cylindrical case.

Figure 5.13 compares the S_{11} parameters for antenna bent in the E-plane obtained using an ideal cylindrical antenna and antennas obtained using uncompensated and compensated GC methods. Two cases are considered namely antenna with a bending radius of R = 6.5 mm, Figure 5.13a) and R=10 mm, Figure 5.13b). Comparing the resonant frequency of the flat and ideal cylindrical antenna it can be seen that the shift

of the resonant antenna frequency to higher frequencies is much larger when antenna is bent in the E-plane i.e. along its length, as reported in [6, 7]. In both H- and E-plane bending cases the bandwidth is preserved which is in agreement with other published results for cylindrically bent antennas [6, 7].



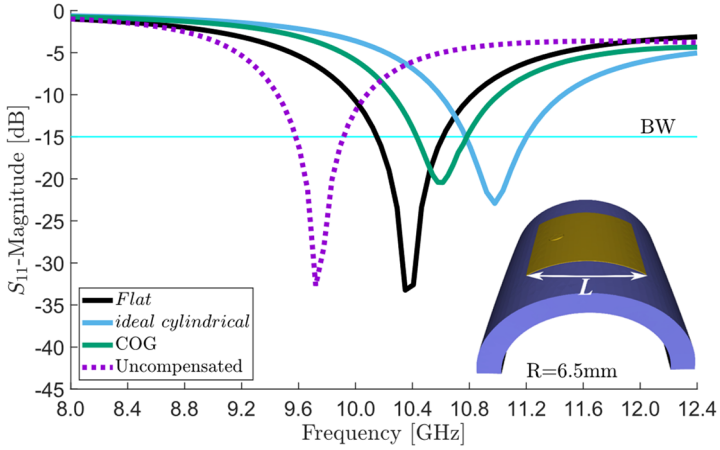
(a)



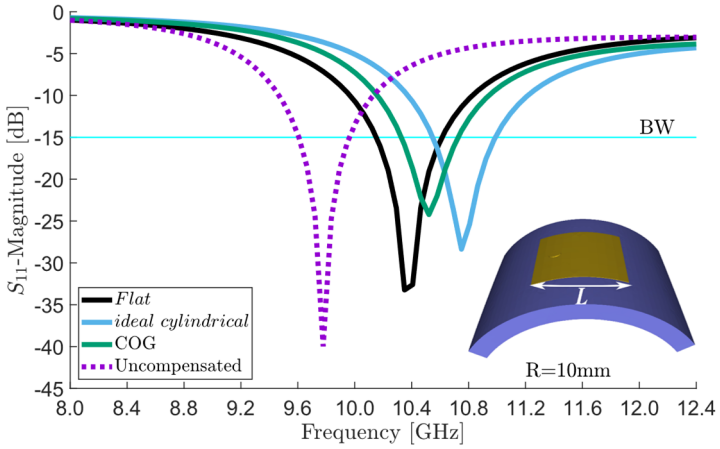
(b)

Figure 5.12 Comparison of S_{11} parameter for the flat antenna and ideal cylindrical, antenna bent in the H-plane using uncompensated and COG compensated method for a) radius R=6.5 mm and b) R=10 mm.

For the case of E-plane bending uncompensated GC method results in an antenna that has resonant frequency much lower than the flat antenna. In contrast, COG compensated antenna are greater than the flat antenna resonant frequency. In fact, in the case of smaller bending radius of 10 mm the relative error in resonant frequency is 2.14% smaller and in the case of smaller bending radius of 6.5 mm, the relative difference in the resonant frequency is 3.39% smaller than the ideal cylindrical case.



(a)



(b)

Figure 5.13 E-plane bending: Comparison of S_{11} parameter of flat, ideal cylindrical, uncompensated and COG compensated method for a) radius R = 6.5 mm and b) R = 10 mm. S11 parameter of the fat antenna is also given for the reference.

Figure 5.14 (a-d) compares the E- and H- far field radiation patterns at 10.5 GHz for antennas bent in the H-plane and generated using uncompensated and compensated GC methods and compares it against the far field of the ideal cylindrical antenna and the flat antenna. Figure 5.14a,b) present the results for the radiation pattern in the E-plane and H-plane respectively for the antenna bent in the H-plane with a 6.5 mm radius of curvature. Figure 5.14c,d) show similar results but for a curvature of 10 mm. Comparing

radiation patterns of GC generated antennas against the one generated using ideal cylindrical geometry it can be seen that in both cases of bending radii the far field radiation pattern is much less sensitive to the errors introduced by the GC method, especially in the direction of the main beam for which all GC generated antenna gives performance that agrees with the ideal cylindrical antenna. Major differences in far field radiation pattern are noticeable in the sidelobes. In general, the differences in the H-plane are lower than the E-plane which can be explained by the fact that changes along the antenna width have much smaller impact on antenna performance.

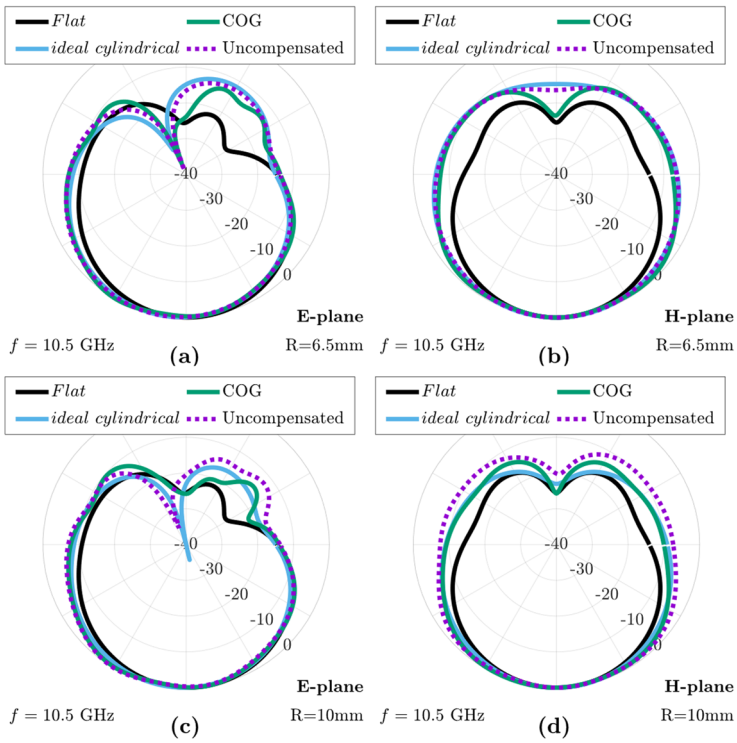


Figure 5.14 Normalised far radiation patterns of antenna bend in the H-plane: (a) E and (b) H-plane far-field for bending radius of 6.5 mm, and (c) E- and (d) H-plane radiation pattern for bending radius of 10 mm. Results are presented for the flat, ideal cylindrical, uncompensated and COG compensated antenna.

Figure 5.15 (a-d) compares E- and H- far-field radiation patterns at 10.5 GHz for antennas bent in the E-plane. Results for the flat antenna, the ideal cylindrical antenna, GC uncompensated and COG compensated antennas are presented. Figure 5.15 (a-d) show good agreement between results in the main beam of radiation with major discrepancies in the sidelobes. These discrepancies are the largest for the antenna

generated using uncompensated GC method and significantly reduce when GC compensation method are applied. Both COG method have good radiation performance, but results obtained from antenna. As the radius of curvature is increased, the performance of the COG method progressively getting worser, especially when the radius of curvature comparable to the size of the patch i.e., 10 mm. The method will be introduced in next section provides better performance and is much more stable over the range of bending radii.

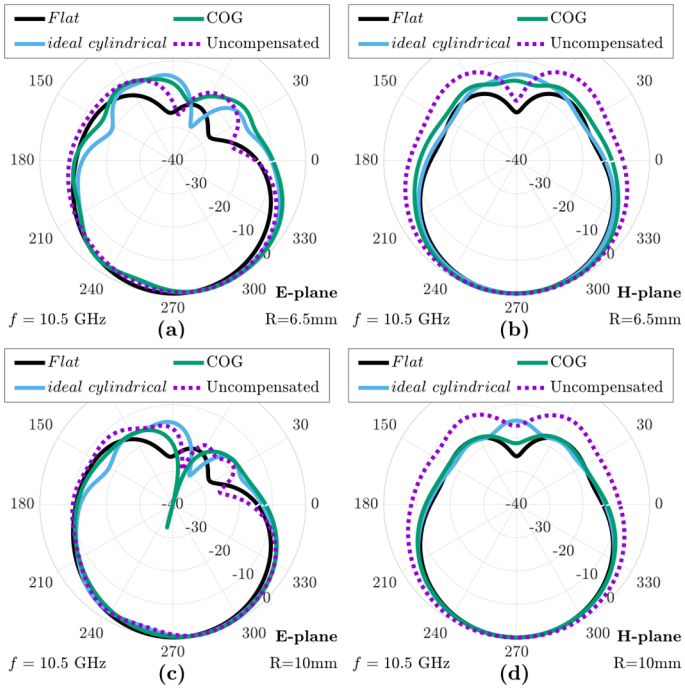


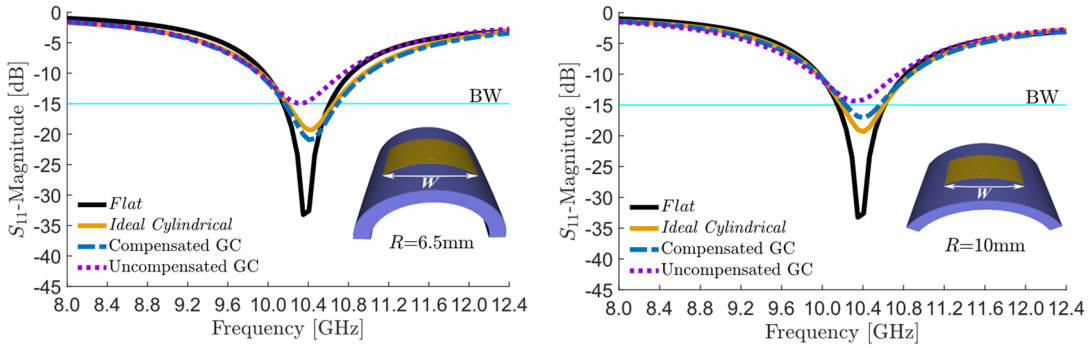
Figure 5.15 Normalised far radiation patterns of antenna bend in the E-plane: (a) E and (b) H-plane far field for bending radius of 6.5 mm, and (c) E- and (d) H-plane radiation pattern for bending radius of 10 mm. Results are presented for the flat, ideal cylindrical, uncompensated and COG compensated antenna.

5.4.2 EM Performance of WL Compensation

The padding value Δ in the GC method is fixed to 6 mm. The WL compensation method uses order (3,3) polynomial surface fitting and iterates until the agreement between the flat and deformed patch width and length agree to a relative tolerance of 0.03%. Fig. 10 compares the return loss, S_{11}, for H-plane bending obtained with the reference antenna geometry and with the uncompensated and compensated GC method along with the flat

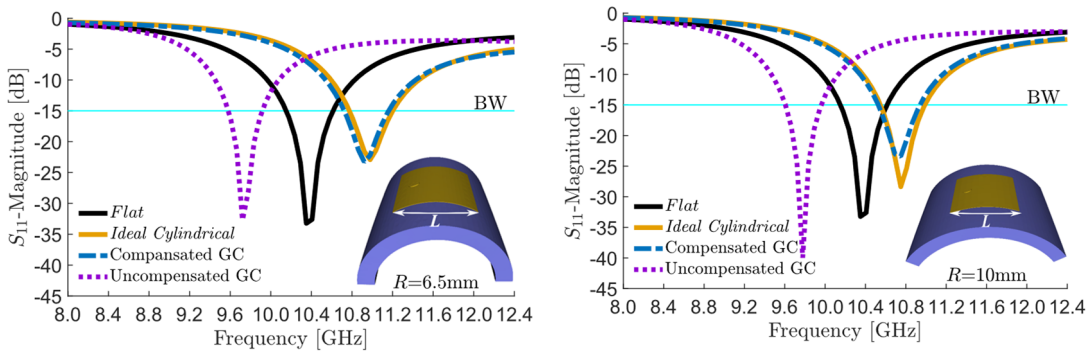
antenna case for comparison. Two bending radii, R=6.5 mm, Figure 5.16a) and R=10 mm, Figure 5.16b) are shown.

First it is seen that the overall impact of H-plane bending on the antenna's resonant frequency is not significant which agrees with published results [6-8]. Second, use of the WL compensated GC geometry predicts a return loss that is in much closer agreement with the reference result than does use of the uncompensated GC geometry.



(a) (b)

Figure 5.16 H-plane Bending: Comparison of S_{11} parameter for the flat antenna and antenna bent in the H-plane using the refence antenna and uncompensated and compensated GC methods for a bending radius of a) R = 6.5 mm and b) R = 10 mm.



(a) (b)

Figure 5.17 E-plane bending: Comparison of S_{11} parameter for the flat antenna and antenna bent in the E-plane using the refence antenna and uncompensated and compensated GC methods for a bending radius of a) R=6.5 mm and b) R=10 mm.

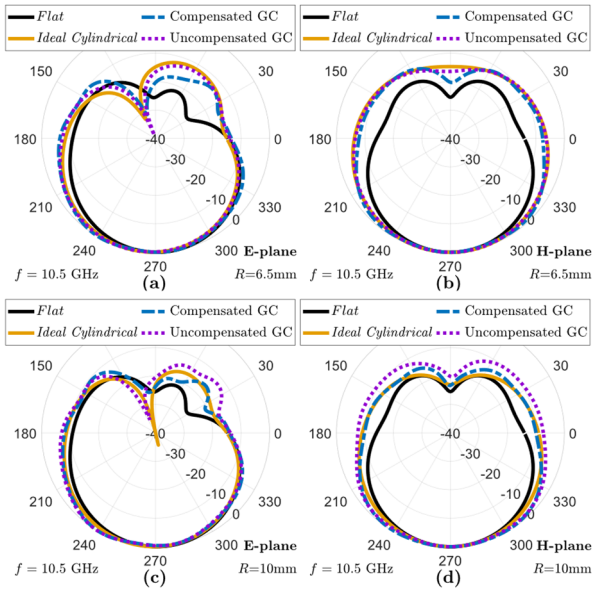


Figure 5.18 Normalised far field radiation patterns of antenna bend in the H-plane: (a) E and (b) H-plane radiation pattern for bending radius of 6.5 mm, and (c) E- and (d) H-plane radiation pattern for bending radius of 10 mm. Results are presented for the flat, ideal cylindrical, uncompensated and compensated GC antennas.

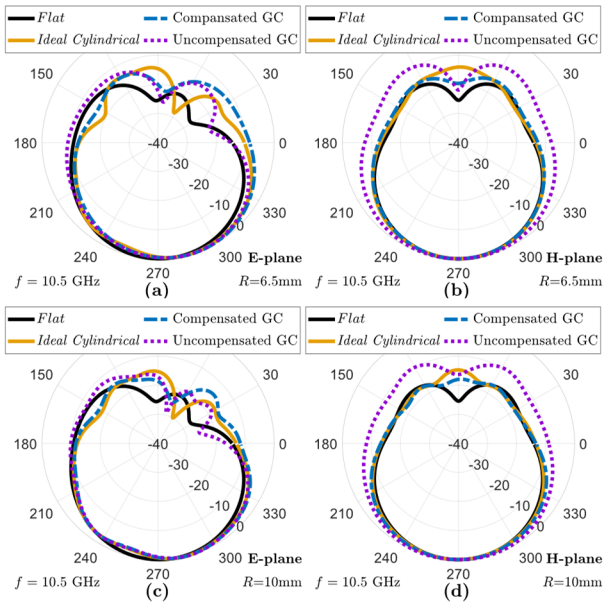


Figure 5.19 Normalised far field radiation patterns of antenna bend in the E-plane: (a) E and (b) H-plane radiation patterns for bending radius of 6.5 mm, and (c) E- and (d) H-plane radiation pattern for bending radius of 10 mm. Results are presented for the flat, ideal cylindrical, uncompensated and compensated GC antennas.

Figure 5.17 repeats analyses the case of E-plane bending. Now the shift of the reference antenna frequency to higher frequencies is more significant compared to the case of H-plane bending as already reported in [6-8]. It is seen that the effect of the uncompensated GC geometry actually leads to a reduction in resonant frequency, i.e., the wrong physical behaviour, but again the compensation method has essentially removed this error, yielding excellent agreement with the reference case results. In fact, with the smaller bending radii the relative error in resonant frequency is 0.552% with no discernible error in bandwidth and with the larger bending radii the relative difference in the resonant frequency is 0.0552% and 2.2% in the bandwidth. Finally, it is noted that in both H- and E-plane bending cases the bandwidth is preserved which is in agreement with other published results for cylindrically bent antennas [6-8].

Figure 5.18 and Figure 5.19 complete this validation assessment by presenting the far field radiation patterns for all cases considered in Figure 5.16 and Figure 5.17. The main beam characteristics of the antenna are not significantly affected by bending in either the E or H-planes, but there are some discrepancies in the minor sidelobes.

5.5 EM Performance of Arbitrary Deformed Antennas

As stated in the introduction, the driver for this work is not to re-investigate the particular case of cylindrical patch antenna deformations, rather to be able to study the impact of more general shape deformations. However, to reiterate, methodically generating robust geometries has been a significant hurdle to achieving this goal and now that the previous section has successfully validated the use of the WL compensated GC method; for this purpose, the remaining space in this Chapter is dedicated to illustrating its use for the greater challenge. Several canonical antenna deformations that cannot be generated using CSG approaches are considered. These cases are illustrated in Figure 5.20 and are labelled as twisted, convex, concave and saddle deformations.

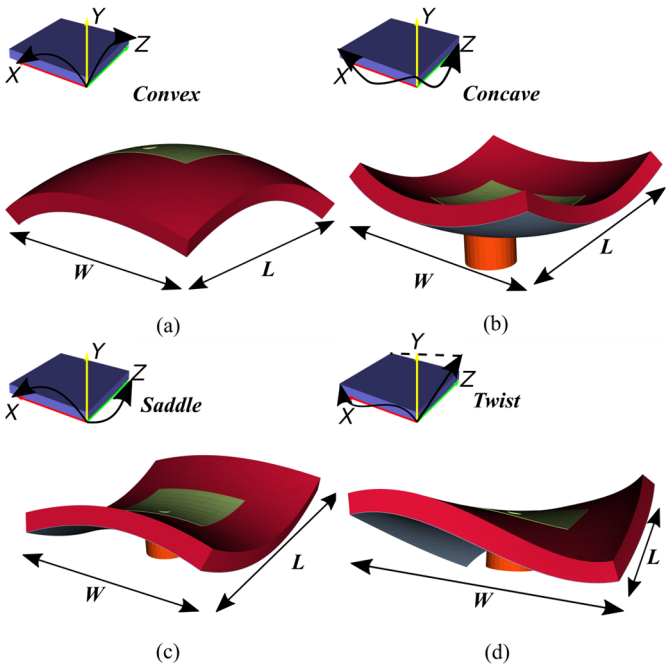


Figure 5.20 Arbitrary antenna deformations showing a) convex, b) concave, c) saddle bending and d) antenna under twisting deformation.

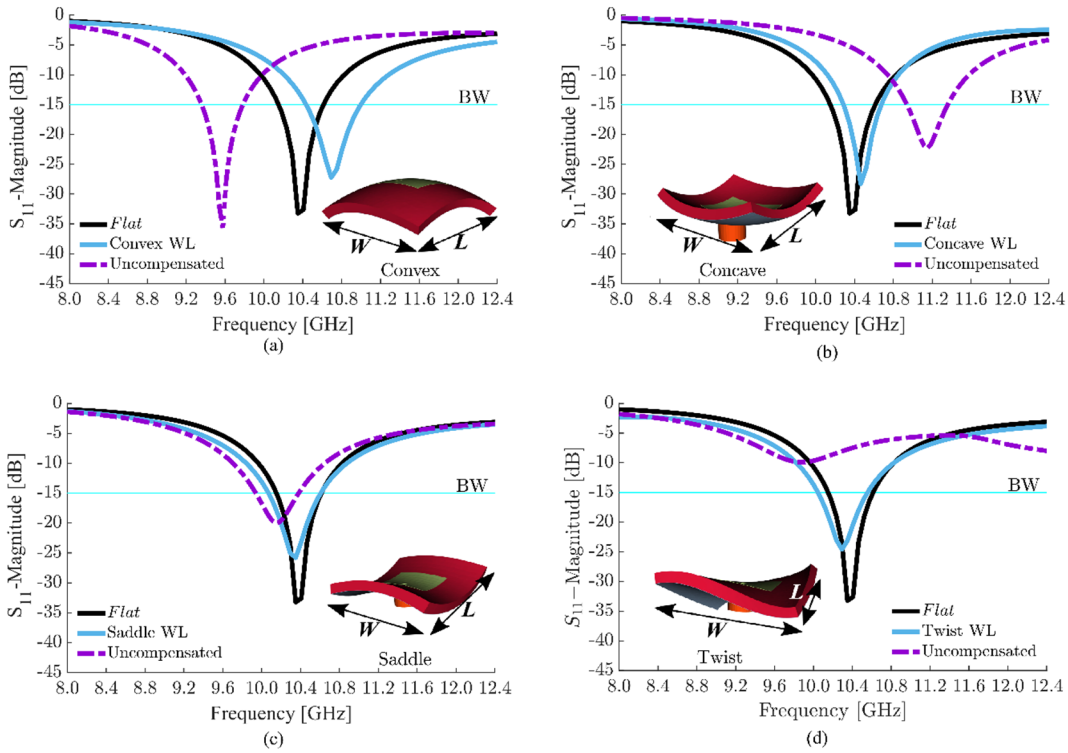


Figure 5.21 Return loss S_{11} of the a) convex, b) concave, c) saddle and d) twisted antennas obtained using uncompensated and compensated GC method in comparison with the flat case.

Results using uncompensated GC geometries will still be shown here to emphasise the importance of compensation of the GC distortion errors when assessing the EM performance of such antennas. For all examples shown, the flat cage is defined using N=10 cage segments along both its width and its length and the padding, Δ, is fixed at 3 mm. The reader is reminded that a key attraction of the GC method is that the desired deformations are then simply produced by relocating a few vertices of the flat cage. Here the convex, concave and saddle examples are all produced using different parts of a double curved polygonal deformed cage that is separable; for all three cases the part - cylindrical cage with bending radius of R = 20 mm and is further deformed by a half a period of sinusoidal variation of amplitude 10 mm along its length. The twisted case is obtained by applying a simple twisting function of 0.01 radians per-meter to the cuboidal undeformed cage along the length of antenna and sinusoidal deformation of amplitude 10 mm along the width of antenna. The resulting antenna geometries are presented in Figure 5.20 and it is noted here that the GC method is not applied to the coaxial feed. The electromagnetic performance, in terms of return loss S_{11} and radiation patterns, of the convex, concave, saddle and twisted antennas generated using the uncompensated and compensated GC method are shown in Figure 5.21 and Figure 5.22. These results are compared with the flat case to show the impact of the deformation. The averaged deformed antenna provides significantly correlated with the flat antenna radiation pattern broadside of antenna. The slight difference of antenna radiation are expectable because of deformed rate of antenna geometries.

In all cases, the uncompensated GC method produces antenna geometries that significantly underestimate, or overestimate resonant frequency compared to the GC compensation method. We note that all deformations are similar in size but different in their nature. Space precludes an exhaustive discussion of these results here, but it is clear that the size of the resonant frequency shifts are similar in all cases. In fact, comparing convex and concave deformations we can conclude that convex deformation is more detrimental to antenna performance as it leads to a larger frequency shift.

It is acknowledged here that the compensation scheme developed above is only addressing the *average* distorting effect of the GC method and naturally more work could be undertaken to further tune it for the arbitrarily deformed antenna case.

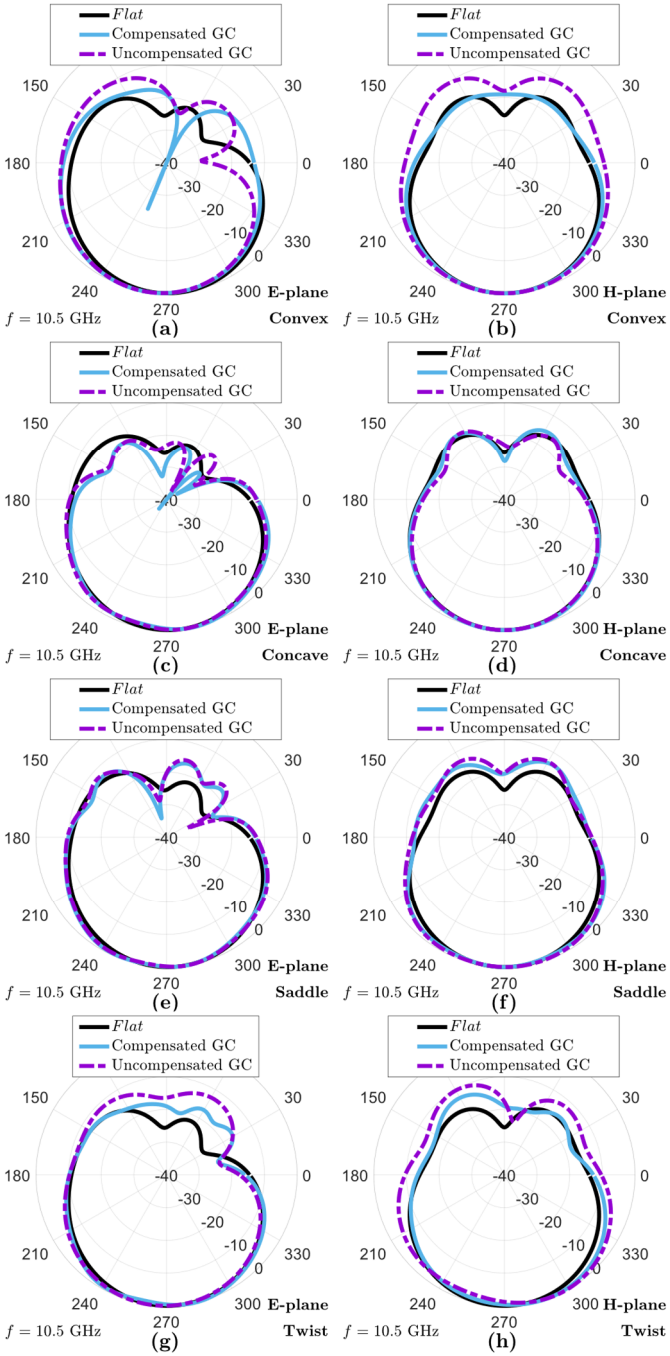


Figure 5.22 Normalised far-field pattern in the E- and H-plane of antenna for: (a-b) convex bending, (c-d) concave bending, (e-f) saddle bending, and (g-h) twisting.

5.6 Conclusions

The GC method provides an approach to holistically deform structures such as patch antennas without introducing the disruptive CAD artefacts that can either block or seriously undermine EM characterisation. The method is ideally adapted to a simple *drag and drop* user interface and yields geometries that provide certain guarantees of physical reality in the deformations, albeit not for all the subtleties of woven materials.

This Chapter has shown that naïve use of the GC method introduces a systematic distortion expressed as an undesirable area scaling. However, this has successfully been compensated for using a straightforward pre-scaling approach, which although not completely general, works well for the widely used class of patch antennas considered here. Furthermore, with the compensation in place a good degree of insensitivity to method parameters such as the padding and complexity of the cage used has been shown which is important for undertaking broad range design studies.

After calibration against a known canonical case whose geometry can be exactly generated, final GC generated antenna performance in terms of return loss and radiation patterns have been examined and shown good agreement with published results. Finally, the scope to address the grander challenge of undertaking a systematic design sweep over the problem space of possible doubly curved deformations has been demonstrated and results from this activity will be further discussed in the next Chapter.

References

[1] Y. Lipman, D. Levin, and D. Cohen-Or, "Green Coordinates," *ACM Trans. Graph.*, vol. 27, no. 3, pp. 1-10, 2008, doi: 10.1145/1360612.1360677.

[2] Y. Lipman and D. Levin, "Derivation and Analysis of Green Coordinates," *Computational Methods and Function Theory*, journal article vol. 10, no. 1, pp. 167-188, June 01 2010, doi: 10.1007/bf03321761.

[3] GGIEMR. "George Green Institute for Electromagnetics Research." https://www.nottingham.ac.uk/research/groups/ggiemr/our-research/large-scale-electromagnetic-modelling/utlm-unstructured-transmission-line-modelling.aspx (accessed 2021).

[4] P. Sewell, T. M. Benson, C. Christopoulos, D. W. P. Thomas, A. Vukovic, and J. G. Wykes, "Transmission-line Modeling (TLM) Based upon Unstructured Tetrahedral Meshes," *IEEE Transactions on Microwave Theory and Techniques*, vol. 53, no. 6, pp. 1919-1928, 2005, doi: 10.1109/TMTT.2005.848078.

[5] S. W. Cheng, T. K. Dey, and J. Shewchuk, *Delaunay Mesh Generation*. CRC Press, 2013.

[6] D. Ferreira, P. Pires, R. Rodrigues, and R. F. S. Caldeirinha, "Wearable Textile Antennas: Examining the Effect of Bending on Their Performance," *IEEE Antennas and Propagation Magazine*, vol. 59, no. 3, pp. 54-59, 2017, doi: 10.1109/map.2017.2686093.

[7] L. Song and Y. Rahmat-Samii, "A Systematic Investigation of Rectangular Patch Antenna Bending Effects for Wearable Applications," *IEEE Transactions on Antennas and Propagation*, vol. 66, no. 5, pp. 2219-2228, 2018, doi: 10.1109/tap.2018.2809469.

[8] F. Boeykens, H. Rogier, and L. Vallozzi, "An Efficient Technique Based on Polynomial Chaos to Model the Uncertainty in the Resonance Frequency of Textile Antennas Due to Bending," *IEEE Transactions on Antennas and Propagation*, vol. 62, no. 3, pp. 1253-1260, 2014, doi: 10.1109/tap.2013.2294021.

Chapter 6 Assessment of Robustness of Flexible Antennas for Complex Deformations

The Chapter focuses on the assessment of the robustness of flexible antennas for complex deformations. The Chapter describes the parameters of a flat patch antenna, parameters of deformed cages, and the effectiveness of compensation of GC (Green Coordinates) induced distortions of the antenna. Then, the Chapter assesses the impact of spherical, saddle, and twisting deformation on antenna performance, namely the S_{11} parameter, fractional bandwidth, and far-field profile.

6.1 Introduction

The next-generation wireless communication systems have increased the demand for flexible and wearable antennas for a variety of applications ranging from sport to biomedical. Considerable research has been focused on developing flexible substrates [1-8], and intrinsically stretchable conductors [9, 10]. It is now well established that the polydimethylsiloxane (PDMS) polymer is one of the most promising substrate materials for wearable electronics due to its high conformability compared to other polymer types, adjustable relative permittivity, acceptable dielectric losses and low-cost (liquid curing) fabrication methods [6, 11, 12]. In addition to PDMS substrates, textile substrates, such as e-textile, woven and knitted textile structures are favourable alternatives [13, 14] but exhibit lower stability in combination with conductive prints and limited design accuracy due to complex geometrical details of conductive threads [13-16].

Integration of antennas into flexible textiles means that the antennas will be affected by the dynamics of human body that can cause bending, twisting, wrinkling, crumpling and stretching of antenna (See Figure 6.1a-c)) [17-21]. These irregular deformations can degrade the system's overall performance and present a challenging design consideration for wearable antennas.

One major issue inhibiting wearable antenna design is that they are usually designed as flat components. The impact of deformations is predominantly assessed experimentally and for a limited number of deformations. To date, the robustness of flexible antennas performance is routinely assessed by assuming that antenna undergoes cylindrical deformation and that is done predominantly experimentally by fixing the antenna to a cylinder of varying radius to account for different bending curvatures [6, 7, 9, 10, 21-25]. This case of bending along only one plane i.e., one-dimensional (1D) cylindrical bending has also been analysed using commercial software such as Ansys and CST [23-27].

Although there are numerous, often conflicting, results on the impact of cylindrical bending on antenna performance, it is now widely accepted that bending antennas along antenna length is more critical for performance as it increases the resonant frequency of antennas [22, 23, 25]. The bending does not significantly affect the bandwidth of antenna or the far field radiation pattern [22, 23, 25]. More recently, the impact of twisting on flexible interconnects [28] and wideband dipole antennas [19] was reported showing small impact on their performance. However, the impact of other types of deformations, in particular more complex two-dimensional (2D) deformations have not been considered. This primarily stems from difficulty in characterising and re-producing irregular deformations both experimentally and computationally. Our recent Chapter 5 highlighted major difficulties in generating arbitrary antenna deformations using commercial electromagnetic CAD tools such as Ansys and CST that are based on Constructive Solid Geometry (CSG) primitives and Boolean geometry. This is due to the difficulty in obtaining well behaved discretised interfaces between the constitutive antenna parts which undermines subsequent numerical simulation [29].

In Chapter 5, we have proposed the use of a computer graphics spatial manipulation technique based on Green Coordinates (GC) for generating arbitrary deformations of antennas [30, 31]. The systematic distortion error in the antenna geometry that is being introduced by the GC method can be compensated by a simple scaling approach. This ensured that the performance of the GC generated cylindrically bent antenna agrees well with the CSG generated antenna opening a way for robust generation of more general antenna deformations [29]. Few representative complex, double curved antenna geometries have been demonstrated in Chapter 5, but a more general analysis on antenna's performance under varying degrees of these complex deformations is needed in order to a) assess the general sensitivity of antenna to a variety of deformations and b) identify deformations that have the most disruptive impact on antenna performance.

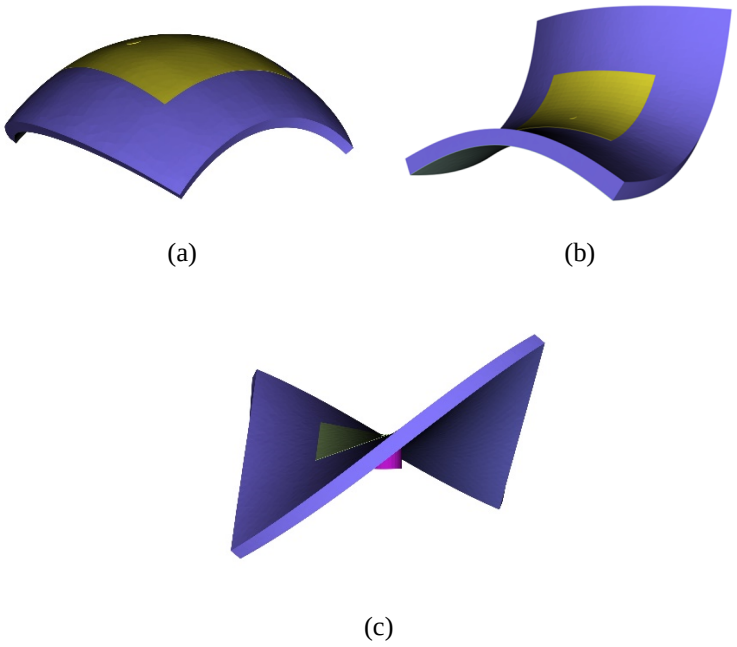


Figure 6.1 Two-dimensional deformations of antenna – example of a) spherical bending, b) saddle and c) twisting deformations.

In that context of the Chapter 6 extends the approach of [29] to consider a more systematic parameter sweep of the problem space for several cases of doubly curved deformations, namely, spherical and saddle bending and twisting deformation. Although these still do span all "irregular" deformations, they are in nature more complex as the curving of the object is in 2D plane and can be considered more general

than simpler case of cylindrical bending. The Chapter explores how these deformations affect the performance of flexible antenna fabricated on the PDMS substrate and operating in the wireless 5.5-6 GHz band. However, in the case of these 2D deformations, such as those shown in Figure 6.1, namely spherical, saddle and twisting deformations of antenna, a certain amount of antenna distortion will be present due to the physical principle of elasticity and these will need to be minimised in the context of the geometry generation.

The Chapter 6 is structured as follows: Section 6.2 briefly overviews the GC method in the context of arbitrary antenna generation, defines the parameters of the warped cages for spherical, saddle and twisting deformations and demonstrates the effectiveness of compensating GC induced distortion of the antenna on these double curved deformations. Section 6.3 assesses the impact of spherical, saddle, and twisting deformation on antenna performance, namely S_{11} parameter, bandwidth and far field profile. Section 6.4 gives the overall conclusions of the Chapter.

6.2 Complex Antenna Deformations

In this section the main principle of the GC method is overviewed and applied to a variety of double-curved antenna deformations. The effectiveness of GC induced distortion compensation on an example of a wearable patch antenna is also discussed. The compensated GC technique has been developed in Chapter 5. This opens a way of generating more complex antenna deformations and these will now be introduced on a typical example of wearable patch antenna fabricated on a flexible PDMS substrate and operating in the wireless 5.5-6GHz band (see Figure 6.2a-d)) . The schematic of the flat patch antenna in shown in Figure 6.3. The substrate's length, L_{sub}, width, W_{sub}, and thickness, h, are 36 mm, 36 mm and 1.5 mm respectively. The metallic patch has the width, W=18mm, and length, L= 14.3 mm. The feeding position is offset by z_o=2.8 mm in z-direction from the middle of the patch. Feeding coaxial cable has inner, r_{in}, and outer radius, r_{out} of 0.625 mm and 2.15 mm respectively. The cable dielectric constant is 2.2. The dielectric constant of the PDMS substrate is 2.7 and its dielectric losses are neglected. The radiating patch and the ground plane are assumed to be perfect metal

with the thickness of 35 μm.

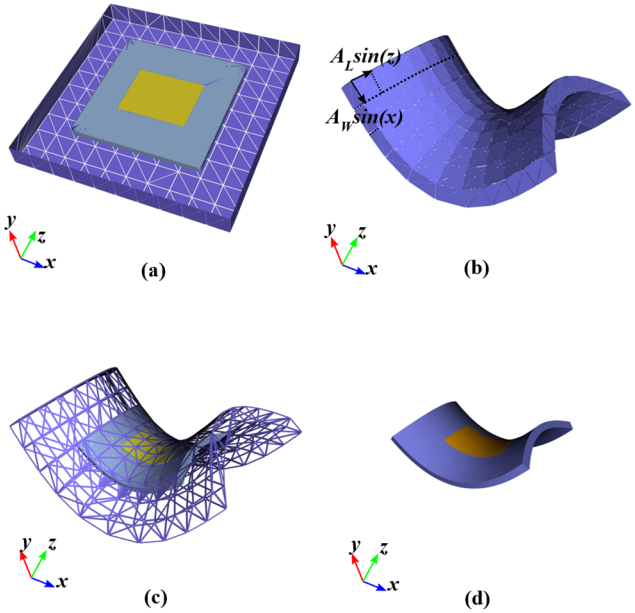


Figure 6.2 GC methodology: a) flat antenna within a flat cage (only faces of the flat cage shown); b) warped cage that describes the nature and level of deformation required; c) deformed interconnect inside the warped cage (only edges of the warped cage shown) d) final geometry of a deformed antenna.

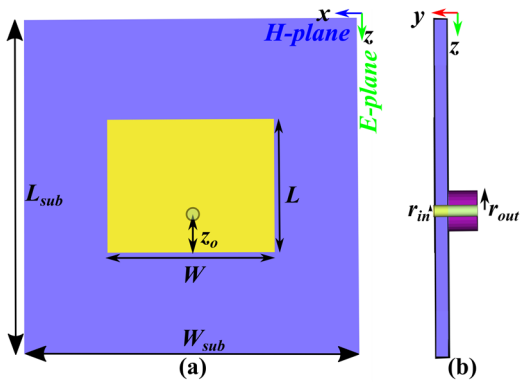


Figure 6.3 Geometry of the flat microstrip patch antenna with a) the top view where x-axis is the E-plane of antenna and z-axis is the H-plane of the antenna and b) the side view where y-axis is the propagation direction of excitation pulse.

Figure 6.4 defines the cages that are considered in this Chapter. In all cases the flat cage width, length and height are 56 mm, 56 mm and 7.5 mm respectively and the antenna is

positioned in the centre of the flat cage. The concave and convex spherical deformation is characterised by a spherical radius, *r*. To generate these spherical deformations a cross-section of a polygonal tube is defined and then curved along the width or the length of the cage (See Figure 6.4a)). By changing the origin of the sphere the concave and convex deformations can be obtained and the radius of the sphere defines the strength of imposed deformation.

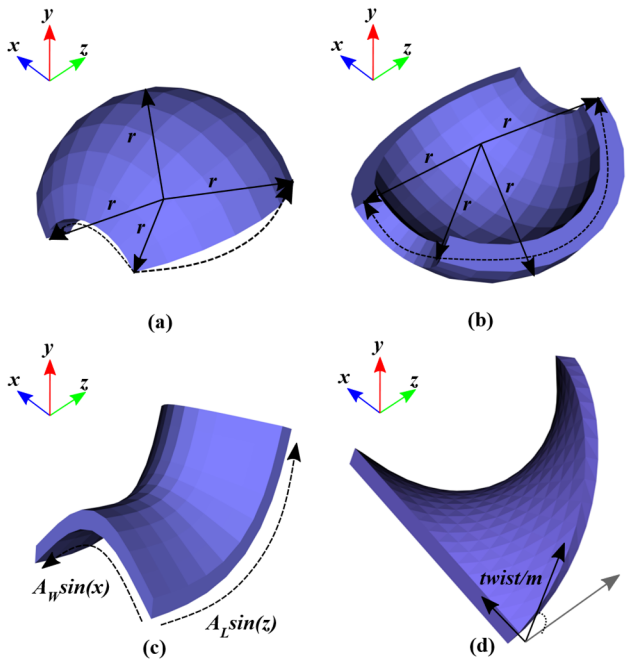


Figure 6.4 Warped cages describe the nature and level of deformation geometry. (a) Concave (b) convex (c) saddle and (d) twisting deformation cages.

Similarly, to generate saddle deformations a cross-section of a polygonal tube is defined across the width (length) of the cage as a sinusoidal parabola and the tube is extruded along the length (width) along a defined parabola. Figure 6.4c) shows an example of saddle cage where the saddle deformation of the cage is controlled by the half period of the sine function $A_W sin(x)$ along the width of antenna and $A_L sin(z)$ along the length of antenna. The strength of the deformation is controlled by the parameter A_W and A_L with the peak value centred at the midpoint along the width and length of the cage respectively. Saddle deformations are obtained when amplitudes A_W and A_L have opposite sign. And finally, the twisting deformation is generated by defining a cross

section of the cage which is then extruded and twisted along the length or width of cage with a defined mean twist per meter parameters, Figure 6.4d).

As GC methods introduces certain amount of anisotropic scaling that results in unphysical distortion of antenna as shown in Chapter 5 [29], it is necessary to compensate or minimise these distortions. Using the approach of Chapter 5, the widths and lengths of the flat and deformed radiating patch are extracted by direct sampling and compared. The ratios of the width and length of the radiating patch before and after the deformation gives a scaling factor, S_W and S_L, for the width and length of the patch respectively, with which the flat antenna is pre-scaled before the GC method is applied as shown in Chapter 5 [29]. This process is iterated until a desired relative difference in the width and/or length of the patch is minimised.

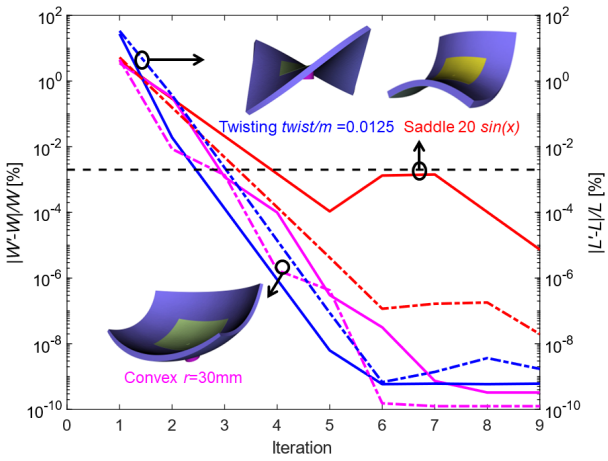


Figure 6.5 Iteration number versus relative error of the GC deformed antenna geometry for convex, saddle and twisting bending for its extreme deformation considered in the Chapter where solid line indicates error of width edge and dashed line indicates length error.

This pre-scaling iterative approach is applied to each of deformations considered in this Chapter namely spherical, twisting and saddle deformations. Figure 6.5 shows the relative error in the width (solid line) and length (dashed line) of the radiating patch for the spherical convex (r = 30 mm), saddle (A=A_W=A_L =20 mm) and twisting (0.0125 twist/m) deformation as a function of number of number of GC iterations. It can be seen that the relative distortion error in the width and length of the patch in the initial GC application is high but that it rapidly reduces with number of pre-scaling iterations. It

can also be seen that the antenna distortion errors for the convex spherical and twisting deformations reduce more rapidly than for the case of saddle deformation.

6.3 Deformed Model of Antenna Geometry and Numerical Simulation

In this section different geometrical models of deformed antennas are imported into the electromagnetic (EM) time-domain numerical code and simulated to analyse the impact of spherical, saddle and twisting deformations on antenna performance. For each case of deformation, a parameter sweep is performed to investigate the impact of the particular nature of the deformation on antenna resonant frequency, reflection coefficient and bandwidth. The generated geometrical models are imported into the EM solver based on Transmission Line Method (TLM) and tetrahedral Delaunay mesh [32, 33]. The tetrahedral TLM method is a well-established extension of the Cartesian mesh TLM method, has been demonstrated to be second-order accurate with respect to wavelength, provides both smooth boundary and graded mesh capabilities, and has been industrially characterised and deployed for a range of applications, including EMC and aerospace [34-36] and readers are specifically referred to [32, 33] for further details.

In all cases the whole problem is meshed with a hybrid mesh that is a combination of a 2.5 mm cubic mesh and a tetrahedral mesh. The antenna near field is meshed more finely with 0.625 mm hybrid mesh as described in [36]. Antenna near field region is captured in a fictitious box of size $0.92\lambda \times 0.92\lambda \times 0.55\lambda$., where λ is the operating wavelength of at 5.5 GHz. An example of the meshed computational problem is given in Figure 6.6 where the inset in the Figure 6.6 gives a closer view of the sampled antenna surface within the box. In all cases the antenna is excited with the fundamental TEM mode of the coaxial feed modulated by a time-domain pulse with 3 dB frequencies of 4.6 and 7 GHz. The fundamental TEM mode is obtained as an eigen solution of the discretised 2D cross section of the coaxial cable [37]. All simulations in this article are run on 8 processor cores of a commodity cluster for 2 million time steps. The threshold for forming cell clusters is 5 μm and the timestep is 0.018 ps [35]. The performance of

the undeformed, flat patch antenna with the resonant frequency of 5.68 GHz, S_{11} at the resonant frequency is -30.6 dB and fractional bandwidth of 3.5% is taken as a reference.

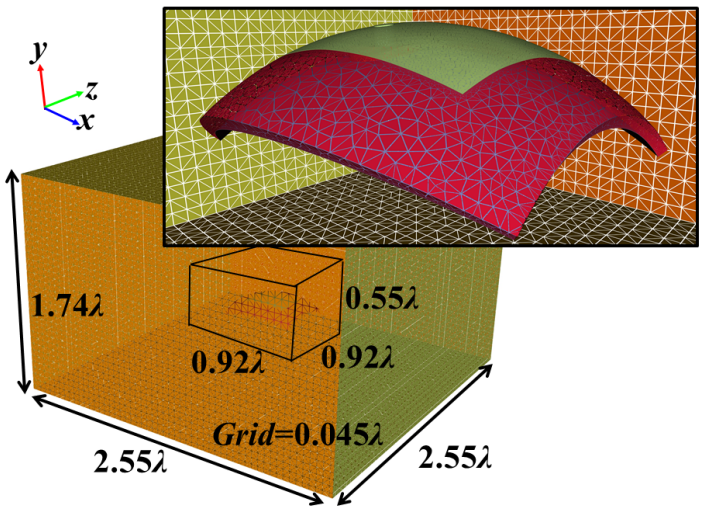


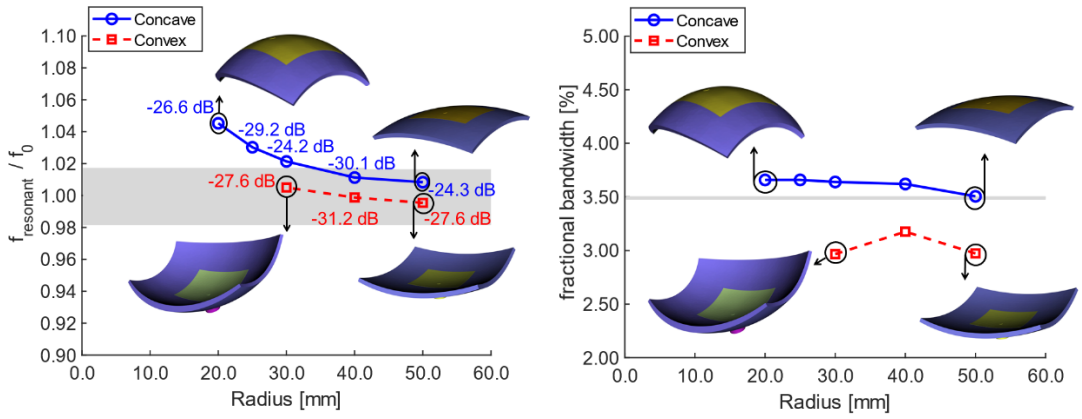
Figure 6.6 Meshed the concave antenna with computational box with inset picture zoomed in concave antenna.

6.3.1 Spherical Concave and Convex Deformations

In this section, the impact of spherical concave and convex deformations on antenna performance is considered. The deformation of the cage is controlled by the radius parameter as shown in Figure 6.4a-b) with the radius varying from 50 mm to 20 mm for the concave case and from 50 mm to 30 mm for the convex case.

Figure 6.7a) shows the impact of the spherical concave and convex deformation on the change of the resonant frequency compared to the resonant frequency of the flat antenna, f_0, and the value of the S_{11} parameter at the resonant frequency. The inset of the figure shows the deformed antenna geometries for selected spherical radii, namely r=50 mm, 30 mm and 20 mm. It can be seen that in the case of both convex and concave bending the resonant frequency increases with increased deformation. The concave deformation can cause up to 5% shift of the antenna resonant frequency whilst the antenna resonant frequency is less sensitive to the convex spherical deformation. In all cases, the S_{11} value at the resonant frequency stays below -25 dB as indicated in Figure

6.7a). Furthermore, the shaded region in Figure 6.7a) shows the 3.5% fractional bandwidth of the flat antenna. It can be seen that for deformations larger than 30mm in the spherical radius, the concave antenna performance moves outside the operating bandwidth of the flat antenna.



(a) (b)

Figure 6.7. (a) Impact of the spherical concave and convex deformation on the resonant frequency change of the deformed antenna compared to that of the flat antenna (f_0) for different spherical radii. Values (dB) indicate the value of S_{11} parameter at the resonant frequency. (b) Impact of the spherical concave and convex deformations on the fractional bandwidth of the deformed antenna.

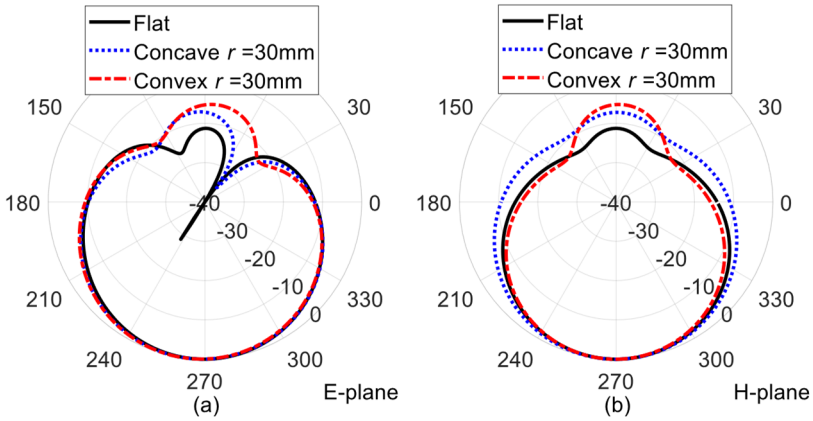


Figure 6.8 Comparison of the far field radiation pattern at 5.6 GHz in a) E-plane and b) H-plane of a flat patch antenna (solid line) with antenna deformed using spherical concave deformation with r = 30 mm, (dotted line) and antenna deformed using spherical convex deformation with r = 30 mm (dashed line).

Figure 6.7b) shows the impact of the concave and convex spherical deformations on the fractional bandwidth of antenna. It can be seen that concave deformation marginally

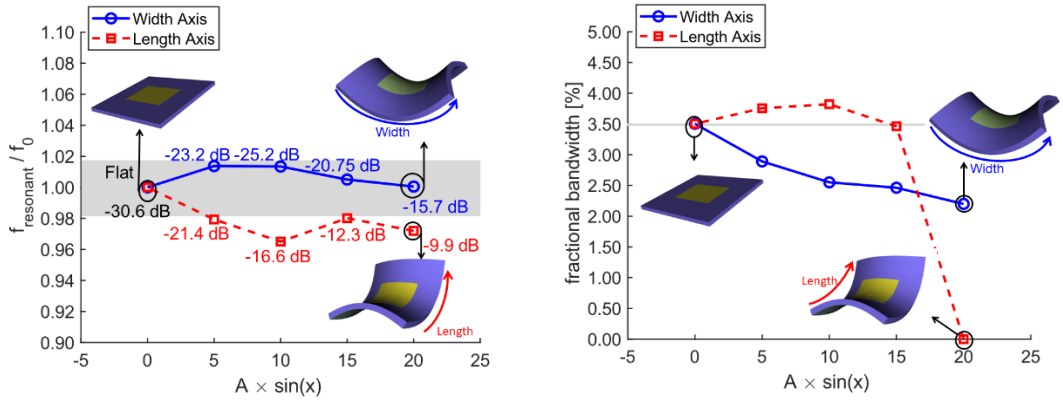
increases the bandwidth of antenna (up to 0.2%) whilst the convex deformation has the opposite effect on antenna bandwidth and results in bandwidth reduction of (up to 0.5%).

Impact of the spherical deformation on the far field radiation pattern is shown in Figure 6.8. Figure 6.8a) compares the E-plane radiation pattern of the flat patch antenna (solid line) with the convex and concave spherically deformed antenna with the radius r=30 mm. Figure 6.8b) shows the same information but for the H-plane radiation pattern. It can be seen that convex and concave deformations do not significantly affect the main beam in the E-plane, with the main change being in the increased sidelobes. However, the concave deformation increases both the main beam and the sidelobe in the H-plane whilst the convex spherical deformation slightly reduces the width of the main beam and increases the width and strength of the sidelobe.

6.3.2 Saddle Deformations

In this section the impact of the 2D saddle deformations on antenna performance is considered. The cage for the saddle deformation is constructed as in Figure 6.4c) and the strength of the deformation is controlled by the parameter $A_W=A_L=A$ that is varied from 0 mm (flat case) to 20 mm. Two cases are considered, namely when convex bending is along the width of antenna (concave bending is along the length of antenna) and vice versa, when convex bending is along the length of antenna (concave bending is along the width of antenna).

The impact of saddle deformations on the change of resonant frequency compared to the resonant frequency of the flat case and the values of S_{11} parameter at the resonant frequency is shown in Figure 6.9a). It can be seen that convex bending along the width increases the antenna resonant frequency by up to 2%, whilst the convex bending along the length of antenna causes reduction in the antenna resonant frequency by up to 4%. This implies that convex nature of the deformation along the length of antenna is more critical for antenna resonant frequency.



(a) (b)

Figure 6.9 (a) Impact of saddle deformations (convex bending along the width and length of antenna) on the resonant frequency change of deformed antenna compared to the resonant frequency of the flat antenna, f_0, Values (dB) indicate the value of S_{11} parameter at the resonant frequency. (b) Impact of the saddle deformations (convex bending along the width and length of antenna) on the fractional bandwidth of antenna.

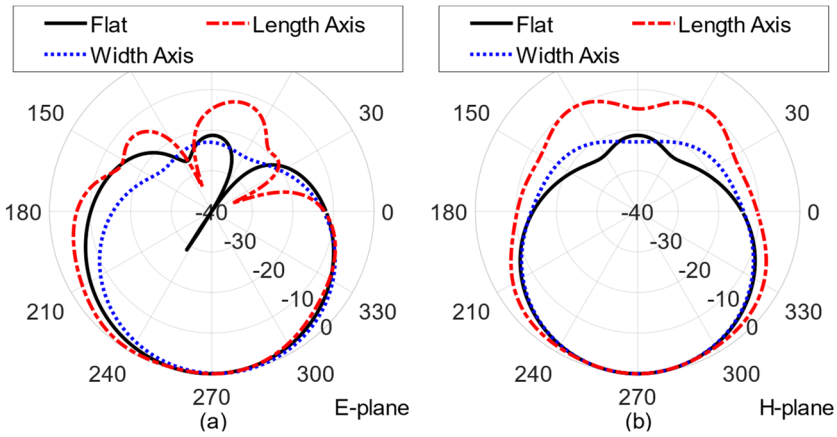


Figure 6.10 Comparison of the far field radiation pattern at 5.6 GHz in a) E-plane and b) H-plane of a flat patch antenna (solid line) with antenna deformed using saddle deformation with convex bending along the length (dashed line) and along the width (dotted line) with A = 20 mm.

Figure 6.9b) shows the impact of saddle deformations on the fractional bandwidth of antenna. It can be seen that convex deformation along the width of antenna generally reduces the operating bandwidth of antenna, whilst the convex deformation along the length slightly increases the bandwidth. However, it is worth noting that convex bending along the length of antenna moves antenna out of the operating band designed for the flat antenna, as shown by the shaded region in Figure 6.9b), whilst in the case

of convex bending along the width the antenna is still operating within the bandwidth of the flat antenna, albeit with reduced bandwidth.

Impact of the saddle deformation on the far field radiation pattern is shown in Figure 6.10. Figure 6.10a) compares the E-plane radiation pattern of the flat patch antenna (solid line) with the deformed antenna for A=20 mm. Figure 6.10b) shows the same information but for the H-plane radiation pattern. It can be seen that convex deformation along the length of antenna has much bigger impact on antenna radiation pattern in both E- and H planes. It is seen that convex deformation along the length generally increases the width of the main beam as well as the widths of the sidelobes. Convex deformation along the width of antenna is seen to reduce the main radiation beam in the E-plane compared to the flat antenna.

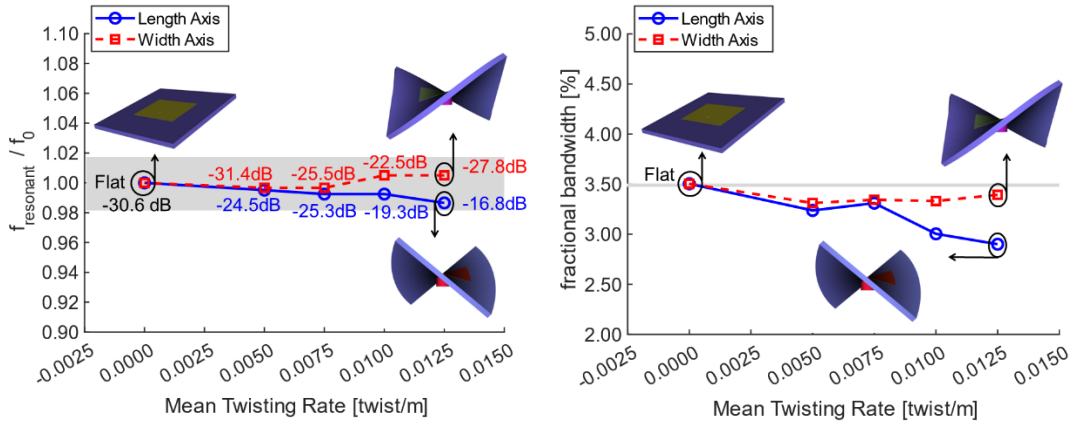
6.3.3 Twisting Deformations

In the final part of the study, the impact of the twisting deformation on antenna performance is investigated. Twisting deformation is imposed on the warped cage by specifying mean rotations per meter along the width and length of the antenna as shown in Figure 6.4d), and ranging from 0.0050 twist/m to 0.0125 twist/m.

Figure 6.11a) shows the ratio of the resonant frequency of the deformed antenna to that of the flat antenna for twisting deformation along length and width of antenna. It can be seen that increasing the twisting along the width antenna of increases the resonant frequency by ~1% whilst the twisting along the length of antenna decreases the resonant frequency by ~2%. The grey shaded region depicts the fractional bandwidth of 3.5% of the flat antenna and it can be seen that the deformed antenna resonant frequency stays within the bandwidth of the flat antenna. In all cases the S_{11} values at the resonant frequency tend to increase but more so for the case of twisting along the length of the antenna.

Twisting deformation along the length of antenna decreases the overall bandwidth of the antenna and has a larger impact than twisting deformation along the width of antenna as shown in Figure 6.11b). In all cases considered the deformed antenna

predominantly operates in the band defined by the flat antenna and depicted by the shaded region in Figure 6.11a).



(a) (b)

Figure 6.11(a) Impact of twisting deformation applied along the width and length of antenna on the change of the resonant frequency of deformed antenna. (b) Impact of the twisting deformation applied along the length and width of antenna on the fractional bandwidth of antenna.

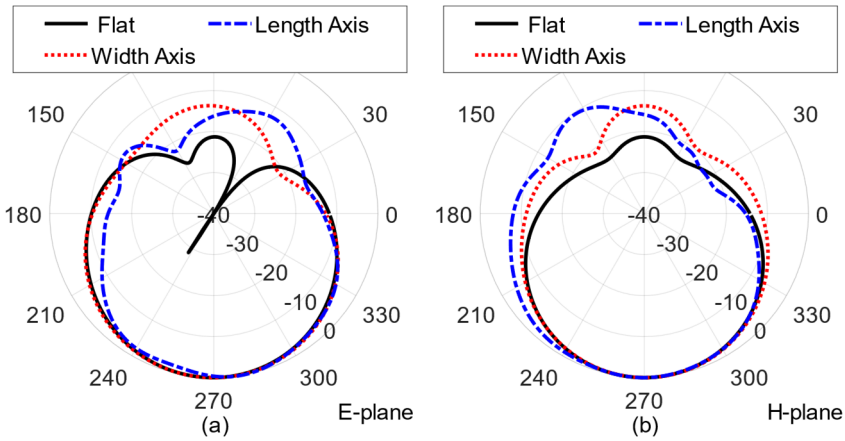


Figure 6.12 Comparison of the far field radiation pattern at 5.6 GHz in a) E-plane and b) H-plane of a flat patch antenna (solid line) with antenna deformed using twisting deformation with 0.0125 twist/m along the length (dashed line) and along the width (dotted line) of antenna.

Impact of the twisting deformation on the far field radiation pattern is shown in Figure 6.12. Figure 6.12a) compares the E-plane radiation pattern of the flat patch antenna (solid line) with the deformed antenna for maximum twisting parameter considered in this Chapter, i.e., 0.0125 twist/m. Figure 6.12b) shows the same information but for the

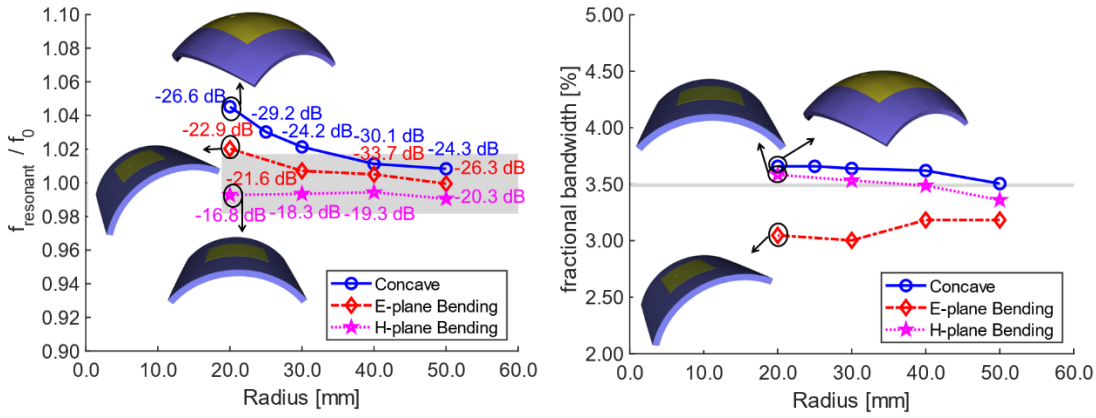
H-plane radiation pattern. Comparing Figure 6.12a) and Figure 6.12b) it can be seen that twisting antenna along its length has much bigger impact on antenna radiation pattern, both in the terms of the main beam and also in the increased back radiation compared to the case when twisting deformation is induced along the width of antenna.

6.3.4 Comparison with Cylindrical Deformations

An important question to consider is how the results from the previous section compare with those of representative 1D deformations along the cylinder plane and whether it is enough to just consider simpler 1D deformations in order to assess antennas stability under deformations. To answer this question this section compares the impact of 2D spherical deformations on antenna performance against the cylindrical deformation along both E and H- plane. GC cage of the cylindrical deformation is controlled by the cylinder radius that is varied from 20 to 50 mm. Four cases are considered, namely concave and convex cylindrical bending and each along both E-plane and H-plane of antenna.

Figure 6.13a) compares the impact of the spherical concave deformation on antenna resonant frequency and S_{11} parameter against the concave cylindrical deformation in the E- and H-plane. It can be seen that the impact of concave spherical deformation is more significant than representative cylindrical deformations. Whilst there seems to be correlation between the results in the frequency shift between the cylindrical deformation along the E-plane and spherical deformation, 1D deformation underestimates the amount of the frequency shift. Furthermore, the values of the S_{11} parameter at the resonant frequency in the case of cylindrical bending increase with increased bending curvature whilst the S_{11} values in the case of spherical bending decrease.

Figure 6.13b) compares the impact of concave spherical and cylindrical deformations on the antenna fractional bandwidth. Cylindrical bending along the E-plane acts to decrease the antenna fractional bandwidth. The results for cylindrical bending in the H-plane are more strongly correlated with the results of spherical bending but again, underestimate the amount of change in the bandwidth.



(a) (b)

Figure 6.13 (a) Resonant frequency of antenna for a concave spherical and E-plane and H-plane bending. Values (dB) indicate the value of S_{11} parameter at the resonant frequency. (b) The fractional bandwidth for a concave spherical and E-plane and H-plane bending.

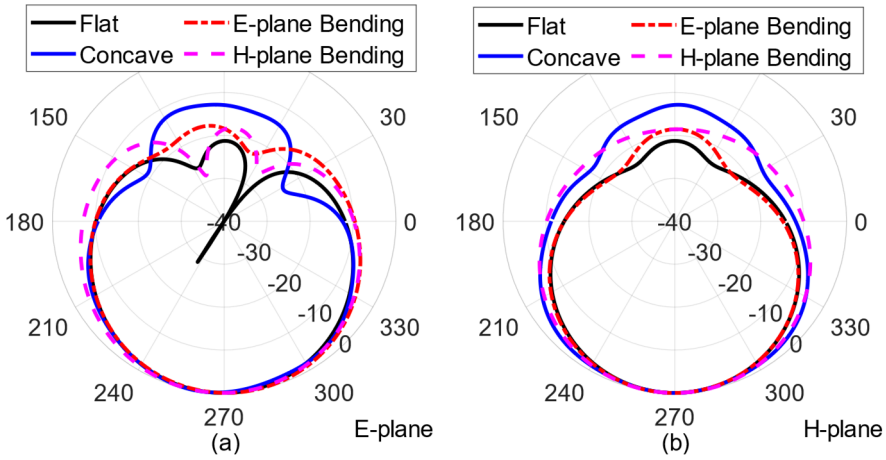


Figure 6.14 Comparison of the far field radiation pattern at 5.6 GHz in a) E-plane and b) H-plane of a flat patch antenna (solid line) with antenna deformed using Concave deformation with radius 20mm, and respective E-plane and H-plane deformation of antenna.

Comparisons of the impact of the concave spherical and cylindrical bending in E- and H-plane on the antenna far field radiation pattern in shown Figure 6.14 for the deformation radius *r*=20 mm. Figure 6.14a) compares the far field radiation patterns in the E-plane of the flat antenna with cylindrically deformed antenna in both E-plane and H-plane and spherically deformed antenna. Figure 6.14b) gives the same information but for the far field radiation pattern in the H-plane. It can be seen that in both cases the

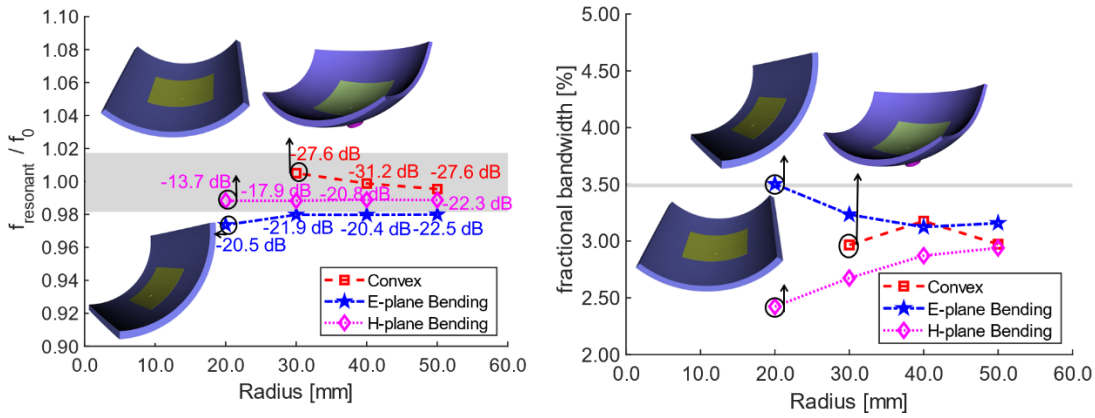
spherical and cylindrical deformations have similar impact on the main lobe but that spherical deformation has much stronger impact on the back lobes.

Figure 6.15a) compares the impact of the convex spherical deformation and the simpler cylindrical deformations on the antenna resonant frequency and the value of S_{11} at the resonant frequency. According to the Figure 6.15a) convex spherical bending does not significantly affect the resonant frequency of antenna whilst the cylindrical deformations in both E- and H-plane predict larger shift of the resonant frequency towards lower frequencies and that E-plane bending has much stronger impact. Furthermore, the S_{11} value at the resonant frequency in the case of spherical bending remains largely unaffected whilst in the case of cylindrical bending the S_{11} value increases and more so in the case of H-plane bending. This can have potential consequences on the antenna bandwidth and this is explored in Figure 6.15b) where impact of convex spherical and cylindrical deformations on antenna fractional bandwidth is investigated.

Figure 6.15b) demonstrates that both spherical and cylindrical deformation in the H-plane predict reduction of antenna fractional bandwidth whilst the cylindrical bending in E-plane results in gradual increase in antenna bandwidth. Cylindrical bending in the H-plane bending has the most significant impact on the antenna bandwidth.

The impact of convex spherical and cylindrical bending in both E- and H- plane on the antenna far field radiation pattern is shown in Figure 6.16a,b) for the case of deformation r = 30 mm and compared against the result of the flat antenna. It can be seen that the major differences are in the back lobe and that all deformations impact similarly the main radiation beam.

Overall, comparing Figure 6.13-Figure 6.16, it can be concluded that when concave deformations are considered the spherical deformation is better correlated with the E-plane cylindrical bending when the impact on the resonant frequency is considered but better correlated to the H-plane cylindrical bending when fractional bandwidth is considered. For the case of convex deformations, the spherical deformation is better



(a) (b)

Figure 6.15 (a) Resonant frequency of antenna for a convex spherical and E-plane and H-plane bending. Values (dB) indicate the value of S_{11} parameter at the resonant frequency. (b) The fractional bandwidth for a convex spherical and E-plane and H-plane bending.

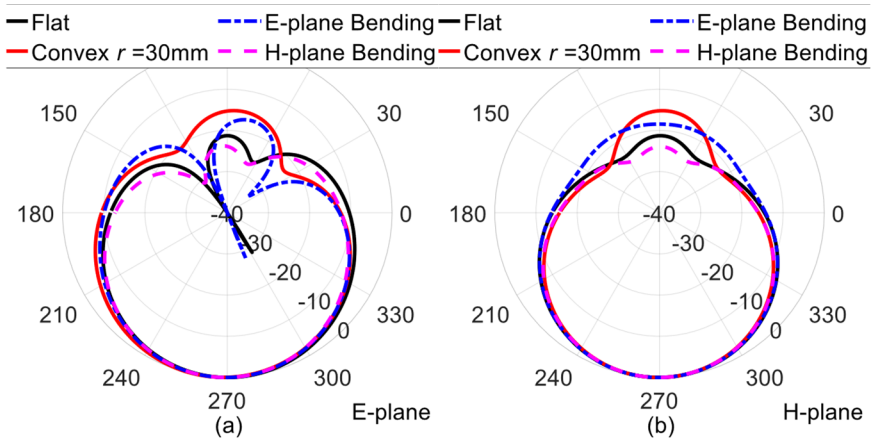


Figure 6.16 Comparison of the far field radiation pattern at 5.6 GHz in a) E-plane and b) H-plane of a flat patch antenna with antenna deformed using a convex deformation with radius 30mm, and respective E-plane and H-plane deformation of antenna.

correlated to the H-plane cylindrical bending when the impact on both the resonant frequency and the bandwidth is considered. However, in each case the simpler cylindrical deformations either underestimate or overestimate the changes in antenna performance parameters by up to 4%. Finally, spherical convex and concave antenna deformations predict similar changes to the main beam pattern as simpler cylindrical deformations with the main changes being in the back lobes.

6.4 Conclusions

This Chapter investigates the impact of complex deformations imposed on the practical flexible antenna designed on the PDMS substrate and operating in the wireless 5.5-6 GHz region. A wide range of 2D deformations of varying strength have been considered namely spherical deformation, both convex and concave in nature, saddle type deformations and twisting deformations. The parameters of deformations are defined in terms of the warped cage of the GC method.

It has been shown that pre-scaling for GC induced distortions is effective and rapidly reduces non-physical distortion errors. Our results show that spherical bending of antenna shifts the resonant frequency of antenna to higher frequencies and that the concave spherical bending has particularly strong impact on the resonant frequency. Concave spherical deformation can act to move the bandwidth of deformed antenna outside the operating bandwidth of the flat antenna.

Saddle and twisting deformation tend to reduce the antenna resonant frequency, and are more detrimental to antenna operation when deformations are applied along the length of antenna. In particular, saddle deformations where convex bending is induced along the length of antenna can reduce the resonant frequency of the antenna and move it outside the operating band designed for the flat antenna.

Our analysis and comparison of the impact of spherical bending with simpler cylindrical bending along the width and length of antenna has found that although some correlation between results can be made when resonant frequency or bandwidth is considered it is found that simpler cylindrical bending can underestimate or overestimate the prediction of antenna performance by up to 4%. This is deemed to be sufficiently high and antenna can be out of the operating band designed for the flat antenna.

The presented analysis of deformed antennas shows that the GC method coupled with electromagnetic simulator is a promising design toolkit that can be confidently used to

assess the impact of deformations on antenna performance and give a more accurate prediction of antenna stability under deformations.

References

[1] S. Wagner and S. Bauer, "Materials for Stretchable Electronics," *MRS Bulletin,* vol. 37, no. 3, pp. 207-213, 2012, doi: 10.1557/mrs.2012.37.

[2] L. Song, A. C. Myers, J. J. Adams, and Y. Zhu, "Stretchable and Reversibly Deformable Radio Frequency Antennas Based on Silver Nanowires," *ACS Appl Mater Interfaces,* vol. 6, no. 6, pp. 4248-53, Mar 26 2014, doi: 10.1021/am405972e.

[3] J. Suikkola *et al.*, "Screen-Printing Fabrication and Characterization of Stretchable Electronics," *Sci Rep,* vol. 6, p. 25784, May 13 2016, doi: 10.1038/srep25784.

[4] A. Kumar *et al.*, "A Highly Deformable Conducting Traces for Printed Antennas and Interconnects: Silver/Fluoropolymer Composite Amalgamated by Triethanolamine," *Flexible and Printed Electronics,* vol. 2, no. 4, 2017, doi: 10.1088/2058-8585/aa8d38.

[5] W. Dang, V. Vinciguerra, L. Lorenzelli, and R. Dahiya, "Printable Stretchable Interconnects," *Flexible and Printed Electronics,* vol. 2, no. 1, 2017, doi: 10.1088/2058-8585/aa5ab2.

[6] R. B. V. B. Simorangkir, Y. Yang, R. M. Hashmi, T. Bjorninen, K. P. Esselle, and L. Ukkonen, "Polydimethylsiloxane-Embedded Conductive Fabric: Characterization and Application for Realization of Robust Passive and Active Flexible Wearable Antennas," *IEEE Access,* vol. 6, pp. 48102-48112, 2018, doi: 10.1109/access.2018.2867696.

[7] R. B. V. B. Simorangkir, Y. Yang, K. P. Esselle, and B. A. Zeb, "A Method to Realize Robust Flexible Electronically Tunable Antennas Using Polymer-Embedded Conductive Fabric," *IEEE Transactions on Antennas and Propagation,* vol. 66, no. 1, pp. 50-58, 2018, doi: 10.1109/tap.2017.2772036.

[8] W. Wu, "Stretchable Electronics: Functional Materials, Fabrication Strategies and Applications," *Science and Technology of Advanced Materials,* vol. 20, no. 1, pp. 187-224, 2019, doi: 10.1080/14686996.2018.1549460.

[9] G. J. Hayes, J. So, A. Qusba, M. D. Dickey, and G. Lazzi, "Flexible Liquid Metal Alloy (EGaIn) Microstrip Patch Antenna," *IEEE Transactions on Antennas and Propagation,* vol. 60, no. 5, pp. 2151-2156, 2012, doi: 10.1109/TAP.2012.2189698.

[10] B. Aïssa *et al.*, "Fluidic Patch Antenna Based on Liquid Metal Alloy/Single-wall Carbon-nanotubes Operating at the S-Band Frequency," *Applied Physics Letters,* vol. 103, no. 6, 2013, doi: 10.1063/1.4817861.

[11] C. Lin, C. Chang, Y. T. Cheng, and C. F. Jou, "Development of a Flexible SU-8/PDMS-Based Antenna," *IEEE Antennas and Wireless Propagation Letters,* vol. 10, pp. 1108-1111, 2011, doi: 10.1109/LAWP.2011.2170398.

[12] N. J. Farcich, J. Salonen, and P. M. Asbeck, "Single-Length Method Used to Determine the Dielectric Constant of Polydimethylsiloxane," *IEEE Transactions on Microwave Theory and Techniques,* vol. 56, no. 12, pp. 2963-2971, 2008, doi: 10.1109/tmtt.2008.2007182.

[13] Y. Bonnassieux *et al.,* "The 2021 Flexible and Printed Electronics Roadmap," *Flexible and Printed Electronics,* vol. 6, no. 2, 2021, doi: 10.1088/2058-8585/abf986.

[14] Y. Wu, S. S. Mechael, and T. B. Carmichael, "Wearable E-Textiles Using a Textile-Centric Design Approach," *Acc Chem Res,* vol. 54, no. 21, pp. 4051-4064, Nov 2 2021, doi: 10.1021/acs.accounts.1c00433.

[15] K. Yan, J. Li, L. Pan, and Y. Shi, "Inkjet Printing for Flexible and Wearable Electronics," *APL Materials,* vol. 8, no. 12, p. 120705, 2020, doi: 10.1063/5.0031669.

[16] L. Song, B. Zhang, D. Zhang, and Y. Rahmat-Samii, "Embroidery Electro-Textile Patch Antenna Modeling and Optimization Strategies with Improved Accuracy and Efficiency," *IEEE Transactions on Antennas and Propagation,* pp. 1-1, 2022, doi: 10.1109/tap.2022.3145443.

[17] J. Zhu, J. J. Fox, N. Yi, and H. Cheng, "Structural Design for Stretchable Microstrip Antennas," *ACS Appl Mater Interfaces,* vol. 11, no. 9, pp. 8867-8877, Mar 6 2019, doi: 10.1021/acsami.8b22021.

[18] F. Nikbakhtnasrabadi, H. El Matbouly, M. Ntagios, and R. Dahiya, "Textile-Based Stretchable Microstrip Antenna with Intrinsic Strain Sensing," *ACS Appl Electron Mater,* vol. 3, no. 5, pp. 2233-2246, May 25 2021, doi: 10.1021/acsaelm.1c00179.

[19] J. Zhu *et al.,* "Stretchable Wideband Dipole Antennas and Rectennas for RF Energy Harvesting," *Mater Today Phys,* vol. 18, May 2021, doi: 10.1016/j.mtphys.2021.100377.

[20] J. Zhu *et al.,* "Strain-Insensitive Hierarchically Structured Stretchable Microstrip Antennas for Robust Wireless Communication," *Nanomicro Lett,* vol. 13, no. 1, p. 108, Apr 9 2021, doi: 10.1007/s40820-021-00631-5.

[21] L. Shao *et al.,* "Flexible Force Sensitive Frequency Reconfigurable Antenna Base on Stretchable Conductive Fabric," *Journal of Physics D: Applied Physics,* vol. 55, no. 19, 2022, doi: 10.1088/1361-6463/ac4f91.

[22] S. Sankaralingam and B. Gupta, "Development of Textile Antennas for Body Wearable Applications and Investigations on Their Performance under Bent Conditions," *Progress In Electromagnetics Research B,* vol. 22, pp. 53-71, 2010, doi: 10.2528/pierb10032705.

[23] D. Ferreira, P. Pires, R. Rodrigues, and R. F. S. Caldeirinha, "Wearable Textile Antennas: Examining the Effect of Bending on Their Performance,"

IEEE Antennas and Propagation Magazine, vol. 59, no. 3, pp. 54-59, 2017, doi: 10.1109/map.2017.2686093.

[24] Y. Mukai, V. T. Bharambe, J. J. Adams, and M. Suh, "Effect of Bending and Padding on the Electromagnetic Performance of a Laser-cut Fabric Patch Antenna," *Textile Research Journal*, vol. 89, no. 14, pp. 2789-2801, 2018, doi: 10.1177/0040517518801202.

[25] L. Song and Y. Rahmat-Samii, "A Systematic Investigation of Rectangular Patch Antenna Bending Effects for Wearable Applications," *IEEE Transactions on Antennas and Propagation*, vol. 66, no. 5, pp. 2219-2228, 2018, doi: 10.1109/tap.2018.2809469.

[26] T. N. Kapetanakis, C. D. Nikolopoulos, K. Petridis, and I. O. Vardiambasis, "Wearable Textile Antenna with a Graphene Sheet or Conductive Fabric Patch for the 2.45 GHz Band," *Electronics*, vol. 10, no. 21, 2021, doi: 10.3390/electronics10212571.

[27] J. Zhang, J. Huang, P. Sun, F. Meng, J. Zhang, and P. Zhao, "Analysis Method of Bending Effect on Transmission Characteristics of Ultra-Low-Profile Rectangular Microstrip Antenna," *Sensors (Basel)*, vol. 22, no. 2, Jan 13 2022, doi: 10.3390/s22020602.

[28] S.-m. Sim, Y. Lee, H.-L. Kang, K.-Y. Shin, S.-H. Lee, and J.-M. Kim, "RF Performance of Ink-jet Printed Microstrip Lines on Rigid and Flexible Substrates," *Microelectronic Engineering*, vol. 168, pp. 82-88, 2017, doi: 10.1016/j.mee.2016.11.011.

[29] E. Altinozen, I. Harrison, A. Vukovic, and P. Sewell, "Systematic Generation of Arbitrary Antenna Geometries," *IEEE Transactions on Antennas and Propagation*, pp. 1-1, 2022, doi: 10.1109/TAP.2022.3165539.

[30] Y. Lipman, D. Levin, and D. Cohen-Or, "Green Coordinates," *ACM Trans. Graph.*, vol. 27, no. 3, pp. 1-10, 2008, doi: 10.1145/1360612.1360677.

[31] Y. Lipman and D. Levin, "Derivation and Analysis of Green Coordinates," *Computational Methods and Function Theory*, journal article vol. 10, no. 1, pp. 167-188, June 01 2010, doi: 10.1007/bf03321761.

[32] P. Sewell, T. M. Benson, C. Christopoulos, D. W. P. Thomas, A. Vukovic, and J. G. Wykes, "Transmission-line Modeling (TLM) Based upon Unstructured Tetrahedral Meshes," *IEEE Transactions on Microwave Theory and Techniques*, vol. 53, no. 6, pp. 1919-1928, 2005, doi: 10.1109/tmtt.2005.848078.

[33] P. D. Sewell, T. M. Benson, C. Christopoulos, D. W. P. Thomas, A. Vukovic, and J. G. Wykes, "Implicit Element Clustering for Tetrahedral Transmission-Line Modeling (TLM)," *IEEE Transactions on Microwave Theory and Techniques*, vol. 57, no. 8, pp. 2005-2014, 2009, doi: 10.1109/tmtt.2009.2025451.

[34] X. Meng, A. Vukovic, T. M. Benson, and P. Sewell, "Extended Capability Models for Carbon Fiber Composite (CFC) Panels in the Unstructured

Transmission Line Modeling (UTLM) Method," *IEEE Transactions on Electromagnetic Compatibility*, vol. 58, no. 3, pp. 811-819, 2016, doi: 10.1109/temc.2016.2531791.

[35] A. Vukovic, P. Sewell, X. Meng, and T. M. Benson, "Installed Antenna Performance in Airborne Radomes of Different Profiles," 2016.

[36] A. Vukovic, P. Sewell, and T. M. Benson, "Holistic Appraisal of Modeling Installed Antennas for Aerospace Applications," *IEEE Transactions on Antennas and Propagation*, vol. 67, no. 3, pp. 1396-1409, 2019, doi: 10.1109/tap.2018.2884769.

[37] P. Sewell, A. Vukovic, T. M. Benson, and X. Meng, "Extracting Modal Field Profiles from 3D Unstructured Transmission Line Modelling Meshes for Use as Sources and Observers," *IET Science, Measurement & Technology*, vol. 11, no. 6, pp. 780-785, 2017, doi: 10.1049/iet-smt.2016.0357.

Chapter 7 Characterisation of Flexible Interconnect

Flexible interconnects are ubiquitous for flexible, foldable, and wearable electronics for power and signal transmission. There is a wealth of different materials for flexible materials reported in literature, both for substrates and for conductive lines. However, effective comparison of flexible interconnects performance fabricated on different platforms has not been comprehensively researched and reported. In addition to that flexible interconnect often suffer from performance degradations due to mechanical deformations. Hence, it is essential to investigate to what degree fully flexible interconnect performance can be degraded in in-situ deformations. However, generating geometries of these deformations, for example twisting, bending and crumpling, is a major challenge of a full assessment of transmission lines.

This Chapter, first, compares the performance of different types of flat interconnects designed for the most popular types of substrates used in flexible electronics, namely PET, PI, PDMS and PU. The Green Coordinates (GC) method is then used to generate bending and twisting deformations of a selection of flexible transmission lines. The unstructured TLM method is used to predict the impact of deformations on flexible transmission lines. This is also done for a range of flexible substrates, namely PET, PI, PDMS and PU with and without conductor losses.

7.1 Introduction

Recent developments in manufacturing flexible, wearable, and foldable materials have opened up new opportunities for wearable electronics components such as wearable interconnects, sensors, displays, antennas and flexible microprocessors [1-4]. A range of new materials have been reported for both substrates and conductive films. Most common substrates used in flexible electronics are polymer-based substrates, such as polyethylene terephthalate, (PET), polyimide (PI) and elastomer-based substrates such as polydimethylsiloxane (PDMS) and polyurethane (PU). In addition, textile substrates are promising alternatives, but show lower stability in combination with conductive prints [5-7].

Typical conductive materials for wearable electronics such as E-fibers [8, 9], conductive polymers [10-12], Ag-inks and pastes [13], nanowires or nanoparticles and 2D materials, such as graphene and MXenes [14-17], have poor structural stability under deformation and suffer from up to two orders of magnitude lower conductivity compared to conventional metals in printed electronics. The electrical conductivity of flexible conductive prints under strain has been experimentally tested for several interconnects and shows that deformation leads to micro and nano cracks resulting in loss of continuous current paths and hence a drop in conductivity, 1.5 times for strain 5% and 5 times for strain 10% [13]. It is also important to note that these conductive materials have at least one or two orders of magnitude lower thickness compared to the industry standard of 0.035 mm metallic thickness on a printed circuit board.

Despite the fact that a variety of flexible substrates are reported in literature, the analysis of performance of interconnects on different substrates is scarce. Simulations of transmission properties of interconnects fabricated using silver paste on the PET substrate of different thicknesses have been reported in [18]. However, that study considered ideal microstrip-to-microstrip transmission loss i.e., without accounting for the Sub Miniature version A (SMA) connector. There is no comparative study of interconnects based on different substrates and therefore in this Chapter the analysis is extended to systematically analyse and compare transmission properties of a range of

interconnects fabricated using a variety of substrates namely PET [18], PI [19], PDMS [12] and PU [20]. A quantitative analysis of transmission and reflection losses introduced by key elements, namely, connector loss, substrate loss, substrate thickness and conductive loss is reported. To better match experimental measurements, sub-miniature, SMA connectors are used to excite and receive the signal [21].

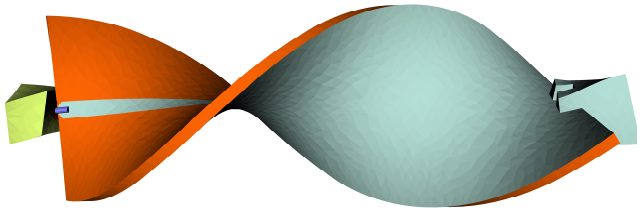


Figure 7.1 Twisting deformation of a flexible interconnect.

An obvious difficulty for the computational modelling of realistic interconnects is the fact that the lossy conductive layer has much smaller thickness than the substrate (over an order of magnitude). Use of direct meshing to correctly capture the skin effect will be computationally expensive. To alleviate this problem a common approach is to “imprint” or embed the behaviour of the thin layer between adjacent cells. An analytic one-dimensional (1D) transmission line model of required thickness and conductivity is implemented between the cells to correctly capture the skin depth effect and embedded into the time domain code using digital filters [22]. This approach has been published in [22] for the case of cartesian TLM and has also been implemented for the unstructured TLM. In this Chapter, the study is also extended by developing CAD model of the flexible interconnects subject to twisting deformation (See Figure 7.1) with using GC method in Chapter 5 to alleviate the geometry challenges indicated challenges in Chapter 1 and investigate the impact of twisting on its electromagnetic performance. The analysis was extended by comparing the performance of interconnects under the impact of deformations, namely bending and twisting. This is done for a range of substrate and metallic print properties with the aim to ascertain the most resilient and stable platform for flexible electronics.

The Chapter is structured as follows: Section 7.2 first calibrated the TLM method on

the case of an interconnect fabricated on a rigid substrate with the SMA connector. Section 7.3 summarises the material and physical properties of interconnects that will be investigated in this Chapter. The performance of a range of flat flexible interconnects is compared against the interconnects fabricated on the rigid substrate. Section 7.4 analyses the performance of a variety of interconnects when exposed to bending and twisting deformation. Section 7.5 summarises the main conclusion of the Chapter.

7.2 Rigid Interconnect with the SMA connector model

The schematic of a typical interconnect with SMA connectors is given in Figure 7.2. The interconnect is defined by the width, W, and the length L of the substrate and the width of the printed line on a particular substrate, W_{sub}. The printed line is tapered down around the coaxial connection for better matching, as shown in Figure 7.2b).

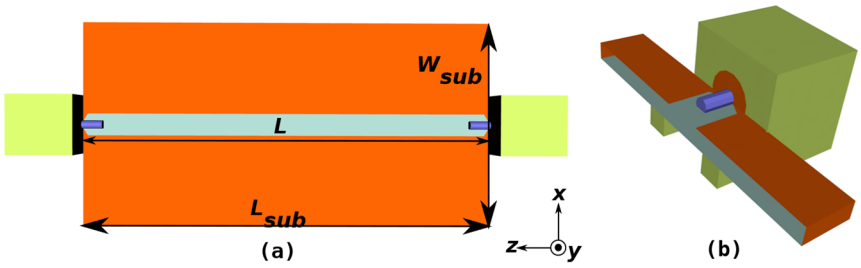


Figure 7.2 Schematic of a flexible interconnect with subminiature SMA.

Sub miniature A (SMA) connecters are used with appropriate coaxial feed at each end of the interconnect. For all cases the form of the coaxial cable is kept the same with relative permittivity, ε_r=2, and has an impedance of 50 Ω. The dimensions of the inner, r_i, and outer radii, r_o, of the coaxial cable that are used for each substrate thickness are given in Table 7.1.

The problem is meshed with a 3 mm background cubic mesh (See Figure 7.3), being refined around the object down to 0.75 mm. Tetrahedra interface this with the non-Cartesian aspects of the geometry. The transmission line is excited with a coaxial TEM mode modulated by a Gaussian pulse providing a 3 dB bounded spectrum from 0.25

GHz to 10.25 GHz. In all cases the total simulation time was 30 ns using an algorithmic timestep of 0.0100069 ps.

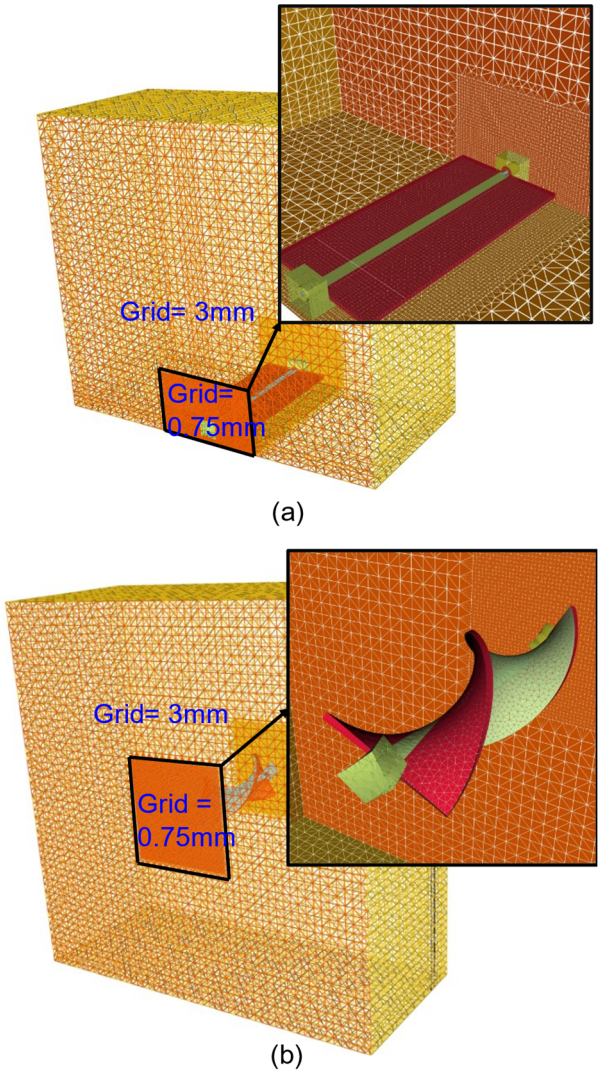


Figure 7.3 Computational mesh of the a) flat and b) deformed interconnect.

To provide comparisons for rigid PCB and flexible microstrip lines, the end launch connector effect should be first investigated and optimised. Microstrip thickness higher than 0.508 mm has radiated loss and impact of dispersion that varies the characteristic impedance line. Besides, since the substrate has a low dielectric constant, the microstrip line width is significantly wider than a coaxial pin that appropriately matches the thickness of the board. Therefore, to observe behaviour properly, one can match to coax: (1) the microstrip line must be matched or tapered properly to coax line or (2)

sufficiently large coax must be used. The first approach and tapered the line in four different ways have been preferred (See Figure 7.4). The classical PCB dielectric namely RO4350 (dielectric constant is 3.48 and dielectric loss is 0.0037), in Figure 7.4 is given for comparison reasons with different coax-to-microstrip transitions (with varying sizes of taper).

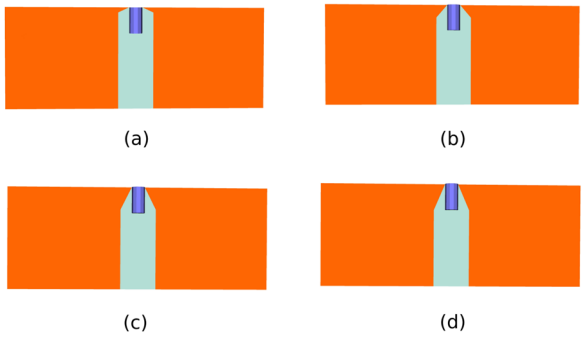


Figure 7.4 The geometry of coax-to-microstrip transitions. The tapered size between end launch connector and the end of the 50 Ω impedance line is (a) 0.30 mm (b) 0.635 mm and (c)1.09 mm and (d) 1.27 mm respectively.

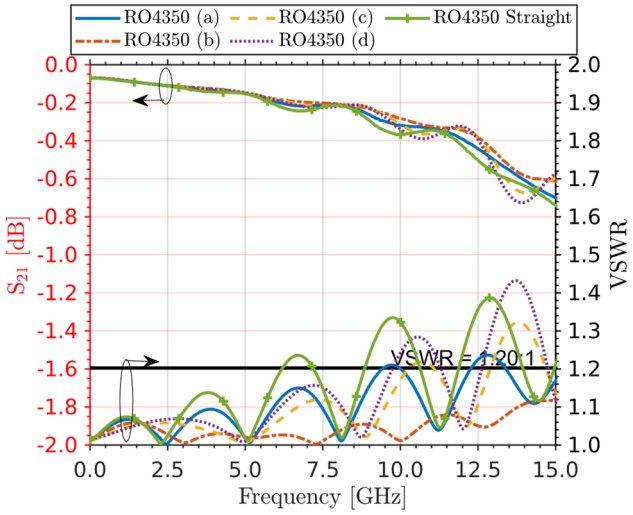


Figure 7.5 S_{21} and voltage standing wave ratio (VSWR) of feed port optimisation comparison with typical with metal as an imprinted PEC. The substrate thickness is 0.762 mm (30 mil) and the length of 25.4 mm (1 inch) board.

The comparison shows that transmission line return and insertion loss is comparable with typical measurements [23, 24]. According to Figure 7.5, shorter tapers (type A and

B) perform better compared to longer tapers (C and D) specifically at higher frequencies. Furthermore, tapered printed line provides lower transmission loss compared to typical measurement loss figure of 1 inch [23, 24]. For the rest of the Chapter the printed line is tapered according to type A.

7.3 Comparison of Flexible Interconnects

In this section the electromagnetic performance of a variety of flat interconnects is assessed and compared with the performance of the interconnect on a rigid substrate. All interconnects are considered to be flat i.e., free of stress and strain. Interconnects design on commercially available substrates are considered, namely, Melinex (PET) [21], Kapton (PI) [25], Sylgard 184 (PDMS) [12], Ninja-Flex (PU) [26] and RO3003 [27] and RO4350 [23, 28, 29]. The electromagnetic performance is systematically analysed by gradually including connector losses, substrate losses and conductor losses. Comparison of the transmission (S_{21}) and the voltage standing wave ratio (VSWR) for a variety of interconnects is given with respect to connector loss, substrate loss, substrate thickness and metallic loss.

Table 7.1 Parameters of different interconnects fabricated on different substrates.

Thickness [mm]	W_{PET} [mm]	W_{PI}[mm]	W_{PDMS} [mm]	W_{PU} [mm]	r_i	r_o
0.508	1.288	1.157	1.359	1.417	0.254	0.822
1.0	2.535	2.35	2.50	2.79	0.635	2.055
	PET [18]	PI [19]	PDMS [12]	PU [20]		
ε_r	3.0	3.5	2.77	2.60		
tan (δ)	0.002	0.0027	0.01	0.07		

The relative permittivity, ε_r, and loss tangent, tan(δ), for these representative substrates are given in Table 7.1. Two separate substrate thicknesses are considered, namely 0.508 and 1 mm. The widths of the printed tracks, W_{sub}, are selected so that the line impedance of each interconnect is maintained as 50 Ω [30]. The physical properties of the interconnects fabricated on a particular substrate with defined thicknesses are summarised in Table 7.1. For each substrate the following parameters are given: substrate thickness, substrate dielectric constant, substrate loss as tan (d), the width of the printed conducting line, W_{sub}, and inner and outer radius of a coaxial cable. The overall substrate size is chosen to be consistent with previous experimental work [23], namely the width of the substrate is taken to be 12.7 mm and the length is varied between 25.4 mm, 50.8 mm and 50 mm.

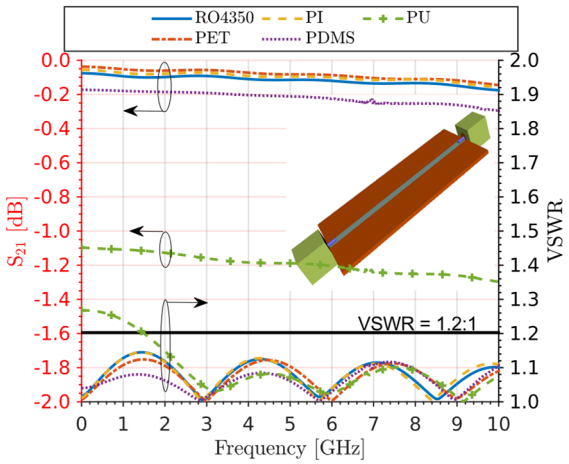


Figure 7.6 S_{21} and VSWR for 50 Ω line interconnects on flexible substrates (PET, PI, PDMS, and PU) compared to equivalent microstrip line on a rigid substrate RO4350. Line length is 25.4 mm and the substrate thickness is 0.508 mm. Metallic losses are neglected.

Figure 7.6 compares S_{21} and the VSWR for interconnects fabricated on different flexible substrates, namely PET, PI, PDMS and PU with those from the rigid substrate case, RO4350. The thickness of the substrate is 0.508 mm and the length of the interconnect is 25.4 mm. For this case, all metallic losses are neglected and only substrate loss is considered. All the other parameters for interconnects are given in Table 7.1. Figure 7.6 shows that the interconnect fabricated on PU has the highest transmission loss whilst those fabricated on PET and PI substrates have the smallest

loss which is comparable to the loss of the equivalent 50 Ω microstrip line on a rigid substrate RO4350.

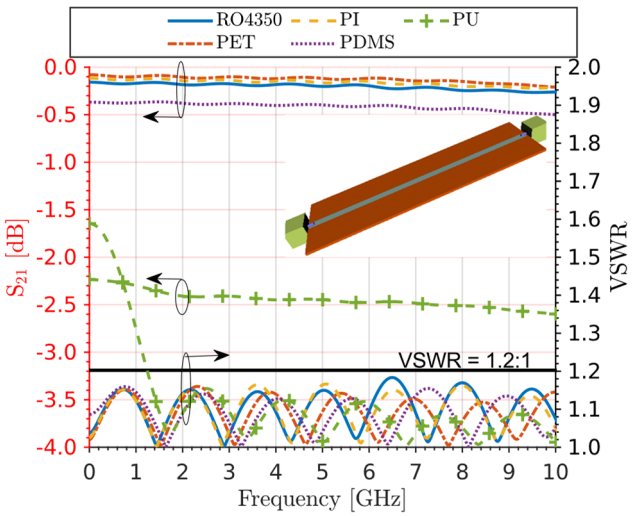


Figure 7.7 S_{21} and VSWR for 50 Ω line interconnects on flexible substrates (PET, PDMS, PI and PU) compared to equivalent microstrip line on a rigid substrate RO4350. Line length is 50.8 mm and the substrate thickness is 0.508 mm. Metallic losses are neglected.

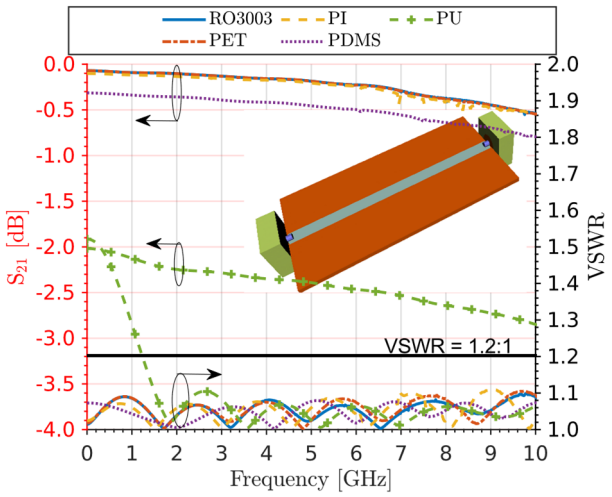


Figure 7.8 S_{21} and VSWR for 50 Ω interconnects on flexible substrates (PET, PI, PDMS and PU). Line length is 50 mm and the substrate thickness is 1 mm. Metallic losses are neglected.

Figure 7.7 shows similar results but for a double length interconnect, i.e., 50.8 mm. As expected, the transmission losses have linearly increased indicating that the loss is predominantly modal loss and is due to the losses in the substrate. Figure 7.8 compares the VSWR and the transmission loss for the thicker substrates that are typical of PET,

PI, PDMS and PU materials. A substrate thickness of 1 mm is considered and the interconnect length is 50 mm. The equivalent 50 Ω microstrip line on the rigid substrate RO3003 [27] (ε_r =3, tan(δ)=0.001) has a width of 2.535 mm. Figure 7.8 shows that the interconnect fabricated on the PET substrate has the smallest loss which is comparable to that of the microstrip line on the rigid laminate. The interconnect fabricated on the PU substrate has the highest loss.

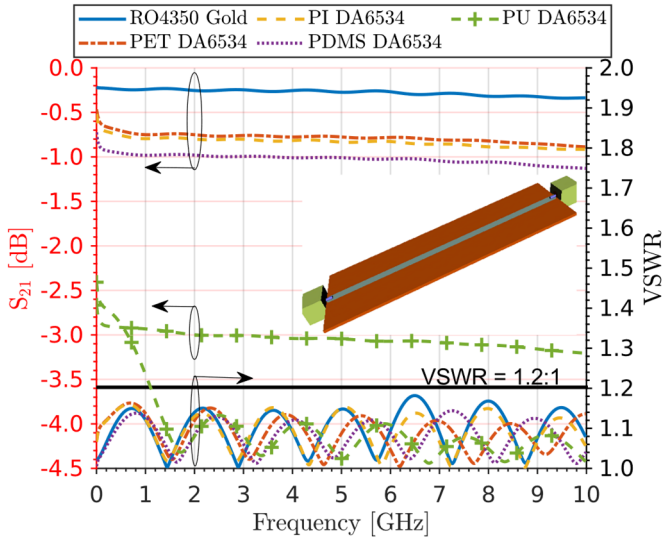


Figure 7.9 S_{21} and VSWR for 50 Ω line interconnects on flexible substrates (PET, PI, PDMS and PU) compared to equivalent microstrip line on a rigid substrate RO4350. Line length is 50.8 mm, and the substrate thickness is 0.508mm.

Finally, Figure 7.9 considers a full model of flexible interconnects that accounts for both substrate and conductive losses. For the flexible interconnects the conductivity of a conductive adhesive layer DA6534 [31] of high thermal conductivity is taken to be $\sigma = 4.5 \times 10^5$ S/m at mid- range frequency of 5 GHz. The conductivity of gold printed on the rigid substrate is taken to be 4.41×10^7 S/m. Figure 7.9 shows that, due to conductive losses, the overall transmission losses have significantly increased over the whole frequency band. Interconnects fabricated on PET and PI substrates have the smallest losses whilst the interconnects fabricated on PDMS and PU substrates have the highest losses. The result for the interconnect fabricated on PET substrate is in excellent agreement with the experimental results of [12, 19, 21].

Results in Figure 7.5 - Figure 7.9 show which flexible interconnect has the highest or lowest transmission losses. The loss is attributable to the dielectric loss of substrates and the conducive loss of printed lines. However, it is worth noting that higher fringing fields of the signal line also result from the lower dielectric constant, typical of PDMS and PU substrates, exhibiting wider track width for 50 Ω line.

7.4 Performance of Flexible Interconnects Under Deformations

In this section, the EM performance of interconnects with various bending and twisting deformations are studied. As before interconnects fabricated on PET, PI, PDMS, and PU substrates are considered, and their material and physical properties are given in Table 7.1.

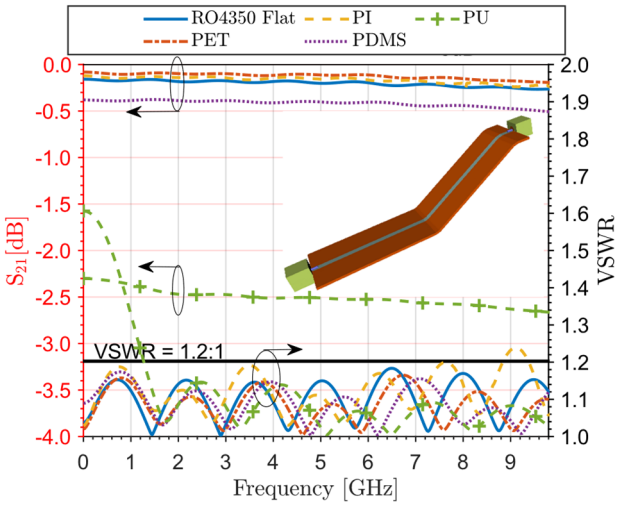


Figure 7.10 S_{21} and VSWR for 50 Ω line interconnects under bending 30° on flexible substrates PET, PI, PDMS and PU compared to equivalent microstrip line on a rigid substrate RO4350.

Figure 7.10 compares the VSWR and the transmission loss of flexible interconnects that are bent by an angle of 30°. The performance for the flat interconnect on a rigid substrate is added for reference. Substrate losses are included but metallic losses are neglected. All interconnects are on the substrate of thickness 0.508 mm and of 50.8 mm length. According to Figure 7.10, this bending has an insignificant effect on return loss

and insertion loss for each substrate, when it is compared their flat cases Similarly, bending transmission lines with an angle of 90° has a minor effect on their electromagnetic performance (See Figure 7.11).

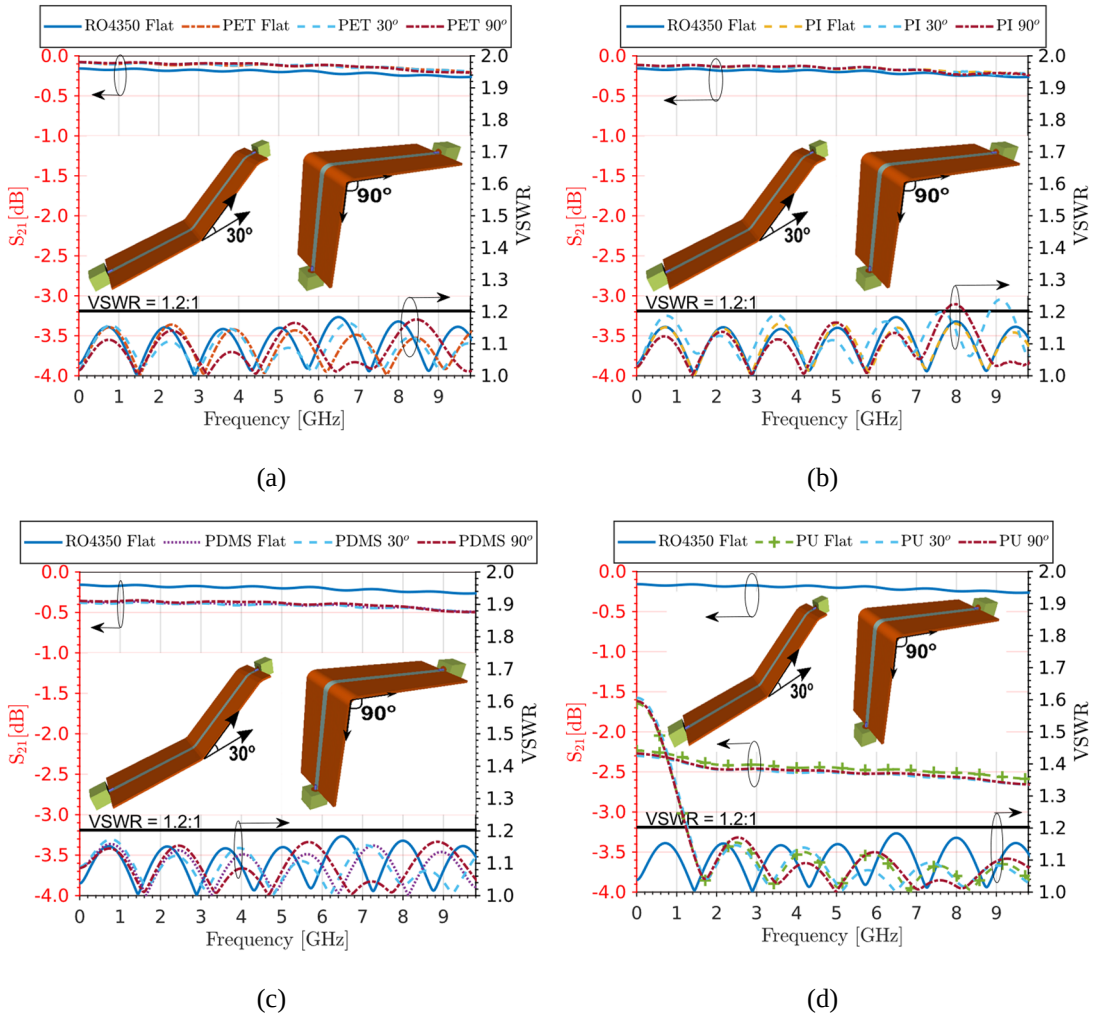


Figure 7.11 S_{21} and VSWR for 50 Ω line interconnects under bending 30° and 90° on flexible substrates a) PET, b) PI, c) PDMS, and d) PU compared to equivalent microstrip line on a rigid substrate RO4350.

It is reasonable to assume that flexible interconnects are simulated with different bending condition with relying realistic and experimental conductivity changes of [32-34] without considering temperature dependence of surface resistivity. Figure 7.12a-d) show microstrip line 30° and 90° bending considered with surface conductivity changes with 5% reduction for compressive bending and 10% increases for tensile bending with relying on [32]. PET and PI substrates provide minimal amount of insertion losses(see

Figure 7.12a-b), where PDMS and PU substrate loss are significantly higher than PET and PI substrate(see Figure 7.12c-d)).

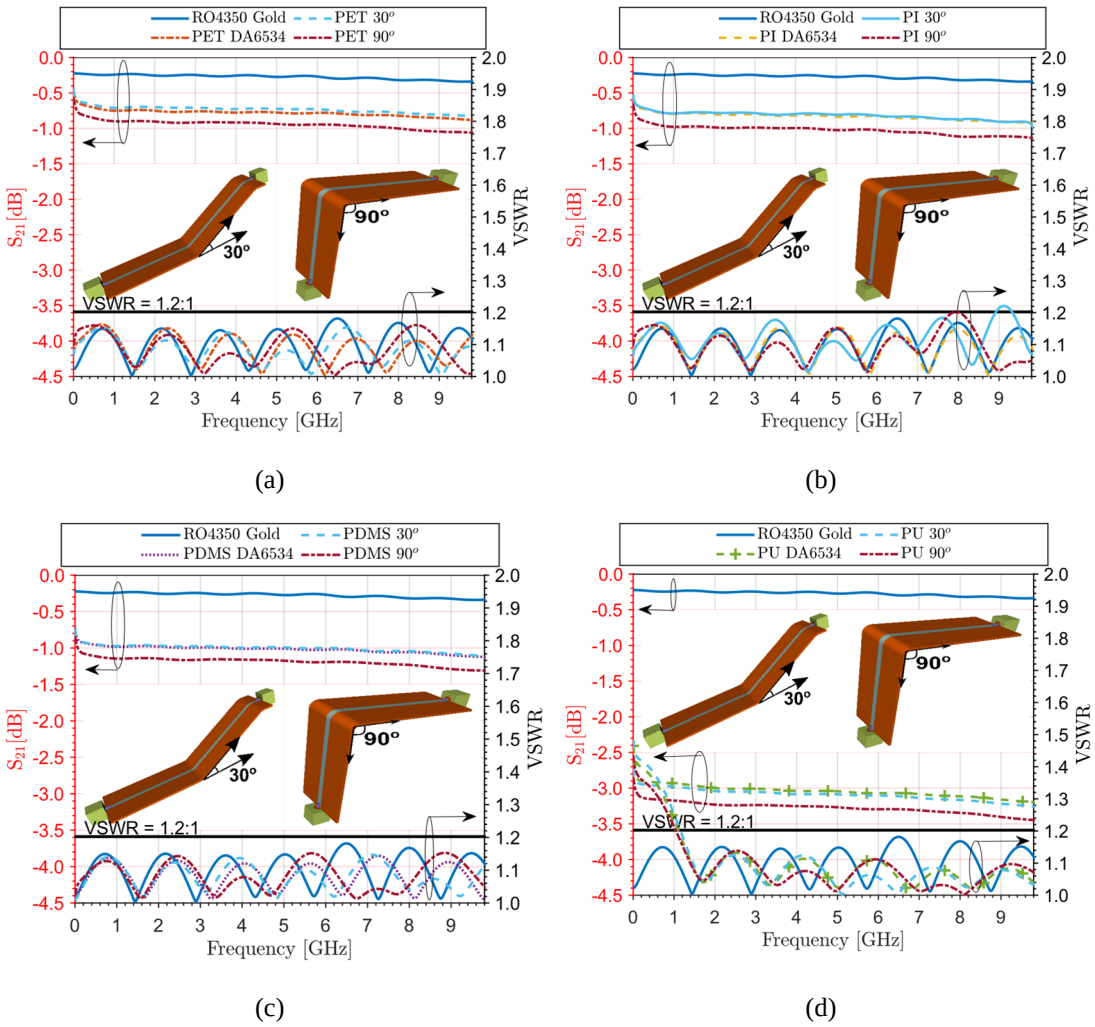


Figure 7.12 S21 and VSWR for 50 Ω line interconnects under bending 30° and 90° on flexible substrates a) PET, b) PI, c) PDMS, and d) PU compared to equivalent microstrip line on a rigid substrate RO4350.

It is well known fact that twisting of bending has more substantial affect for bending along the current path flow. Therefore, this performance change should be investigated. This section describes the GC approach that is used to impose deformations on the flexible interconnect. Figure 7.13 summarises the GC approach. The schematic of the flat interconnect enclosed in the flat cage is shown in Figure 7.13a). The flat cage has similar topology as the interconnect and is defined as a simple polygonal tube that has a dimension width, length and height are 40 mm, 75 mm and 12 mm, respectively with

14 segments along the twisting axis direction. Figure 7.13a) only shows the edges of the flat cage and the flat interconnect geometry. Next, a new warped cage is defined that characterises the twisting deformation as shown in Figure 7.13b). The GC approach is then used to map the deformations of the cage onto the object. Figure 7.13c) shows the deformed interconnect inside the warped cage. Finally, the warped cage is removed to reveal the deformed object, Figure 7.13d).

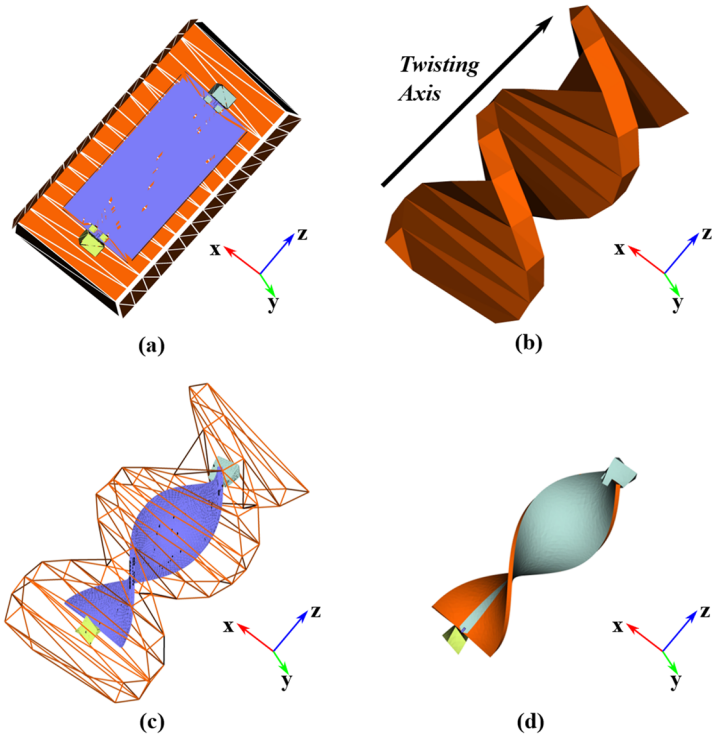


Figure 7.13 GC methodology: a) flat interconnect within a flat cage (only triangular faces of the flat cage shown); b) warped cage that describes the nature and level of deformation required; c) deformed interconnect inside the warped cage (only edges of the warped cage shown) d) final geometry of a deformed interconnect.

In two-dimensions (2D) the GC operator does not introduce any distortions but in three-dimensions (3D) the operator exhibits only a quasi-conformal mapping which means a certain amount of anisotropic scaling. Therefore, it is essential to compensate GC induced distortions to protect the components' manipulation that can, if not minimised, impact the accuracy of electromagnetic (EM) deformations [35]. Earlier study has shown that these distortions can be minimised when the cage is defined to be close to the object [35]. The distortions introduced in the geometry are compensated by pre-

scaling iteratively with the GC method [35]. In the case of a patch antenna, pre-scaling is done on the antenna width and length [35], and in the case of interconnect,

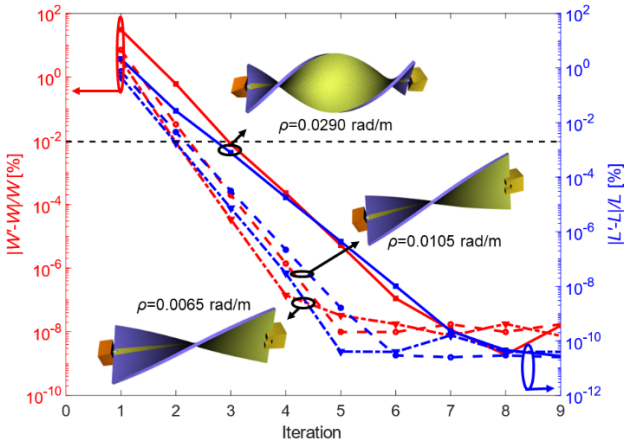


Figure 7.14 GC induced relative distortion error in the width and length of the microstrip transmission line as a function of the number of pre-scaling iteration for generation of twisting deformation with mean twisting ρ=0.0065 rad/m, ρ=0.0105 rad/m, and ρ=0.0290 rad/m.

the pre-scaling is done using the width and length of the metallic trace of the interconnect. The compensation process is based on comparing the total width and length of signal trace before and after deformation. Since the GC method maps the flat geometry onto the deformed one, the constraint edge of the flat case is directly mapped to deformed geometry [35]. Therefore, the ratio of the total width and length edge of the signal trace gives an up- or down- scaling factor. The pre-scaling of GC methods are applied iteratively until prescribed relative difference for the width and length of signal traces is satisfied. Figure 7.14 shows the relative error in percent in the width and length of microstrip transmission line for twisting deformation with mean twisting rate of ρ=0.0065 rad/m, ρ=0.0105 rad/m, and ρ=0.0290 rad/m as a function of the number of iterations. The distortion relative error in the width and length of the transmission line in initial GC applications is high but it sharply reduces with the number of pre-scaling iterations.

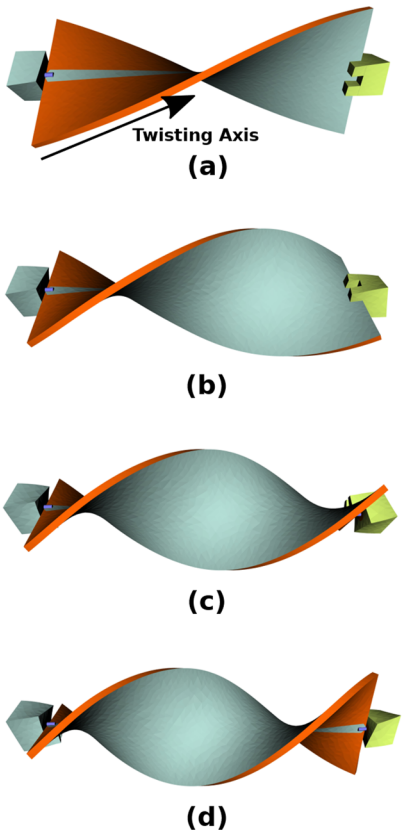


Figure 7.15 GC deformed geometry of microstrip line on 1mm PDMS with coaxial cable port inner and outer radius 0.4233 mm and 1.37 mm with mean twisting rotation per meter (a) 0.0105, (b) 0.0205, (c) 0.0255, and (d) 0.0290 respectively.

Figure 7.15 reveals twisting deformation for different mean twisting rotation per meter parameter, ρ, from 0.0105 rad/m to 0.0290 rad/m. The TLM method based on unstructured tetrahedral mesh is ideally placed to discretise a problem that does not align to a cartesian grid. A 3D Delaunay Mesher [36-38] which is a special implementation of the Delaunay meshing technique [39], is used to provide a hybrid mesh that combines a cubic mesh around uniform regions and a tetrahedral mesh around the object and the curved regions [40]. The near field of the microstrip line is meshed with background cubic cells of 0.75 mm size, whereas the far-field region is sampled with 3 mm cubic cells (See Figure 7.3) shows the surface triangulation of the computational box and the interconnect. For computational memory and run time cost, the region below under the ground plane is reduced for the case of flat interconnect, as shown in Figure 7.3. However, the computational box is made larger for the

interconnects with twisting and bending deformation as in these cases the size of the computational box is more critical. Therefore, with intention of overcoming reflections from the computational box, the computational box is made larger with the dimensions of $1.67\lambda \times 1.03\lambda \times 1.67\lambda$.

Figure 7.16 reveals the VSWR and transmission loss of the GC deformed interconnect on the PDMS substrate with mean twisting rotation from 0.0015 rad/m to 0.0290 rad/m. The inset in the figure shows the anticlockwise rotation direction of twisting deformation. According to Figure 7.16, increasing rotation exhibits higher radiation and insertion loss. It is important to note that the mean rotation twisting per meter 0.0065 is the critical deformation that results in the maximum VSWR=1.2. The increasing deformation above this value results in higher insertion loss from 3 GHz to 5 GHz because of coupling fringing fields and surface waves.

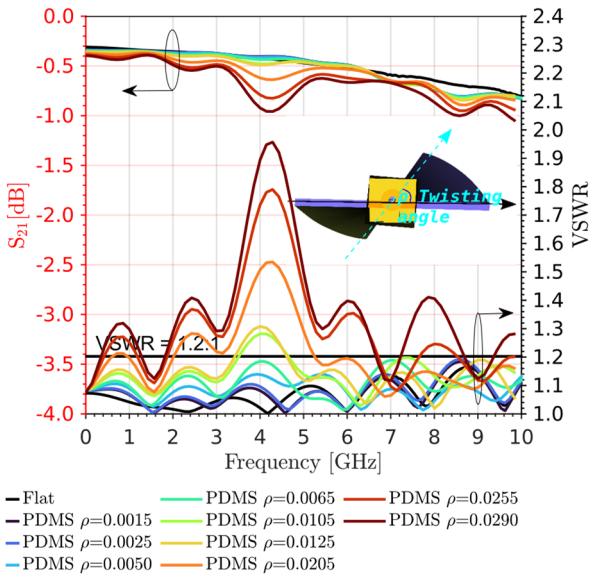


Figure 7.16 S_{21} and VSWR for 1 mm PDMS substrates (GC deformed) with microstrip line with twisting angle ρ, 0.0015, 0.0025, 0.0050, 0.0065, 0.0105, 0.0125, 0.0205, 0.0255 and 0.0290 rad/m respectively. Inset figure shows the rotation direction of twisting deformation. Metallic losses are neglected.

Figure 7.17 reveals PET, PI, PDMS and PU substrate has indiscernible from their flat case similar to [19, 41]. Figure 7.18 demonstrates return and insertion loss of 1 mm PDMS, PET, PU and PI substrates (GC deformed) with microstrip line with twisting

angle ρ, 0 0.0065 rad/m with reducing conductivity 50%, 50%, 50% and 20% respectively with relying on recent refs. [33, 34]. The insertion loss of microstrip line have increasing in loss 0.5 dB for 50% conductivity. In addition, the insertion loss of microstrip line has increasing in loss 0.2 dB for 50% conductivity reduction.

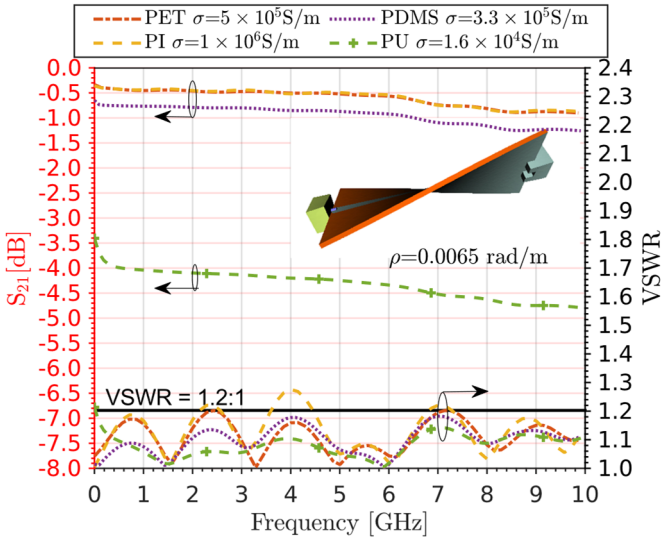


Figure 7.17 S_{21} and VSWR for 1 mm PET, PI, PDMS, and PU substrates (GC deformed) with microstrip line with twisting angle ρ, 0.0065 rad/m respectively.

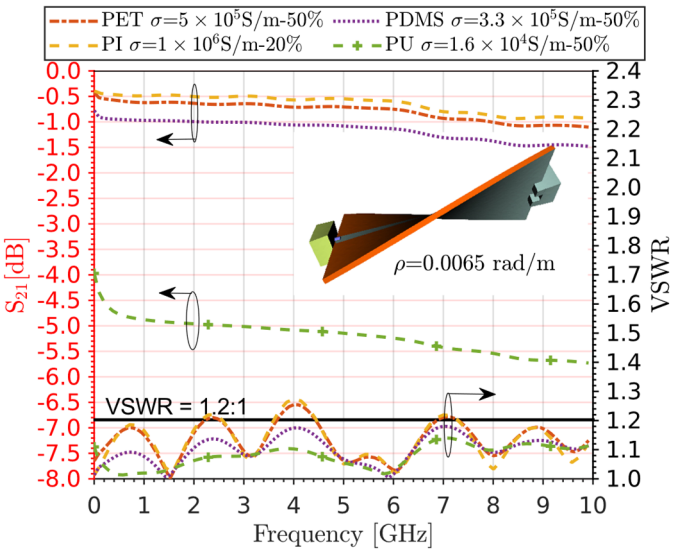


Figure 7.18 S_{21} and VSWR for of 1 mm PET, PI, PDMS, and PU substrates (GC deformed) with microstrip line with twisting angle ρ, 0.0065 rad/m respectively. Conductivity of line has changed according to [33, 34].

Figure 7.19 reveals insertion and transmission losses of enforcing extreme deformations similar to Figure 7.15d). Although this high rate of twisting rate deformation can be higher than expected average deformation for semi-rigid PET and PI substrates; however, there is a strong probability of direct printing of microstrip line of these kinds of irregular deformation. Therefore, complex geometry generation perspective, it is useful to simulate and characterise performance to validate model under extreme deformation. Figure 7.19 shows microstrip line on PET substrates has the minimum insertion loss, whereas the PDMS has better return losses than PU substrates for entire frequency range of transmission line.

The change of conductivity resulting from the deformation has been considered relying on [33, 34]. For microstrip line on PET, conductivity reduction has assumed 60% and microstrip line on PDMS and PU have a 100% reduction in conductivity. However, microstrip line on PI has a 20% reduction. Figure 7.20 reveals impact of changing conductivity in terms of return and insertion loss for extreme deformation. Similar to other deformation cases, PET and PI provides good performance compared to PDMS and PU substrates.

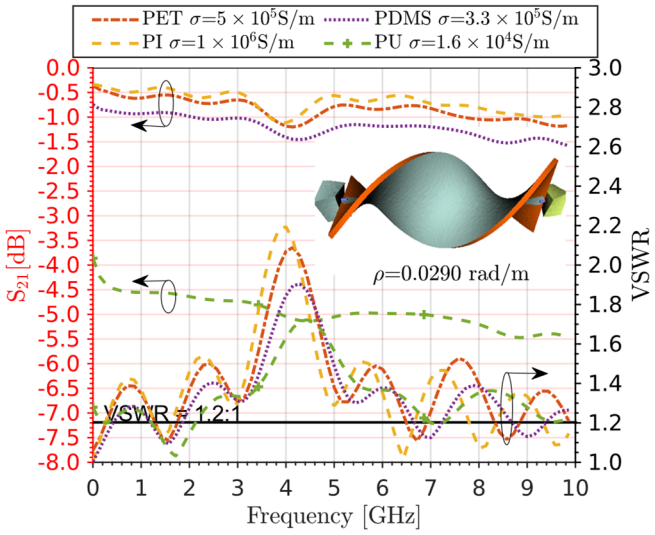


Figure 7.19 S_{21} and VSWR for 1mm PET, PI, PDMS, and PU substrates (GC deformed) with microstrip line with twisting angle ρ, 0 0.0290 rad/m respectively.

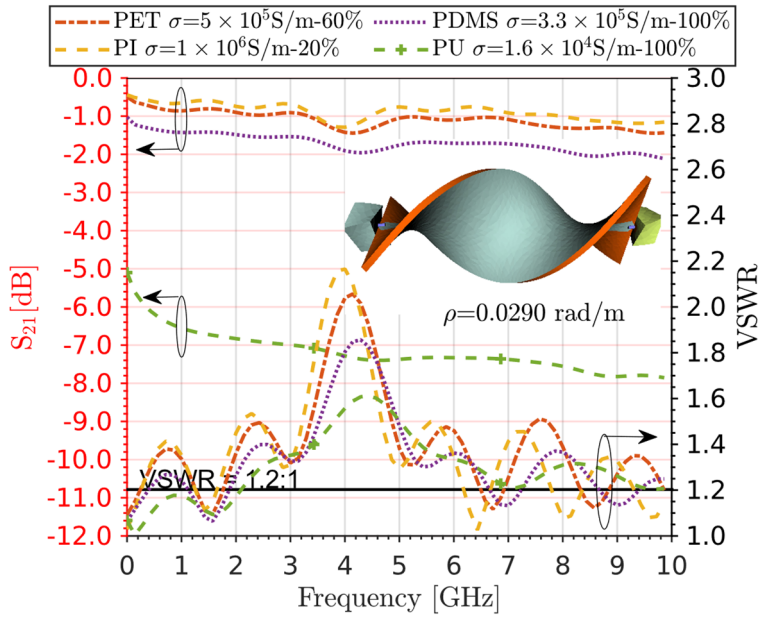


Figure 7.20 S_{21} and VSWR for 1mm PET, PI, PDMS, and PU substrates (GC deformed) with microstrip line with twisting angle ρ, 0 0.0290 rad/m respectively. Conductivity of line has changed according to [33, 34].

7.5 Conclusions

This Chapter provides holistic design guidelines for flexible microstrip interconnect with different flexible, semi-rigid, and soft materials.

The Chapter investigated flexible interconnects designed on a variety of flexible substrates, namely PET, PI, PDMS and PU. Both flat and deformed interconnects are considered. In contrast to traditional conformal interconnects whose geometry previously fixed and optimised, wearable and foldable interconnects must perform reasonably with the wide variety of deformations. This introduces a new set of challenges for RF engineer who focus on system performance from back-end to front-end of problems, such as (a) which substrate need to be used for desired performance and (b) designing for the in-situ performance.

In the first instant the impact of the SMA connector was considered. The signal trace is tapered with different types of taper transition regions and their performance analysed.

It has been shown that tapered printed line exhibits lower transmission loss compared to typical measurement loss figure of 1 inch. The results agree very well with published results [23, 24].

The Chapter compares the performance of 50 Ω interconnects designed for a variety of substrates with the performance of the standard rigid interconnect. In the 1st instance this is done for the case of flat interconnects, i.e., in the absence of the stress and strain. This is done systematically by gradually introducing the substrate and metallic losses. The results show that flexible interconnects fabricated on PET and PI substrates have the smallest transmission losses whilst interconnects fabricated on PU substrates have the highest losses. The losses are predominantly due to increased substrate and conductive losses of flexible dielectric and conductive materials.

The impact of bending deformation is discussed for a range of flexible interconnects and compared to the case of flat rigid interconnect. It has been shown that when metallic conductivity is neglected, bending deformation has insignificant effect compared to flat counterparts.

The Chapter then presented the use of GC method to generate interconnects with the twisting deformations. The distortion introduced by GC method is minimised using a compensation method proposed in Chapter 5. It is shown that twisting does not have significant impact on the EM performance of the interconnects which agrees well with the experimental results of [19]. The Chapter confirms that the computer graphics method can be used with confidence when assessing arbitrary deformations of components in flexible.

References

[1] J. Biggs *et al.*, "A Natively Flexible 32-bit Arm Microprocessor," *Nature*, vol. 595, no. 7868, pp. 532-536, 2021/07/01 2021, doi: 10.1038/s41586-021-03625-w.

[2] Q. Lyu, S. Gong, J. Yin, J. M. Dyson, and W. Cheng, "Soft Wearable Healthcare Materials and Devices," *Adv Healthc Mater*, p. e2100577, May 21 2021, doi: 10.1002/adhm.202100577.

[3] Y. Yang *et al.*, "A laser-engraved wearable sensor for sensitive detection of uric acid and tyrosine in sweat," *Nat Biotechnol*, vol. 38, no. 2, pp. 217-224, Feb 2020, doi: 10.1038/s41587-019-0321-x.

[4] C. H. Kim, D. H. Lee, J. Youn, H. Lee, and J. Jeong, "Simple and Cost-effective Microfabrication of Flexible and Stretchable Electronics for Wearable Multi-functional Electrophysiological Monitoring," *Sci Rep*, vol. 11, no. 1, p. 14823, Jul 20 2021, doi: 10.1038/s41598-021-94397-w.

[5] Y. Bonnassieux *et al.*, "The 2021 Flexible and Printed Electronics Roadmap," *Flexible and Printed Electronics*, vol. 6, no. 2, 2021, doi: 10.1088/2058-8585/abf986.

[6] K. Yan, J. Li, L. Pan, and Y. Shi, "Inkjet Printing for Flexible and Wearable Electronics," *APL Materials*, vol. 8, no. 12, p. 120705, 2020, doi: 10.1063/5.0031669.

[7] Y. Wu, S. S. Mechael, and T. B. Carmichael, "Wearable E-Textiles Using a Textile-Centric Design Approach," *Acc Chem Res*, vol. 54, no. 21, pp. 4051-4064, Nov 2 2021, doi: 10.1021/acs.accounts.1c00433.

[8] A. Kiourti, C. Lee, and J. L. Volakis, "Fabrication of Textile Antennas and Circuits With 0.1 mm Precision," *IEEE Antennas and Wireless Propagation Letters*, vol. 15, pp. 151-153, 2016, doi: 10.1109/lawp.2015.2435257.

[9] Z. Wang, L. Zhang, Y. Bayram, and J. L. Volakis, "Embroidered Conductive Fibers on Polymer Composite for Conformal Antennas," *IEEE Transactions on Antennas and Propagation*, vol. 60, no. 9, pp. 4141-4147, 2012, doi: 10.1109/TAP.2012.2207055.

[10] S. Choi *et al.*, "Highly conductive, stretchable and biocompatible Ag-Au core-sheath nanowire composite for wearable and implantable bioelectronics," *Nat Nanotechnol*, vol. 13, no. 11, pp. 1048-1056, Nov 2018, doi: 10.1038/s41565-018-0226-8.

[11] I. Cherukhin, S. P. Gao, and Y. X. Guo, "Fully Flexible Polymer-based Microwave Devices: Materials, Fabrication Technique, and Application to Transmission Lines," *IEEE Transactions on Antennas and Propagation*, pp. 1-1, 2021, doi: 10.1109/TAP.2021.3083855.

[12] R. A. Liyakath, A. Takshi, and G. Mumcu, "Multilayer Stretchable Conductors on Polymer Substrates for Conformal and Reconfigurable Antennas," *IEEE Antennas and Wireless Propagation Letters,* vol. 12, pp. 603-606, 2013, doi: 10.1109/lawp.2013.2260123.

[13] D. Ding, R. Li, J. Yan, J. Liu, Y. Fang, and Y. Yu, "Influence of Microcracks on Silver/Polydimethylsiloxane-Based Flexible Microstrip Transmission Lines," *Applied Sciences,* vol. 11, no. 1, 2020, doi: 10.3390/app11010005.

[14] A. Sarycheva, A. Polemi, Y. Liu, K. Dandekar, B. Anasori, and Y. Gogotsi, "2D Titanium Carbide (MXene) for Wireless Communication," *Science Advances,* vol. 4, no. 9, p. eaau0920, 2018, doi: 10.1126/sciadv.aau0920.

[15] X. Huang, T. Leng, K. H. Chang, J. C. Chen, K. S. Novoselov, and Z. Hu, "Graphene Radio Frequency and Microwave Passive Components for Low Cost Wearable Electronics," *2D Materials,* vol. 3, no. 2, 2016, doi: 10.1088/2053-1583/3/2/025021.

[16] X. Huang *et al.*, "Highly Flexible and Conductive Printed Graphene for Wireless Wearable Communications Applications," *Sci Rep,* vol. 5, p. 18298, Dec 17 2015, doi: 10.1038/srep18298.

[17] A. Lamminen *et al.*, "Graphene-Flakes Printed Wideband Elliptical Dipole Antenna for Low-Cost Wireless Communications Applications," *IEEE Antennas and Wireless Propagation Letters,* vol. 16, pp. 1883-1886, 2017, doi: 10.1109/lawp.2017.2684907.

[18] J. Wang, S. Lam, and E. G. Lim, "RF performance evaluation of microstrip lines printed on flexible polyethylene terephthalate (PET) films," in *2015 IEEE MTT-S International Microwave Workshop Series on Advanced Materials and Processes for RF and THz Applications (IMWS-AMP)*, 1-3 July 2015 2015, pp. 1-3, doi: 10.1109/IMWS-AMP.2015.7324924.

[19] S.-m. Sim, Y. Lee, H.-L. Kang, K.-Y. Shin, S.-H. Lee, and J.-M. Kim, "RF Performance of Ink-jet Printed Microstrip Lines on Rigid and Flexible Substrates," *Microelectronic Engineering,* vol. 168, pp. 82-88, 2017, doi: 10.1016/j.mee.2016.11.011.

[20] D. Mitra *et al.*, "Conductive Electrifi and Nonconductive NinjaFlex Filaments based Flexible Microstrip Antenna for Changing Conformal Surface Applications," *Electronics,* vol. 10, no. 7, 2021, doi: 10.3390/electronics10070821.

[21] Y. Shi, Z. Jiang, S. Lam, M. Leach, J. Wang, and E. G. Lim, "Multi-GHz Microstrip Transmission Lines Realised by Screen Printing on Flexible Substrates," presented at the 2017 IEEE Electrical Design of Advanced Packaging and Systems Symposium (EDAPS), 2017.

[22] X. Meng, P. Sewell, S. Phang, A. Vukovic, and T. M. Benson, "Modeling Curved Carbon Fiber Composite (CFC) Structures in the Transmission-Line Modeling (TLM) Method," *IEEE Transactions on Electromagnetic Compatibility,* vol. 57, no. 3, pp. 384-390, 2015, doi: 10.1109/temc.2015.2400055.

[23] H. Votsi, J. Urbonas, and P. H. Aaen, "Experimental Verification and Imaging of Radiation Due to Coaxial-to-Microstrip Transitions," in *2019 93rd ARFTG Microwave Measurement Conference (ARFTG)*, 7-7 June 2019 2019, pp. 1-4, doi: 10.1109/ARFTG.2019.8739235.

[24] S. Microwave, "Optimizing Test Boards for 50 GHz End Launch Connectors," 2007. [Online]. Available: https://mpd.southwestmicrowave.com/wp-content/uploads/2018/07/Optimizing-Test-Boards-for-50-GHz-End-Launch-Connectors.pdf

[25] R. Li *et al.*, "Laser-Scribed Lossy Microstrip Lines for Radio Frequency Applications," *Applied Sciences*, vol. 9, no. 3, 2019, doi: 10.3390/app9030415.

[26] D. Mitra *et al.*, "Conductive Electrifi and Nonconductive NinjaFlex Filaments based Flexible Microstrip Antenna for Changing Conformal Surface Applications," *Electronics*, vol. 10, no. 7, p. 821, 2021. [Online]. Available: https://www.mdpi.com/2079-9292/10/7/821.

[27] R. Corporations. "RO3003™ Laminates." Rogers Corporations. https://rogerscorp.com/advanced-electronics-solutions/ro3000-series-laminates/ro3003-laminates (accessed 02.02.2022, 2022).

[28] S. Microwave, "The Design & Test of Broadband Launches up to 50 GHz on Thin & Thick Substrates," 2011. [Online]. Available: https://www.hasco-inc.com/content/Technical_Articles/Design_and_Test_Broadband_Launches.pdf

[29] R. Corporations. "RO4350™ Laminates." Rogers Corporations. https://rogerscorp.com/advanced-electronics-solutions//ro4000-series-laminates/ro4350b-laminates (accessed 02.02.2022, 2022).

[30] D. M. Pozar, *Microwave Engineering*, 4th ed. Hoboken, N.J. : Wiley, 2012.

[31] Dowsil. "DOWSIL™ DA-6534 Adhesive Datasheet." DOWSIL™. https://www.dow.com/en-us/pdp.dowsil-da-6534-adhesive.04045124z.html (accessed 02.02.2022, 2022).

[32] B. Huber, J. Schober, M. Kaiser, A. Ruediger, and C. Schindler, "Rotate-to-bend Setup for Fatigue Bending Tests on Inkjet-printed Silver Lines," *Flexible and Printed Electronics*, vol. 3, no. 3, 2018, doi: 10.1088/2058-8585/aad5a4.

[33] R. Mukherjee, A. S. Dahiya, and R. Dahiya, "Torsional and Bending Endurance Analysis of Screen-printed Interconnects on Various Flexible Substrates," in *2022 IEEE International Conference on Flexible and Printable Sensors and Systems (FLEPS)*, 10-13 July 2022 2022, pp. 1-4, doi: 10.1109/FLEPS53764.2022.9781508.

[34] A. Christou, A. S. Dahiya, and R. Dahiya, "Finite Element Analysis of Stress Distribution in Soft Sensors Under Torsional Loading," in *2022 IEEE International Conference on Flexible and Printable Sensors and Systems (FLEPS)*, 10-13 July 2022 2022, pp. 1-4, doi: 10.1109/FLEPS53764.2022.9781555.

[35] E. Altinozen, I. Harrison, A. Vukovic, and P. Sewell, "Systematic generation of arbitrary antenna geometries," *IEEE Transactions on Antennas and Propagation*, 2021. [Online]. Available: https://nottingham-repository.worktribe.com/output/7022934.

[36] P. Sewell, T. M. Benson, C. Christopoulos, D. W. P. Thomas, A. Vukovic, and J. G. Wykes, "Transmission-line Modeling (TLM) Based upon Unstructured Tetrahedral Meshes," *IEEE Transactions on Microwave Theory and Techniques*, vol. 53, no. 6, pp. 1919-1928, 2005, doi: 10.1109/tmtt.2005.848078.

[37] P. D. Sewell, T. M. Benson, C. Christopoulos, D. W. P. Thomas, A. Vukovic, and J. G. Wykes, "Implicit Element Clustering for Tetrahedral Transmission-Line Modeling (TLM)," *IEEE Transactions on Microwave Theory and Techniques*, vol. 57, no. 8, pp. 2005-2014, 2009, doi: 10.1109/tmtt.2009.2025451.

[38] GGIEMR. "George Green Institute for Electromagnetics Research." https://www.nottingham.ac.uk/research/groups/ggiemr/our-research/large-scale-electromagnetic-modelling/utlm-unstructured-transmission-line-modelling.aspx (accessed 2021).

[39] S. W. Cheng, T. K. Dey, and J. Shewchuk, *Delaunay Mesh Generation*. CRC Press, 2013.

[40] P. D. Sewell, T. M. Benson, A. Vukovic, and X. Meng, "Complexity Reduction of Multiscale UTLM Cell Clusters," *IEEE Journal on Multiscale and Multiphysics Computational Techniques*, vol. 2, pp. 18-28, 2017, doi: 10.1109/jmmct.2017.2670613.

[41] D. Vital, S. Bhardwaj, and J. L. Volakis, "Bending and Twisting Tests for RF Performances of Textile Transmission Lines," in *2019 IEEE International Symposium on Antennas and Propagation and USNC-URSI Radio Science Meeting*, 7-12 July 2019 2019, pp. 2173-2174, doi: 10.1109/APUSNCURSINRSM.2019.8888541.

Chapter 8 Conclusions and Future Works

This Chapter highlights the significance of outcome and the main contribution of thesis along with the conclusion. Suggested direction of future works is discussed, highlighting the limitations of the current version of the deformation methodology and potential improvements.

8.1 Conclusions

Flexible antennas and interconnects play an indispensable role in high-frequency wireless applications as an essential component of wireless data transmission. Next-generation designs will involve new advanced manufacturing processes and materials for exhibiting high flexibility and reversibility. However due to their flexibility the components are prone to deformations that can take the form of bending, crumpling, twisting, and combinations of these effects. Therefore, it is important to assess to what degree the performance of flexible components is affected by these in-situ deformations. This poses new challenges for RF designer as to systematically define, the continuous problem space of the deformations is difficult. More practical approach is to identify a finite set of suitable deformations for a testing and then from these results extrapolate the impact of other possible deformations. It is imperative that systematic studies are undertaken to inform future designs and this Thesis has addressed a notable hurdle preventing this activity, namely the generation of robust deformed geometries of antennas and interconnects.

Chapter 2 overviews basics of antenna and interconnect figure of merit such as, reflection coefficient, voltage-standing-wave-ratio, radiation pattern, directivity, gain and realised gain, bandwidth. Then, the numerical modelling technique Unstructured

Transmission-line Modelling method introduced, then simulation software used as the main electromagnetic simulator for this thesis.

The aim of Chapter 3 reveals the main objective of conducting this research. This Chapter overviews the next generation of dielectric and conductive materials for flexible electronics. The most commonly used flexible dielectric substrates are polyethylene terephthalate, (PET), polyimide (PI), polydimethylsiloxane (PDMS), polyurethane (PU), and textiles. The most commonly used conductive materials are silver pastes, nanowires, graphene related materials and MXenes. The Chapter also overviews the reported antennas and interconnects with respect to the type of the deformation they are exposed to, namely, cylindrical bending, stretching and torsional deformation. The most studies are done experimentally. Although passive devices are enforcing a similar kind of cylindrical deformation for the width and length edge of antennas, where some of main resonant frequency are increasing with deformation, others are decreasing with raising rate of their resonant response. It is important to note that there are conflicting conclusions on the impact the cylindrical deformation makes on the antenna performance. For the case of cylindrical bending of antennas evidence the results of predicting uncertainties to usage with operational issues of in-situ performance or susceptibility to mechanical deformations. The Chapter concludes that the majority of experimental measurements and the computational analysis are predominantly considering the case of 1D cylindrical bending, and to a much smaller degree stretching and twisting deformation. Thus, it is concluded that there is a clear gap in the knowledge on the impact of other, more complex deformations, on flexible components performance.

The Chapter 4 overviews the issue of mapping a flat object to a curved surface and introduces a developable and non-developable surface. It states that a flat object cannot be mapped onto non-developable surface without introducing strain and stretch. the Chapter introduces several spatial deformation techniques for object manipulation that are commonly used in computer graphics, namely Mean Value Coordinates, MVC, Harmonic Coordinates, HC, and Green Coordinates, GC techniques. All three techniques use the cage to enclose the object and by manipulating the cage vertices the

deformations of the cage are smoothly transferred to the object. The methods differ by the amount of the distortion they introduce in the object and by the way they are computationally implemented. From the three techniques the GC method stands out as it introduces the minimal amount of distortion compared to MVC and HC techniques with slightly higher computational cost. The Chapter overviews the theoretical background of the GC method and also compares the distortion of the GC method against MVC and HC methods.

In Chapter 5 the GC method is used to generate arbitrary deformations of patch antennas. It has been shown that the GC method provides an approach to holistically generate arbitrary geometries without introducing the disruptive CAD artefacts that can either block or seriously undermine EM characterisation. However, the GC method introduces unwanted distortion into the object and it is important to examine whether these distortions are important in the context of EM simulations. To do that the GC method is calibrated for the simple case of 1D cylindrical bending for which no distortions should occur. The Chapter examines the impact of the GC parameters namely cage complexity and cage padding on the accuracy of the resulting 1D deformation. It was shown that the errors are insensitive to the cage complexity but that tight cages result in more accurate geometries. The Chapter shows that distortion errors introduced by GC method are significant and that they increase with increasing the deformations.

However, this can be successfully compensated for by using as pre-scaling approach and the Chapter 5 introduces two different simple compensation methods, namely Centre of Gravity (CG), and Width and Length (WL) compensation. The effectiveness of these approaches is assessed by comparing the EM performance of compensated GC antennas with the special cases of cylindrical bending antennas whose geometries are produced using exact Boolean geometry. WL compensation provides a more robustness approach compared the CG method for a wide range of deformations. Furthermore, with the compensation in place a good degree of insensitivity to method parameters such as the padding and complexity of the cage used has been shown which is important for undertaking broad range design studies. After calibration against a known canonical

case whose geometry can be exactly generated, final GC generated antenna performance in terms of return loss and radiation patterns have been examined and shown good agreement with published results. The Chapter shows that naïve use of the GC method introduces a systematic distortion that can significantly undermine EM simulations if not correctly compensated.

Chapter 6 explores the greater challenge of undertaking a systematic design sweep over a larger problem space of doubly curved deformations. It has been shown that pre-scaling for GC induced distortions is effective for these double curved surfaces and rapidly reduces non-physical distortion errors. The Chapter considers double curved deformations namely, spherical, saddle and twisting and explores a range of deformations for each case. According to the results, spherical bending of antenna shifts the resonant frequency of antenna to higher frequencies and that the concave spherical bending has particularly strong impact on the resonant frequency. However, saddle and torsion deformation tend to reduce the antenna resonant frequency and are more detrimental to antenna operation when deformations are applied along the length of antenna. Only consideration of simple cylindrical deformation can be overestimate or underestimate the antenna performance. The Chapter reveals that GC method is a promising design toolkit used to extract the impact of deformation on antenna performance and leads to a more accurate prediction of in-situ performance of an antenna.

In Chapter 7, flexible transmission lines with deformation and without deformation have been systematically investigated systematically. Transmission properties of a range of interconnects fabricated on a variety of substrates, namely PET, PI, PDMS, and PU have been reported. The computational study is further extended to assess the impact of the bending and torsion deformation of flexible interconnects. The deformed geometries are generated using the GC method. It is shown that torsion does not significantly impact the EM performance up to a specific deformation rate. The Chapter reported a holistic design guideline for the flexible, soft and semi-rigid materials. A range of substrates namely PET, PI, PDMS, and PU are systematically analysed and compared EM performance of interconnects under the impact of deformations, namely

bending and torsion for interconnects fabricated using. The transmission properties are analysed with regards to the substrate material, and metallic properties. This is done for a range of substrate and metallic print properties with the aim to ascertain the most resilient and stable platform for flexible electronics.

8.2 Future Works

The proposed cage-based deformation with the GC method described in this thesis can be used as a foundation to implement more complex geometry models for the EM study of predictive flexible and conformal components. Some of the suggested further applications of the GC method are highlighted in this section.

Studies of the strategically structured stretchable antenna and woven textile antenna have been extensively reported [1, 2]. The GC method, which is implemented in this thesis, can be directly extended to deliver geometric models for these types of antennas. Similarly, flexible frequency selective surfaces (FFS) [3] with woven or knitting nano-composite materials, substrates could be generated as an anisotropic structure. GC method could be used to directly deform the whole structure that would be otherwise very difficult to do point by point for complicated metamaterial patterns. Moreover, the deformability of FFS results in anisotropic stretching; hence, frequency detuning of array structure becomes elusive. This is one of the exciting areas of research that can be studied thoroughly.

A knitted textile waveguide is another component [4, 5] for which the analysis of the impact of deformations on its performance is important. These foams or dielectric materials filled with waveguides are used for X-Band applications. The GC can be used to design the waveguide to be resilient in the presence of deformations by using it in conjunction with inverse optimisation techniques such as swarm optimisation [6]. However, a much faster solver is needed to be combined with the GC method so that a large problem space can be explored.

The upgrade of single-core computation of GC method algorithm to shared or distributed systems implementation, or graphical core implementation is an area of development that can also be suggested. That becomes an essential factor in the model when modelling large-scale problems involving a wide range of microstrips or metal printed on large-scale structures, such as antenna printed on a plane fuselage, wing, or a frequency selective surface on a plane meta-radome. This large-scale deformation costs more run time than the dual and single antenna structures. Furthermore, multicore implementation of GC method is a specific computation of geometric integration of GC method is a suggested area of development that can add more wide area of EM problems coverage to the modelling with GC method.

The soft robotic field with intention of providing robots that adapt to the natural environment better than their traditional counterparts attracts significant attention. Soft robots are made from materials that could change passively based on environmental conditions and are based on soft materials, such as polymers and elastomers [7]. he shape of robots is morphed by applying voltage, pressure, magnetic field, and heat source to it [7-9]. The soft robot will have a flexible or soft antenna component placed on them for the purposes of communication that would also change the shape as the robot body is adapting to the environmental conditions. The GC method can be used to simulate soft robots with antenna scenarios. Therefore, the generation of their combined elastic behaviour coupled with physical excitation would allow for the direct predictive study of many different configurations, these could also be verified with measurements in the anechoic chamber. Furthermore, depending on the applied form of the physical excitation source in models, electromagnetic field behaviour is dynamically configurable for series triggering physical fields with embedded control systems. This is another interesting area of research that can be investigated.

References

[1] J. Zhu *et al.*, "Strain-Insensitive Hierarchically Structured Stretchable Microstrip Antennas for Robust Wireless Communication," *Nanomicro Lett*, vol. 13, no. 1, p. 108, Apr 9 2021, doi: 10.1007/s40820-021-00631-5.

[2] F. Nikbakhtnasrabadi, H. El Matbouly, M. Ntagios, and R. Dahiya, "Textile-Based Stretchable Microstrip Antenna with Intrinsic Strain Sensing," *ACS Appl Electron Mater*, vol. 3, no. 5, pp. 2233-2246, May 25 2021, doi: 10.1021/acsaelm.1c00179.

[3] L. Alonso-Gonzalez, S. Ver-Hoeye, M. Fernandez-Garcia, and F. Las-Heras Andres, "Broadband Flexible Fully Textile-Integrated Bandstop Frequency Selective Surface," *IEEE Transactions on Antennas and Propagation*, vol. 66, no. 10, pp. 5291-5299, 2018, doi: 10.1109/tap.2018.2858141.

[4] X. Jia, A. Tennant, R. J. Langley, W. Hurley, and T. Dias, "A Knitted Textile Waveguide," in *2014 Loughborough Antennas and Propagation Conference (LAPC)*, 10-11 Nov. 2014 2014, pp. 679-682, doi: 10.1109/LAPC.2014.6996485.

[5] X. Jia, A. Tennant, R. J. Langley, W. Hurley, and T. Dias, "Knitted Textile Waveguide Bending," in *2015 9th European Conference on Antennas and Propagation (EuCAP)*, 13-17 April 2015 2015, pp. 1-4.

[6] J. Robinson and Y. Rahmat-Samii, "Particle Swarm Optimization in Electromagnetics," *IEEE Transactions on Antennas and Propagation*, vol. 52, no. 2, pp. 397-407, 2004, doi: 10.1109/tap.2004.823969.

[7] M. Wehner *et al.*, "An Integrated Design and Fabrication Strategy for Entirely Soft, Autonomous Robots," *Nature*, vol. 536, no. 7617, pp. 451-5, Aug 25 2016, doi: 10.1038/nature19100.

[8] C. Yuan *et al.*, "3D Printed Reversible Shape Changing Soft Actuators Assisted by Liquid Crystal Elastomers," *Soft Matter*, vol. 13, no. 33, pp. 5558-5568, Aug 23 2017, doi: 10.1039/c7sm00759k.

[9] R. F. Shepherd *et al.*, "Multigait Soft Robot," *Proc Natl Acad Sci U S A*, vol. 108, no. 51, pp. 20400-3, Dec 20 2011, doi: 10.1073/pnas.1116564108.

Appendix A Algorithms for Green Coordinates

A.1 Green Coordinates Algorithm 2D

Input: cage $T = (\mathbb{V}, \mathbb{F})$, set of points $\Lambda = list(r'_p)$
Output: 3D GC $g^V_{v_i}(r'_p),\ g^F_{f_j}(r'_p),\ i \in I_{\mathbb{V}},\ j \in I_{\mathbb{F}},\ r'_p \in \Lambda$
`/*Initialization */`
Set all $g^V_{v_i} = 0\ and\ g^F_{f_j} = 0$
`/*Coordinates computation */`
foreach *point* $r'_p \in \Lambda$ **do**
  foreach *edge* $j \in I_{\mathbb{F}}$ with vertices v_{j_1}, v_{j_2} **do**
    $\boldsymbol{a} \leftarrow v_{j_2} - v_{j_1};\ \boldsymbol{b} \leftarrow v_{j_1} - r'_p$
    $Q \leftarrow \boldsymbol{a} \cdot \boldsymbol{a};\ S \leftarrow \boldsymbol{b} \cdot \boldsymbol{b};\ R \leftarrow 2\boldsymbol{a} \cdot \boldsymbol{b};$
    $BA \leftarrow \boldsymbol{b} \cdot \|\boldsymbol{a}\| n(f_j);\ SRT \leftarrow \sqrt{4SQ - R^2}$
    $L0 \leftarrow \log(S)\,; L1 \leftarrow \log(S + Q + R)$
    $A0 \leftarrow \frac{\tan^{-1}(\frac{R}{SRT})}{SRT}$
    $A1 \leftarrow \frac{\tan^{-1}((2Q+R)/SRT)}{SRT}$
    $A10 \leftarrow A1 - A0;\ L10 \leftarrow L1 - L0;$
    $g^F_{f_j}(r'_p) \leftarrow -\|\boldsymbol{a}\|/(4\pi)\left[\left(4S - \frac{R^2}{Q}\right)A10 + \frac{R}{2Q}L10 + L1 - 2\right];$
    $g^V_{j_2} \leftarrow g^V_{j_2} - \frac{BA}{2\pi}\left[\frac{L10}{2Q} - A10\frac{R}{Q}\right]$
    $g^V_{j_1} \leftarrow g^V_{j_1} + \frac{BA}{2\pi}\left[\frac{L10}{2Q} - A10\left(2 + \frac{R}{Q}\right)\right]$
  End
End

Figure A.1 2D Green Coordinates Algorithm [1, 2].

A.2 Green Coordinates Algorithm 3D

Input: cage $T = (\mathbb{V}, \mathbb{F})$, set of points $\Lambda = list(r'_p)$
Output: 3D GC $g^V_{v_i}(r'_p),\ g^F_{f_j}(r'_p),\ i \in I_{\mathbb{V}},\ j \in I_{\mathbb{F}},\ r'_p \in \Lambda$
`/*Initialization */`
Set all $g^V_{v_i} = 0\ and\ g^F_{f_j} = 0$
`/*Coordinates computation */`
foreach *point* $r'_p \in \Lambda$ **do**
  foreach *face* $j \in I_{\mathbb{F}}$ with vertices $v_{j_1}, v_{j_2}, v_{j_3}$ **do**
    foreach $l = 1,2,3$ **do**
      $v_{j_l} \leftarrow v_{j_l} - r'_p$
    $p \leftarrow \left(v_{j_1} \cdot n(f_j)\right) n(f_j)$
    foreach $l = 1,2,3$ **do**
      $s_l \leftarrow sign\left(\left((v_{j_l} - p) \times (v_{j_{l+1}} - p)\right) \cdot n(f_j)\right)$
      $I_l \leftarrow GCTriInt(p, v_{j_l}, v_{j_{l+1}}, 0);$
    $II_l \leftarrow GCTriInt(0, v_{j_l}, v_{j_{l+1}}, 0);$
      $q_l \leftarrow v_{j_{l+1}} \times v_{j_l};\qquad N_l \leftarrow q_l / \|q_l\|;$
    $I_l \leftarrow -\left|\sum_{k=1}^{3} s_k I_k\right|;\quad g^V_{v_i}(r'_p) \leftarrow -I\ ;$
    $w \leftarrow n(f_j) I + \sum_{k=1}^{3} N_k II_k;$

    If $\|w\| > \epsilon$ **then**
      foreach $l = 1,2,3$ **do**
        $g^F_{f_{j_l}}(r'_p) \leftarrow g^F_{f_{j_l}}(r'_p) + \frac{N_{l+1} \cdot w}{N_{l+1} \cdot v_{j_l}}$

  End
End

Procedure $GCTriInt(p, v_{j_l}, v_{j_{l+1}}, r'_p)$
$\alpha \leftarrow \arccos\left(\frac{(v_2 - v_1)\cdot(p - v_1)}{\|v_2 - v_1\|\|p - v_1\|}\right);\ \ \beta \leftarrow \arccos\left(\frac{(v_1 - p)\cdot(v_2 - p)}{\|v_1 - p\|\|v_2 - p\|}\right);$
$\lambda \leftarrow \|p - v_1\|^2 \sin^2(\alpha)\ ;\quad c \leftarrow \left\|p - r'_p\right\|^2;$
foreach $\theta = \pi - \alpha, \pi - \alpha - \beta$ **do**
  $S \leftarrow \sin(\theta)\ ;\ C \leftarrow \cos(\theta);$
  $I_\theta \leftarrow \frac{-sign(S)}{2}\left[2\sqrt{c}\arctan\left(\frac{\sqrt{c}C}{\sqrt{\lambda + S^2 c}}\right) + \sqrt{\lambda}\log\left(\frac{2\sqrt{\lambda}S^2}{(1-C)^2}\left(1 - \frac{2cC}{c(1+C) + \lambda + \sqrt{\lambda^2 + \lambda c S^2}}\right)\right)\right]$
return $\frac{-1}{4\pi}\left|I_{\pi-\alpha} - I_{\pi-\alpha-\beta} - \sqrt{c}\beta\right|$

Figure A.2 3D Green Coordinates algorithm [1, 2].

The procedure $GCTriInt\left(p, v_{j_l}, v_{j_{l+1}}, r_p'\right)$ in Figure A.2 computes Green Coordinates integral eq. (4.14) $\int_{r_p \in f_j} G\left(r_p, r_p'\right) d\sigma_{r_p}$ for each point of triangular face of the surface. For more detail derivation, we have referred to reader to [1, 2].

References

[1] Y. Lipman and D. Levin, "Derivation and Analysis of Green Coordinates," *Computational Methods and Function Theory*, journal article vol. 10, no. 1, pp. 167-188, June 01 2010, doi: 10.1007/bf03321761.

[2] Y. Lipman, D. Levin, and D. Cohen-Or, "Green Coordinates," *ACM Trans. Graph.*, vol. 27, no. 3, pp. 1-10, 2008, doi: 10.1145/1360612.1360677.